

# **UXO DISCRIMINATION IN CASES WITH OVERLAPPING SIGNATURES**

## **Final Technical Report**

### **SERDP PROJECT 1282**

**Approved for public release;  
Distribution is unlimited**

Mar 7, 2007

Kevin O'Neill

USA CoE Engineer Research and Development Center (ERDC)  
Hanover Site – Cold Regions Research and Engineering Laboratory

72 Lyme Rd

Hanover, NH 03755

[koneill@CRREL.usace.army.mil](mailto:koneill@CRREL.usace.army.mil)

<b>REPORT DOCUMENTATION PAGE</b>				<i>Form Approved OMB No. 0704-0188</i>	
<small>The public reporting burden for this collection of information is estimated to average 1 hour per response, including the time for reviewing instructions, searching existing data sources, gathering and maintaining the data needed, and completing and reviewing the collection of information. Send comments regarding this burden estimate or any other aspect of this collection of information, including suggestions for reducing the burden, to the Department of Defense, Executive Services and Communications Directorate (0704-0188). Respondents should be aware that notwithstanding any other provision of law, no person shall be subject to any penalty for failing to comply with a collection of information if it does not display a currently valid OMB control number.</small>					
<b>PLEASE DO NOT RETURN YOUR FORM TO THE ABOVE ORGANIZATION.</b>					
<b>1. REPORT DATE (DD-MM-YYYY)</b> 07-03-2007		<b>2. REPORT TYPE</b> Final Technical Report		<b>3. DATES COVERED (From - To)</b> 01-01-2002 to 30-09-2005	
<b>4. TITLE AND SUBTITLE</b> UXO DISCRIMINATION IN CASES WITH OVERLAPPING SIGNATURES				<b>5a. CONTRACT NUMBER</b>	
				<b>5b. GRANT NUMBER</b>	
				<b>5c. PROGRAM ELEMENT NUMBER</b>	
<b>6. AUTHOR(S)</b>  Kevin O'Neill				<b>5d. PROJECT NUMBER</b>  MM-1282	
				<b>5e. TASK NUMBER</b>	
				<b>5f. WORK UNIT NUMBER</b>	
<b>7. PERFORMING ORGANIZATION NAME(S) AND ADDRESS(ES)</b> U.S. Army Corps of Engineers, Engineer Research and Development Center				<b>8. PERFORMING ORGANIZATION REPORT NUMBER</b>	
<b>9. SPONSORING/MONITORING AGENCY NAME(S) AND ADDRESS(ES)</b> DoD Strategic Environmental Research and Development Program 901 North Stuart Street, Suite 303 Arlington, VA 22203 Phone: (703) 696-2117				<b>10. SPONSOR/MONITOR'S ACRONYM(S)</b>	
				<b>11. SPONSOR/MONITOR'S REPORT NUMBER(S)</b>	
<b>12. DISTRIBUTION/AVAILABILITY STATEMENT</b> Unlimited					
<b>13. SUPPLEMENTARY NOTES</b>					
<b>14. ABSTRACT</b> <p>New technology, modeling, and processing methods were investigated to attack the problem of buried UXO discrimination in highly contaminated sites. Such sites features a number of scenarios that challenge established subsurface sensing and data processing approaches, in particular 1) widely dispersed small metallic clutter items; 2) screening or obscuration of larger items by distributions of smaller clutter; 3) multiple target problems, in which a number of UXO-sized objects present simultaneously in the field of view of a sensor, so that their signals overlap and are difficult to distinguish. There were attacked with ultra-wideband electromagnetic induction (EMI) and fully polarimetric ground penetrating radar (GPR) developments were pursued, both individually and together. GPR was largely immune to problems caused by smaller near-surface metallic objects but suffered signal clutter from soil heterogeneity. While less soil sensitive, EMI was substantially hindered by discrete or dispersed near surface clutter, with some apparent discrimination advantage to be had from elevating the sensor. GPR helped suppress EMI false alarms in blind tests.</p>					
<b>15. SUBJECT TERMS</b> <p>Unexploded ordnance, UXO, Highly contaminated sites, clutter, environmental cleanup, electromagnetic induction, ground penetrating radar</p>					
<b>16. SECURITY CLASSIFICATION OF:</b>			<b>17. LIMITATION OF ABSTRACT</b>	<b>18. NUMBER OF PAGES</b>	<b>19a. NAME OF RESPONSIBLE PERSON</b>
a. REPORT	b. ABSTRACT	c. THIS PAGE			<b>19b. TELEPHONE NUMBER (Include area code)</b>
U	U	U	UU		

Reset

This report was prepared under contract to the Department of Defense Strategic Environmental Research and Development Program (SERDP). The publication of this report does not indicate endorsement by the Department of Defense, nor should the contents be construed as reflecting the official policy or position of the Department of Defense. Reference herein to any specific commercial product, process, or service by trade name, trademark, manufacturer, or otherwise, does not necessarily constitute or imply its endorsement, recommendation, or favoring by the Department of Defense.

## **ACKNOWLEDGEMENT**

The results in this report derived from work sponsored by the U.S. Department of Defense Strategic Environmental Research Program, under Executive Director Brad Smith, Technical Director Dr. Jeff Marqusee, and Munitions Management Program Manager Dr. Anne Andrews. HydroGeoLogic, Inc. of Herndon VA furnished administrative support. The project was led from the U.S. Army Corps of Engineers Engineer Research and Development Center, Cold Regions Research and Engineering Laboratory (ERDC-CRREL), under PI Dr. Kevin O'Neill. In addition to ERDC personnel, researchers participated from the Thayer School of Engineering at Dartmouth College, under Professor Keith D. Paulsen, with Dr. Fridon Shubitidze, Dr. Keli Sun, and Ms. Irma Shamatava; from the Center for Electromagnetic Theory and Applications at MIT, under Professor J.A. Kong, with Dr. Tomasz Grzegorzczuk and Ms. Beijia Zhang; and from the Ohio State University Electroscience Laboratory, under Dr. Chi-Chih Chen, with Mr. Hyoung-sun Youn. Heartfelt thanks are extended to all these individuals and organizations.



# TABLE OF CONTENTS

1. EXECUTIVE SUMMARY.....	14
2. EMI MODELING AND PROCESSING APPROACHES .....	20
2.1. The Method of Auxiliary Sources (MAS).....	22
2.1.1. Basic MAS Formulation .....	22
2.1.2. Implementation of the TSA in the FD MAS .....	26
2.1.3. The Multi-body MAS.....	28
2.2. The Hybrid Finite Element – Boundary Integral equation Method in the TD with TSA .....	32
2.2.1. Formulation.....	33
2.2.2. Time Domain Thin Skin Approximation .....	34
2.3. Analytical Forms: Magnetic Dipoles and Homogeneous Spheroids .....	37
2.3.1. Infinitesimal Magnetic Dipole Representations.....	37
2.3.2. Analytical Solutions for Homogeneous Spheroids .....	45
2.4. The Standardized Excitations Approach (SEA) .....	48
2.4.1. Basic Concept of the SEA.....	48
2.4.2. Use of the MAS to Construct "Universal" SEA Models in both FD and TD .....	51
2.4.3. Optimal SEA and the NSMC.....	55
2.4.4. Validation of the NSMC and the Invariance of $Q(f)$ .....	58
2.5. Ground Response Consequences for Processing .....	61
2.5.1. Phenomenology.....	61
2.5.2. Ground Effect on Signals from Buried Metallic Objects .....	69
2.5.3. Spatial Variability .....	71
2.5.4. Processing Implications .....	78
2.6. EMI Inversion and Classification Processing Implementations .....	80
2.6.1. Optimization by Differential Evolution (DE) .....	83
2.6.2. Simple Least Squares and Statistically Weighted Least Squares Objective Functions .....	85
2.6.3. Unconstrained Inference of $Q(f)$ followed by Constrained Pattern Matching .....	88
2.6.4. Dipole representations, isolation of contributors, and multi-stage processing.....	91
2.6.5. Blind Source Separation/ Independent Component Analysis .....	96
3. GROUND PENETRATING RADAR (GPR).....	104
3.1. GPR Parameter Extraction.....	104
3.2. UXO Classification by GPR Alone In Cases With Discrete Clutter .....	108
3.2.1. Setup and Signal Features of the UXO Alone .....	108
3.2.2. Scenario #1: Ordnance Scrap Edge-Up & 105 mm Projectile Tilted Outward.....	115
3.2.3. Scenario #2: Ordnance Scrap Flat & 105 mm Projectile Tilted Outward.....	120
3.2.4. Scenario #3: Edge-UP Ordnance Scrap & 105 mm Projectile Tilted Inward.....	125
3.2.5. Scenario #4: Ordnance Scrap Flat & 105 mm Projectile Tilted Inward .....	129
3.2.6. Conclusions.....	131
3.3. The New Improved GPR .....	131
4. EMI INTERACTION BETWEEN OBJECTS NEAR ONE ANOTHER .....	133

5.	EMI SENSING IN CASES WITH DIFFUSE DISTRIBUTIONS OF SMALL CLUTTER.....	140
5.1.	Overall Scenario, Assumptions, and Basic Relations.....	143
5.2.	Orientation Distributions .....	146
5.3.	Effect of Sensor Elevation $h$ .....	150
5.4.	Tests of Basic Formulation Against Measurements .....	153
5.5.	Layers of Finite Thickness .....	155
5.6.	Monte Carlo Analysis of Signal Statistics vs Sensor Elevation for Sparse Distributions ....	157
5.7.	Sensor Elevation in the Screening Problem.....	164
5.8.	Pattern Matching EMI Discrimination with Diffuse Clutter .....	169
5.8.1.	Simple Least Squares (SLS) .....	170
5.8.2.	Statistically Weighted Least Squares (SWLS) with Limited Data .....	174
5.8.3.	Pattern Matching SWLS for UXO Signals in Large Ensembles with Ideal Noise .....	178
5.9.	Summary Discussion .....	184
6.	DISCRETE CLUTTER AND UXO OBSCURATION IN EMI .....	185
6.1.	Phenomenology: Modeling Results.....	185
6.1.1.	AL Scrap above Steel UXO .....	187
6.1.2.	Steel Scrap above AL UXO .....	194
6.2.	Phenomenology: Measurement Examples.....	200
7.	DISCRIMINATION OF MULTIPLE OBJECTS VIA EMI ALONE.....	203
7.1.	Multiple Object Discrimination Using the NSMC .....	203
7.1.1.	Cases with Unknown Number of Objects.....	203
7.1.2.	NSMC Blind Tests for One or Two Objects – UXO and/or Discrete Clutter.....	205
7.2.	ICA Tests.....	207
7.2.1.	Effects of Gaussianity, constant and variable noise.....	208
7.2.2.	ICA using EMI spectra for metallic objects.....	214
8.	GPR AND EMI.....	219
8.1.	Obscuration by Shallow Targets: GPR vs EMI.....	220
8.2.	GPR, EMI, and Obscuration by Diffuse Clutter .....	222
8.3.	Multi-stage Collaborative Processing Example.....	228
8.4.	GPR and EMI Blind Processing of Testplot Data .....	235
8.4.1.	Processing Results.....	249
9.	REFERENCES .....	253
10.	ABBREVIATIONS .....	258
11.	PUBLICATIONS.....	260

12. APPENDIX A: NEW IMPROVED GPR .....	265
12.1. Introduction .....	265
12.2. Improved Radar Design.....	265
12.2.1. Front-End RF Design .....	266
12.2.2. Digital Receiver .....	269
12.2.3. Digital RF Source.....	272
12.2.4. System Clock Design .....	274
12.3. Operating Software.....	275
12.3.1. Data acquisition procedure: .....	277
12.3.2. Encoder Calibration .....	279
12.3.3. System Calibration .....	280
12.3.4. Antenna Calibration .....	281
12.3.5. Gray scale plot ( Waterfall data plot ).....	283
12.4. Improved small GPR ANTENNA .....	283
12.5. Conclusions .....	289
13. APPENDIX B: HFE-BIEM .....	290

## LIST OF FIGURES

Figure 1. Geometry of the problem, showing the object's physical surface ( $\partial D$ ), the external auxiliary surface $\partial D^{\text{ou}}$ on which the equivalent sources lie producing the fields inside the object, and the interior auxiliary surface $\partial D^{\text{in}}$ on which the equivalent sources lie that produce the external field. ....	24
Figure 2. Thin volume $V_d$ just below the physical surface of an object, the complete surface of which is $S_d$ . ....	27
Figure 3. Two bodies with their physical surrounding surfaces $S_\ell$ and also their surrounding and interior auxiliary surfaces. ....	29
Figure 4. Scattered magnetic fields versus frequency for real UXO oriented with the nose up (left), the tail up (middle), and horizontal (right). ....	30
Figure 5. Two objects, or pieces of an object, and the dashed auxiliary surfaces containing the equivalent source distributions $Q$ (charges) and $P$ (dipoles) needed to express the fields at the indicated point on $S_1$ . ....	31
Figure 6. Left, electric current loop producing magnetic field lines, near view. Right: same, far view. ....	38
Figure 7. Axial infinitesimal magnetic dipole moment (magnetic polarizability) inferred from data taken at different positions relative to the 105 mm projectile. ....	43
Figure 8. Axial infinitesimal magnetic dipole moment (magnetic polarizability) inferred from data taken at different positions relative to the 81 mm mortar. ....	43
Figure 9. Measured ratio of transverse to axial response by composite cylinder, using the GEM-3, with steel section towards the sensor during the axial orientation. ....	44
Figure 10. Same as Figure 9, but with aluminum section towards the sensor during the axial orientation. ....	44
Figure 11. GEM-3 measurements (markers) compared to modeling results from the displaced dipole model and from the SEA (FXM-RSS). ....	45
Figure 12. Piece of ordnance scrap about 10 cm in length, showing broader side (3~4 cm wide, left) and narrower side (~2cm wide, right). ....	47
Figure 13. Comparison of the GEM-3 response from the scrap shown above (lines) with the prolate spheroid solution (dots) for semi-axis lengths $a = 1.25\text{cm}$ , $b = 5\text{cm}$ , with $\sigma = 2.6 \times 10^6 \text{ (S/m)}$ , $\mu = 36\mu_0$ . Different line types indicate measurements from different angles (i.e. up and down for axial case and the four principle lateral directions for transverse case). Quadrature sign convention is reversed relative to other plots. ....	48
Figure 14. EMI response of steel cylinder, measured in the FD, reconstructed by the SEA with extension by MAS, and inverted to the TD. Left: FD; Right: TD; Top: Transverse orientation; Bottom: Axial orientation. ....	54
Figure 15. A UXO is surrounded computationally by a surface on which equivalent magnetic charges are distributed, represented through the parameters $\Omega$ . ....	56
Figure 16. The GEM-3D was used to obtain vector data for each of these UXO, buried, as well as for comparable sized clutter. ....	60
Figure 17. Comparison of $Q(f)$ for the 37 mm mortar to that obtained from processing for blind tests M2 (a, top) and M3 (b, bottom). ....	60
Figure 18. Inphase ground response $I$ as a function of sensor height (930 Hz), compared to theoretical line for $A/Z^3$ dependence from halfspace solution, with $A$ arbitrary. ....	63
Figure 19. Soil response in GEM-3 ppm vs log of frequency. ....	64

Figure 20. Hypothetical ground response to a downward step input of $u_{00}$ at $t = 0$ , showing two phenomena: instantaneous response, followed by relaxation.....	65
Figure 21. Hypothetical relaxation impulse response, for single relaxation time $1/a$ , with $a = 2\pi \times 10^3$ . Blue = imaginary part, red = real part. ....	66
Figure 22. Relaxation response in the FD from (50) with $\tau_1 = 10^{-6}$ s and $\tau_2 = 10^{-3}$ s. Left: FD impulse response. Right: corresponding TD step input response. ....	67
Figure 23. Ground response spectrum for a testplot observed at 10 cm elevation, with air response at 1 m subtracted. ....	68
Figure 24. Ben Barrowes's machined steel sphere S1. ....	70
Figure 25. Left: Blue rig over measurement patch in which sphere is buried about 3.5 cm deep (to its surface); GEM-3 to be inserted in the slots at each elevation, 10 cm apart. Right: Measurement of sphere in air, in reality level. ....	70
Figure 26. Measured impulse response of sphere in air (markers); and in soil, including soil response (green line); and with independently measured soil response subtracted from the latter (dashed orange). ....	71
Figure 27. Left, measurement surface over artificially smoothed soil surface. Right, ranges of response for different soils in this scenario, at sensor elevations $h_1 \sim 1$ cm, $h_2 \sim 6$ cm $h_3 \sim 11$ cm. ....	72
Figure 28. Grid measurements producing some of the data in Figure 27. ....	73
Figure 29. Example of spatial variability of soil response, inphase component, over a grid away from known targets in testplot #2. Top row Nov 27, bottom row Nov 29. Left column "ground level" ( $\sim 1.5$ cm elevation), right column $\sim 6.6$ cm elevation. ....	74
Figure 30. Plot of inphase de-measured inphase soil response vs position number, for testplot #2, over 25 point grid at 20 cm point spacing. ....	75
Figure 31. Quadrature component for same case as in Figure 29, left column, Nov 27. ....	77
Figure 32. Testplot #2 data contours at 810 Hz, Nov 27, for a case with target present. ....	79
Figure 33. Schematic representation of the fates of individuals $\alpha_1$ and $\alpha_2$ between the $m$ and $m+1$ generation in DE. ....	84
Figure 34. Items used in blind tests of the NSMC classification, on the basis of $Q(f)$ . ....	89
Figure 35. Left: 14 cm square clutter item placed 5 cm above and slightly offset from the approx 43 cm long UXO on the right. ....	91
Figure 36. Data from a 7 x 7 point grid of GEM-3 measurements above an assemblage of the two clutter items in Figure 35. Inphase component at 210 Hz. ....	92
Figure 37. Comparison of modeled inphase (solid) and quadrature (dashed) measured fields from two objects, corresponding to two (blue, magenta) measurement distances, over the center of the grid in Figure 36. Markers indicate measured values. ....	94
Figure 38. Three distributions with their respective kurtoses. ....	98
Figure 39. Results from two different ICA runs using FastICA to unmix pictures of Maxwell and Millikan. ....	101
Figure 40. Low noise ICA test. Left: input signals, corresponding to two sources and (bottom) some added Gaussian noise. Right: IC's output by FastICA. Numbers in upper right of each plot are the respective signal kurtoses. ....	102
Figure 41. Two target types, and their representations by sets of orthogonal magnetic dipoles. ....	103
Figure 42. GPR parameter extraction flow chart. ....	107
Figure 43. A 105mm projectile (tail visible) buried at a depth of one foot and inclined 45 degrees. ....	108
Figure 44. An elongated thin piece of ordnance scrap located close to a 45-degree inclined 105mm projectile. ....	109
Figure 45. Site layout of a 45-degree inclined 105 mm projectile and GPR passes conducted for collecting UWB fully polarimetric data. ....	110
Figure 46. Background-removed $S_{11}$ data and extracted CNR, ELF and ETO for Pass #1 (parallel to UXO, filtered to extract 100~600 MHz). ....	111

Figure 47. End diffractions and side reflections from an inclined UXO with different dipping angles. Left: steep; Right: slight .....	112
Figure 48. Background removed data ( $S_{11}$ & $S_{22}$ ) and extracted ELF and ETO for Pass #2 (DOT is transverse to UXO, offset to the left, as per Figure 45).....	113
Figure 49 Background removed data ( $S_{11}$ & $S_{22}$ ) and extracted ELF and ETO for Pass #4 (DOT is transverse to UXO, offset to the right, as per Figure 45). ....	114
Figure 50. An edge-up, elongated piece of ordnance scrap buried with a 105 mm projectile tilted away from the scrap. ....	115
Figure 51. Measured GPR data from Scenario #1, for paths #2, #4, and #6.....	117
Figure 52. Extracted features for the RIGHT object (scrap) from Path #2 for Scenario #1. ....	118
Figure 53. Extracted features for the LEFT object (UXO) from Path #2 for Scenario #1.....	119
Figure 54. A flat, elongated piece of ordnance scrap is buried with a 105mm projectile tilted away from the scrap. ....	120
Figure 55. Measured GPR data from Scenario #2 for paths #2, #4, and #6.....	122
Figure 56. Extracted features for the LEFT object from pass #2 for Scenario #2. ....	123
Figure 57. Extracted features for the RIGHT object from pass #2 for Scenario #2.....	124
Figure 58. Target arrangement in Scenario #3 - An edge-up, elongated piece of ordnance scrap is buried with a 105mm projectile tilted away from the scrap. ....	125
Figure 59. Measured GPR data from Scenario 3 for passes #2, #4, and #6.....	127
Figure 60. Extracted features for the LEFT object (scrap) from pass #2 for Scenario #3. ....	128
Figure 61. Target arrangement in Scenario #4 – A flat elongated ordnance scrap with a 105 mm projectile tilted towards the scrap.....	129
Figure 62. Measured GPR data from Scenario 4, for paths #2, #4, and #6.....	130
Figure 63. Integrated new dual-channel GPR radar with a miniaturated HFB antenna.....	132
Figure 64. Measurement and modeled scattered fields from the two-cylinder combination with sensor above. a) stainless steel up, magnetic steel down; b) magnetic steel up, stainless down; c) horizontal.....	134
Figure 65. Scattered fields from axial excitation of two cylinders of diameter $2a$ , placed end to end, at different separations $d$ . Solid line = simple superposition; dashed markers = full interaction. ....	135
Figure 66. Same as Figure 65, but for spheres instead of cylinders.....	136
Figure 67. Inphase and quadrature components of the scattered field from a magnetic sphere. ....	137
Figure 68. Near field responses $\mu_r \mathbf{H} $ for $d = a/2$ , when both objects are magnetic. Left: near low frequency limit; Right: near high frequency limit.....	138
Figure 69. Top: 40 cm diameter GEM-3 sensor head above a manually randomized dense surface distribution of steel spheres; Bottom: Similarly randomized dense distribution of short AL cylinders spread over approximately 1.2 m by 1.2 m. ....	141
Figure 70. A sparse distribution of clutter items, some collected from firing ranges, relative to 10 cm spacing of grid marks. ....	142
Figure 71. A sensor resides at the origin, above the ground surface. A clutter layer extends from $z =$ $h$ to $z = d$ .....	143
Figure 72. Local scatterer axes ( $x_t, y_t, z_t$ ) and associated rotation angles, in relation to the global system.....	147
Figure 73. GEM-3 quadrature response vs frequency, for different sensor elevations over the clutter layer in Figure 69. ....	154
Figure 74. Markers: GEM-3 response magnitude vs antenna height above a dense surface distribution of randomly dispersed pellets, “BB’s” (30 Hz) and of the steel spheres (11 kHz) and of the AL cylinders in Figure 69 (930 Hz). ....	155
Figure 75. Calculated GEM-3 responses $R$ from well-distributed clutter in layers of various thicknesses $t$ , compared to a line with log-log slope of $-3$ for $R \sim 1/h^3$ .....	156
Figure 76. Sparse clutter example used in measurements, on 10 cm grid .....	158

Figure 77. GEM-3 signal contours 10 cm above the sparse clutter distribution. Top: 30 Hz; Middle: 930 Hz; Bottom: 47.8 kHz. ....	159
Figure 78. Simulations of response vs height from randomized 4 m <sup>2</sup> surface layers of anisotropic clutter items beneath a dipole source, with $N_p = 100$ , $N_{min} = 20$ , $\langle N_c \rangle = 26$ and $StdDev\{N_c\} = 3.7$ , showing (dashed) envelope of one standard deviation about $\langle  H_z  \rangle$ .....	161
Figure 79. The percent StdDev of $ H_z $ is approximately proportional to $1/h$ .....	161
Figure 80. $N_p = 150$ , $N_{min} = 30$ , $\langle N_c \rangle = 37$ and std dev $N_c = 8$ .....	162
Figure 81. $StdDev\{ H_z \}$ for $N_p = 150$ , $N_{min} = 30$ , $\langle N_c \rangle = 37$ and $StdDev\{N_c\} = 8$ as in case of Figure 80, for both dipole source and uniform excitation field.....	162
Figure 82. Average magnitude of deviation of received $H_z$ from the locally modeled value $H_{zm} = A/h^4$ for different clutter densities. ....	163
Figure 83. Setup for analysis of SCR vs sensor height, with target (red) below surface.....	164
Figure 84. Received signals as a function of antenna height under a dipole primary field, for surface and half space clutter layers, and from a discrete object at indicated depths below ground surface. ....	165
Figure 85. SCR relative to its value at the initial sensor height $h_0$ , as a function of $h/h_0$ .....	167
Figure 86. Independently normalized quadrature components measured with the GEM-3, for the surface layer of steel spheres and for the vertical large steel cylinder, each alone. ....	168
Figure 87. Response from randomized surface layer of steel spheres with the large vertical steel cylinder beneath, for successive antenna heights above the surface between $h_1 \sim 18.3$ cm and $h_4 \sim 33.5$ cm.....	169
Figure 88. Target #1 (correct answer) and others sought by pattern matching in signals contaminated by diffuse clutter.....	171
Figure 89. Simulated spectra over a 5 by 5 grid for 81 mm UXO buried in magnetic soil, with (blue) and without clutter (magenta) from a scattering of dipoles.....	171
Figure 90. Residual mismatch (objective function value) at convergence when different possible targets are sought in cluttered synthetic signals. The 81 mm UXO correctly produces the lowest mismatch. ....	172
Figure 91. Three possible UXO's sought in the actual cluttered signal, using spheroidal mode based SEA to find best match with observed (scalar) magnetic fields.....	173
Figure 92. Correct target (188) produces the lowest mismatch with the case that includes its signal plus clutter. ....	173
Figure 93. Mean (left) and standard deviation (right) of measurements over the clutter in Figure 70, as functions of frequency. ....	175
Figure 94. Values of target $a$ and $b$ obtained from inversion for different depths of target below the clutter, using the SLS and SWLS optimization formulations. ....	176
Figure 95. Performance of the Bayesian inspired system (BIS = SWLS) vs SLS for characterizing a UXO-sized object beneath the clutter in Figure 70. ....	176
Figure 96. Standard deviation of inferred $a$ and $b$ from 100 random realizations ....	177
Figure 97. comparison of SEA modeled (line) and measured response (markers) for 105 mm projectile.....	180
Figure 98. Variation of inferred parameters in sequence of optimization cases, comparing simple least squares (SLS) and statistically weighted least squares (SWLS) objective function performances. ....	182
Figure 99. Model for flattened scrap above a UXO-sized target. ....	186
Figure 100. Response spectra for flattened AL scrap and steel UXO-like target, separately, under unit magnitude axial primary field and an observation point 1 m from the center of each target.....	187
Figure 101. Signal when AL scrap is located above a steel UXO-like target, with dipole sensor at various elevations $h$ . Solid lines are inphase component, dashed quadrature. ....	188

Figure 102. Normalized time domain solutions for the same case as in Figure 101, translated to the time domain for a perfect step shutoff of the primary field.....	189
Figure 103. Steel UXO and AL scrap, each responding alone in the TD to sudden turn on of a uniform primary magnetic field at time = 0, observed from 1 m away.....	190
Figure 104. Same as in Figure 102, but for a perfect step turn-on of the primary field (dipole source), with curves normalized to the same initial magnitude. ....	191
Figure 105. Response from AL oblate scrap over steel UXO, under uniform primary field, observed at various elevations h. Solid lines are inphase component, dashed quadrature. ....	192
Figure 106. Normalized TD responses for oblate AL scrap and steel UXO, under a uniform primary field, each observed alone from a large distance or in combination at various elevations h above the scrap. ....	193
Figure 107. Turn on case for flattened AL scrap over steel UXO under uniform primary field, with all responses normalized to be the same magnitude at earliest time. ....	194
Figure 108. Reference response spectra of oblate steel scrap and an AL "UXO" alone, for a uniform, unit magnitude axial primary field and an observation point 1 m from the center of each target.....	195
Figure 109. Response from the combination of steel scrap above an AL UXO, at various observation elevations h, under a uniform primary field. ....	196
Figure 110. FD response of flattened steel scrap over the AL UXO, with dipole source and observation point at various elevations h. ....	198
Figure 111. TD decay curves for the AL UXO and various steel scrap items described in the text, each alone under a uniform primary field, observed in the positions in Figure 99 with h = 87 cm. ....	199
Figure 112. Signal contours at low, medium, and high frequency, on a plane over the vertical UXO and offset horizontal steel plate. Left column: Inphase component; Right: Quadrature component. ....	201
Figure 113. Left column: Response spectra with (top) and without (bottom) the steel plate in the position shown by the UXO's tail. ....	202
Figure 114. GEM-3 signal profiles over a measurement grid above a vertical 81 mm mortar and a nearby piece of ordnance scrap. ....	204
Figure 115. Left: Match of Q(f) to UXO that was present. Right: Inferred null object for second object, when none was present.....	205
Figure 116. The three UXO's used as unknowns in the NSCM multi-object blind test. ....	206
Figure 117. Left to right: clutter items 16, 12, and 20 used in the NSCM multi-object blind test. ....	206
Figure 118. Signals to be mixed, with their respective kurtoses (left); value distributions for each (right).....	209
Figure 119. Signals to be mixed, with their respective kurtoses (left); IC's obtained from processing of three mixtures (right). ....	210
Figure 120. Signals to be mixed, with their respective kurtoses (left); IC's obtained from processing of 500 mixtures (right) ....	211
Figure 121. Signals to be mixed, with their respective kurtoses (left); IC's obtained from processing of 500 mixtures with invariant noise just added at different percentages (right).....	212
Figure 122. Same as previous figure, but with results (right) when different noise is added to each mixture. ....	213
Figure 123. Real and imaginary parts of signals vs frequency, from spheroids 1 and 2 (left), with their distributions of value over frequency (right). ....	216
Figure 124. Real (inphase) components of the two spheroidal contributors. Left: original signals. Right: Corresponding extracted IC's.....	217
Figure 125. Imaginary (phase quadrature) components of the two spheroidal contributors. Left: original signals. Right: Extracted IC's .....	218



Figure 126. Left: GPR profile along a survey line (horizontal axis) over two UXO's, one shallow and the other deeper. Vertical time axis corresponds approximately to depth. Right: EMI signal contours over a horizontal surface on the testplot above the location of the targets...	221
Figure 127. Top: plot of ground under which 105 mm projectile (middle) is buried. Bottom: GPR profile of measurements along the string across the plot. ....	224
Figure 128. GPR profile (bottom), along same measurement transect as in the previous figure, but with the medium intensity clutter mat emplaced above the target. ....	225
Figure 129. EMI signal contours measured over the 105 mm UXO, as emplaced for measurements in Figure 127 and Figure 128. ....	226
Figure 130. Same case as in previous figure, but after addition of the clutter mat on the ground surface. ....	227
Figure 131. Example EMI signal contours over the scrap plus 105 mm combination, on a 1 m by 1 m grid. ....	229
Figure 132. Upper left: Ordnance scrap and 105 mm projectile, in approximately the relationship in which they are to be buried. Upper right: survey path geometry. $S_{11}$ (lower left) and $S_{22}$ (lower right) signal profiles along path 2. ....	230
Figure 133. Different polarizations in the same GPR profile indicate two objects. Analysis of GPR processing parameters produces estimates of object properties. ....	231
Figure 134. Magnetic polarizability values obtained for the two objects by optimization. ....	232
Figure 135. Two UXO's and their matching factor $\alpha$ values, for object #1. ....	233
Figure 136. UXO selection used in the testplots, with more than one of some types used. ....	237
Figure 137. Clutter items used in the testplot scenarios, in addition to two steel spheres. ....	238
Figure 138. Different soil conditions were established in each concrete walled testplot. ....	239
Figure 139. Plots #3 and #4 base layers. ....	240
Figure 140. Heterogeneous material in Plot #3: Left: base; right: added top layer. ....	240
Figure 141. Grain size distribution for base of Plot #3, containing predominately New England Silt. ....	241
Figure 142. Grain size distribution for base of Plot #4 and top of Plot #3, showing strong silt and clay fractions. ....	242
Figure 143. Testplot #2 target arrangements. $s$ = separation of target edges; $d$ = depth to shallowest point. ....	243
Figure 144. Testplot #3 target arrangements. ....	244
Figure 145. Testplot #4 target arrangements. ....	245
Figure 146. Top: GEM-3 surveys were performed over grids over each target cluster within plots #2, #3, and #4. Bottom, left: Grid of points at 10 cm increments for survey at soil level; right, same for raised grid. The peg at the center of the sensor head fits into holes at each designated position. ....	247
Figure 147. GPR cart with antenna pulled behind. ....	248
Figure 148. GPR survey pass pattern on testplots, with half meter spacing between lines. ....	248
Figure 149 New OSU/ESL GPR System Block Diagram. ....	266
Figure 150 Hardware of the new dual-channel GPR radar. ....	268
Figure 151 Integrated new dual-channel GPR radar with a miniaturated HFB antenna. ....	269
Figure 152 Conventional radar receiver architecture employing analog devices. ....	270
Figure 153 New radar receiver architecture utilizes digital receiver design. ....	270
Figure 154 OSU/ESL digital receiver block diagram. ....	271
Figure 155 Dual channel digital receiver developed and built by OSU-ESL, originally with the support of the MIT Lincoln Laboratory. ....	272
Figure 156. Digital RF source block diagram. ....	273
Figure 157 DDS boards for generating phase-locked RF and LO signals. ....	274
Figure 158. Digital synthesizer (SPLH100SB) for supplying clock source. ....	275
Figure 159 GPR Operating Software GUI Interface. ....	278
Figure 160 Flowchart of the New OSU/ESL GPR Operating procedure. ....	279

Figure 161 Popup window for the encoder calibration.....	280
Figure 162 Popup window for the system calibration .....	281
Figure 163 Antenna calibration procedure.....	282
Figure 164 Window for the waterfall data plot.....	283
Figure 165 Profile and actual design of the miniaturized UWB dual-polarization HFB antenna.....	285
Figure 166 Termination of the antenna with a 120 $\Omega$ lump resistances. ....	285
Figure 167 The miniaturized UWB HFB antenna shielded by the ground cavity. ....	286
Figure 168 S11 response comparison between the old HFB and new miniaturized HFB antenna. (Targets were drainage pipes under a parking lot) .....	287
Figure 169 S22 response comparison between the old HFB and new miniaturized HFB antenna. (Targets were drainage pipes under a parking lot) .....	288

## 1. EXECUTIVE SUMMARY

This document constitutes the final technical report for SERDP project #1282, UXO Discrimination in Cases with Overlapping Signatures. The work was carried out in response to SON NUMBER: UXSON-02-01, dated 9 Nov 2000, UXO Site Characterization And Remediation Alternatives For Highly Contaminated Sites. It focused on subsurface remote sensing for UXO discrimination in highly contaminated environments. “Highly contaminated” can refer either to the density of UXO’s or of clutter or both. Three scenarios were targeted for investigation:

1. Fragment cloud: many small metallic non-UXO items together, which must be distinguished from a target of interest;
2. The screening problem: a single UXO-sized object beneath or among a distribution of smaller fragments;
3. Few sizeable objects: two UXO-sized objects close enough together so that their sensor signals overlap spatially.

The technologies applied consisted of UWB electromagnetic induction (EMI) sensing, for the most part over a frequency range from about 30 Hz up to about 50 kHz; and UWB fully polarimetric ground penetrating radar (GPR), operating from about 10 MHz up to about 800 MHz. These were used both separately, to investigate the characteristics and performance of each; and together, to investigate where the two technologies, with some innovative processing, might help one another.

A diverse arsenal of modeling and processing approaches was employed. For EMI, modeling included the use of infinitesimal magnetic dipole idealizations, new analytical solutions for spheroidal objects, and detailed numerical attacks based on first principles physics. Substantial limitations are shown for the infinitesimal dipole models of UXO type objects. Nevertheless these models can offer some clues as to the generic nature of an object, hinting at rotational symmetry and directional dominance. Because they are simple to compute, they are useful for helping to infer the number and general character of objects present when more than one contributes to some data at hand. Perhaps most crucially, while non-unique and incapable of reliable prediction, they can serve as functional equivalent sources for each of multiple contributing objects. This can allow the analyst to extract the signals for

individual objects, each of which can then be analyzed by more advanced methods (multi-stage processing).

The new EMI analytical solutions developed for both oblate and prolate spheroids served many useful purposes in this project. Innovative measures brought to bear for evaluating special functions in problematical ranges removed any remaining restrictions on the domain of applicability within the EMI band. In addition to providing the “gold standard” for testing numerical models and for examining basic EMI phenomenology, they provided proxies for both UXO-like and clutter items under diverse scenarios studied.

First principals numerical solutions developed were a Hybrid Finite Element – Boundary Integral Equation Method (HFE-BIEM) body of revolution (BOR) formulation in the time domain; and a BOR Method Of Auxiliary Sources (MAS) program, producing solutions in either the frequency or time domains. Within the BOR restriction, these were capable of modeling efficiently almost any variation of geometry and material properties. The MAS particularly formed the basis for a number of fundamental studies of object interaction, obscuration, and general EMI phenomenology for highly contaminated scenes. An equally rigorous formulation designed for much faster execution – as in optimization computations – is the Standardized Excitations Approach (SEA). This synthesizes an object’s total response in terms of its responses to each of a set of individual, fundamental excitations. A superposition of these excitations can describe any complete excitation. Hence the corresponding complete response consists of the same superposition of known responses to each such excitation. The method is fast, and includes all relevant physical effects, such as near and far field differences, arbitrary material and geometrical heterogeneity, and internal interactions within the object. An object’s basic responses to each fundamental excitation can be obtained either numerically or experimentally.

A specialization and optimization of the SEA, as well as a development in its own right, is the Normalized Surface Magnetic Charge (NSMC) formulation. This innovative system is the fastest of the SEA’s devised. It also defines new quantities that show discrimination potential, central among them being the total (integrated) NSMC, denoted  $Q$ . This represents a kind of magnetic capacitance that can be derived for any object, possessing its own frequency spectrum or time behavior. Inference of the  $Q$  spectrum from data for unseen objects illustrates that it can be used to identify objects from known classes quite effectively. Processing succeeded in separating the distinct  $Q$ ’s of contributing objects when more than one contributed to a given set of data.

Optimization calculations for inversion and classification require both an objective function to be minimized and a search method for finding the minimum. Inspired by – but not rigorously following – Bayesian statistical forms, we construct statistically weighted least squares (SWLS) functionals as objective functions, to be compared with simple least squares (SLS) formulations. The purpose of introducing the SWLS forms was to implement some way of including the kind of clutter statistics that might be derived from highly contaminated environments. In many instances, the SLS and SWLS objective functions were subjected to a recent descendent of the Genetic Algorithm, Differential Evolution (DE), as a global search algorithm that is well-designed to avoid local minima. All this was applied in the processing of EMI data for discrimination in environments with widespread small clutter items, as described below.

Explorations of a Blind Source Separation (BSS) formulation using Independent Component Analysis (ICA) showed that results depend significantly on how Gaussian the distribution of signal values is from contributing sources. The BSS/ICA formulation separates contributing signals based on the assumption that individual coherent signals are statistically independent of one another and each is less Gaussian than any mixture of them, the ultimate mixed signal being noise. Investigations here used a popular freeware BSS/ICA algorithm that has been applied in other studies related to UXO discrimination. Measuring “Gaussianity” in terms of kurtosis, results of simple tests with mixtures of two signals show that the more Gaussian the signals of interest are, the more difficulty ICA seems to have correctly identifying/extracting them. Empirically, useful thresholds found were found to be kurtosis values greater than about ten for “very non Gaussian”; and less than about three for “very Gaussian.” In these terms, performance was worst when two signals to be separated both met the “very Gaussian” criterion. Further, when one of the signals classes as very Gaussian, the other signal must have a kurtosis of greater than 10 or else the solutions cannot be identifiable as corresponding to the original sources.

Very non-Gaussian signals were required when noise was present. Most significantly, even modest noise that varied mixture by mixture wreaked havoc on the BSS/ICA processing. Further, UXO EMI spectra only vary smoothly over the band, between high, low, and mid-frequency values. From the point of view of BSS/ICA, their Gaussianity may be marginal. Probably more significant is that realistic spectra from contrasting objects may not be sufficiently statistically independent for the BSS/ICA to succeed. This reason is suggested for the failure of the BSS/ICA algorithm to separate some example EMI signatures. Overall, we conclude that the applicability of BSS/ICA to the UXO EMI sensing problem remains to be shown.

Experimental and simulation EMI evidence both showed case dependent indications that nearby metallic objects might or might not interact significantly. Detailed investigation of key cases revealed that interaction will only be significant, from the point of view of observation from some distance, when two magnetic (permeable) bodies are near one another. Two non-permeable objects, or one permeable and one non-permeable object, will not show evidence of interaction in signals obtained on the order of one characteristic length away. Numerical examination of fields close around and between nearby objects, together with considerations of basic EMI physics, suggests explanations for this. Among other things, this means that one can conveniently simulate many sorts of heterogeneous objects by just superposing signals from separate homogeneous objects, taking their relative locations into account, even if they are extremely close together (e.g. touching). To show significant evidence of interaction, permeable objects must be separated by only a fraction of their radius-equivalent  $a$ , when  $a$  is also approximately the characteristic length over which they are near one another; and  $a$  must be a significant fraction of the other dimensions of the object.

Analyses also reveal that in EMI sensing discrete objects do not interact by shadowing or blocking signals from one another. This is implicit in the conclusion that simple superposition of separate responses provides accurate portrayal of combined responses from two objects in so many circumstances. The potential fields involved have no difficulty “going around” one object to impinge on another, discounting combinations of objects with relative dimensions beyond the realm of consideration here (e.g. an extremely broad metal plate completely covering and extending far beyond the edges of another object).

An analytical theory of EMI response by well-distributed, dispersed small clutter items is presented. This shows that signal strengths as a function of sensor elevation will obey power laws different from those that apply to discrete objects, such as UXO's. This holds regardless of the orientation distribution that applies to the clutter population. For sparse clutter distributions, Monte Carlo simulations reveal that the same power laws apply as in well-distributed cases, but in a statistical sense, i.e. on average. In investigations of the screening problem, results indicate that elevating the sensor may improve the signal to clutter ratio (SCR). Benefits will be greater for dipole type as opposed to uniform field antennas; more benefit is gained the deeper a target is relative to the depth of the diffuse clutter. We note that elevating a dipole-type sensor brings the danger of diminishing the overall signal strength to the level of insuperable background noise. Discrimination exercises with the SLS and SWLS formulations suggest significant gains from including approximate clutter statistics in the optimizations. One may need

specific noise floor protection, weighting, and possibly data segmentation, beyond the precepts of the ideal statistical formulations.

Both measurement and modeling show that a shallower, discrete clutter-like object easily obscures a deeper UXO-like object in EMI sensing. This assumes that the clutter object is some significant fraction of, but is notably smaller than the size of the UXO-like object. Obscuration occurs purely by virtue of the greater magnitude of its response, not via any electromagnetic interaction, signal blockage or shadowing. Again, in some instances elevation of the sensor helps, with the attendant danger of intolerable overall signal attenuation. Ability to distinguish a deeper UXO-like item is better for transmitted primary fields that are more uniform in space, as from larger loop antennas. In the time domain, with a non-ferrous clutter item above a ferrous UXO, one may benefit from sensing in the “turn on” mode, in which signals are recorded while the transmitter is active.

Blind tests of the NSMC-based EMI processing were performed, using lab data from UXO’s and clutter items in air. When significant signal strengths were obtained simultaneously from both of two contributing objects, the processing was able to distinguish and characterize each object successfully, even though their signals overlapped greatly.

Ground penetrating radar parameter extraction focused on late time responses, in which only resonances from elongated objects persist; and on polarimetric effects that highlight directional sensitivity of reflections from UXO-like objects. The processing quantifies a measure of target elongation via the Estimated Linearity Function (ELF); of azimuthal orientation via the Estimated Target Orientation (ETO); and of resonant frequency response (and implied target length) via the Complex Natural Resonance (CNR). In backyard sandbox tests with two nearby targets, these parameters were able to highlight the contributions of each item when they were differently oriented and separated so that their signals did not overlap too greatly. In a multi-stage, collaborative GPR-EMI processing example, GPR-derived estimates of target number, location, and orientation were fed into dipole-based EMI processing. The latter distinguished the signal emanating from one object as being UXO-like, unlike that from a large piece of nearby ordnance clutter. The next stage of more advanced, SEA-based processing correctly identified the UXO.

In additional sandbox GPR tests, for UXO inclinations that projected the main UXO response directly over a clutter item, the GPR processing of data from a pre-existing radar was unable to distinguish the items very well. Overall, the large physical footprint of the pre-existing system, as well as

its unwieldiness, hampered discrimination acuity. Therefore a new smaller, faster, handier system was developed that allowed more localized querying of designated areas of interest, with greater data density. The system included a miniaturized antenna that retained lower GPR frequency capability and broad bandwidth; an advanced digital down converter and direct digital frequency synthesis. The new system was also outfitted with a convenient, user-friendly GUI, enabling the user to calibrate and control the system readily and to monitor data acquisition effectively.

For blind tests, both EMI and GPR surveying was done in three outdoor testplots, with moist, (dielectrically) cluttered, heterogeneous soil, containing a total of 15 multi-target scenarios. These included single targets or clusters of two targets, any of which could be either clutter items or UXO's. When two targets were present, they were clustered closely enough so that their sensor signals overlapped spatially at least to some degree. On a target-by-target basis, EMI processing based on the NSMC correctly indicated UXO's in a strong majority of the cases (73% to 77%). The false alarm rate ranged from 12% to 21%, depending on the criterion. Especially in view of the difficult soil conditions, this is a noteworthy performance. Perhaps more important is the EMI processing performance on a scenario by scenario basis, in terms of correctness of a dig/no-dig judgment. We view a dig judgment as correct if at least one object in the ground truth for a scenario is in the UXO class. A no-dig judgment is correct only if neither of the objects is in the UXO class. Correct detection of dig scenarios was very good, with only a single one missed. In the smaller number of no-dig cases, the processing produced false alarm rates of 40% ~ 50%.

On the whole, in the blind testplot analyses the GPR processing was not used alone to make decisions on UXO-likeness per se. Rather the results were examined for evidence of key factors, most notably the ELF determined for each object that the GPR processing perceived. For the most part, the GPR processing would not have helped EMI in the cases with missed UXO's. In the two scenarios with unambiguous EMI false alarms, GPR showed no presence of any elongated, substantial objects. Steered by this, the EMI data were reprocessed for these cases, using only the quadrature component of the EMI signal because it generally escapes ground effects. Both reprocessings produced corrected results, eliminating all false alarms that would cause unnecessary digs. Overall, comparing the NSMC based multi-object processing of lab data with that from the testplots suggests that the prominence and especially the variability of ground response was the main factor limiting EMI discrimination performance in the testplot cases.



## 2. EMI MODELING AND PROCESSING APPROACHES

The different EMI modeling methods applied feature different levels of complexity and of rigor, as appropriate to different purposes. We shall see that a high level of rigor does not necessarily imply the greatest complexity. Two approaches developed in this project consist of detailed, rigorous numerical attacks, namely the Method of Auxiliary Sources (MAS) and the Hybrid Finite Element – Boundary Integral Equation Method (HFE-BIEM). These work from first principles in the relevant physics (Maxwell’s equations), retaining all relevant terms and modeling in detail the electromagnetic activity within and around the object of interest. Both employ special formulations to treat high permeability and/or high frequency situations that produce thin skin depths of activity on targets, i.e. the Thin Skin Approximation (TSA) [5, 6]. The MAS formulation can treat geometrically arbitrary, materially inhomogeneous objects by dividing them into piecewise homogeneous segments, which is typically true to the reality. It’s ability to treat multiple objects is an extension of the kind of segmentation in that one simply specifies some distance between the nearby pieces. While full 3-D MAS programs have been developed and applied under this project, the “work horse” program, user-friendly and currently being disseminated, assumes that the object is a body of revolution (BOR) [1, 2, 3] . The excitation and sensing configuration need not be rotationally symmetric. Computations are performed in the frequency domain (FD), with ready translation in the time domain (TD) via algorithms specially designed to handle the kind of spectra that appear in problems of interest.

The HFE-BIEM [4, included as Appendix B] proceeds directly in the time domain, although the program can also be run in such a way that it produces FD results frequency by frequency. It is strictly a BOR program. It’s finite element rendering of the object allows for essentially arbitrary (continuous) variation of electromagnetic properties, with the caveat that the distribution of properties must be rotationally symmetric. In practice, treatment of material heterogeneity beyond piecewise homogeneous structure is cumbersome and was rarely pursued. Perhaps the greatest innovation of the HFE-BIEM is its addition of a TD TSA formulation. This is necessarily a bit more complex than the FD TSA, based on the local application of a TD 1-D analytical solution as well as a convolution in time. However in the end it is efficient and is as effective as the FD TSA. The end result is that both MAS-TSA and HFE-BIEM-TSA programs have no restrictions on EMI frequency or material type, from the static case up to the limits of the EMI band ( $\sim 100$ ’s of kHz). In practice, the MAS based program was used for most of the detailed investigations in this project, with the HFE-BIEM program used as an independent approach, for

verification. For that reason the former is treated in more detail here, with the latter described primarily in references.

The Standardized Excitations Approach (SEA) is a physically complete method that relies essentially on a series representation of the solution [7, 8]. An instrument's transmitted primary field is decomposed into a series of terms, each of which is an SEA. The response to each SEA, and hence to the entire excitation, can be obtained either numerically or experimentally. Used just as a forward model, the method possesses rigor but not generality in the sense that it is tied to the particular objects for which it was derived. That is, one obtains by prescribed protocols a method for producing the scattered field from an object, produced by any relevant kind of excitation and any configuration of object and sensor. However, one cannot generalize to any other object just by, say, changing a material parameter, as one can with the aforementioned numerical methods. That said, one can in fact exploit the method in general inversion studies for unknown buried objects. By solving for SEA response parameters based on above-ground survey data, one obtains parameters for the object under investigation. Again, they are tied to the specific (albeit unknown) object, which is exactly the point: our purpose is to distinguish this object or object class from others, in this case based on the parameters obtained. By using the MAS and SEA approaches together, one can construct a "universal" model for a given metallic item, computing its response to any instrument whose characteristics are known, in both the frequency and time domain (Section 2.4.2).

The Normalized Surface Magnetic Charge (NSMC) [28] represents in part an optimization of the SEA, being its most efficient rendition. It also introduces new discrimination quantities in the course of an innovative way of generating the response to the combined basic excitations. This method and its parameters are used centrally in what follows, to perform discrimination studies involving multiple objects simultaneously.

At many junctures, analytical forms prove invaluable. The highly idealized infinitesimal magnetic dipole model is quite useful for representing simple sources, such as dispersed clutter items. Under appropriate restrictions, it can serve as a first order equivalent source of UXO responses, enabling one to extract and separate the overlapping contributions of different objects to a single data set. The spheroid solution, valuable in itself to representing either UXO-sized or clutter objects, could also furnish realistic dipole moment values to be used then in the dipole modeling.

These methods, their bases, limitations, and specialization to the highly contaminated site application are summarized in the following sections.

## 2.1. The Method of Auxiliary Sources (MAS)

### 2.1.1. Basic MAS Formulation

From Maxwell's four equations governing electromagnetic phenomena, we begin with Ampere's law.

$$\nabla \times \mathbf{H} = \mathbf{J} + \frac{\partial \mathbf{D}}{\partial t} \quad (1)$$

where  $\mathbf{H}$  is the magnetic field [A/m]. Throughout all media (soil, air, metallic targets) in the EMI range, the displacement current term  $\partial \mathbf{D} / \partial t$  is negligible [10, 11, 12], where  $\mathbf{D}$  is the electric displacement field [C/m<sup>2</sup>]. This is a fundamental, defining tenet of magneto-quasistatics (MQS), which is taken here to define the EMI regime here. The electric current density  $\mathbf{J}$  [A/m<sup>2</sup>] is the result of transmitted or induced electric fields, which are quite weak. While these weak fields may still produce significant electric currents in highly conductive metallic targets, the soil is subjected to the same fields but with conductivity about seven to ten orders of magnitude smaller. Therefore the induced currents in the soil are negligible as sources of EMI signal response. This also applies to the air, which has virtually no electrical conductivity. Thus ultimately the magnetic fields in the media surrounding the target are irrotational.

$$\nabla \times \mathbf{H} = 0 \quad (2)$$

With the right hand side of (1) zero, no material (electromagnetic) properties appear in the equation. An irrotational magnetic field may be represented in terms of the gradient of a more convenient scalar magnetic potential,

$$\mathbf{H} = -\nabla \psi \quad (3)$$

Maxwell's magnetic field divergence law states that

$$\nabla \cdot \mathbf{B} = Q \quad (4)$$

where  $\mathbf{B} = \mu \mathbf{H}$ ,  $\mu$  is the magnetic permeability of the medium (H/m), and  $Q$  [H/m<sup>2</sup>] represents magnetic charge density. In nature, there are no magnetic charges and the right hand side of (4) is zero. However one may employ a nonzero  $Q$  as a convenient mathematical device to act as sources of the fields in question, provided that resulting fields ultimately satisfy the divergence-free condition in regions of interest. The strategy of the MAS is to locate such auxiliary sources just outside of each region of interest where the divergence equation supplies the governing relation.

For homogeneous regions, the combination of (3) and (4) produces the Laplace (Poisson) equation

$$\nabla^2 \psi = - \frac{Q}{\mu} \quad (5)$$

as a scalar governing relation. This equation admits relatively simple solutions and solution techniques. Overall, in integral form,

$$\psi(\mathbf{r}) = - \int_{\partial D^{\text{in}}} \frac{q(\mathbf{r}')}{4\pi\mu R} dS' \quad (6)$$

where  $q$  denotes magnetic charge density over the surface  $\partial S$  and  $R = |\mathbf{r} - \mathbf{r}'|$  is the distance between observation  $\mathbf{r}$  and source points  $\mathbf{r}'$ . The scattered field from the object,  $\mathbf{H}^s(\mathbf{r})$ , is expressed as the gradient of (6) as per (3). Note that the gradient of the right hand side only operates on  $R$ .

At root, the MAS formulation is much like other, more common integral equation methods such as the Method of Moments. The difference is that here the sources within the integral are placed on a surface  $\partial D^{\text{in}}$  that is displaced from the object's physical boundary (Figure 1). This introduces both efficiency and convenience relative to conventional integral methods. With a relatively small number of sources or source distribution functions on  $\partial D^{\text{in}}$  inside the object, one achieves a smooth field on the surface  $\partial D$  itself, and does

not have to integrate directly over the singularities where the sources reside. In practice,  $Q$  consists of some assemblage of discrete charges or charge rings, with magnitudes to be solved for.

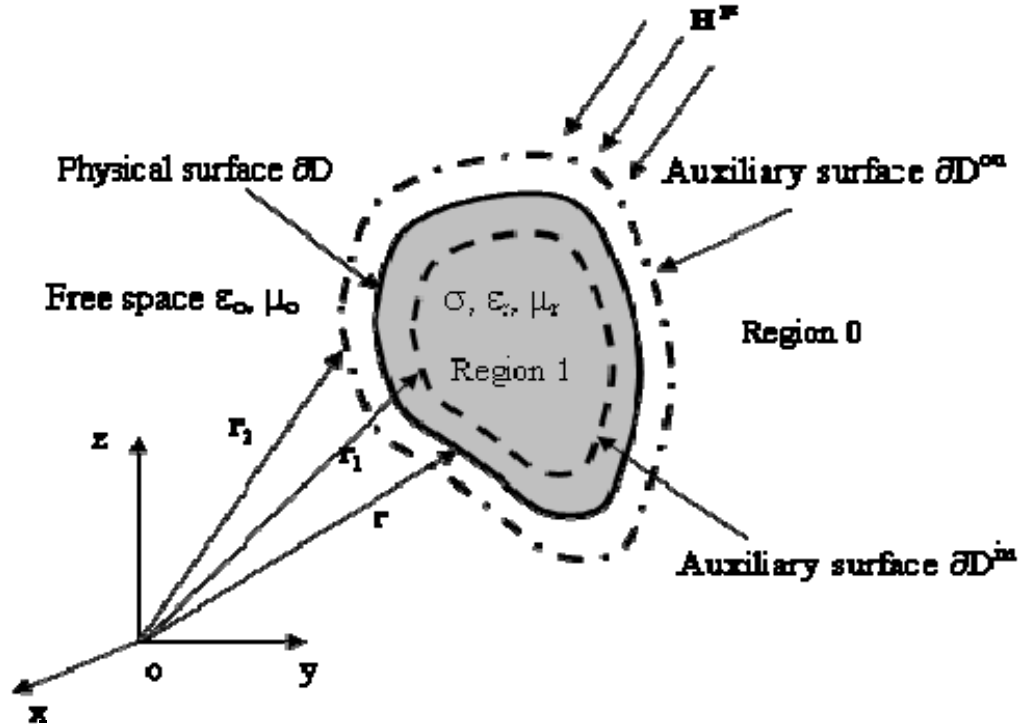


Figure 1. Geometry of the problem, showing the object's physical surface ( $\partial D$ ), the external auxiliary surface  $\partial D^{ou}$  on which the equivalent sources lie producing the fields inside the object, and the interior auxiliary surface  $\partial D^{in}$  on which the equivalent sources lie that produce the external field.

Inside the metallic target one cannot neglect the electric current  $\mathbf{J}$ , which is

$$\mathbf{J} = \sigma \mathbf{E} \quad (7)$$

where  $\sigma$  is the electrical conductivity of the metal (S/m) and  $\mathbf{E}$  is the electric field (V/m). Combining (7) with (1) and the other Maxwell equations yields the classical Helmholtz equation.

$$\nabla^2 \mathbf{H} + k^2 \mathbf{H} = \mathbf{P} \quad (8)$$

where  $k = \sqrt{i\omega\sigma\mu}$ . By analogy with the situation at higher frequencies,  $k$  is commonly called the “wave number.” However, it should be noted that in this frequency range, at our scale of observation with  $\partial\mathbf{D}/\partial t = 0$ , there are no actual waves present but only diffusive fields. The source term on the right hand side,  $\mathbf{P}$ , is, like  $Q$ , generally a fictional device, i.e. equivalent as opposed to real sources. Whereas it made sense to apply scalar equivalent sources in the form of fictitious charges  $Q$  in the scalar potential problem in the exterior (5), in the vector problem here it is most consistent and efficient to apply vector equivalent sources. These are the equivalent of magnetic current elements or continuous distributions of small magnetic dipoles which inherently satisfy the divergence-free requirements of the ultimate field  $\mathbf{H}$  in the region of interest, i.e. away from the source locations.

$$\mathbf{H}(\mathbf{r}) = \int_{\partial D^{\text{ou}}} dS' \left[ \mathbf{I} + \frac{1}{k^2} \nabla \nabla \right] g(\mathbf{r}, \mathbf{r}') \cdot \mathbf{P}(\mathbf{r}') \quad (9)$$

$\mathbf{I}$  is the identity operator and the Green function  $g$  is

$$g(\mathbf{r}, \mathbf{r}') = \frac{e^{ikR}}{4\pi R} \quad (10)$$

Note that the equivalent sources  $\mathbf{P}$  reside on an exterior auxiliary surface  $\partial D^{\text{ou}}$  outside the object, radiating into its interior.

Solution for these unknown sources is obtained by matching internal and external fields appropriately on the physical boundary  $\partial D$ . The boundary conditions specify continuity of tangential components of  $\mathbf{H}$  and normal component of  $\mathbf{B}$ . Specifically, in terms of the tangential ( $\ell = 1, 2$ ) and normal ( $\ell = 3$ ) vectors as seen from the region 0 and region 1 sides of  $\partial D$ ,  $\hat{\xi}_{0,\ell}(\bar{\mathbf{r}})$  and  $\hat{\xi}_{1,\ell}(\bar{\mathbf{r}})$ , respectively,

$$\hat{\xi}_{0,\ell}(\mathbf{r}) \cdot \left[ \mathbf{H}^{\text{sc}}(\mathbf{r}) + \mathbf{H}^{\text{pr}}(\mathbf{r}) \right] - \hat{\xi}_{1,\ell}(\mathbf{r}) \cdot \mathbf{H}(\mathbf{r}) = 0 \quad (11)$$

where  $\mathbf{H}^{\text{pr}}$  is the primary field transmitted by the sensor. In the case of the tangential vectors,

$\hat{\xi}_{1,\ell}(\mathbf{r}) = \hat{\xi}_{0,\ell}(\mathbf{r})$ , while for the normal vectors  $\hat{\xi}_{1,3}(\mathbf{r}) = \frac{\mu_1}{\mu_0} \hat{\xi}_{0,3}(\mathbf{r})$ .  $\mathbf{H}^{\text{sc}}$  contains the scattered fields from

*all* objects. This is the key difference between the multi-body MAS formulation and that developed and implemented heretofore. Applying boundary conditions (11) at selected points produces a linear system of equations from which the amplitudes of auxiliary sources  $\mathbf{Q}$  and  $\mathbf{P}$  can be determined.

To translate MAS frequency domain solutions to the time domain one must perform an inverse Fourier Transform. Care must be taken because one typically has relatively sparse data over the EMI frequency band, i.e. from perhaps 10's of Hz up through 100's of kHz. Points are usually more or less equally spaced on a  $\log(f)$  scale. Though these points may be sparse, the spectra that they sample are smooth on the log scale. Thus one may interpolate or curve or spline fit to obtain intermediate frequency data to any degree of detail. In practice here, we perform spline or quadratic fits over connected segments of the spectra and invert piecewise analytically. Comparisons between FD MAS computations and direct TD HFE-BIEM calculations validate each program. Inverted FD-MAS signals also agree well with measurements taken in the TD (e.g. Section 2.4.2).

### **2.1.2. *Implementation of the TSA in the FD MAS***

The electromagnetic skin depth  $\sqrt{2}/|k|$  is a measure of how quickly magnetic fields inside the object decay with distance from a source, i.e. boundary. For high frequencies and over a large portion of the entire frequency range for high  $\mu$ , this distance is substantially smaller than the object's characteristic dimensions. This means that it is extremely difficult to resolve the fields in directions normal to the object's interior surface; it also means that numerical connections between nearby points on the surface become tenuous (the exponential in (10) decays very rapidly). In consequence, the system of equations becomes numerically unstable. One version or another of this problem afflicts every other numerical system applied to this kind of problem to date. To avoid this difficulty, a hybrid formulation was developed, combining the MAS with the Thin Skin Approximation (TSA) [5, 6]. The resulting MAS-TSA has tested well for high frequency application [13, 14]. For details about the MAS-TSA readers are referred to those references. Here we summarize the method briefly.

The governing equation consists of the divergence law  $\nabla \cdot \mathbf{B} = 0$ , combined with a 1-D analytical solution of the Helmholtz equation. This is applied in a thin sub-volume within a thin layer just inside the object's surface, as depicted in Figure 2.

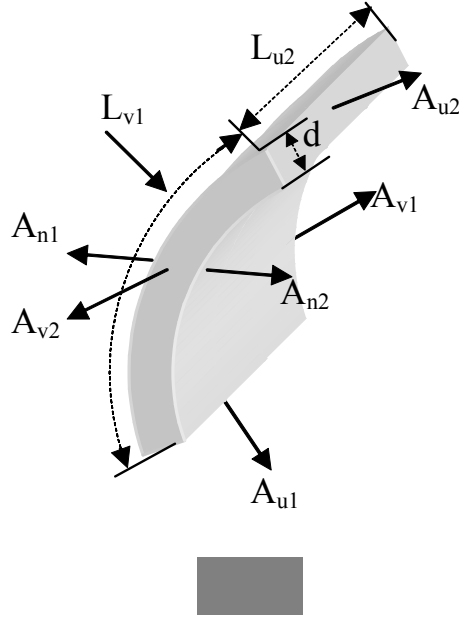


Figure 2. Thin volume  $V_d$  just below the physical surface of an object, the complete surface of which is  $S_d$ .

Integrating the divergence law over this volume

$$\int_{V_d} dV \nabla \cdot \mathbf{B} = \int_{S_d} dS \hat{\mathbf{n}} \cdot \mu_1 \mathbf{H} = 0 \quad (12)$$

produces difference expressions, in effect, involving the normal H field components on opposing sets of surface segments in  $S_d$ . Noting that  $A_{v1} = L_{v1} d$ ,  $A_{v2} = L_{v2} d$ , etc, this is

$$(L_{u2}d)H_{u2} - (L_{u1}d)H_{u1} + (L_{v2}d)H_{v2} - (L_{v1}d)H_{v1} + A_{n2}H_{n2} - A_{n1}H_{n1} = 0 \quad (13)$$

Dividing through by  $d$  and taking the limit as  $d$  approaches zero produces the governing numerical relation. The first four terms simply become expressions in terms of the tangential derivatives of  $\psi$ , because internal and external tangential H fields are equal. The last two terms give rise to

$$\lim_{d \rightarrow 0} \frac{A_{n2}H_{n2} - A_{n1}H_{n1}}{d} \Rightarrow H_n \frac{\partial A_n}{\partial n} + A_n \frac{\partial H_n}{\partial n} \quad (14)$$



The first term is essentially just  $-\frac{\mu_1}{\mu_2} \frac{\partial \psi}{\partial n}$  times a surface curvature related factor. The crucial assumption of the TSA is that the expression  $\partial H_n / \partial n$  in the second term can be expressed as if  $H_n$  varies approximately one-dimensionally normal to the surface, i.e. as a one-dimensional solution to (8) in the normal direction,  $H_n \sim e^{ikn}$ . In particular, in the limit as  $d \rightarrow 0$

$$\frac{\partial H_n}{\partial n} \sim i k H_n \quad (15)$$

This is the thin skin approximation, or TSA.

Altogether, by employing the integration in (12), taking the limit as  $d$  approaches zero, and using the TSA relation (15), one obtains a sufficient boundary condition on  $\psi$  for solving over the entire exterior region. One does not solve over the interior region at all. The relation (15) ensures consistency with a solution of (8) and (12) enforces the divergence free condition. The resulting boundary condition is entirely in terms of the external field variable  $\psi$ , the object's geometry, and the object's electromagnetic properties in  $k$ .

### **2.1.3. The Multi-body MAS**

Figure 3 below shows the basic setup considered for the multi-body MAS problem. These objects could actually just be different individually homogeneous parts of a single heterogeneous object. See Section 4 regarding the latter. The method can treat near and far separation of two objects with equal ease: it does not matter if the objects are very close or in fact seamlessly touching. This is because the equivalent sources are placed mathematically on surfaces displaced from the physical surfaces. Thus in enforcing boundary or compatibility conditions on nearby or common surfaces, one does not run upon singularities at the source locations or upon other numerical distortions that come from passing computationally too near a source.

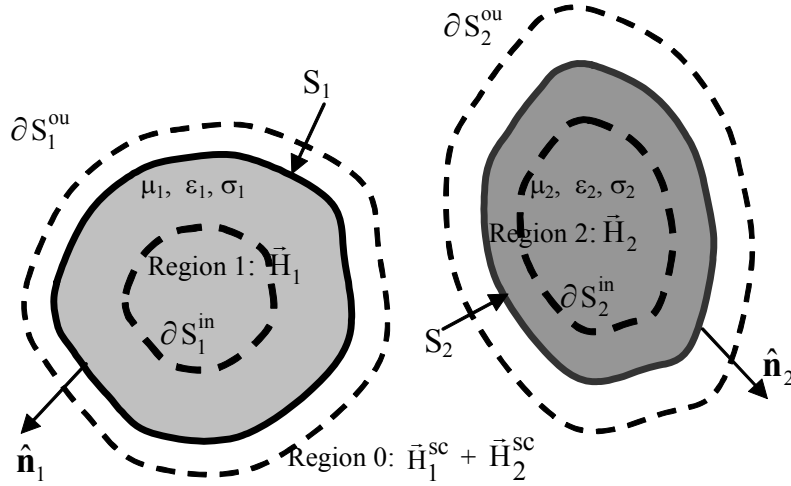


Figure 3. Two bodies with their physical surrounding surfaces  $S_\ell$  and also their surrounding and interior auxiliary surfaces.

The essential difference between the single and multi-body MAS resides in the fact that, in generating the governing algebraic equations by applying (11) at, for example, a point on  $S_1$ , one includes in  $\mathbf{H}^{\text{sc}}$  the scattered fields from *all* objects.

As a test, the method is used to simulate GEM-3 measurements on a UXO consisting of two parts: a tail with fins (length 8 cm and diameter 3.15 cm), and main part (largest diameter 8 cm, smallest diameter 3.15 cm), with the total length of UXO 26 cm. For determination of EM parameters of each section, the UXO was disassembled. The EMI response of each part was measured separately and inversion calculations determined their EM parameters: For the main part  $\sigma = 1.6 \times 10^6$  S/m,  $\mu_r = 85$ , and for the tail  $\sigma = 2 \times 10^6$  S/m,  $\mu_r = 130$ . The comparison between measured and simulated data for the fully assembled UXO is shown in Figure 4 with different target orientations. Agreement is very good.

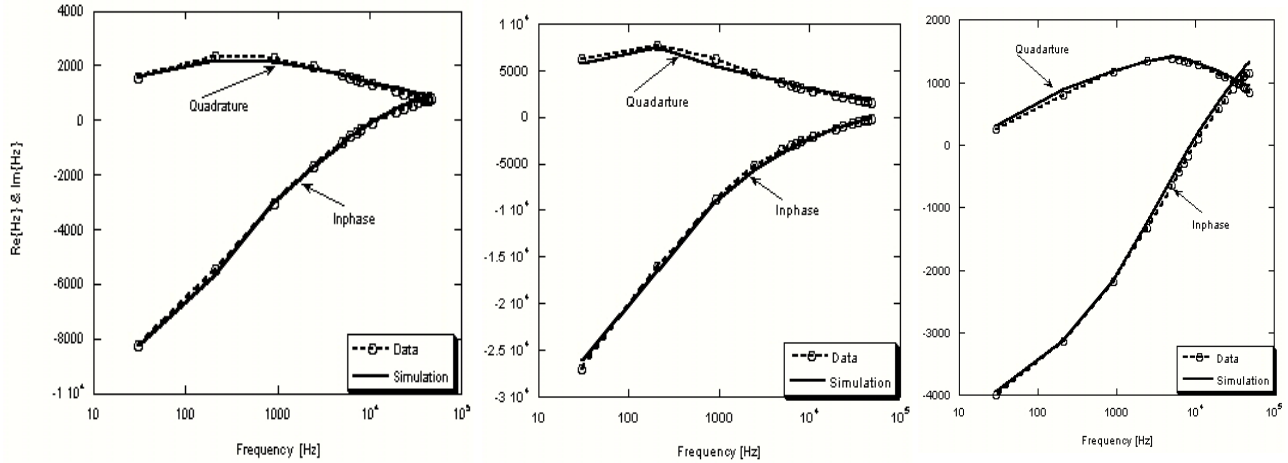


Figure 4. Scattered magnetic fields versus frequency for real UXO oriented with the nose up (left), the tail up (middle), and horizontal (right).

This case represents the most stringent kind of test for objects near one another, i.e. microns apart so that they are nearly touching. This microscopic separation is intended to simulate the typically poor electrical connection between sections of a UXO. Numerous other cases and comparison with measurements have shown that this assumption generally produces agreement with actual target data. (The MAS can simulate a completely solid connection as well, although the MAS-TSA must be modified for that case). A number of cases investigated indicated that the degree of electrical contact assumed between adjacent pieces was not a significant influence on fields observed even a small distance away (Section 4).

We return for emphasis to the distinct advantage that the MAS has, for objects in very close proximity to one another, relative to its various cousins such as the Method of Moments and other Green function based integral methods. Figure 5 shows the auxiliary surfaces and the associated magnetic charge ( $Q$ ) and dipole ( $\mathbf{P}$ ) distributions needed to express the fields internal and external to surface  $S_1$  at the indicated point.

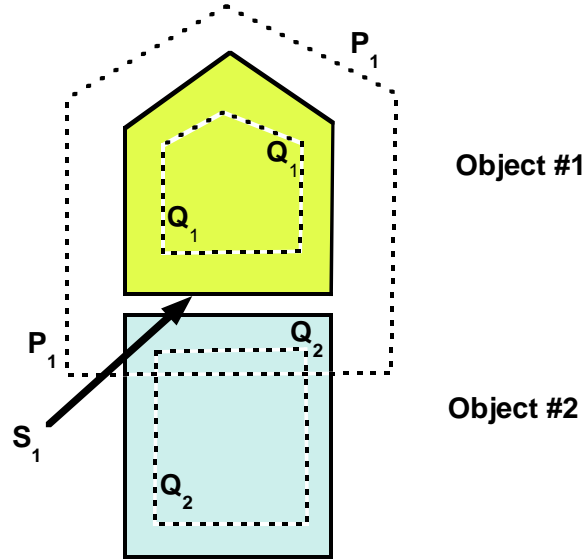


Figure 5. Two objects, or pieces of an object, and the dashed auxiliary surfaces containing the equivalent source distributions  $Q$  (charges) and  $P$  (dipoles) needed to express the fields at the indicated point on  $S_1$ .

Because the sources  $Q$  and  $P$  are located on the auxiliary surfaces, displaced from the physical surfaces, proximity of the physical surfaces does not bring singularities at source points on one surface near those on another surface. Proximity between source points on different surfaces has complicated application of other integral formulation methods. Here the problem does not arise.

## **2.2. The Hybrid Finite Element – Boundary Integral equation Method in the TD with TSA**

Probably the majority of EMI sensors operate in the time domain. That is, instead of simultaneously sending and receiving chosen frequencies, they transmit some variation of a square wave in time, recording the scattered or secondary field during the "off" portion of the duty cycle. The abrupt change caused by shutoff of the transmitted field produces a transient, decaying response from the target, and this forms the essence of the TD signature. With some newer instrumental variations it is possible to receive signals both during the "on" and the "off" phases of the cycle (see analyses of both kinds of response below in Section 6). It is possible, as in Section 6, to convert frequency domain records into time domain, provided that sufficient care is taken to accommodate the special character of the Fourier Transform of the TD input function. This presupposes FD data with sufficient resolution within the band as well as asymptotic values far out into the ends of the band, a formidable requirement. Alternatively, one can model EMI behavior directly in the TD. Both to avail ourselves of this more direct route and to provide another method for comparison of results and treatment of special cases, we have therefore developed a TD method capable of handling UWB BOR problems with heterogeneous or multiple objects. It employs finite elements in the object interior(s) and a boundary integral equation formulation in the exterior space surrounding the object. The resulting computer code is capable of dealing with multiple objects of the same sort as are treated by BOR MAS/ MAS-TSA program described above, with the additional capability of treating continuous as opposed to piecewise constant variation of electromagnetic properties.

In TD simulations one encounters the same difficulties regarding thin skin depth and spatially rapid field decay as in the FD, however these difficulties are manifested in a different manner. In the FD these difficulties only arise in a certain (high) frequency range. That range can be identified, segregated computationally, and given special treatment. In the TD the same kind of problems occurs in a transient way, in "early time" after an imposed sudden change in the primary field. In some ways, TD simulation is more tolerant in that the effect of inaccuracies in early time tend to wash out during later time, given the diffusive nature of the fields and the step function form of the forcing. However we wish to examine early time in some detail and in any case prefer to avoid some unknown degree of persistence by early time errors.

The FD TSA exploited a locally 1-D solution normal to the object interface, of the general form  $H_n \sim H_n(0) \exp\{ikn\}$ , where  $H_n(0)$  is the value of  $H_n$  at the (interior of the) object's surface, i.e. at  $n = 0$ . In the TD there is no fixed  $k$  and  $H_n(0)$  varies in time. Nevertheless, by using a 1-D TD analytical solution normal to the object's surface, for arbitrary fixed  $H_n(0)$ , one can derive analytical and numerical expressions for 1-D normal variation of  $H_n$  as a function of  $H_n(n=0;t)$ . Then computational maneuvers may be performed in the TD numerical formulation that are analogous to those in the FD formulation. The result is an accurate and very efficient code, applicable to multiple or composite objects in the TD, from the very earliest possible time up through steady state. The current code is restricted to BOR configurations, although that is not inherent in the formulation. The method models arbitrary (non-BOR) excitations.

A brief sketch of the numerical method follows in the remainder of this section, with details in Appendix B. While the finite, possibly heterogeneous interior region is attacked with the finite element method, an integral equation over the homogeneous exterior extends the surrounding space to infinity. After special treatment of boundary singularities, the formulations for the two regions are stitched together by application of standard magnetic field interface conditions (11). These are expressed through boundary integrals that appear in the formulations for each region. Treatment of singularities, while successful, requires care under the assumed BOR geometry.

### 2.2.1. *Formulation*

In summary, outside of the metallic target the governing equation remains the Laplace equation, (5). Time only enters through forcing functions and boundary conditions. In integral form, the solution is expressed here as

$$\frac{\psi(\mathbf{r})}{2} + \int_S dS' \left[ \psi(\mathbf{r}') \frac{\partial g(\mathbf{r}, \mathbf{r}')}{\partial n'} - g(\mathbf{r}, \mathbf{r}') \frac{\partial \psi(\mathbf{r}')}{\partial n'} \right] = \psi^{PR}(\mathbf{r}) \quad (16)$$

assuming a smooth surface shape (with no irreducibly angular corners). Inside the metallic target Ampere's equation applies, again modified in keeping with the fundamental MQS tenet that the displacement current term is negligible.

$$\nabla \times \mathbf{H} = \sigma \mathbf{E} \quad (17)$$

Expressing the magnetic field  $\mathbf{H}$  and electric field  $\mathbf{E}$  in terms of a vector potential, under MQS approximations

$$\mathbf{B} = \mu\mathbf{H} = \nabla \times \mathbf{A}, \quad \mathbf{E} = -\frac{\partial \mathbf{A}}{\partial t} \quad (18)$$

provides a governing equation in  $\mathbf{A}$  that simplifies matters numerically for the BOR geometry,

$$\nabla \times \frac{1}{\mu} \nabla \times \mathbf{A} - \nabla \frac{1}{\mu} \nabla \cdot \mathbf{A} - \sigma \frac{\partial \mathbf{A}}{\partial t} = 0 \quad (19)$$

with associated gauge and charge conservation conditions as per the Appendix. Taking the dot product of (19) with an azimuthally tangential basis function  $\mathbf{W}$  yields, after manipulations via vector identities,

$$\begin{aligned} \int_V dV \frac{1}{\mu} (\nabla \times \mathbf{W}) \cdot (\nabla \times \mathbf{A}) - \int_S dS \frac{1}{\mu} \mathbf{W} \times (\nabla \times \mathbf{A}) \cdot \mathbf{n} \\ + \int_V dV \frac{1}{\mu} (\nabla \cdot \mathbf{W})(\nabla \cdot \mathbf{A}) - \int_S dV \mathbf{W} \cdot \sigma \frac{\partial \mathbf{A}}{\partial t} = 0 \end{aligned} \quad (20)$$

Equations (16) and (20) are the governing equations in  $\psi$  and  $\mathbf{A}$ . The two quantities are connected over the BOR object boundary by the standard boundary conditions (11), in integral form, translated into these potentials. The object's domain is divided into finite elements, over which the weighting function is only locally non-zero, and the parameters  $\mu$  and  $\sigma$  may vary over the elements in the internal mesh.

### **2.2.2. Time Domain Thin Skin Approximation**

In early time, i.e. right after the shutoff of the primary field, induced electromagnetic activity just penetrates a thin layer of the target's surface, only gradually diffusing into its interior as the response dies out. TD solution for the object's response in early time thus presents much the same challenges as in high frequency and/or high permeability FD situations, where responses is limited to a thin surface layer ("skin"). A significant difference however lies in the fact that the thickness of the TD layer of activity continually changes (increases), while it remains steady for each frequency in the FD case. Further, one

may ordinarily assume in a FD problem that a single (complex) boundary value applies to a point on the object's surface, i.e. the magnitude of excitation associated with a given frequency in the case at hand. However in the TD problem that surface magnitude changes as the time history progresses.

All these additional challenges of the TD thin skin problem can be dealt with by means of a specifically TD one-dimensional solution, together with a convolution calculation that is repeated at each time step. For both the TD and FD TSA formulations, the basic structure of the computational scheme is as follows:

1. Apply an integral form of the magnetic field divergence equation in a thin layer just inside the object's surface;
2. Express derivatives of vectorially tangential quantities in terms of their exterior equivalents, as tangential fields are continuous;
3. Express  $\partial H_n / \partial n$  in terms of  $H_n$  on the inside of the surface, using a locally applicable 1-D solution for  $H_n$  (this is the Thin Skin Approximation);
4. Express the interior  $H_n$  value as  $H_n(\text{exterior})/\mu_1$

These four steps allow one to produce a sufficient boundary condition on the object surface entirely in terms of exterior quantities; hence the problem can be approached entirely in terms of the much simpler exterior solution for a scalar potential.

In the TD, steps 1 and 2 above are the same as for the FD. For step #3 in the TD, one must use the 1-D TD solution for  $H_n$  normal to the surface. Suppose a steady initial condition applies at  $t_0$  so that  $H_n(n, t_0)$  is uniform over the entire small volume inside the object surface (Figure 2) is at the value  $H_n(0, t_0)$ . Right after  $t_0$  the surface value is changed to  $H_n(0, t_1)$ , where it remains through time  $t_1$ . Assuming that the most significant spatial variation of  $H_n(n, t)$  is normal to the surface, i.e. across much more than tangential to the layer, the solution during this time interval is

$$\begin{aligned}
 H_n(n, t) &= [H_n(0, t_1) - H_n(0, t_0)] \operatorname{erfc} \left( \frac{n}{2\sqrt{(t - t_0)/\sigma\mu}} \right) \\
 &= [H_n(0, t_1) - H_n(0, t_0)] f(n, t - t_0)
 \end{aligned} \tag{21}$$



where  $erfc$  is the complementary error function [15]. To obtain  $\partial H_n / \partial n$  on the interior of the object surface, note

$$\frac{\partial}{\partial n} erfc(an) = \frac{2a}{\pi} e^{-(an)^2} = \frac{\partial f}{\partial n} \Rightarrow \frac{2a}{\pi} \text{ as } n \rightarrow 0 \quad (22)$$

To approximate an extended time history, i.e. over successive time steps  $t_m$ , one simply superposes the effects of a sequence of such step changes. This can be cast in terms of a convolution integral in various forms [e.g. Appendix B], in any case equivalent to the computation

$$\frac{\partial}{\partial n} H_n(n, t_M) = \sum_{m=1}^M [H_n(0, t_m) - H_n(0, t_{m-1})] \frac{\partial}{\partial n} f(n, t_M - t_{m-1}) \quad (23)$$

Combining (22) and (23) or the equivalent with step #4 above produces the approximation needed for the interior  $\partial H_n / \partial n$  in terms of exterior  $H_n$  values.

The code containing this TD TSA formulation shows quite good results in early time and excellent results overall in comparison both to other numerical results from the MAS-TSA code (with FD to TD inversion); also in comparison to data obtained from the Zonge NanoTEM TD EMI sensor and related equipment [16]. It also performs well for a composite object with an assumed microscopic gap between the two sections. This is a severe test of the method's ability to model two objects close to one another. Comparisons to analytical multi-body solutions were also successful as well.

[

## 2.3. Analytical Forms: Magnetic Dipoles and Homogeneous Spheroids

### 2.3.1. *Infinitesimal Magnetic Dipole Representations*

Finite bodies inherently produce EMI responses related to those of an infinitesimal magnetic dipole, if viewed in at a large enough scale. The basis for this lies in the fundamentals of induction physics, best apprehended by examination of the governing Ampere's law (1). The simplification wrought by neglecting the displacement current term is crucial for the current considerations. In conjunction with the charge conservation statement

$$\nabla \cdot \mathbf{J} = -\frac{\partial \rho}{\partial t} \quad (24)$$

where  $\rho$  is electric charge density (C/m<sup>3</sup>). Taking the divergence of Ampere's law produces the relation

$$\nabla \cdot [\nabla \times \mathbf{H} = \mathbf{J}] \quad (25)$$

By vector identity, the first term is uniformly zero for any  $\mathbf{H}$ . This leaves then the equation

$$\nabla \cdot \mathbf{J} = 0 \quad (26)$$

Which is to say, in terms of flow of electric charge or charge carriers, “what goes in (to an elemental volume) must come out.” In view of (24), no change in charge density can ever occur. Assuming some quiescent initial state, as one always can, a primary field that impinges on an object can never induce the concentration of free charge. Among other things, this means that a “tube” of current between induced streamlines can never end, as happens in an electric dipole. Termination or even just change of magnitude of current along a line or within a “tube” would necessarily mean development of charge concentrations or deficits, as charges joined or left the flow. Thus a fundamental feature of EMI phenomenology is that all induced currents must form continuous, closed loops.

Figure 6 shows two views of the same current loop, near and far. However irregularly shaped, the current loop generates a bundle of magnetic field lines passing through the area of the loop. The configuration on the left in the figure is a (finite) magnetic *dipole* in the sense that the current loop generates this bundle of field lines with a positive (upper) and negative (lower) side. Viewed from a large distance relative to the size of the loop, the precise shape of the loop is not important (Figure 6, right). The field lines curve around into continuous closed loops in essentially the same form as they would from an infinitesimal dipole at the finite loop's location. For any electric current loop or set of loops in the EMI regime, the dipole portion of the associated magnetic fields represents the most fundamental, lowest order response that persists farthest into the distance.

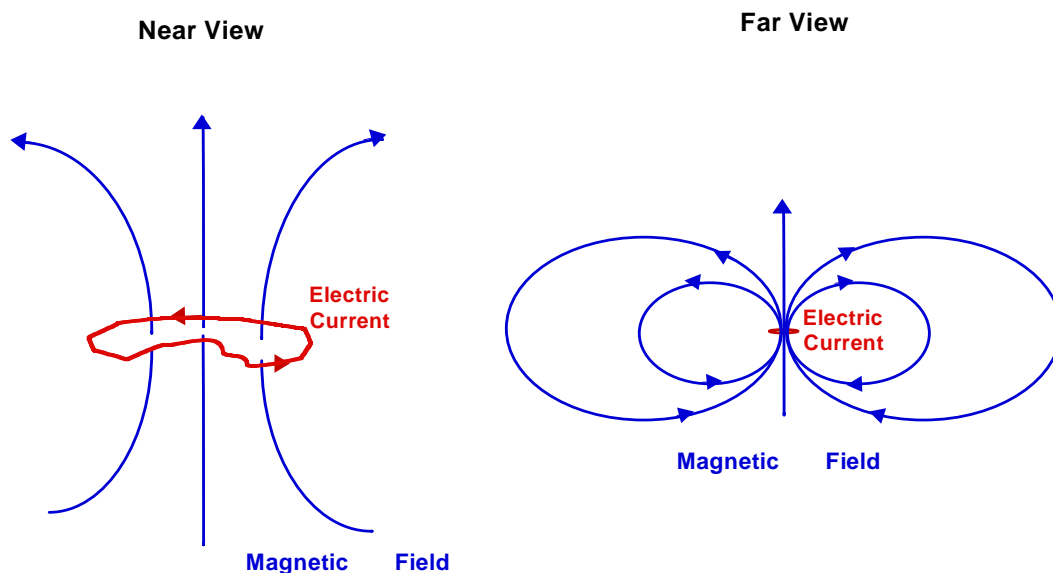


Figure 6. Left, electric current loop producing magnetic field lines, near view. Right: same, far view.

The observations above help explain the popularity of dipole models for representing UXO responses. Some sort of dipole response is always present, at least as a fundamental part of a more complex mix with even-numbered higher order poles. In particular, investigators typically assume the existence of an equivalent responding source in the form of a set of 3 orthogonal dipoles (i.e. single tri-axial dipole), the response of which along any of its principal directions is proportional to the magnitude of the impinging primary field. Thus, it is as if the responding object consists of three small circular wire loops with axes pointing in mutually perpendicular directions. Transient primary fields passing through

the loops induce currents around the loops (Faraday's Law) in proportional to the primary field flux through the loops; and these currents in turn produce secondary magnetic fields as per Figure 6.

In equations, for reference in what follows, a tri-axial infinitesimal magnetic dipole  $\mathbf{m}$  produces a magnetic field  $\mathbf{H}$  given by [11]

$$\mathbf{H}(\mathbf{r}) = \frac{3\hat{\mathbf{R}}\hat{\mathbf{R}} - \mathbf{I}}{4\pi R^3} \cdot \mathbf{m}(\mathbf{r}') \quad (27)$$

where  $\mathbf{r}$  is the observation point,  $\mathbf{r}'$  is the source point (dipole location),  $\mathbf{R} = \mathbf{r} - \mathbf{r}'$ ,  $R = |\mathbf{R}|$ , and

$\hat{\mathbf{R}} = \mathbf{R} / R$ . The dipole moment  $\mathbf{m}$  stimulated by the primary field is typically represented in terms of a magnetic polarizability matrix  $\mathbf{M}$

$$\mathbf{m}(\mathbf{r}') = \mathbf{M}(\mathbf{r}') \cdot \mathbf{H}^{\text{PR}}(\mathbf{r}') \quad (28)$$

which, when the coordinate system is oriented along the magnetic dipole's principal axes, is a diagonal matrix

$$\mathbf{M} = \begin{bmatrix} \beta_{xx} & 0 & 0 \\ 0 & \beta_{yy} & 0 \\ 0 & 0 & \beta_{zz} \end{bmatrix} \quad (29)$$

This model can diverge from reality in a number of ways. First, observing that any inductive source will produce a dipole-type field when viewed from a sufficient distance does not mean that a given field impinging on the source will always produce *the same* secondary field, although the field geometry may always be the same form. An infinitesimal dipole idealization of the sort described here does have positive and negative sides or “ends,” but has no finite extent between the poles, much less different characteristics around the different poles. Rotating the dipole axis 180° should have no effect on its response, just as flipping over a wire loop should not affect the current induced in it by an impinging magnetic field. However UXO's, which are typically heterogeneous along their longitudinal axes, respond differently from one end as opposed to the other. Primary fields from survey instruments are

typically non-uniform, frequently highly non-uniform. One end of the target will be stimulated more strongly than the other, and will also be closer to the receiver than the other end. Because in UXO surveying the instruments are generally only a few characteristic lengths away, such finite geometry effects can be significant or dominant in the data patterns. The picture resembles that on the left in Figure 6 more than that on the right.

To illustrate this, Figure 7 and Figure 8 show values of  $\beta_{zz}$  inferred for a 105 mm projectile and an 81 mm mortar, respectively, assuming that the corresponding infinitesimal dipole resides at the center point of the UXO. Each value was inferred from a single measurement on a line along the axis of the UXO (Z axis), using the Geophex Ltd GEM-3 instrument [17], up to an observation distance about one target length away. Even for a UXO that appears as homogeneous as the 105 mm, values for some frequencies are symmetrical head to tail but depend on distance from the UXO (30 kHz); or they indeed converge with distance from the UXO but to different values on different sides. For the 81 mm mortar, values for some frequencies are roughly symmetrical relative to the two ends of the UXO. However values for some frequencies flip in one direction (22 kHz) or in the opposite direction (150 Hz). Observing from a greater distance does not help greatly, with this instrument, up to the limit of its practical viewing distance.

These limitations of the infinitesimal dipole model complicate greatly its use as a discrimination tool when one attempts to base classifications on certain uses of the polarizability eigenvalues  $\beta_{ii}$ . For example, it is commonly assumed that a BOR such as a UXO will have a dominant axial value  $\beta_{zz}$  with two smaller but approximately transverse values. Even for homogeneous objects this is not reliably the case. Figure 9 shows the measured ratio of transverse to axial moments,  $\beta_{xx}/\beta_{zz}$ , for a composite cylinder when the steel portion faces the GEM sensor in the axial orientation. As the sensor moves farther and farther away, to an observation point several times the object length of 14 cm, the ratio stabilizes into a curve over the spectrum reminiscent of others we have seen for homogeneous ferrous bodies [12]. In particular, the ratio is less than unity at low frequencies, moves through a transition over mid-frequencies, and is ultimately greater than unity at high frequencies. Other researchers have noticed related patterns, and noted associated difficulties borne of the non-uniqueness of these polarizability relations, e.g. [18]. In the least, without further considerations one cannot fix on a particular ratio as indicative of any particular degree of elongation, composition, etc. This is especially the case when only isolated frequencies are employed; or when some range of frequencies is combined, as in TD measurements.

The full reality of the  $\beta_{xx}/\beta_{zz}$  situation for composite objects, however, is generally worse than the relatively orderly picture in Figure 9. Figure 10 shows a similar plot but for the case when the aluminum portion of the composite cylinder faces the sensor. Again, the figure shows convergence as the sensor moves farther and farther away, ultimately to a distance at the limit of its range. Comparing Figure 9 and Figure 10 shows that, even when the sensor is moved as far away as possible, no unique value or relation of the dipole moments appears at a given frequency, much less over the entire band. The different excitation of and reception from one portion of the target as opposed to the other shifts with its orientation and with the frequency used. By manipulating the material properties of each portion of the object one can shift the lumps and bumps in Figure 10 around into essentially arbitrary irregular forms.

Given its limitations, then, the question arises, what legitimate or profitable uses the infinitesimal dipole model might be put to here. While its usefulness as a predictive model or unique parameterization of an object is limited, it does nonetheless reflect some aspects of an object: a given object under any specific circumstances produces given dipole responses, and no other. It is possible that statistical learning machines might be trained to recognize object classes that different clusters of dipole values are tied to in common, through the haze of non-uniqueness, e.g. [20]. In any case, our experience shows that homogeneous bodies can usually be represented rather effectively by an infinitesimal dipole idealization, at a given frequency, provided that the body is simple in shape and that an impinging primary field does not vary too greatly over the object. This suggests the strategy of modeling a heterogeneous object such as a UXO by assuming an equivalent infinitesimal dipole responding source in each homogeneous section of the object, “displaced dipole” approach [21]. Applied to the composite in Figure 9 and Figure 10 or similar objects it will in fact succeed quite well as a predictive model. That is, it will succeed in reproducing the EMI response for data other than that used to derive the  $\beta_{ii}$  values, as long as one is not terribly close to the object and the primary field is not too sharply varying.

A crucial point, however, is that “similar objects” must consist of clearly separable sections with particular combinations of materials such that interaction between the sections does not manifest itself significantly in the scattered field. Unfortunately, interaction frequently does have a significant effect for common material combinations and geometries. For exploration of the basis for this, see Section 4. Here an illustration suffices. In the displaced dipole approach, one assumes that each tri-axial dipole responds only to the primary field striking that point, independently of the other dipole(s). Pursuing this, suppose one takes apart the two-section UXO in Figure 11 and determines the response of each section separately. The head and tail are both magnetic, but apparently consist of different metals. The figure compares the measured GEM-3 response to that determined by the two-(displaced) dipole model and to

our SEA approach (Section 2.4). When the GEM-3 "looks" from the tail end of the UXO from about half an object length away, the displaced dipole solution is clearly in error (Figure 11, blue line). The picture does not improve appreciably if one moves the antenna further away, until the GEM signal fades to noise. The reason for this error resides in the interaction between the two magnetic sections. Investigations show that superposition of responses by different sections can also fail when *non*-magnetic materials are involved in certain geometries with magnetic materials. If instead of inferring the  $\beta_{ii}$  values independently for each section, one obtains them simultaneously from a set of observations, this picture will improve significantly – but only for data obtained under conditions like that used to infer the  $\beta_{ii}$  values. For general modeling purposes, we note that our ultra-fast SEA modeling method (green line in Figure 11) avoids all these issues. It accurately accounts for all relevant effects, including near and far field, heterogeneity and internal target interactions.

For the purposes of attacking highly contaminated sites, in particular, for addressing sensor views of more than one object simultaneously, the infinitesimal dipole model might be used as an equivalent source that will produce one object's contribution to data that contains spatially overlapping responses. The inferred model parameters are not considered to be unique or to be inherent properties of the object and are not used for predictive modeling purposes. Rather, they may simply allow one to perform the crucial task of separating the two superposed contributions to a particular data set. They also might be used here to infer generic as opposed to specific object properties. In particular, we look for orderly frequency patterns and suggestions of symmetry such as a UXO should produce, as opposed to the irregular frequency patterns and non-BOR behavior one might obtain from a piece of clutter. Both of these possible uses must be approached with caution. Among other things, non-BOR objects such as bent plates can produce BOR-like  $\beta_{ii}$  patterns [2 below]. Also, flattened BOR's can produce patterns that can only be distinguished from those from an elongated ferrous (UXO-like) object by careful analysis of the broadband response of all three  $\beta_{ii}$  values, ideally together with some knowledge of material properties. That said, it is unquestionably the case that an elongated ferrous BOR *will* produce  $\beta_{ii}$  values in which two are similar and one is distinct, usually being dominant at least at lower frequencies. The observation of such patterns in data at least *suggests* the possibility that the object is UXO-like, i.e. does not rule it out; and the lack of such a pattern suggests that the object is *not* a UXO.

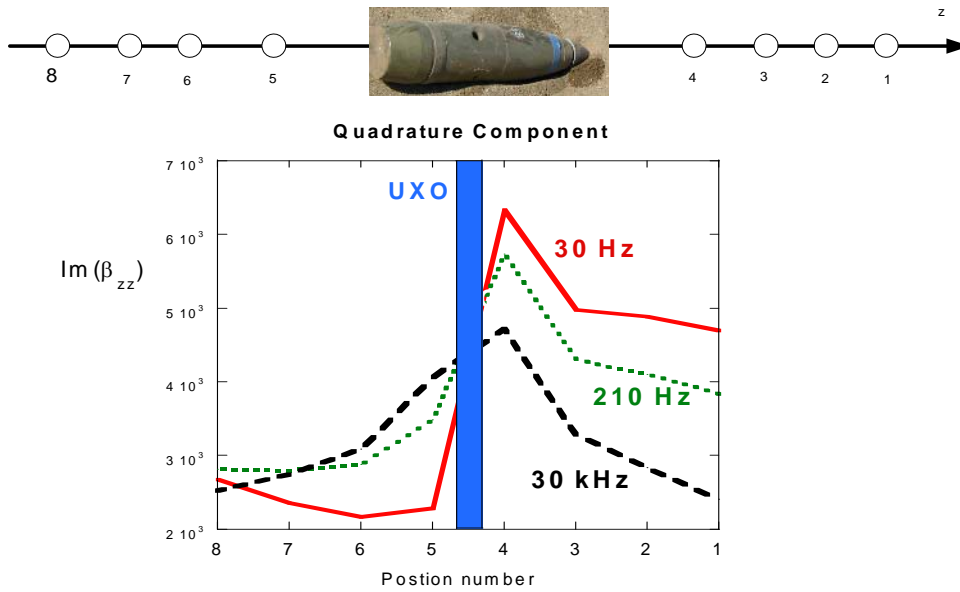


Figure 7. Axial infinitesimal magnetic dipole moment (magnetic polarizability) inferred from data taken at different positions relative to the 105 mm projectile.

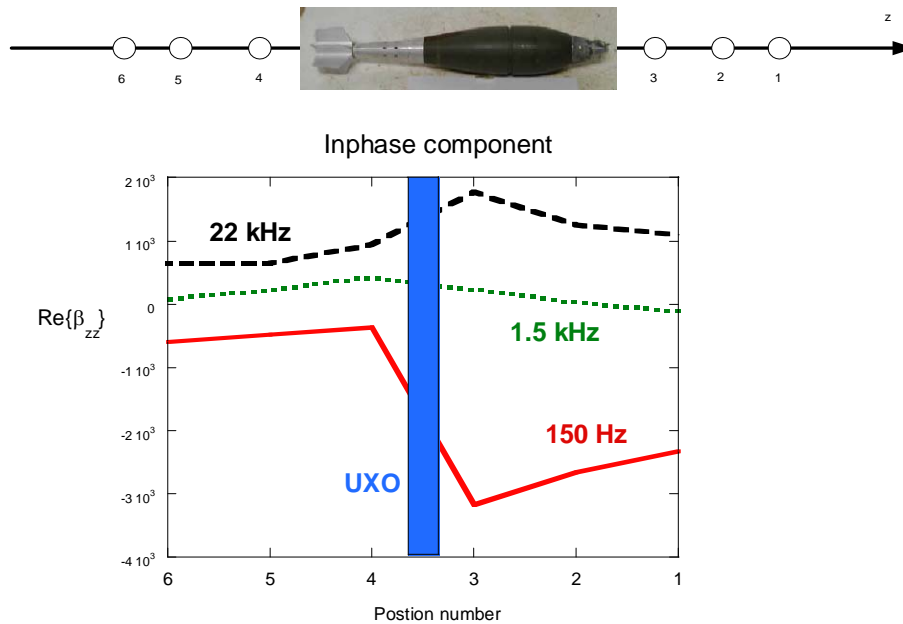


Figure 8. Axial infinitesimal magnetic dipole moment (magnetic polarizability) inferred from data taken at different positions relative to the 81 mm mortar.



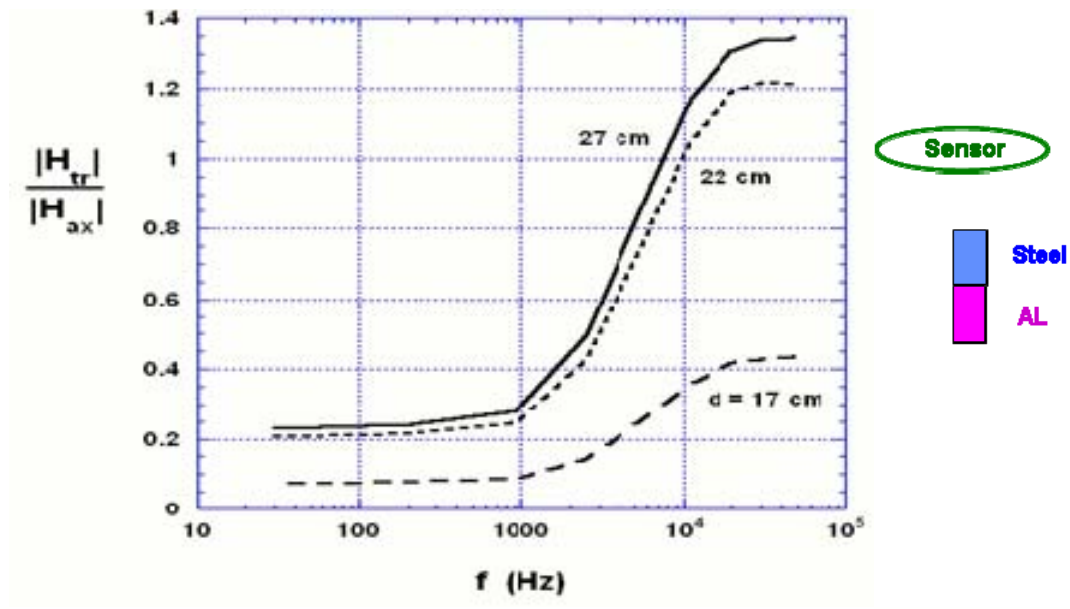


Figure 9. Measured ratio of transverse to axial response by composite cylinder, using the GEM-3, with steel section towards the sensor during the axial orientation.

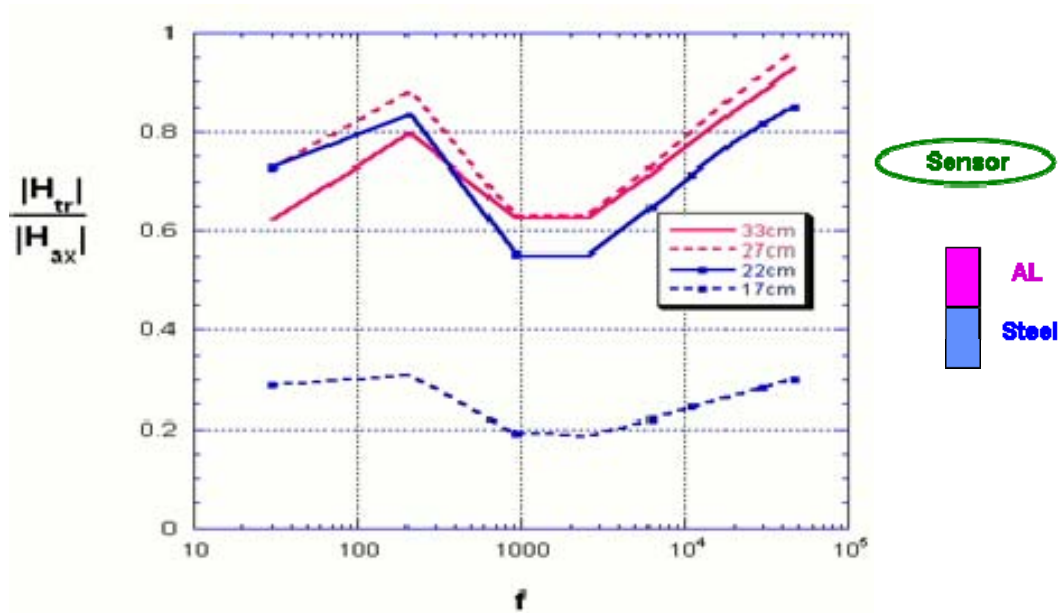


Figure 10. Same as Figure 9, but with aluminum section towards the sensor during the axial orientation.

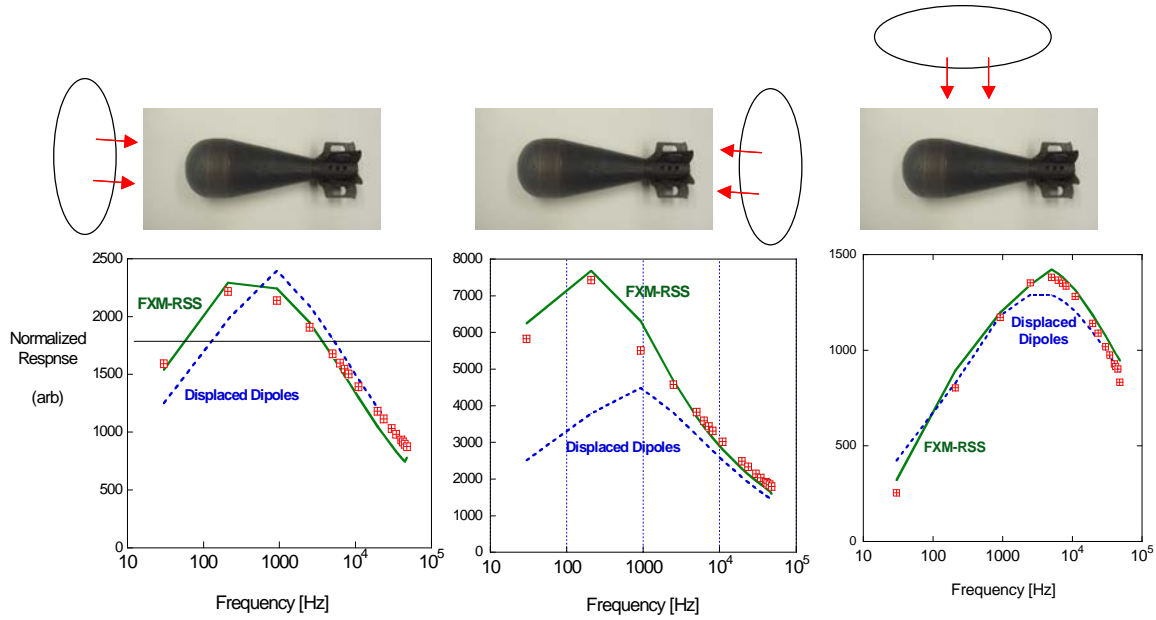


Figure 11. GEM-3 measurements (markers) compared to modeling results from the displaced dipole model and from the SEA (FXM-RSS).

### 2.3.2. *Analytical Solutions for Homogeneous Spheroids*

Research has shown that details of surface features have little effect on EMI response, relative to the influence of overall shape and proportions of an object, e.g. [2]. This encourages us to consider spheroids to represent many objects because spheroids can assume a great variety of proportions, from flattened (oblate) to elongated (prolate) forms. In addition to providing canonical shapes for UXO-sized objects in this study, they are excellent for providing realistic signals from small, homogenous clutter items in processing tests. The EMI spheroid solution has not been in the forefront in discrimination processing in part because, until recently, only the solution for the magnetostatic case was available. In the last few years a complete solution was developed, under SERDP auspices [22]. This includes special methods for evaluating problematical vector spheroidal wave functions for object interiors [23] and some

handy simplified versions for special, problematical cases (high magnetic permeability, extreme aspect ratio). An analytical solution was also developed for two interacting spheroids [24].

From the point of view of numerical processing, in particular the Standardized Excitations Approach (SEA), the solution form that applies outside of the metallic target is of greatest interest. The magnetic scalar potential can be expressed in standard spheroidal coordinates  $(\eta, \xi, \phi)$  as

$$\Psi(\xi, \eta, \phi) = \sum_{m=0}^{\infty} \sum_{n=m}^{\infty} \sum_{p=0}^1 b_{pmn} P_n^m(\eta) \left\{ \begin{matrix} P_n^m(\xi) \\ Q_n^m(\xi) \end{matrix} \right\} T_{pm}(\phi) \quad (30)$$

where

$$T_{pm}(\phi) = \begin{cases} \sin(m\phi), & p=1 \\ \cos(m\phi), & p=0 \end{cases} \quad (31)$$

and  $P_n^m$  and  $Q_n^m$  are associated Legendre functions of the first and second kinds, respectively, of order  $m$  and degree  $n$ . Each of the functions in this summation is a solution of the Laplace equation governing fields in the environment around the target, whether that field emanates from the sensor or target. In particular, they can be used as a basis into which the transmitted primary field can be decomposed. Each such term is a “standardized excitation,” scaled in any particular instance by the coefficient  $b_{pmn}$ .

Overall, the spheroid solution reproduces the response of some irregular objects remarkably well. See frag item in Figure 12 on which the measurements in Figure 13 were made. The GEM-3 sensor head was about 10 cm from the center of the object, that being about the length of the object. Note that the item has many irregular jigs and jags in its surface, and presents a rather different profile when viewed from its broader and narrower sides. Nevertheless, its response fits that of a comparably proportioned prolate spheroid remarkably well (Figure 13). [footnote: The assumed values of  $\sigma$  and  $\mu$  are probably low. Doubling them is more realistic and produces about the same result. This non-uniqueness is fundamental, for magnetic materials, i.e. response depends inherently on the ratio  $\sigma/\mu$ , not their individual values.]

Perhaps the most remarkable thing in Figure 13 is how well the transverse analytical solution (excitation from the side) continues to resemble the frag response as the object is rotated about its long axis, presenting broader and narrower profiles to the sensor. The point to be made here is that this object

is rather forgiving of a highly symmetrical mathematical idealization *because it is homogeneous in composition*. In fact, a crossed (point) dipole representation of this object would probably perform comparably well, depending a little on how far away from the object the sensor and observation point are. Overall, accumulating results suggest that when the object is homogeneous, whether flattened or elongated, the point dipole model will perform about as well as the spheroid unless 1) the primary field varies very significantly over the scale of the object, and/or 2) the observation point is closer than about half the object length.

Just as a spheroid may represent a rather irregular object pretty well, a composite object consisting of a sequence of sections could also be represented by a sequence of spheroids, end to end, each with different properties. This is done most simply, by superposition, when interaction between the sections has little effect on the scattered field, a state of affairs that is considerably more common than one might imagine. Alternatively, new analytical solutions for multiple spheroids, including all interactions could be used to model a multi-section object.

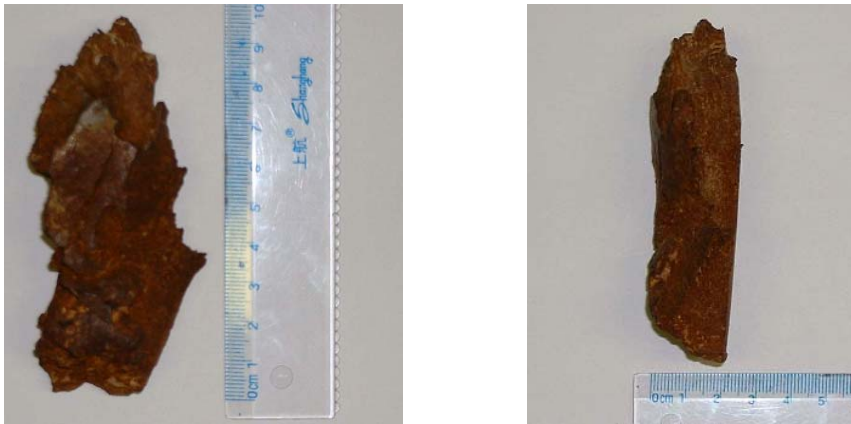


Figure 12. Piece of ordnance scrap about 10 cm in length, showing broader side (3~4 cm wide, left) and narrower side (~2cm wide, right).

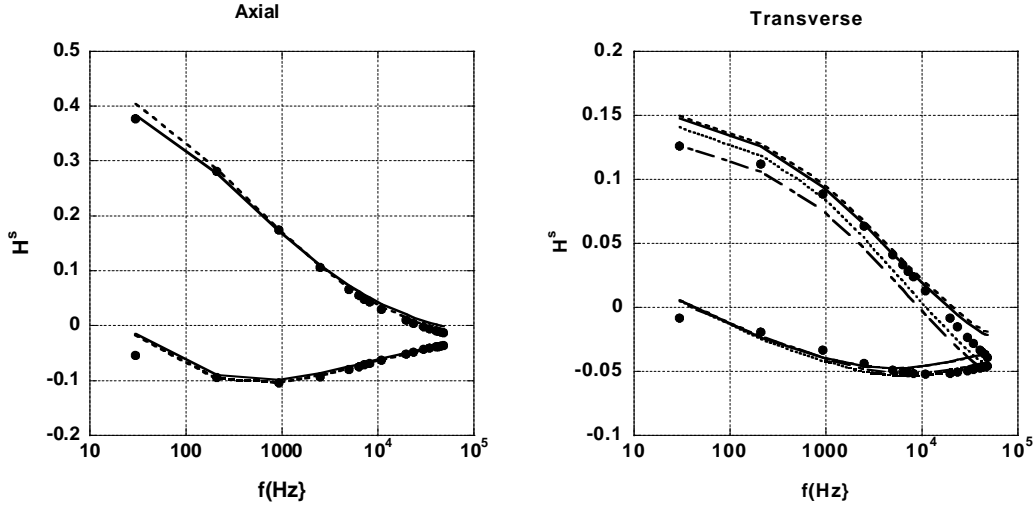


Figure 13. Comparison of the GEM-3 response from the scrap shown above (lines) with the prolate spheroid solution (dots) for semi-axis lengths  $a = 1.25\text{cm}$ ,  $b = 5\text{cm}$ , with  $\sigma = 2.6 \times 10^6 \text{ (S/m)}$ ,  $\mu = 36\mu_0$ . Different line types indicate measurements from different angles (i.e. up and down for axial case and the four principle lateral directions for transverse case). Quadrature sign convention is reversed relative to other plots.

## 2.4. The Standardized Excitations Approach (SEA)

This section describes an ultra-fast, highly rigorous computational scheme for determining the EMI responses of a metallic object of arbitrary complexity, subject to any specifiable excitation. The framework can either be used to perform forward computations for known object types; or one can work backwards from data to infer the SEA parameters, on the basis of which classification judgments may be based.

### 2.4.1. Basic Concept of the SEA

In any particular circumstance, including any sensor and any target-sensor configuration, the complete object response can be constructed as a simple superposition of the contributing responses from the corresponding basic excitations. The response of the entire object to the entirety of each basic

excitation is an inherent property of the object. In outline, to construct the formulation one proceeds as follows:

1. Pre-define a collection of basic excitation fields  $\Psi_j^{PR}$ ,  $j = 1, 2, \dots, N$ , such that any EMI primary (transmitted) field can be construed as a linear combination of them.
2. Describe the primary field impinging on a target, from any sensor in any position, as a simple sum of the basic excitations:

$$\text{complete } \Psi^{PR} = \sum^J b_j \Psi_j^{PR} \quad \Leftarrow \text{ascertain } b_j \quad (32)$$

3. Having decomposed any known excitation into  $J$  primary field modes, find a target's characteristic response  $\Psi_j^s$  to each  $j^{\text{th}}$  basic excitation:

$$\Psi_j^{PR} \Rightarrow (\text{target}) \Rightarrow \Psi_j^s, \quad j=1, 2, 3 \dots N \quad (33)$$

4. For any new excitation, i.e. a different superposition ( $b_j$ ) of the standardized excitations, construct the complete response simply as the corresponding superposition of responses:

$$\text{complete } \Psi^s = \sum b_j \Psi_j^s \quad (34)$$

The method presupposes that one can calculate the primary field produced by any instrument of interest, which is in fact relatively easy to do. The key to the development of the SEA was identification of various kinds of excitation modes or components from which general EMI fields can be rigorously constructed, i.e. Step #1 above. Overall, one can either use fields corresponding to collections of particular (equivalent) sources arrayed about an object's contemplated position; or one can simply use sets of admissible functions, a linear combination of which can reliably produce transmitted fields. For most results reported here, fundamental solutions of the governing Laplace equation in spheroidal coordinates are used for the  $\Psi_j^{PR}$  (see Section 2.3.2).

Step #3 can be accomplished either by detailed numerical modeling or by processing of physical measurements. Using measured data, it is no more difficult (in principle) for a complicated target than for a simple target. Basically, one must start with (32), knowing (calculating) the  $b_j$  for any target position and measuring the complete  $\Psi^s$ . Then, on the basis of these  $b_j$  and  $\Psi^s$  values, one can invert (34) to

obtain the individual modal responses  $\Psi_j^s$ . In reality, one doesn't solve for or store the  $\Psi_j^s$  fields themselves, but rather obtains some compact set of response parameters  $\{S\}_j$  through which each  $\Psi_j^s$  can be expressed efficiently. These  $\{S\}_j$  typically consist of a set of coefficients for pre-defined field components (modes); or a set of responding source magnitudes (charges, dipoles...) that define an appropriate source distribution that will produce the object's response. Whatever each set of  $\{S\}_j$  consists of, one can solve for these entities by sampling the complete  $\Psi^s$  at enough points: If there are  $J$  of the  $\{S\}_j$  and  $M$  elements in each vector  $\{S\}_j$  then inverting (34) requires sampling  $\Psi^s$  at at least  $J \times M$  (well-chosen) points.

All the above is somewhat parallel to what must be done in multiple independent ("displaced") dipole modeling of a UXO: In that approach, each  $j^{\text{th}}$  dipole radiates  $\Psi_j^s$  in response to the primary field at its location ( $\Psi_j^{\text{PR}}$  consists of the excitation imposed at the  $j^{\text{th}}$  dipole location). The  $\{S\}_j$  associated with each  $\Psi_j^s$  consist of the magnetic polarizabilities in each principal direction. The difference in the SEA is that the  $\Psi_j^s$  contain the *complete* response of the target to the *complete*  $j^{\text{th}}$  excitation over the entire target, including all internal interactions, finite geometry effects, primary field non-uniformity, near and far field effects, etc. At the same time, because in application the method only requires a linear combination of the stored  $\Psi_j^s$  response patterns, it is an extremely fast forward model.

Real transmitted fields are typically very non-uniform. A particular advantage of the SEA is that it allows one to treat data from real sensors by extracting responses from the most basic excitations that lie within the complete primary field, e.g. uniform fields impinging from each principal direction. It can also extract from the complete response the rigorously determined dipole portion, corresponding to each of the uniform, uni-directional excitation modes. Many analyses using infinitesimal dipole models of targets suffer because they implicitly assume that the primary field at the responding dipole's location is representative of excitation over the entire target. This is only reliably the case only for uni-directional primary fields that are uniform over the region of the target. Non-uniqueness in response parameters appears at least in part because different configurations of target and sensor in fact produce quite varying patterns of excitation over the target. One possible discrimination strategy with the SEA is to base classification only on the most basic excitations and responses – uniform primary fields and dipole responses – but to determine them rigorously, comparing "apples to apples" whatever the details of the sensing scenario.

Discrimination schemes using the SEA can either proceed by 1) using the  $\{S\}_j$  that have been stored for known target types to produce extremely fast forward models for those items, and basing classification on an examination of the modeled and measured secondary fields; or 2) by inferring the  $\{S\}_j$  for unknown targets without reference to a library of items, and basing classification on a generic examination of these response coefficients. *Pattern matching* is the easiest application of the SEA under option #1: The basic response parameters  $\{S\}_j$  of some particular targets of concern are recorded, by processing under some controlled conditions. Confronting any particular measured signal, one just uses the  $\{S\}_j$  in a fast forward model via (34) to construct responses from each candidate target, when it is in any hypothetical position or orientation (when any particular collection of calculable  $b_j$  applies).

$$\left\{ \begin{array}{l} \text{target-sensor configuration} \rightarrow \Psi^{\text{PR}} \rightarrow b_j \\ \text{target library} \rightarrow \{S\}_j \rightarrow \Psi_j^s \end{array} \right\} \rightarrow \sum_j b_j \Psi_j^s \Rightarrow \Psi^s \quad (35)$$

A search through admissible dispositions of each particular target in the library determines which produces a good match with the observed fields.

By contrast, in *general inversion* (option #2), one does not limit the processing by assuming a particular set of possible targets from a library. Rather, some appropriate processing scheme determines the set of  $\{S\}_j$  that produces fields that best fit the data at hand. The  $\{S\}_j$  are basic characteristics of the object, or rather, of its EMI response. They are not affected by the particular sensing scheme or instrumental view point that produced data leading to their identification. Therefore one can construct or train a classification processor such as the Support Vector Machine (SVM) to sort the  $\{S\}_j$  into UXO-like or non-UXO piles, or into other categories. The rudiments of this sort of general inversion processing have been demonstrated for basic cases [25, 26, 27].

#### **2.4.2. Use of the MAS to Construct "Universal" SEA Models in both FD and TD**

In the preceding section, the SEA's ability to treat any relative disposition of target and sensor was implicitly tied to the use of some particular sensor. If a particular instrument, e.g. here the Geophex



GEM-3, was used both to produce the primary field and to obtain the observations in (33) and (34), then the SEA will relate  $\psi^{\text{PR}}$  and  $\psi^s$  for new prospective configurations of this same target and instrument. However application of the SEA based on archived  $\Psi_j^s$  from one particular instrument need not be limited in this way. Using the UWB data of the GEM, one can construct ultra-fast, rigorous SEA responses for the same set of targets but for any other instrument, either in the TD or FD, in the following ways.

The simplest generalization of the GEM-based SEA is possible if one only desires FD data that would be obtained by another similar instrument, but with a larger or simpler coil arrangement. For example, for a single, larger Tx coil with some known impressed current pattern, one simply uses elementary algorithms (Bio-Savart Law) to compute the transmitted field around a prospective target location and thereby determines the applicable  $b_j$  in (35). That is, one simply determines the applicable decomposition of the new primary field into constituent excitation modes  $\Psi_j^{\text{PR}}$ . The target's response to each of these modes is the same regardless of what sensor produces them. Also, because we assume the new instrument has a larger or simpler coil structure than the relatively complex GEM system, no more modes should be required to express the primary field than were necessary for the GEM-3. Therefore the response can still be calculated as per (35). Further, that response can be applied to receivers located elsewhere besides the center of the sensor (where it resides in the GEM instruments). The  $\{S\}_j$  obtained by inference in construction of the SEA solution serve as equivalent sources of the responding field, no matter where the observation point is. They will also produce complete 3-D field values at any prospective receiver location, not only the  $H_z$  values used in the original determination of the  $\{S\}_j$ .

The only remaining caveats in this kind of SEA generalization concern field units and Rx loop size. Initially, any fields computed using calculated  $b_j$  with  $\{S\}_j$  inferred from GEM data will be obtained in terms of the ppm units peculiar to the GEM instrument originally used. However, knowing only the loop geometries and obtaining data for objects (e.g. spheres) with known properties allows one to perform an “absolute” calibration of GEM data in terms of standard magnetic field units,  $H \sim \text{A/m}$ . That was done successfully in this project. Also, because the Rx loop on the GEM instruments is relatively small ( $\sim 10$  cm diameter here), no attempt was made to deal with field variation across the loop area. For instruments with large Rx loops and for configurations in which a relatively small target is close to it, one would have to integrate the varying response over the Rx loop area. This can be done simply by using the  $\{S\}_j$  obtained to calculate the secondary field at a set of locations over the Rx loop area.

While doing so requires considerably more complex computations, one can also use the MAS (Section 2.1) to generalize a GEM-based SEA model to frequencies outside the band used in the original data and can also thereby infer equivalent FD or TD responses for arbitrarily complex instruments. One first obtains frequency response data for the object, across as wide as possible a frequency band, using the GEM-3. This data is used to validate a detailed numerical model of the object's response, via the MAS. Validating the MAS model with a substantial variety of observations of the object serves to identify its characteristics sufficiently (section sizes, material make up). The MAS model can then be used to fill out gaps in the measured frequency response, and to calculate SEA  $\{S\}_j$  parameters over all frequencies of interest. It can also calculate responses for any modes of excitation whatsoever, not only those pertaining to the original (e.g. GEM) data set. Extending the frequency range of the original data also means being able to construct a wide enough rendering of the object's impulse response so that it can be inverted into the time domain, thereby predicting responses from other instruments.

Altogether, the steps involved in producing a universal SEA formulation for a UXO type at hand can be listed as follows.

1. Perform UWB FD measurements around the UXO at diverse positions;
2. Iteratively perform detailed numerical MAS forward calculations for the relevant geometry until material parameter assumptions produce data that match the observations from step 1 satisfactorily;
3. Use this MAS model to solve for responses  $\{S\}_j$  to any and all SEA modal excitations that might be needed, over an extended frequency range;
4. For any new instrument or new target-sensor configuration, simply determine the applicable distribution of SEA excitation modes in the FD, i.e. just determine  $b_j$  in (35);
5. If necessary, invert the result to the TD.

Figure 14 shows an example of this “universal” generalization of SEA modeling for a steel cylinder 7.5 cm in diameter with length 30.5 cm starting with data obtained at a distance of  $h \sim 44$  cm. The process begins with extensively archived FD data (solid lines in left column of plots). The MAS is used to infer a sufficient set of object material properties so that the frequency response can be filled in and extended convincingly beyond the initial band (dashed lines in left plots). This allows easy computation of an extended set of SEA responses,  $\{S\}_j$ . Then, using the known Tx waveform of the EM-63 instrument, an applicable set of  $b_j$  is determined for the same steel cylinder but under other conditions. The

corresponding secondary field produced by the object is then inverted into the TD and calibrated to account for the particular units in which the EM63 reports signals. Clearly the method was quite successful (right column of plots). (Data collection and processing with the EM-63 was carried out in conjunction with personnel from Sky Research, also under SERDP sponsorship). We have also developed simpler methods for the inferring TD response for different instruments directly from their TD data; this will be reported elsewhere. In any case, the ability to construct a “universal” SEA model, beginning with readily available FD data, means that a powerful tool is at our disposal for ultra-fast, rigorous investigation of target responses to any prospective instruments and sensing scenarios.

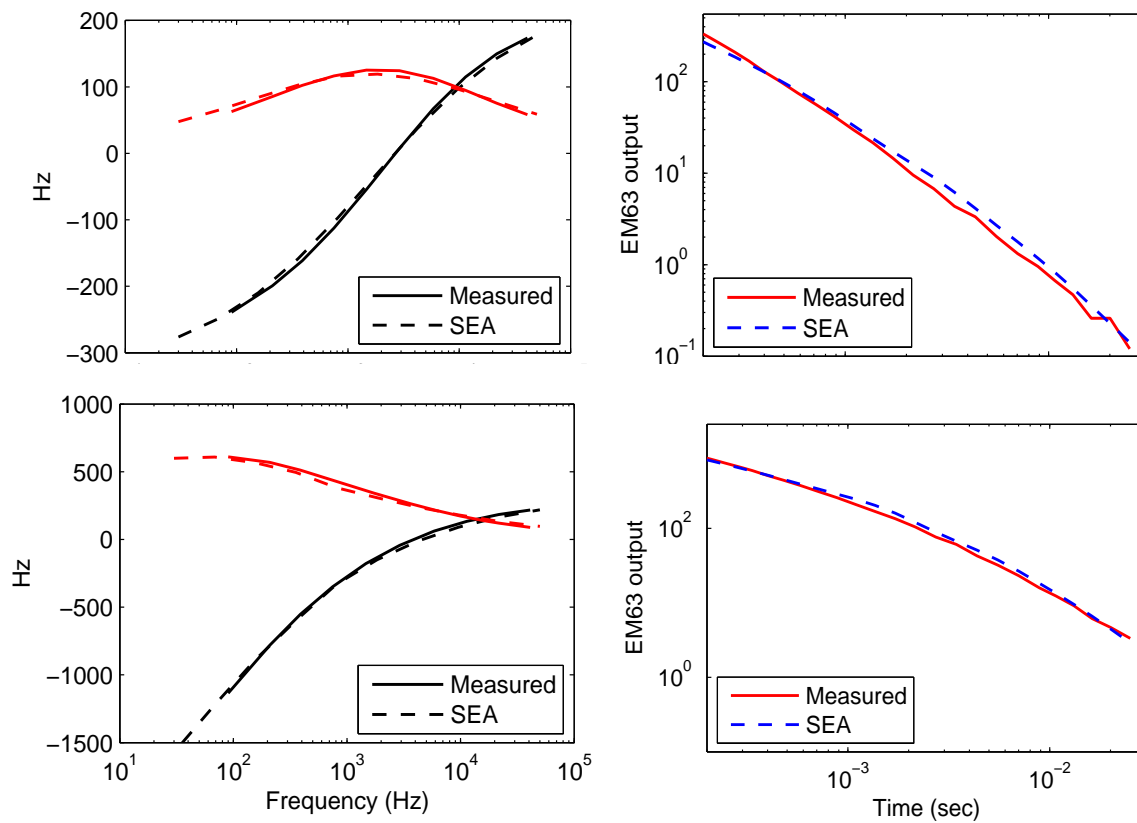


Figure 14. EMI response of steel cylinder, measured in the FD, reconstructed by the SEA with extension by MAS, and inverted to the TD. Left: FD; Right: TD; Top: Transverse orientation; Bottom: Axial orientation.

### 2.4.3. *Optimal SEA and the NSMC*

This section presents results of the search for optimal means for generating mathematically both the excitation modes and responses of targets, within an SEA context. Different choices for the input and output modes (in parameter terms, different kinds of  $b_j$  and  $\{S_{jj}\}$ ) can have very significant effects on the accuracy and especially the efficiency of an SEA system. While all the SEA systems are very fast forward models, capable of reproducing the signals from complex targets in a few moments on a PC, for inversion and classification calculations a forward model must be run many times, possibly many, many times. Ultra-fast methods are required. Further, we seek variants of the SEA in which the inferred response parameters are revealing and potentially useful in discrimination schemes. Experience to date recommends the normalized equivalent surface magnetic charge (NSMC) formulation. The NSMC, developed in the course of this project, is extremely fast, and also appears to be advantageous for both pattern matching and general inversion purposes.

The NSMC method proceeds by using equivalent magnetic charges  $\sigma_m$  arrayed on a surface constructed mathematically about an object's location. In response to any impinging primary field, these produce the same scattered field (signal) as the actual object, via the integral relation

$$\mathbf{H}^{sc}(\mathbf{v}, \mathbf{r}) = \sum_{i=1}^N \int_{\Delta S_i} \sigma_m(\mathbf{v}, \mathbf{r}') \mathbf{G}(\mathbf{r}, \mathbf{r}') d\mathbf{s}' \quad (36)$$

where  $\mathbf{G}$  is the standard Green function for the field at  $\mathbf{r}$  from a charge at  $\mathbf{r}'$

$$\mathbf{G}(\mathbf{r}, \mathbf{r}') = \frac{(\mathbf{r} - \mathbf{r}')}{4\pi\mu_0 |\mathbf{r} - \mathbf{r}'|^3} \quad (37)$$

and  $\mathbf{v}$  designates either frequency or time. The charges are distributed sinusoidally around the surface circumference, over  $N$  belts, each with area  $\Delta S_i$ , which together completely surround the object. Only a single parameter is required for the amplitude of each sinusoidal distribution around each belt.

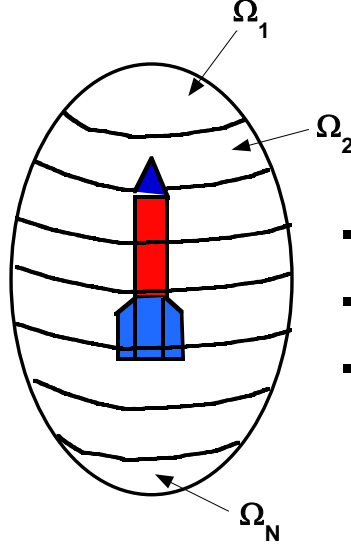


Figure 15. A UXO is surrounded computationally by a surface on which equivalent magnetic charges are distributed, represented through the parameters  $\Omega$ .

The crucial assumption of the NSMC is that one can rewrite the integral in (36) in terms of a proportionality constant  $\Omega_i$  for each charge ring and the value of the primary field  $H_{n,i}^{pr}$  that impinges on that ring.

$$\mathbf{H}^{sc}(\mathbf{v}, \mathbf{r}) = \sum_{i=1}^N \int_{\Delta S_i} \Omega_i(\mathbf{v}) H_{n,i}^{pr}(\mathbf{r}', \mathbf{v}) \mathbf{G}(\mathbf{r}, \mathbf{r}') ds' \quad (38)$$

This is the central assumption of the NSMC. Its ultimate justification is not quite as simple as theorizing that one can just replace  $\sigma_m$  point by point by  $\Omega_i(\mathbf{v}) H_{n,i}^{pr}(\mathbf{r}', \mathbf{v})$ . A rigorous treatment of the basis for the method will appear in upcoming publications. Meanwhile, published results demonstrate the applicability of the method [28]. Suffice it to say here that the  $\Omega_i$  associated with the  $i^{\text{th}}$  ring is not determined solely by the local properties of that portion of the surface around the scatterer, as all  $\Omega_i$  are solved for together.

The quantity  $\Omega_i$  represents a normalized charge, i.e. equal to the induced charge for a unit excitation (unit value of  $H_{n,i}^{pr}$ ) on the  $i^{\text{th}}$  ring. The relation (38) simplifies SEA calculations greatly, because now one does not need to decompose the primary field into constituent modes of any complexity and solve for the corresponding coefficients  $b_j$ . Rather the “standardized excitations”  $\Psi_i^{PR}$  are simply “hat functions,”

$\Pi_i$ , each of which is unity over the  $i^{\text{th}}$  ring and zero on all others. In SEA terms,  $b_i$  just equals  $H_{n,i}^{\text{pr}}$ , which is easily calculated, and the response coefficient  $\{S\}_j$  is just  $\Omega_j$  (more than one  $\Omega$  value for the  $j^{\text{th}}$  ring can be used if more than one circumferential sinusoidal mode is used, though this has rarely been necessary). One obtains the  $\{S\}_j$  by measuring  $\mathbf{H}^{\text{sc}}$  at a sufficient number of observation points  $\mathbf{r}$ , and then just solving (38) directly for the  $\Omega_i$ . One advantage that this approach has over a distribution of dipoles as responding sources is that a finer discretization of responding entities can be used with fewer parameters, assuming sinusoidal distributions of  $\sigma_m$  in rings around the object.

The value of the NSMC formulation depends on the assumption that the  $\Omega_i$  that pertain to a given target are characteristics of the object itself. That is, we require that the  $\Omega_i$  or at least their integral behavior be independent of the particular  $H_{n,i}^{\text{pr}}$  that produced the data from which they were acquired (i.e. for which (36) - (38) were solved). Preliminary results indicate that this is so: Both modeling exercises and tests with limited numbers of real UXO's and sensors support the view that the  $\Omega_i$  are independent of  $H_{n,i}^{\text{pr}}$  and of the particular geometrical constructions used to obtain them.

The NSMC system can be used to construct extremely fast forward models and then be applied in straight-forward  $\mathbf{H}^{\text{sc}}$  pattern recognition calculations. However a more intriguing possibility is to reduce the NSMC response to a single (time or frequency dependent) parameter, the pattern of which can be used for discrimination. Exploiting a measure of the  $\Omega_i$  collectively rather than examination of the  $\Omega_i$  details themselves would ideally offer both simplicity and uniqueness of representation. For this purpose, note that the sum of all the normalized charge

$$Q(v) = \sum_{i=1}^N \Omega_i(v) \Delta S_i \quad (39)$$

represents a kind of magnetic capacitance, analogous to electrical capacitance. As an integral of the  $\Omega_i$ ,  $Q$  is less subject to pointwise variability in computations around the surface of the object.

Overall, capacitance constitutes a measure of the charge (or charge separation) induced by some potential difference or gradient

$$\text{Capacitance} \equiv \frac{\text{Charge}}{\text{Potential Gradient}} \quad (40)$$

Here the potential gradient is  $H_{n,i}^{\text{pr}}$ , which is the gradient of the scalar magnetic potential, normal to the surface considered. The quantity  $\Omega_i \Delta S_i$  represents the charge induced on the  $i^{\text{th}}$  ring by a unit value of that gradient. Thus  $Q$  represents a form of magnetic capacitance for the whole responding body. Preliminary tests suggest that this quantity will be unique for a given scatterer, in the sense that different primary fields, different computational constructs to obtain the  $\Omega_i$ , and different target-sensor configurations all produce the same  $Q(v)$  for a given object. Therefore  $Q(v)$  appears to recommend itself as an efficient discriminator in general inversions. We will particularly pursue inversion systems that only attempt to sort objects according to gross size, so that clutter sized and UXO-sized objects can be distinguished.  $Q(v)$  appears to be an especially promising parameter for this purpose.

#### **2.4.4. Validation of the NSMC and the Invariance of $Q(f)$**

As a test of the validity of the NSMC, vector FD data were taken with the Geophex Ltd GEM-3D instrument along lines above the three UXO's in Figure 16, disposed as they are shown in the figure. This data constitutes the left hand side of (38). Because the value of the primary field from the GEM-3D can readily be calculated at any points over the surrounding surface, the only unknown on the right hand side of the equation is  $\Omega_i$ . By choosing enough different observation points  $\mathbf{r}$  in (38), one obtains a sufficient set of equations to solve for the set of  $\Omega_i$  values. Note that, having obtained parameters that allow specification of equivalent responding source values for any primary field, one is guaranteed a complete, consistent solution for the object considered, at all points beyond the surface on which the synthetic  $\sigma_m$  reside. In particular, these  $\Omega_i$  values will produce valid observations  $\mathbf{H}^{\text{sc}}$  at other observation points and under other  $\mathbf{H}^{\text{pr}}$  than were used in the cases from which the  $\Omega_i$  values were obtained. The sets of  $\Omega_i$  and in particular the  $Q(f)$  constructed from them (equation (39)) were then regarded as invariant signatures of these particular UXO's, and placed in a library for reference during processing.

To test the validity of this notion, the three targets in the figure were buried in different orientations and at different distances from the lines of observation points, relative to those for the case in Figure 16. These three new cases were labeled M1, M2, and M3 and treated as unknowns by an analyst not involved with the measurement nor privy to the ground truth. The analyst was told that each of the unknown cases corresponded to one of the familiar ones from the library, but was not informed which was which. After using optimization to determine a  $Q(f)$  for each unknown case, in each instance the analyst succeeded in matching correctly the  $Q(f)$  spectra from the library of spectra with those from the unknown cases. This is illustrated in Figure 17, where the spectrum  $Q(f)$  for the 37 mm UXO (Figure 16, far left) is compared to two obtained for unknown cases M2 and M3. The library  $Q(f)$  for the 37 mm agrees well with that obtained from the optimization for M3 (correct UXO) but not with that for M2 (incorrect UXO). As do many other tests not shown, these results support the assertion that the NSMC formulation provides a valid forward model for UXO responses to general excitation, including heterogeneous material composition and object geometry, for varied observation points. In the tests pertaining to the objects in Figure 16, obtaining the correct  $Q(f)$  was only possible because  $\mathbf{H}^{sc}$  from the forward model based on (38) and from the measurements matched well.

Sections 7 makes wider use of this kind of pattern matching of inferred and prospective  $Q(f)$  spectra, relying on them as distinguishing features of different targets in multi-object problems. The  $Q$  of an object is indeed a property of the object, not dependent on the computational route leading to it (beyond numerically induced variations) or on the particular set of observations from which it is derived. This is tantamount to saying that it is unique in the sense that it is *invariant*, but not in the sense that every object must necessarily have a different  $Q$ . Pursuing the concept of  $Q$  as a kind of magnetic capacitance, note that one can design a number of rather different items that will have the same electrical capacitance, if that is set as a goal. However it is extremely unlikely that two randomly selected heterogeneous objects designed according to other criteria will happen to have the same capacitance.



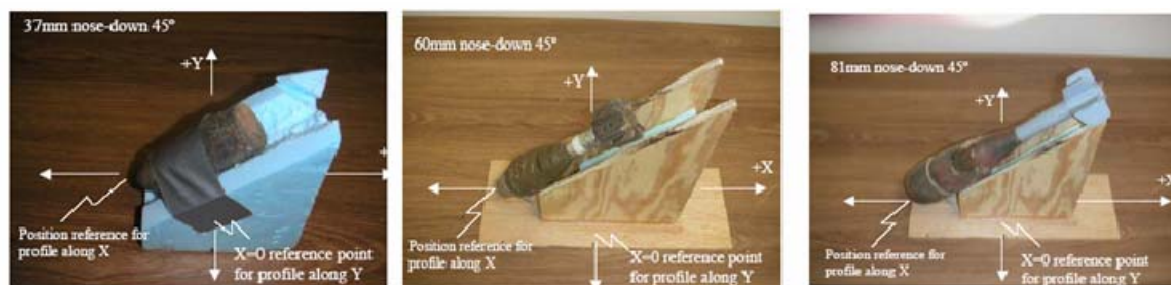


Figure 16. The GEM-3D was used to obtain vector data for each of these UXO, buried, as well as for comparable sized clutter.

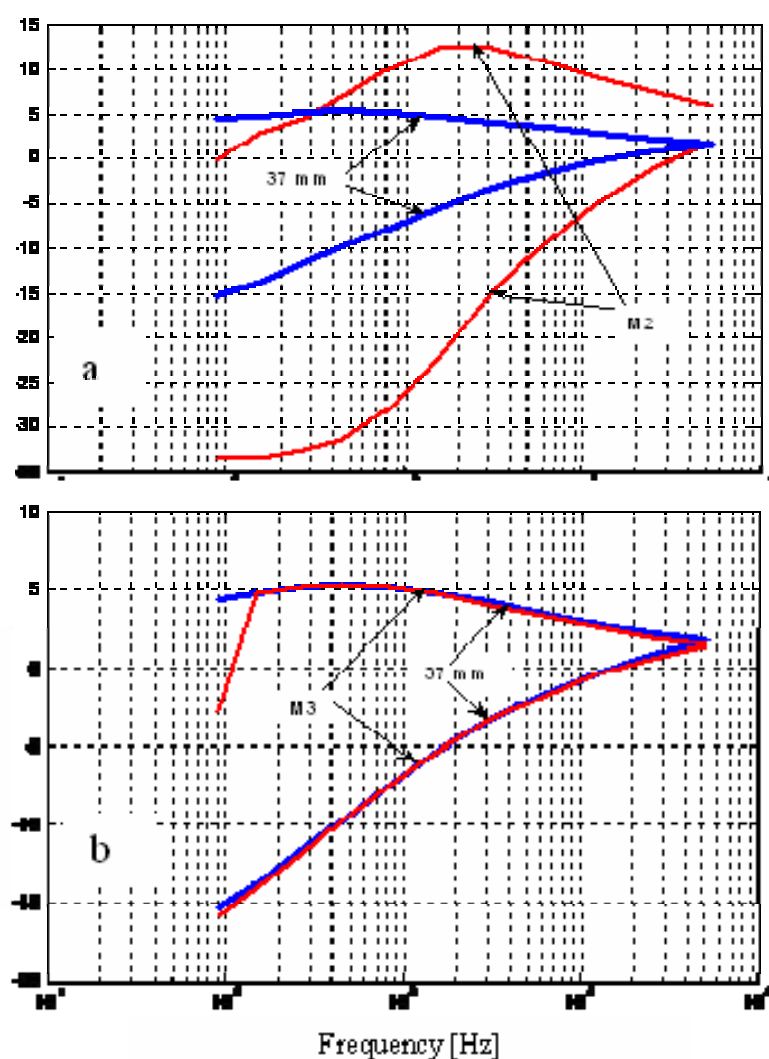


Figure 17. Comparison of  $Q(f)$  for the 37 mm mortar to that obtained from processing for blind tests M2 (a, top) and M3 (b, bottom).

## 2.5. Ground Response Consequences for Processing

### 2.5.1. Phenomenology

To model the EMI ground response and include it in processing one must first determine the relevant physics and phenomenology. In general, the physics of ground magnetic response is still a developing science, and pursuit of its cutting edge is beyond the scope of this study. However, as its effects are sometimes prominent when targets are in fact buried (as in our testplots), and in as much as variable ground response generates survey signals that are “highly contaminated,” *per force* ground response becomes a concern here. Therefore a number of basic physical considerations and observations are employed to arrive at working assumptions, on the basis of which we may approach the field data.

Ground response is treated in some detail in the FY04 Annual report for this project. To summarize the basic physics here, the basic assumptions and considerations of Section 2.1.1 apply, to the effect that the subsurface irrotational magnetic field outside of the target may be represented in terms of the gradient of a more convenient scalar magnetic potential.

$$\mathbf{H} = -\nabla\psi \quad (41)$$

Gauss’s magnetic field divergence law states that

$$\nabla \cdot \mathbf{B} = 0 \quad (42)$$

where  $\mathbf{B} = \mu\mathbf{H}$  and  $\mu$  is the magnetic permeability of the medium (H/m). We have previously treated  $\nabla\mu$  as effectively zero, which appears reasonable in that  $\mu$  is unlikely to vary much beyond the order of about 0.1% [29, 30]. Therefore the combination of (3) and (4) just produces the Laplace equation

$$\nabla^2\psi = 0 \quad (43)$$

as a scalar governing equation. This equation admits relatively simple solutions and solution techniques, and we would like to argue that its use can be retained.

However, one must note that even when  $\nabla\mu$  is effectively zero within the soil,  $\mu$  may still have significant effects because it also appears in the boundary conditions:  $\mu$  of the soil and air may be different, and the boundary condition at the soil-air interface is

$$(\mu H_n)_{air} = (\mu H_n)_{soil} \quad (44)$$

This is tantamount to saying that  $\nabla\mu$  is zero in each subregion outside the scatterer, but that it is a delta function over the soil-air interface. Accounting for this variation of  $\mu$  in terms of the boundary condition (44) means applying to (5) the constraint over the surface of the ground

$$\left(\frac{\partial\psi}{\partial n}\right)_{air} = \mu_r \left(\frac{\partial\psi}{\partial n}\right)_{soil}, \quad \mu_r \equiv \frac{\mu_{soil}}{\mu_{air}} = 1 + \chi \quad (45)$$

where  $\chi$  is volumetric magnetic susceptibility. Of course, there may be other interfaces as well across which there is  $\mu_r$  variation, as between rocks and surrounding soil, or layers and lenses of different soil types, in which case  $\mu_r$  pertains to the ratio of permeabilities across other relevant interfaces.

The question arises whether  $\mu_r$  in (45) is enough greater than unity to make a difference. Considering the benchmark example of a homogeneous halfspace of permeable soil, should one expect a significant EMI ground response? At first glance this seems quite unlikely in view of the small values of  $\chi$  cited in the references above. It turns out, however, that even this small parameter jump across the interface is still sufficient to produce a notable response. The material in this project's FY04 annual report describes a modeling and measurement investigation of this issue in some detail, the main points of which we summarize here. Based on the halfspace solution, if the EMI transmitter is an ideal infinitesimal magnetic dipole at elevation  $Z$  above the ground surface, then the vertical scattered magnetic field (signal) from the ground will be

$$H_z^s = \frac{K_{01} m_{z0}}{16\pi} \frac{1}{Z^3} \quad (46)$$

where  $K_{01} = (\mu_{\text{soil}} - \mu_{\text{air}}) / (\mu_{\text{soil}} + \mu_{\text{air}})$  and  $m_{z0}$  is the dipole moment of the transmitter [31]. All quantities are assumed to be real valued, to a first approximation. Figure 18 shows a comparison of a  $1/Z^3$  pattern and data measured with the Geophex GEM-3 over in situ soil in the backyard of CRREL. This soil is not noted for its peculiar magnetic properties; similar measurements over other (imported) soils on site produced similar results, in both pattern and magnitude, in the inphase (real valued) data component only.

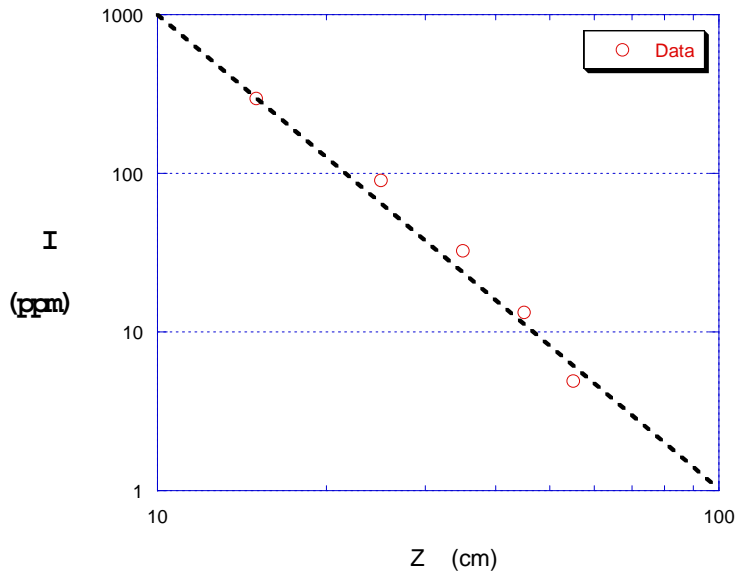


Figure 18. Inphase ground response  $I$  as a function of sensor height (930 Hz), compared to theoretical line for  $A/Z^3$  dependence from halfspace solution, with  $A$  arbitrary.

The general agreement between the power law relationship ( $A/Z^3$ ) and the GEM measurements in the figure (as well as various others) suggests that, at least over a single spot on the ground, one may assume a halfspace-like ground response. This does not require deep homogeneity because the sensor responds primarily to a shallow layer of soil directly beneath it. Section 5 shows that, with this instrument, most of the ground response comes from a depth of soil only on the order of the elevation of the sensor above the soil surface.

The range of elevations in the test in Figure 18 is approximately that which might be employed with this instrument in a UXO survey. In terms of the units peculiar to GEM output (ppm of reference coil signal), the order of magnitude of significant field responses from UXO range from some tens to at most some 1000's of ppm. Thus the magnitude of backyard soil response in Figure 18 is quite significant relative to that from a target of interest. Analytical solutions for a metallic sphere buried in a permeable

halfspace [FY04 Annual report], based on a range of ground permeabilities measured at the standardized UXO test sites [30], show that one should expect inphase ground responses at those sites that are similar to those in the figure. Further, calibration of the GEM responses in ppm so that they can be translated into standard magnetic field units (A/m) allows one to estimate the ground magnetic susceptibility from data such as that shown here. These calculations indicate that the susceptibility in all testplots for this study and all “backyard” soils used is on the order of what has been measured at the standardized UXO sites. Thus, for soils at a variety of locations, one should expect very significant FD soil responses.

Figure 19 shows the complete spectral response of the soil in Figure 18, with air response background subtracted, observed by the GEM-3 from a height comparable to that used in our measurements over targets. Patterns like this appear at each elevation of the sensor, with the flat real-valued response changing only in magnitude as per Figure 18. While it is marginally possible that the excursions in the curves around the highest frequencies in Figure 19 are caused by complex valued soil permeability or induced currents, investigation indicates it is more likely that it is just distortion from high frequency drift in the instrument. Overall, the dominant pattern is one with negligible quadrature response, and flat inphase response. This is the response that one expects from a magnetic material with negligible conductivity, producing a purely magnetic response, e.g. the ferrite used to calibrate this instrument.

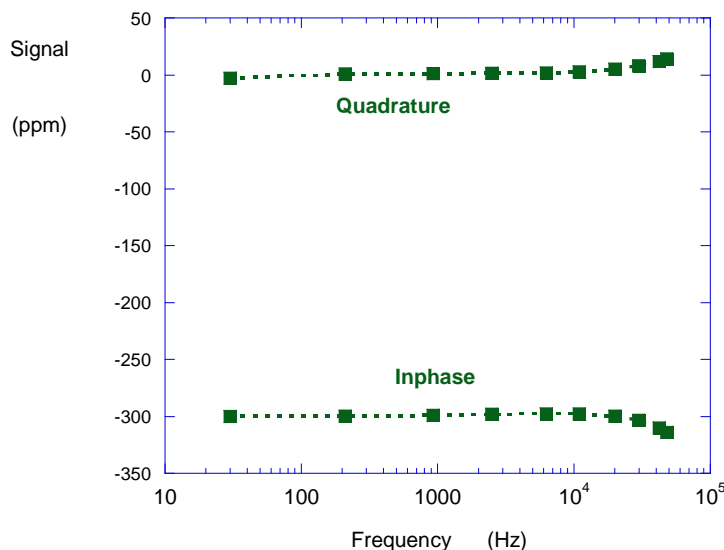


Figure 19. Soil response in GEM-3 ppm vs log of frequency.

The problem with the view encouraged by Figure 19 is that it does not explain the fact that significant soil responses are seen by time domain instruments. To understand the issue, consider a FD expression for  $\mu_r$  in terms of magnetic susceptibility  $\chi$  as

$$\mu_r(\omega) = 1 + \chi(\omega) = 1 + \chi'(\omega) + i\chi''(\omega) \quad (47)$$

The implication of spectral patterns like that in Figure 19 is that

$$\chi'(\omega) \approx \text{constant}, \quad \chi''(\omega) \approx 0 \quad (48)$$

Such a constant, real valued  $\chi$  should have no effect in time domain measurements. Given negligible electrical conductivity in the soil, its response would simply be proportional to  $\chi'$  times the magnitude of the transmitted field at any given point in time, *with no delay*. All response would be instantaneous. When the transmitted field from a TD instrument is shut off during the recording of data, the soil response would also shut off, producing no data other than noise. However, many time domain measurements do indeed show some soil response. Evidently some kind of relaxation effect takes place, beyond the instantaneous response.

Overall, one might hypothesize a soil response in the form of the schematic in Figure 20, given a downward step input in the primary field at  $t = 0$ .

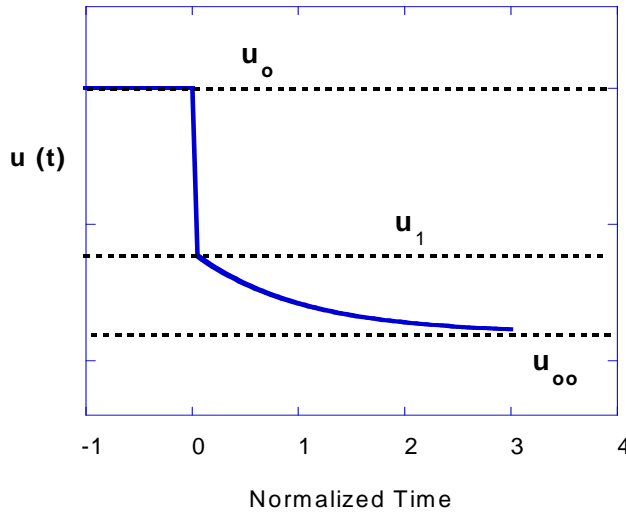


Figure 20. Hypothetical ground response to a downward step input of  $u_{00}$  at  $t = 0$ , showing two phenomena: instantaneous response, followed by relaxation.

The instantaneous response is from the system's initial value of  $u_0$  to  $u_1$  which persists for all  $t > 0$ . This would correspond to the flat real-valued impulse response in Figure 19. On top of that is a relaxation to the ultimate response of  $u_{\infty}$ . Available models of soil magnetic relaxation feature exponentially asymptotic forms, governed by characteristic relaxation times [32, 33]. For perspective, consider the time and frequency domain expressions when an impulse response  $h$  consists of a simple exponential decay, i.e. pure relaxation:

$$h(t) = \begin{cases} e^{-at}, & t > 0 \\ 0, & t < 0 \end{cases}, \quad h(f) = \frac{a - i\omega}{a^2 + \omega^2} \quad (49)$$

where the single relaxation time  $\tau$  here is just  $1/a$ . Changing this to our sign convention and arbitrarily choosing  $a = 2\pi \times 10^3$  produces the FD relaxation impulse response in Figure 21.

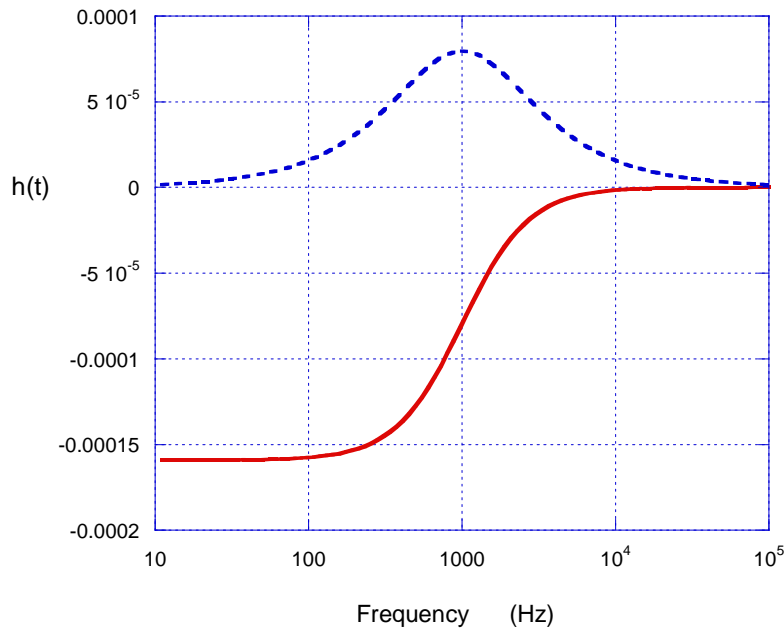


Figure 21. Hypothetical relaxation impulse response, for single relaxation time  $1/a$ , with  $a = 2\pi \times 10^3$ . Blue = imaginary part, red = real part.

The physical complexity of soil suggests that more than one characteristic relaxation time  $\tau$  may operate. It is convenient to assume a flat logarithmic distribution of contributing  $\tau$  values between bounds  $\tau_1$  and  $\tau_2$ , because that can be approximated by the closed form FD expression [32, 33]

$$\chi(\omega) = \chi_o \left[ 1 - \frac{1}{\ln(\tau_2/\tau_1)} \ln \left( \frac{i\omega\tau_2 + 1}{i\omega\tau_1 + 1} \right) \right] \quad (50)$$

This is the equation that has been used in those references to express the relaxation effect that produces soil response signals in the TD after the transmitter has been shut off. Plotting (50) for  $\tau_1$  and  $\tau_2$  equal to  $10^{-6}$  s and  $10^{-3}$  s, respectively, produces the pattern in Figure 22. Clearly this relaxation spectrum (left plot) is quite similar to that in Figure 21, with the locus, width, and peakedness of response just governed by the interval specified via  $\tau_1$  and  $\tau_2$ . In the TD inversion of this spectrum (right plot), note the linear log-log portion of the TD plot, roughly between the two relaxation time limits. Presumably this pattern of initial period, middle quasi-linear period, and ultimate falloff is what one sees with the Geonics EM-63 and other TD instruments.

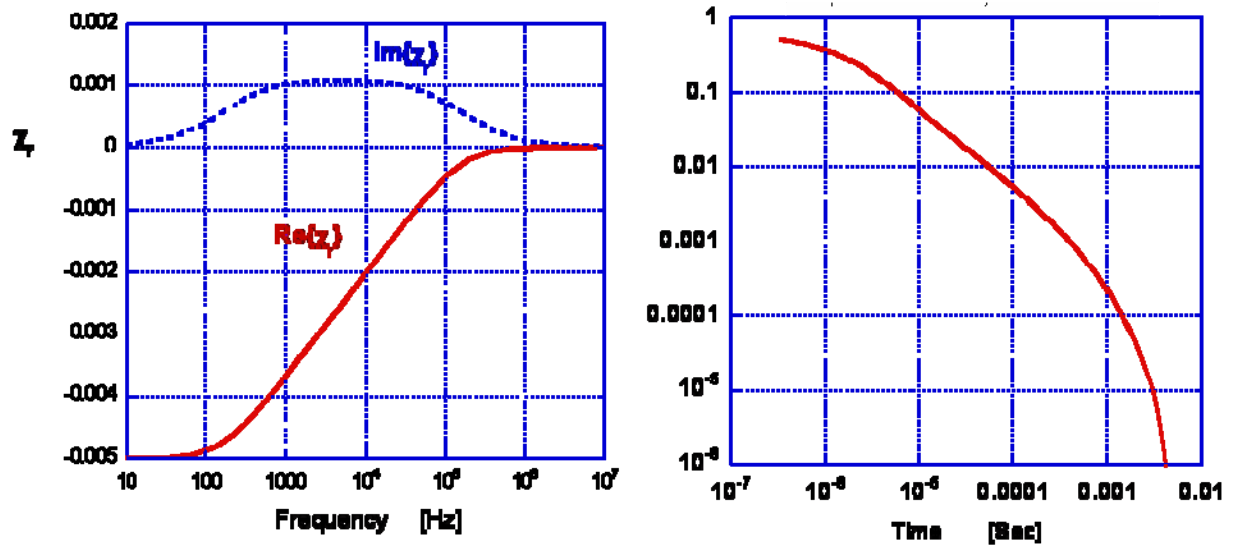


Figure 22. Relaxation response in the FD from (50) with  $\tau_1 = 10^{-6}$  s and  $\tau_2 = 10^{-3}$  s. Left: FD impulse response. Right: corresponding TD step input response.



Returning to our actual observations of soil response, one must ask why spectra like that in Figure 19 appear instead of that in Figure 22. While no definitive answer is at hand, it seems likely that, with reference to Figure 20,  $(u_1 - u_0)$  is simply much greater than  $(u_{00} - u_1)$  for the soils observed. Further, some of the observed soil spectra encountered during this project may not really be quite as flat as they appear at first glance. Consider the spectrum for a different testplot soil than the one producing the data in Figure 19, namely that in Figure 23. The first interpretation of this figure is that the inphase part is “trying to be” flat, while the quadrature curve values are basically negligible; and the apparent variations from this are caused primarily by the roughness of the background subtraction. That may in fact still be the best explanation. At the same time, others have observed similar near-linear inphase curves like this, similarly offset below zero. While the approximations of the background subtraction prevent a definitive judgment in connection with the data dealt with here, it is still distinctly possible that relaxation effects are indeed present in the measured spectra, although they are quite faint.

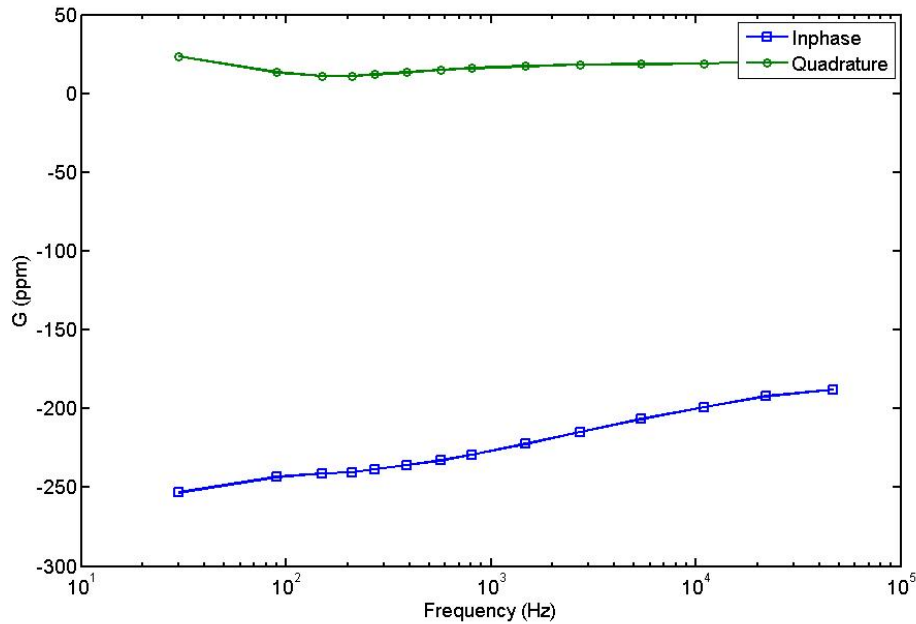


Figure 23. Ground response spectrum for a testplot observed at 10 cm elevation, with air response at 1 m subtracted.

With all this in mind, the most general representation of soil susceptibility may be something like:

$$\chi(\omega) = \chi_{o1} + \chi_{o2} R(\omega) \quad (51)$$

where  $\chi_{o1}$  and  $\chi_{o2}$  are constants. The parameter  $\chi_{o1}$  would account for the larger flat response,  $(u_1-u_0)$ .  $\chi_{o2} \sim (u_{oo}-u_1)$  would be the separate magnitude of the relaxation response,  $R(\omega)$ . In all the FD data treated here  $\chi_{o2} \ll \chi_{o1}$ . As yet we have not found (51) or similar in the literature. This is not entirely surprising in that, for people working *only* in the TD, (50) or some similar  $R(\omega)$  *does* represent the entirety of what would appear in their data. In that sense the model (50) provides a complete TD model, represented in the FD but applicable only in the TD.

### **2.5.2. Ground Effect on Signals from Buried Metallic Objects**

Overall, despite a lack of significant currents induced in the ground there are at least five ways in which ground permeability could possibly affect EMI signals from a buried metallic object, as measured from above ground:

1. Response of the ground itself, superposed on the target signal;
2. Volumetric alteration by the ground of the fields transmitted by the sensor, thereby changing the excitation of the target;
3. Alteration of the frequency response of the object, as changes in surrounding permeability affect the soil-target relative permeability, i.e. they alter a boundary condition like (44) but applied to the target-soil interface;
4. Interaction between the scattered fields from the target and the ground-air interface, analogous to - but not the same as - signals bouncing back and forth between the buried object and soil surface in a radar or acoustic wave problem (EMI signals are *not* waves).
5. “Refraction” of the magnetic fields passing through the soil interface, changing their geometry or spatial dependence relative to what they would be in free space.

Detailed analytical investigation of the problem of a metallic sphere buried in a permeable halfspace [FY04 annual report] supports the observation in the data analysis that only item #1 above will be significant, for reasonable values of ground permeability. Additionally, experiments were performed with the steel sphere in Figure 24 and the blue frame in Figure 25, left, with slots for the sensor head at predetermined heights. First the sphere’s response was measured in air, i.e. when placed about 1 m above

the soil, a height at which no soil response was evident (Figure 25, right). Then it was buried 3.5 cm deep (to its upper edge) below the frame, and the sensor head was lowered progressively through the sequence of slots in 10 cm increments. Figure 26 shows comparisons of the spectra of the sphere in air and in the ground with height dependent soil response simply subtracted, normalized by the maximum value in the quadrature component so that they can be plotted together. The soil's permeability just adds a halfspace response to the pattern. When this flat pattern (e.g. Figure 19) is subtracted from the data for the buried sphere, it effectively just shifts the inphase curve upwards and into agreement with the pattern for the sphere in air. Agreement with air values after such a shift was seen at all elevations at which significant ground response could be detected.



Figure 24. Ben Barrowes's machined steel sphere S1.



Figure 25. Left: Blue rig over measurement patch in which sphere is buried about 3.5 cm deep (to its surface); GEM-3 to be inserted in the slots at each elevation, 10 cm apart. Right: Measurement of sphere in air, in reality level.

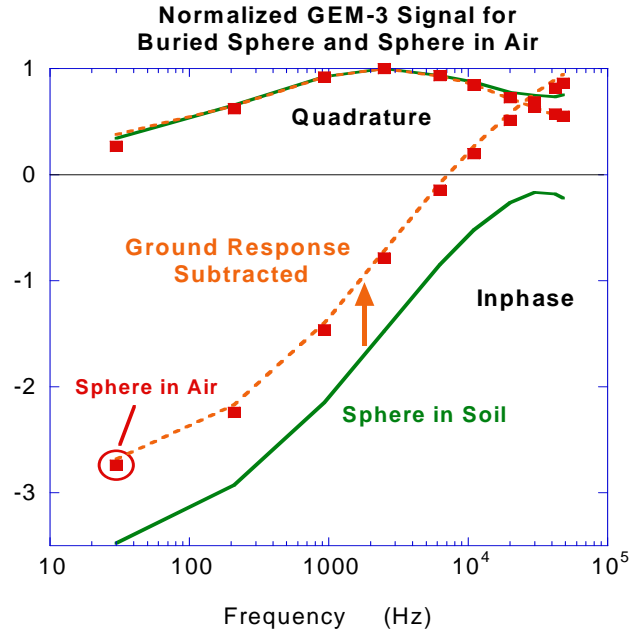


Figure 26. Measured impulse response of sphere in air (markers); and in soil, including soil response (green line); and with independently measured soil response subtracted from the latter (dashed orange).

This figure supports the conclusions that emerge from the calculation of responses for a buried sphere in the FY04 annual report. In particular, after considering every manner in which the sphere, soil, and soil surface could interact, we conclude that for our purposes the object's and the soil's responses can just be superposed. Within the limits of our data resolution, essentially the entire soil effect is just a "rigid body" (constant, flat across frequency) shift in the real valued (inphase) portion of the impulse response.

### 2.5.3. *Spatial Variability*

Some successful inversion and classification processing was performed in the course of this work by assuming that the soil response over a small grid area caused an elevation dependent shift in the inphase response such as that seen above [Section 5.8.1]. This shift simply had to be solved for as part of the optimization computations, in which it was assumed to be flat over frequency as per Figure 19, and

also spatially invariant over a measurement grid at a given nominal elevation. More generally, however, typical soil data are problematical in this regard because of spatial variability. Figure 27 shows data for the lowest frequency used. The overall picture is more or less consistent over frequency (Figure 28). Figure 29 illustrates reasonable consistency over time and over small changes in elevation, in that subsequent grids of measurements were taken at different elevations at different times.

Unfortunately these figures all also illustrate very considerable spatial variability of the ground response. No “air response,” i.e. inherent instrumental response was subtracted from the raw data shown, which thus includes together the unavoidable, relatively steady instrument background together with that from the soil. However virtually all variability is caused by the soil, as evidenced by the repeatability of the measurements over the same physical area (Figure 29). The magnitude of soil responses that appear in Figure 27 are on the same order as that frequently obtained from objects of interest. Further, the variability shown in the figure for responses at a given nominal sensor elevation also represents a substantial percentage change from place to place over the grid.

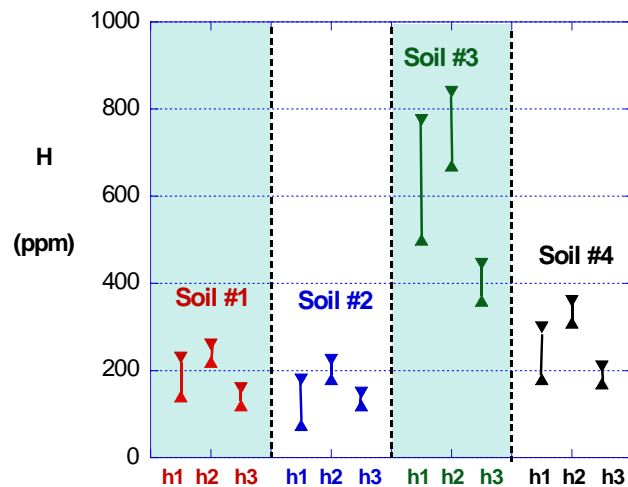


Figure 27. Left, measurement surface over artificially smoothed soil surface. Right, ranges of response for different soils in this scenario, at sensor elevations h1 ~ 1 cm, h2 ~ 6 cm h3 ~ 11 cm.

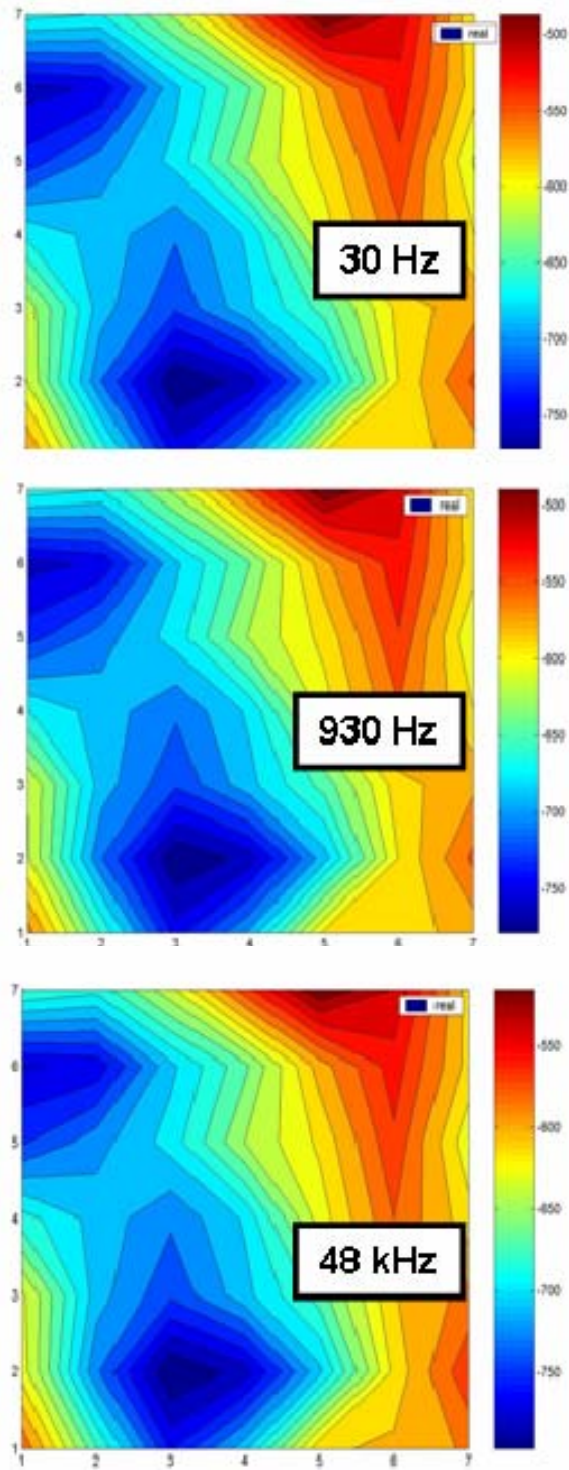


Figure 28. Grid measurements producing some of the data in Figure 27.



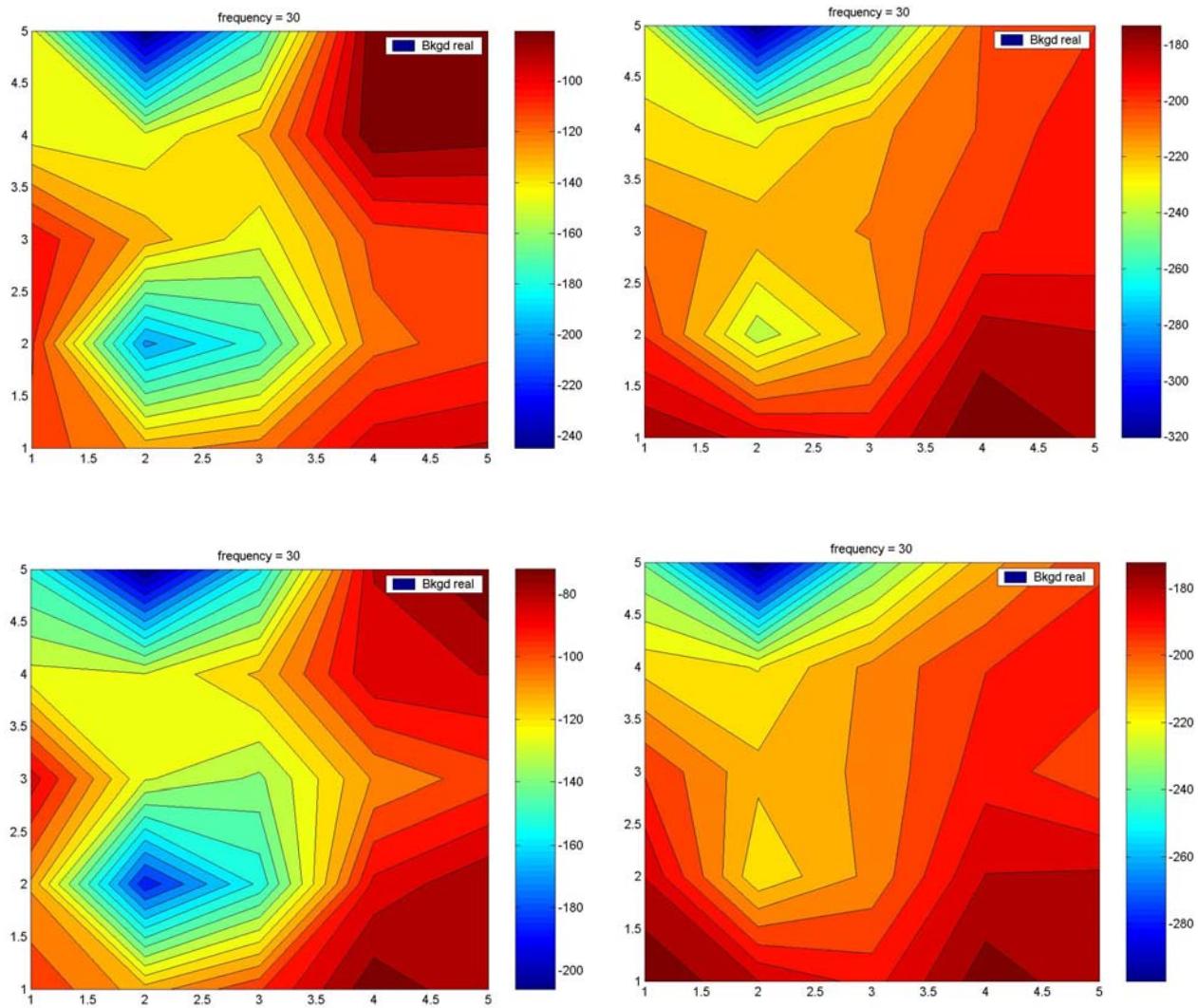


Figure 29. Example of spatial variability of soil response, inphase component, over a grid away from known targets in testplot #2. Top row Nov 27, bottom row Nov 29. Left column “ground level” (~ 1.5 cm elevation), right column ~ 6.6 cm elevation.

Many calculations in the course of this project [34, 35] indicated the likelihood of substantial signal distortions when the GEM sensor head passed very near a bump in the soil surface. Other things being equal, raising the sensor might help as it would then respond less to individual surface perturbations. However the magnitude of spatial variation of response at the higher elevation in Figure 29 is about the same as at the lower elevation. This is because the overall soil response is stronger at the higher elevation, given the particular design of this instrument: The instrument effectively receives the signal

transmitted by its image in the soil. As the sensor head is lowered very near the soil surface, the instrument and its image nearly coincide. At the same time, the sensor head is designed to have a transmission null around its center receiver. Thus when the head and its image nearly coincide, the sensor effectively only receives the fringes of the transmission null. Modeling and comparison to measurements show that the ground response reaches a maximum as the head is raised to about 10 or 15 cm, after which it declines.

The contouring in Figure 29 may be misleading in that the data on which it is based are sparse. Figure 30 shows the variation of recorded ground responses over the 5 by 5 grid relative to the grid average. Overall, the most extreme variations occur at isolated positions (e.g. positions #7 and #22), with the main variation ranging between about  $\pm 35$  ppm. Raising the sensor as much as was done in Figure 29 was not enough to smooth these spikes. Further elevation might lead to greater smoothing but is impractical and probably undesirable, as the target signals would begin to suffer. Absent the application of a different instrument, one must live with the kind of variability in soil response shown above. Variability of soil magnetic response, as opposed to the average response *per se*, produced the greatest difficulties in processing and interpreting the outdoor testplot data in this project.

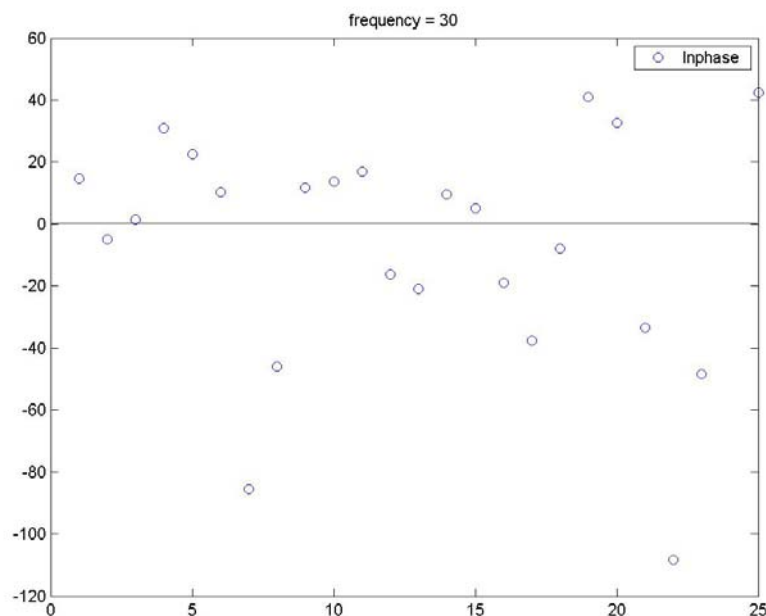


Figure 30. Plot of inphase de-meaned inphase soil response vs position number, for testplot #2, over 25 point grid at 20 cm point spacing.



The measured quadrature component of soil response is generally small (e.g. Figure 23) and, in absolute terms, its variability is commensurately less as well. Figure 31 shows plots of quadrature soil response from a grid in testplot #2. Invariably the greatest variability occurred at 30 Hz, rapidly declining with frequency to about the level shown in the figure for 210 Hz, i.e.  $\sim \pm 3$  ppm relative to the grid average. The spatial distribution of the variation was also relatively consistent over frequency, at least up to the highest frequencies (see figure), at which point the variation becomes quite minimal. This suggests a strategy of only processing the quadrature component data as a way of eluding soil response signal clutter. It also suggests resorting to instruments in which horizontal field components are also measured which, for the most part, should be largely free of soil response: In as much as a receiver perceives an image of the transmitter, an Rx coil placed near the center of a level Tx coil should only receive vertical field components from the ground response.

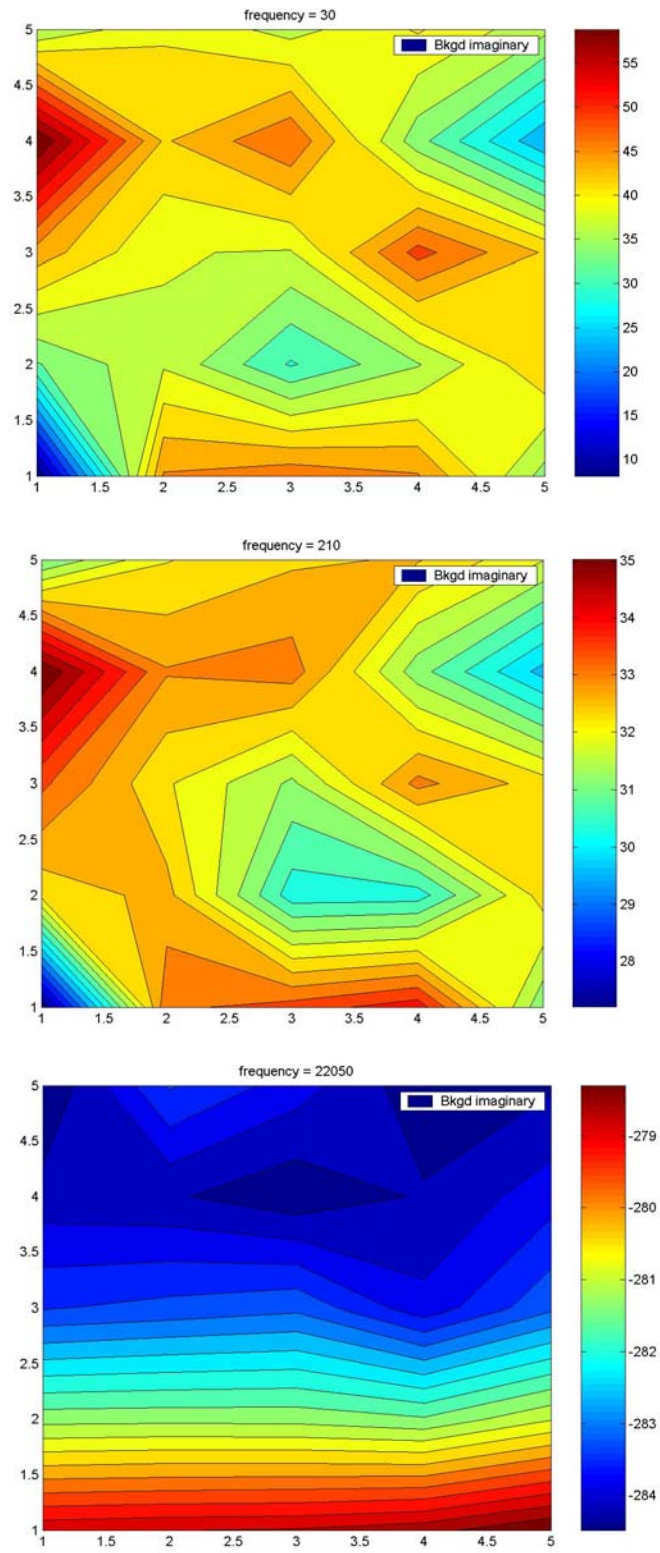


Figure 31. Quadrature component for same case as in Figure 29, left column, Nov 27.

#### **2.5.4.                    *Processing Implications***

Our working assumption based on the observations and analysis above is that response from the soil will be approximately flat over frequency and may be treated as simply superposed on the target response. It may just be subtracted from cases with target present to obtain signatures for comparison to targets in air. Equivalently, in comparing to prospective target response spectra, one may compensate for the soil effect just by seeking a constant shift in the inphase curve relative to a target's air values. In the testplot exercises, as opposed to the simulation and lab analyses, the working assumption is implemented indirectly: Background measurements are made over grids where apparently there are no targets (e.g. Figure 29), or at grid points away from apparent target locations on grids above targets. These background signal values contain both ground response and inherent instrument transfer function (background as would be seen in any case, in air). A spatially averaged or interpolated value for this total background is subtracted from the data from the target vicinity in the grid.

Applying averages over the grid as an elevation dependent background for subtraction is compromised somewhat by possible spikiness in the data. While not visible, such spikes may be buried within other stronger signals such as those above a buried target, e.g. Figure 32. To treat the testplot data specifically, background values were used that seemed most likely to be the best representation of the soil responses in the specific target vicinities, as opposed to over a separated background measurement grid. Thus grid edge or corner values such as those in Figure 32 were used. This requires a certain amount of *ad hoc* attention: clear, individual spikes in background response must be avoided, together with any regions in which non-soil responses seems to appear near the corners or edges. For example, regions such as the lower left in Figure 32, upper plot, might cause concern. Cases with off-center clutter items amplify this difficulty. The quadrature component data for target cases typically showed quieter edge and corner values (Figure 32, bottom). This reinforces the prospect that processing might benefit from using this component alone, although in doing so one discards half of the data content.

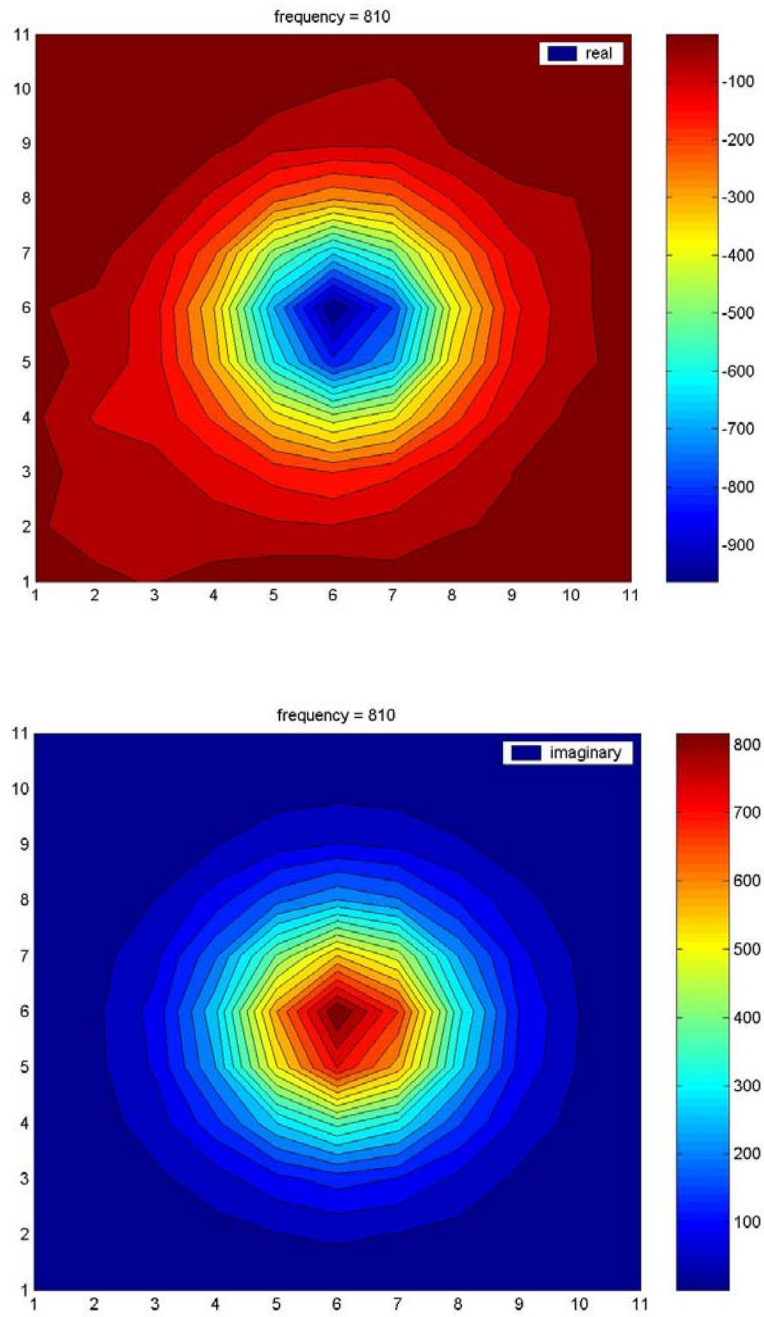


Figure 32. Testplot #2 data contours at 810 Hz, Nov 27, for a case with target present.

## **2.6. EMI Inversion and Classification Processing Implementations**

Essentially all EMI inversion or classification processing involves some kind of optimization calculations. Instead of performing a once-around, direct solution for the parameters in some sort of target model, one searches through sets of possibilities, usually constrained to a chosen parameter space and signal mechanism. A limited number of direct solution approaches is possible, but these generally suffer from non-uniqueness or ill-conditioning problems. Optimization, by contrast, usually proceeds by solving instead a large number of smaller forward computations, each constrained to have stable, unique results, as in evaluation of the field produced by an assumed dipole in a trial set of locations and orientations. The algorithms are designed to converge upon a set of parameters which, through the assumed forward model mechanism, produce data that most closely matches what is observed. One then interprets the implications of these parameters, to see whether they imply a UXO-like object, a non-UXO, a particular class of UXO, etc. Such search computations can be very resource intensive, and more efficient and reliable techniques are continually being sought. In addition to common, tried and true approaches such as gradient methods, this project implemented newer methods with attractive properties, in particular differential evolution [36].

In the sense described above, all inversion or classification methods ultimately depend on matching model calculations with data. However different approaches proceed from the search and matching to a classification decision in quite different ways. Perhaps the simplest or most direct method consists of pattern matching, that is, the matching of observations with predictions that can be produced from a library of possible signal sources. For example, one can assume that each of a set of UXO's that could be present has a uniquely defined axial and transverse frequency pattern of response (something we have argued strenuously is often not the case). Then one assumes further that in any orientation these UXO's will each produce in the data some linear combination of these two constituent responses. In the optimization one works quickly through a search of possible orientations by each object to see which one can produce a linear combination of axial and transverse responses that best matches the observed pattern. In the frequency domain this has been termed "fingerprinting" [37]. Here we pursue a related approach, but instead produce response patterns from members of a UXO library by using the SEA model described in Section 2.4. Because the SEA produces a rigorous computation of response at any observation point from a known set of UXO types, one need not worry about the uniqueness of axial or transverse

responses; or whether a UXO will produce one sort of response when its nose is very close, and another when that nose is further away; or that the primary field might vary greatly over the surface of the object. The model accounts for all such variations.

Pattern matching with the SEA represents, in the end, a very simple kind of classification processing in the sense that whatever object in a library produces the best match with the data is assumed to be the most likely target present. If, by some measure, no object produces a very good match then one assumes that the object actually present does not represent anything in the library. By default it is classed as clutter. Sophistications of the method may enter through strategic definition or construction of the system objective function (quantity to be minimized in the optimizations), reflecting probabilistic notions or statistical weighting. Also, from any degree of matching of the data different measures of goodness of fit may be defined, on the basis of which decision criteria are constructed.

In more general inversion one does not proceed in the forward calculations from a defined set of forward models in a library, but rather just seeks whatever set of parameters in a chosen model type will produce the best match with the data. These parameters could be, for example, magnetic polarizability coefficients in a general tri-axial dipole model. Once the optimization calculations converge upon a set of such parameters, one examines them for clues to *generic* classification of the object – is it a body of revolution, elongated or flattened, large or small, etc – leading then to a judgment on whether the object is likely to be a UXO or not.

Inference of generic object type from parameters produced by the optimization can be based on experience, as when some range of the ratio of axial to transverse dipole moments ( $\beta_a/\beta_t$ ) is taken to imply an elongated object. The classification can only be as good as the solidity of the connection between the model parameters and object characteristics. We have demonstrated above (Section 2.3) that the ratio  $\beta_a/\beta_t$  and dominance of  $\beta_a$  will depend on frequency or time range and metal type, even for a homogeneous object. And some non-BOR objects may produce BOR-like sets of  $\beta$ 's [2]. Be that as it may, one can at least say that a BOR should not produce non-BOR-like sets of  $\beta$ 's. In the approach described below we use dipole-based modeling in terms of such  $\beta$ 's to estimate whether an object is non-UXO-like (three mutually contrasting or “disorderly”  $\beta$ 's associated with its principal axes); and which objects are “suspicious” (likely a BOR and possibly elongated).

One can generalize generic sorting based on inferred parameters by employing statistical learning machines such as computational neural nets (CNN) and support vector machines (SVM). These too will

depend for their success on how solid the connection is between clusters of parameter values and generic target characteristics. One must also choose how much weight to give to parameter values with any degree of similarity or difference from those in a training set for which answers are known. The methods work best when UXO's feature parameter sets in clusters, however scattered, while non-UXO items do not produce parameters in those same clusters. Statistical learning machines are not magic, in that they generally cannot infer characteristics of complex targets when simply fed raw or unprocessed data. That is, most of important of all one must choose what parameters to input to the algorithms in the first place. While we have argued that dipole moment or magnetic polarizabilities are ambiguous measures of target characteristics for complex items like UXO's as viewed by real sensors, we have had some success using SVM based on  $\beta$  values for simple objects [20]. Others have pursued that approach in related work. It can be shown rigorously that a certain class of SEA response parameters  $B_k^j$  are unique in the sense that objects which produce different EMI responses must necessarily produce different sets of  $B_k^j$ . SVM and CNN may therefore have the best chance of reliably classifying objects based on these parameters. Our initial studies in this area have been encouraging [25]. On the whole, however, this is work in progress and was not used to address the problem of highly contaminated sites or multiple targets.

The NSMC processing (Section 2.6.3) constitutes a blend of a general inversion and pattern matching: First the total NSMC ( $Q(f)$ ,  $Q(t)$ ) of possibly multiple sources producing the signal is determined, with little constraint. In the work reported here, the spectra of the contributing  $Q(f)$  patterns are examined relative to known UXO types. If any closely resemble known  $Q(f)$  for UXO's, then the corresponding source is deemed to be that UXO type. As  $Q$  represents a kind of magnetic capacitance, it is likely associated with object size or mass. UXO's of different size have shown markedly different  $Q(t)$  in our measurements. Thus  $Q$  recommends itself for general inversion, without the  $Q$ -pattern matching step. Once the  $Q$  values are determined from data, instead of matching members of a library of  $Q(f)$  or  $Q(t)$ , a statistical learning machine such as SVM or NN might produce generic size classifications of the corresponding sources. That goes beyond the range of this project, and is pursued in subsequent work. In what follows here, we simply examine  $Q$  to see whether, based on data for a sampling of UXO types, the  $Q$  on hand resembles those from UXO's in a chosen size range.

In our multi-stage approach (Section 2.6.4), the dipole model based analysis identifies signal contributions from more than one possible source (multiple targets present simultaneously). Suspicious sources are then subjected to further analysis by SEA-based pattern matching to see if they correspond to any known UXO type. Information from the dipole-based analysis is used to constrain the SEA pattern

matching, thus saving considerable computing time in the more complex calculations. This approach is designed to use the dipole based forward models to do what they in fact can do – produce a first order representation of the source of some particular data – but not do what they cannot reliably do, namely serve as predictive models; or, based on limited data sets, provide sets of parameters that uniquely correspond to particular classes of targets.

### **2.6.1. Optimization by Differential Evolution (DE)**

Differential evolution is a direct, heuristic global search method suitable for nonlinear optimization. Because of the role played by position in the problems treated here, the optimization is inherently non-linear. DE descends from the genetic algorithm and is cast in much the same terms, but it is designed to treat continuously varying parameters, as opposed to those that can only assume discrete states. The method is efficient and, as a global search method, is designed to avoid getting stuck in local minima. It was developed initially by Price and Storn in the mid-1990's [36] when they realized that differential mutation combined with discrete recombination and pair-wise selection could allow one to bypass the “genetic annealing” process in antecedent combinatorial work. While still classed as “new,” the method has been developed recently into an increasingly robust and recognized computational approach [38]. To our knowledge, before this project it had never been applied to problems of the sort treated here.

Among its other virtues, DE has the advantages that it is easy to understand and to implement. Its most essential innovation is the way in which trial members of a population of possible forward model parameter sets are generated. One begins with an initial population ( $m = 0$  generation) of  $N_p$  members, the  $i^{\text{th}}$  one of which  $\alpha_i$  consists of a set of relevant parameters,  $\{a_i, b_i, c_i, \dots\}$ . Each such member or “individual” in the population is tested by using its parameter set in the forward model to evaluate fields in an objective function. This essentially measures some goodness of fit between the prediction produces and the observations. Individuals who do well are retained in the  $m+1$  generation. Those who do not are deselected and replaced by new members with “genes” generated by combinations of those from their neighbors. Figure 33 illustrates this schematically, where

$$\alpha'_2 = \alpha_j + F \cdot (\alpha_k - \alpha_n) + M_2 \quad (52)$$



$F$  is termed the amplification factor;  $M_2$  is a possible random mutation term; and  $\alpha_j$ ,  $\alpha_k$ , and  $\alpha_n$  are randomly selected other members of the population. Other simple operations producing  $\alpha_2'$  can also be brought to bear involving genetic transposition or “crossing over” of genetic content, as opposed to straight differencing and linear combination.

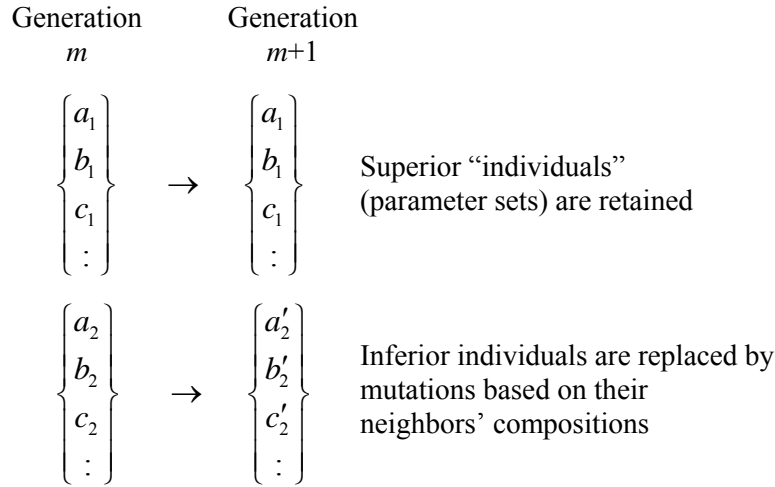


Figure 33. Schematic representation of the fates of individuals  $\alpha_1$  and  $\alpha_2$  between the  $m$  and  $m+1$  generation in DE.

Once the  $m+1$  generation is constituted, each member of its population is tested as before and then either retained or replaced. New generations follow until a converge criterion is met. This can either be based on the value of the objective function or a measure of goodness of fit; or one can simply stop iterating when all members in the population become similar so that little improvement can be expected, barring lucky, aggressive random mutation.

While DE is considered to be robust in its tendency to avoid sticking in local minima, in this project our experience indicated that one did well to have relatively large populations in each generation. More than any other strategy, this tended to assure enough interacting genetic diversity so that all individuals in the population wouldn’t drift into the same genetic content without providing the best possible match.

One of the most notable features of DE is that the computational formulation is inherently parallel. The corresponding algorithms are easily parallelized. Each individual’s performance is evaluated only in

terms of the objective function and the merits of its immediate predecessor, not (necessarily) relative to any or all other members of the population. Thus in a sense the evolution involves  $N_p$  separate, parallel streams that only interact between generations, via (52). In this project, many DE runs were performed on the DoD High Performance Computing System, which offered supercomputing capacity for parallel computation. In some applications such as multi-stage processing (Section 2.6.4), the most computationally economical course was to do initial processing with gradient methods, then use the results as initial guesses in the DE framework. This constituted then a kind of “guided” DE.

### **2.6.2. Simple Least Squares and Statistically Weighted Least Squares Objective Functions**

Most discrimination processing here and elsewhere requires comparison of observed and calculated fields. Probably the simplest, most direct, well established way to construct an objective function to measure goodness of fit is by simple least squares (SLS). One calculates and minimizes the summed square difference between some model predictions  $H_m$  and observed fields (data)  $H_d$

$$\Phi = \sum_{i=1}^{N_o} \sum_{n=1}^{N_f} |H_d - H_m|^2 \quad (53)$$

over the total number of observation points  $N_o$  and frequencies  $N_f$  in our FD data. This formulation of objective function or error measure has some shortcomings. Among them is that  $\Phi$  will tend to be dominated by larger amplitude terms, even if fainter data (e.g. from a higher sensor elevation) is equally or more relevant and reliable. It also contains no weighting or scaling based on quality of the data or on prior knowledge of likely parameter ranges.

The ability to determine at least some approximate statistical parameters from observed data encourages the quest for some kind of implementation of them that will benefit the optimization calculations. As guidance in this realm, investigators often appeal to Bayesian probability theory [39, 40, 41]. Bayesian formulations begin with reference to the relation

$$P(\mathbf{m}|\mathbf{d}) = \frac{P(\mathbf{d}|\mathbf{m})P(\mathbf{m})}{P(\mathbf{d})} \quad (54)$$

where  $P(\mathbf{m}|\mathbf{d})$  is the probability of occurrence of the “model,” i.e. applicability of the forward model parameter vector  $\mathbf{m}$ , given the data  $\mathbf{d}$ ;  $P(\mathbf{d}|\mathbf{m})$  is the probability of  $\mathbf{d}$  occurring, given  $\mathbf{m}$ ;  $P(\mathbf{m})$  and  $P(\mathbf{d})$  are the overall probabilities that  $\mathbf{m}$  and  $\mathbf{d}$  will occur, respectively. While (54) incorporates basic joint probability relations and as such is not subject to controversy, one must adduce additional relations, approximations, and definitions of the relevant distributions to be able to apply the relation.

For any particular data set under consideration, the first simplification here is that  $P(\mathbf{d})$  is effectively 100%, or is in any case fixed. Thus maximizing the left side of (54) is tantamount to maximizing the numerator on the right side. If the probability density  $P(\mathbf{d}|\mathbf{m})$  is an ideal Gaussian distribution, then

$$P(\mathbf{d}|\mathbf{m}) = \frac{1}{\sqrt{2\pi}|\mathbf{C}_d|} \exp \left\{ -\frac{1}{2} [(\mathbf{H}_d - \mathbf{H}_m(\mathbf{m})) \cdot \mathbf{C}_d^{-1} \cdot (\mathbf{H}_d - \mathbf{H}_m(\mathbf{m}))] \right\} \quad (55)$$

where  $\mathbf{C}_d$  is the data's correlation matrix and  $\mathbf{f}(\mathbf{m})$  is the rendition of the data provided by the forward model, assuming the parameters  $\mathbf{m}$  apply. Further, for specificity, assume that we are seeking some object parameters  $\mathbf{m} = \{a, b\}$ , and that their distribution  $P(\mathbf{m})$  is also an ideal Gaussian form,

$$P(\mathbf{m}) = \frac{1}{\sigma_a \sqrt{2\pi}} \exp \left\{ -\frac{1}{2} \left( \frac{a - a_0}{\sigma_a} \right)^2 \right\} \frac{1}{\sigma_b \sqrt{2\pi}} \exp \left\{ -\frac{1}{2} \left( \frac{b - b_0}{\sigma_b} \right)^2 \right\} \quad (56)$$

where  $a_0$  and  $b_0$  are constants, and  $\sigma_a$  and  $\sigma_b$  are standard deviations of the observations. Because all distributions are assumed to have exponential forms, substituting (55) and (56) into (54) and maximizing the numerator means minimizing the exponent

$$\Phi(a, b) = \{H_d - H_m\}^T \cdot [\mathbf{C}_d^{-1}] \cdot \{H_d - H_m\} + \left( \frac{a - a_0}{\sigma_a} \right)^2 + \left( \frac{b - b_0}{\sigma_b} \right)^2 \quad (57)$$

where  $H_d$  is "de-measured," i.e. its value adjusted by any non-zero mean clutter level or background, so that here  $H_d \Rightarrow H_d - \mu_d$ . The function  $\Phi$  in (57), rather than the right hand side of (54) itself, becomes the objective function.

To proceed with the calculations one must still somehow evaluate the inverse of the correlation matrix  $[C_d^{-1}]$ . Just as one rarely really knows the underlying distributions for the data, investigators also rarely can or do calculate the actual correlation matrix. A common assumption is that it has the form corresponding to the case where there is no correlation between data elements so that the matrix is a diagonal containing  $\sigma_{d,j}^2$  for each  $j^{\text{th}}$  datum (for each frequency and position). This simplifies matters greatly, as  $[C_d^{-1}]$  is then just a diagonal matrix with elements  $1/\sigma_{d,j}^2$ . Under all these assumptions, minimizing only the first term in (57) would be equivalent to applying a maximum likelihood approach. Minimizing the entire expression is frequently termed a Bayesian approach.

Equation (57) is recognizable as a weighted least square problem with penalty terms. As such, it is worth noting that one could have arrived at this via other considerations besides Bayesian theory. Further, the simplifying assumptions are so extreme - veritably contrary to fact, in most UXO applications - that one must view objective functions like (57) as being at most "Bayesian inspired." The form and content of the weighting and penalties are merely suggested by other highly idealized, not to say unrealistic parallels to the problem at hand. Both the treatment of the correlation matrix and also the form of the distributions assumed, e.g. (56), assume that the variables are statistically independent. It is easily verified that EMI signals at neighboring spatial points or frequencies are significantly correlated. One need only glance at a contour plot of clutter signals (Section 5) or a typical EMI spectrum to see that this is true. Each distribution  $P$  that was assumed, leading to (57), was an ideal Gaussian form. Our experience here is that clutter statistics virtually never have any recognizable distribution, much less a Gaussian one (they do, nonetheless, have means and standard deviations).

Pursuing the Bayesian analogy, here the inclusion of "prior information" via  $P(\mathbf{m})$  simply means seeking an estimate of  $a$  and  $b$  centered or weighted in a certain range about their expected dimensions. This may be done in order to query the data for evidence that a certain kind of object is present, or simply to restrict the search to a domain of reasonable values of  $a$  and  $b$ . In the end, shorn of the motivating presumptions regarding the underlying distributions, use of (57) is essentially just a least squares approach, weighted by factors proportional to the variability of the data, with the inversion search penalized when it strays too far from likely candidate dimensions. The theoretical framework

simply serves to provide guidance for the selection of the tuning parameters. In practice, further guidance (and attendant tuning) is furnished by ulterior motives, priorities, or observations of the nature of the data or data quality. The  $1/\sigma_{d,j}^2$  factors in particular serve to de-emphasize data that falls below the level of the noise. However, if the variance of some signals is roughly proportional to the magnitude of the signals, these factors tend to equalize the influence of all data, which may be quite undesirable where signals are weak. Hence in practice one typically adds a noise floor factor to each  $\sigma_{d,j}^2$ . The data may also be segmented so that different adjustments are applied to the variance for different circumstances, e.g. for data taken from different elevations of the sensor. None of this has anything to do with Bayesian theory, and has everything to do with pragmatic insight into the nature of the problem at hand.

In summary, although a rigorous basis in statistical theory is lacking, formulations such as the one in (57) offer some concrete framework in which to apply statistical parameters in the optimization processing. Sections 5.8.2 and 5.8.3 show some benefit from this approach in example UXO discrimination exercises.

### ***2.6.3. Unconstrained Inference of $Q(f)$ followed by Constrained Pattern Matching***

Applying the NSMC approach requires some specific computational decisions, such as those regarding the size and shape of the surface used to surround the target mathematically, on which the responding NSMC's reside. However in the end the results are independent of these choices in that the total NSMC ( $Q$ ) does not depend on the surface chosen, but is rather a property of the object. While in any computation the NSMC's are assumed to sit on the chosen surface, beyond that the search for an applicable set of those parameters is in general unconstrained. The optimization determines together whatever set of NSMC's and surface position works best, based on their ability to produce scattered fields matching observations, without reference to any library of known examples. Following the unconstrained optimization we compare the results to a constrained set of possibilities of interest. The second step constitutes "pattern matching," but not in the sense applied with reference to other SEA work reported here. In the latter matches patterns of received magnetic fields; in connection with the NSMC we match patterns of spectra that are extracted from the received patterns.

The following blind test is designed to expand upon the single validation test in Section 2.4.4 and to foster confidence in the spectrum of  $Q$  as a distinguishing feature of UXO's and clutter objects. Figure 34 shows the five UXO's and three clutter assemblages that were used in the test. Each UXO had been studied previously and its  $Q(f)$  determined. The clutter items were unfamiliar to the analysts. In the blind tests, each item was arranged in air in the lab at some unspecified distance and orientation relative to a GEM-3 sensor. Grids of data were taken above each object, from which the analysts (working at a different institution from the lab) inferred an applicable  $Q(f)$  by SLS optimization.



Figure 34. Items used in blind tests of the NSMC classification, on the basis of  $Q(f)$ .

Table 1 shows the results of the analyst's discrimination judgments relative to the lab truth. Of the ten cases, only one was incorrectly identified. This test with diverse UXO and clutter items offers substantial support for the pursuit of Q(f) as a discriminant. Significantly for what follows, the test does not include cases with multiple objects nor the complication of ground response.

Table 1. Results of blind NSMC Q(f) classifications of single objects

Case	Inverted ID (green = correct)
#1	Heat Rnd (tail up)
#2	Clutter
#3	2.75" Rocket M230
#4	105 mm M60
#5	2.75" Rocket M230
#6	Clutter
#7	Clutter
#8	81 mm M374
#9	Heat Rnd (nose up)
#10	57 mm M86

#### **2.6.4.                    *Dipole representations, isolation of contributors, and multi-stage processing***

Application of infinitesimal dipole modeling of UXO's or of comparable objects frequently fails in the sense that the inferred (tri-axial) dipoles will not accurately predict an object's response in a diversity of circumstances (Section 2.3.1). That said, one can often successfully use infinitesimal dipole representations as a reasonable first approximation of an equivalent source *for a particular set of data at hand*. That is, a tri-axial dipole may succeed in reproducing the data being considered, e.g. over a particular grid of observations at one elevation. This presents no problem as long as one does not try to use the inferred model to predict any other data. This section describes a multi-stage, multi-object processing scheme in which infinitesimal dipole representations are used as the first stage, in order to separate the contributions from each object, to estimate their locations, and to provide basic clues as to the nature of each object. This information is then fed into more advanced processing steps. As an illustration, a lab test features data from the two objects in Figure 35. Figure 36 shows an example of the signal contours over a measurement grid above the two objects. Clearly signals from the two contributors cannot easily be separated without some sort of computational processing.



Figure 35. Left: 14 cm square clutter item placed 5 cm above and slightly offset from the approx 43 cm long UXO on the right.



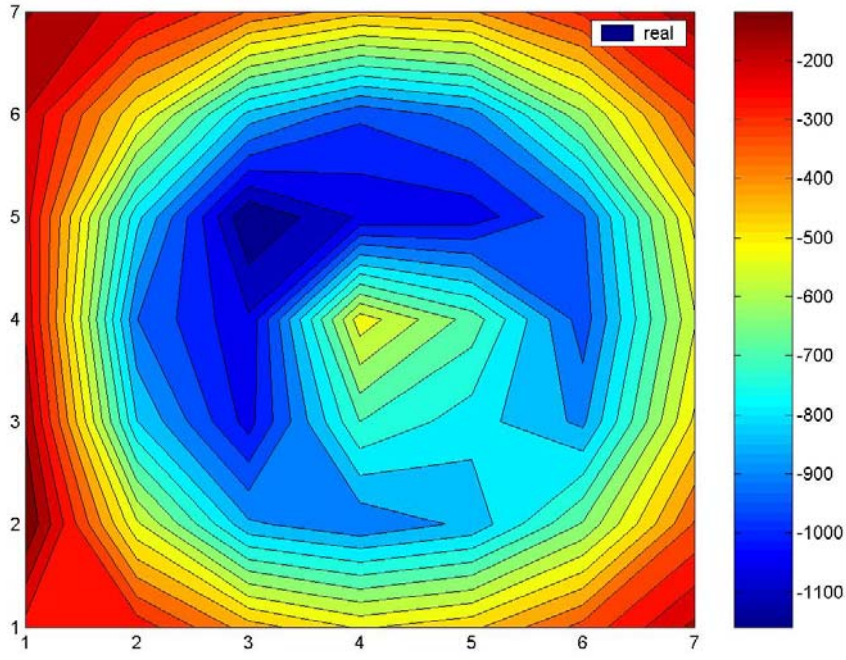


Figure 36. Data from a 7 x 7 point grid of GEM-3 measurements above an assemblage of the two clutter items in Figure 35. Inphase component at 210 Hz.

The combined signal from the two objects can be written as

$$\mathbf{H}(\mathbf{r}) = \mathbf{G}(\mathbf{r}, \mathbf{r}_1) \cdot \mathbf{m}_1 + \mathbf{G}(\mathbf{r}, \mathbf{r}_2) \cdot \mathbf{m}_2 \quad (58)$$

where the Green function  $\mathbf{G}(\mathbf{r}, \mathbf{r}_i)$  corresponds to that for a dipole at position  $\mathbf{r}_i$ ,

$$\mathbf{G}(\mathbf{r}, \mathbf{r}_i) = \frac{3\hat{\mathbf{R}}_i \hat{\mathbf{R}}_i - \mathbf{I}}{4\pi R_i^3} \quad (59)$$

where  $\mathbf{R}_i = \mathbf{r} - \mathbf{r}_i$ , and the  $i^{\text{th}}$  dipole is

$$\mathbf{m}_i = \mathbf{M}_i \cdot \mathbf{H}^{\text{PR}}(\mathbf{r}_i) \quad (60)$$

The magnetic polarizability matrix for the  $i^{\text{th}}$  object is

$$\mathbf{M}_i = \begin{bmatrix} p_{11} & p_{12} & p_{13} \\ & p_{22} & p_{23} \\ \text{symm} & & p_{33} \end{bmatrix}_{i^{\text{th}} \text{ object}} \quad (61)$$

where, by the electromagnetic reciprocity theorem, the symmetry of  $\mathbf{M}$  is assumed and enforced. The total received field from the two dipoles, each excited in its position by the applicable  $\mathbf{H}^{\text{PR}}$  there, is

$$\mathbf{H}(\mathbf{r}) = \frac{3\hat{\mathbf{R}}_1\hat{\mathbf{R}}_1-\mathbf{I}}{4\pi R_1^3} \cdot \mathbf{M}_1 \cdot \mathbf{H}^{\text{PR}}(\mathbf{r}_1) + \frac{3\hat{\mathbf{R}}_2\hat{\mathbf{R}}_2-\mathbf{I}}{4\pi R_2^3} \cdot \mathbf{M}_2 \cdot \mathbf{H}^{\text{PR}}(\mathbf{r}_2) \quad (62)$$

Altogether then, the optimization to identify the two contributing dipoles consists of obtaining a sufficient number of observations  $\mathbf{H}(\mathbf{r})$  at different  $\mathbf{r}$ ; the searching through different combinations of  $\mathbf{r}_1$ ,  $\mathbf{M}_1$ ,  $\mathbf{r}_2$ , and  $\mathbf{M}_2$  until the best match with  $\mathbf{H}(\mathbf{r})$  is obtained. Figure 37 shows results for the case in Figure 36, when (62) is used to reproduce the signal based on a decomposition of the source into two infinitesimal dipoles.

As a final step, the eigenvalues and eigenvectors of  $\mathbf{M}_1$  and  $\mathbf{M}_2$  are obtained in accordance with the relationship

$$\mathbf{M}_i = \mathbf{Q} \cdot \begin{bmatrix} \beta_{11} & 0 & 0 \\ 0 & \beta_{22} & 0 \\ 0 & 0 & \beta_{33} \end{bmatrix}_i \cdot \mathbf{Q}^T \quad (63)$$

The  $\mathbf{Q}$  matrices are essentially rotation matrices containing the normalized eigenvectors of  $\mathbf{M}$ , which can also provide the orientation of the principal axes of the dipole, if desired. In other words, only object positions  $\mathbf{r}_1$  and  $\mathbf{r}_2$  need be solved for, while the object orientations are implicit in the eigenvectors of  $\mathbf{M}_1$  and  $\mathbf{M}_2$ . An alternative approach sometimes applied in this project consisted of solving only for the  $\beta_{ii}$  eigenvalues of  $\mathbf{M}$ , together with position and angular orientation information, including polar, azimuthal, and also twist angle to accommodate non-BOR objects. For each solution obtained, the rotation variables produce the elements in  $\mathbf{Q}$  and hence ultimately a full matrix  $\mathbf{M}$ .

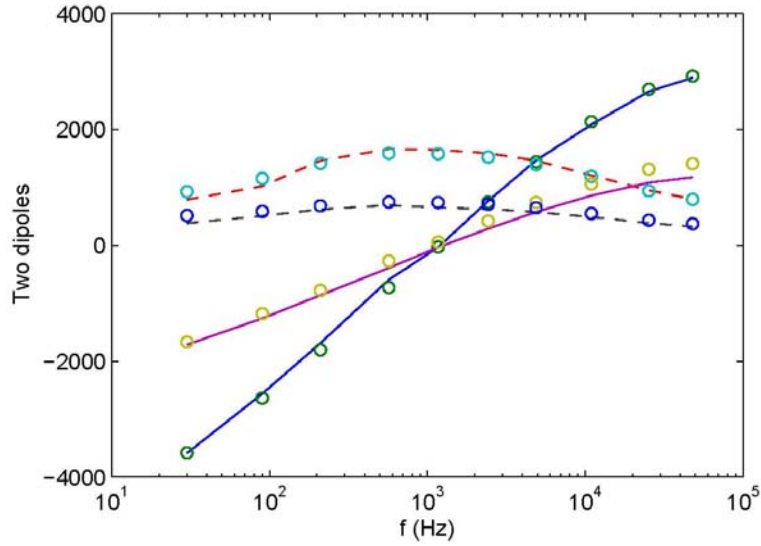


Figure 37. Comparison of modeled inphase (solid) and quadrature (dashed) measured fields from two objects, corresponding to two (blue, magenta) measurement distances, over the center of the grid in Figure 36. Markers indicate measured values.

Together with the position/orientation information, the eigenvalues  $\beta_{ii}$  are key results. They are magnetic polarizabilities along the object's principal axes, tantamount to the dipole strength produced by a uniform unit magnitude (primary magnetic field) excitation in that direction. All results from this stage of the analysis can now provide guidance, constraint, and input for subsequent processing stages. However, the  $\beta_{ii}$  themselves can also be analyzed in themselves for classification clues. In any case, one must decide at this point how to deal with the frequency dependence of the results. Because different portions of a heterogeneous target respond differently at different frequencies, an analysis frequency by frequency will infer different dipole locations/orientations at different frequencies. Thus one can analyze the frequency dependence of the inferred locations for evidence of heterogeneity, that being more likely an indication of a UXO than of a piece of clutter. In most applications here, the inferred positions and orientations were averaged over frequency to produce a single dipole location and disposition. This was then input as a starting value in a rerun of the optimization, performed under the constraint that only a single position and orientation was allowed over all frequencies, to determine a “consolidated” as opposed to “frequency-by-frequency” equivalent dipole.

Information from the dipole analysis of the data feeds into subsequent processing according to the considerations below.

1. Some sets of  $\beta_{ii}$  values may suggest that an item is clutter, e.g. if the values are mutually contrasting and relatively disorderly across the frequency band, in keeping with a lack of geometrical symmetry.
2. Some sets of  $\beta_{ii}$  values may suggest that an item is a body of revolution or is otherwise “suspicious,” meriting further investigation to determine whether it should be classed as a UXO or UXO-like object.
3. In further analysis following step #2, e.g. SEA pattern matching with known UXO types, the dipole analysis provides guidance/ prior information in the form of
  - a. an estimate of object position and orientation
  - b. isolation of the signal of the contributing object to be investigated.

Item #3b is an absolutely essential outcome of the dipole decomposition if any subsequent analysis is to be performed. Once  $\mathbf{M}_i$  and  $\mathbf{r}_i$  are obtained for the relevant object, the signal specifically associated with that object can be isolated by evaluating one but not the other of the terms in (62). Overall, the dipole decomposition allows one to extract the contribution of an object of interest from the complete data. In the multi-stage dipole-SEA pattern matching discrimination processing results described below (Section 8.3), the dipole representations sufficed quite well in reproducing the individual object contributions – within the limited data sets treated.

### **2.6.5.      *Blind Source Separation/ Independent Component Analysis***

Our interest in application of Blind Source Separation (BSS) and Independent Component Analysis (ICA) follows recent work at Duke University [42]. This work descends in turn from a root of statistical signal processing techniques, e.g. [47], that have given rise to successful methods in other applications. The overall approach differs fundamentally from those discussed above in that, at least in principle, it requires no real physical forward model that computes signals produced by source objects. One might say that BSS/ICA approaches model the signal, not the physical process. In practice, the assumptions of the methods require at least some sort of idealization of the signal production process. As explained below, this can be supplied conveniently by the (multiple) independent dipole idealization of UXO's or similarly discrete metallic targets.

The BSS/ICA tests below attempt to pursue the limits and characteristics of ICA analysis of the multi-target or cluttered signal EMI problem. While the results of straight application are not encouraging, some of the underlying concepts may yet prove valuable when transplanted into other approaches. For example, Section 5 in this report treats pattern matching processing of signals with diffuse clutter in quite significant but ultimately tolerable amounts. The approach can succeed in correctly ranking a possible target as the one most likely to be present compared to a few others. However, one is still left with the question: Quantitatively, how likely is it to be present? That is, a good relative ranking is achieved, but an absolute evaluation of probability of presence is lacking. With goodness of fit always subject to some residual clutter level, how good a fit is good enough to indicate dig vs don't dig? This leaves us still wanting either to extract the target signal more completely from the clutter signal, or at least to somehow characterize signals as to their clutter or noise-like character. BSS/ICA suggests some statistical criteria that might distinguish noise or highly cluttered signals from those produced by single coherent sources. The approach assumes that each of these classes of signal should exhibit certain (differing) statistical characteristics. While application of such statistical concepts is not pursued here outside of the BSS/ICA framework, this may merit further investigation.

The common paradigm for the BSS problem is the "cocktail party" problem: A number of speakers are present in a room, all talking at once. The recorded sound at each point in the room is some unknown mixture of all of the speakers' voices (sources). How can one process a set of records of these different mixtures so as to extract the voice of any one speaker or of each individual speakers? Independent

Component Analysis (ICA) is an approach to solving the BSS problem. It rests on two fundamental notions, namely that each speaker (source of signal) is independent of the others, and that a mixture of two or more independent signals will exhibit a more Gaussian distribution of values than a single independent signal. Regarding the second point, the Central Limit Theorem is a well established result, stating that a random mixture of a large number of (e.g. deterministic) signals will in fact approach a Gaussian distribution. The ICA approach assumes that even a single mixture of two signals is likely to be more Gaussian than either is alone. “More Gaussian” must be measured in some way, and the most common parameter to rate “Gaussianity” (we did not make up that usage) is the kurtosis of the distribution of signal values. Illustrations are shown below; Other measures may also be applied. Regarding *independence* of contributions to the signal mixtures, the term is used in the strict statistical sense in the theory of the method, though in practice other sorts of independence may serve as proxies because they can be measured or enforced more directly.

Overall, consider that we have  $n$  contributing sources  $s_i$  so that the complete list of sources is the vector  $\mathbf{s} = [s_1, s_2, \dots, s_n]$ . In any application, each  $s_i$  can itself be a function of some other variable, i.e. a vector of values at different times or frequencies,  $s_i = s_i(f_j)$  or  $s_i = s_i(t_j)$ . By analogy, each  $s_i$  is the voice of an individual speaker in the cocktail party problem. Each complete recorded signal  $\mathbf{x}$  is some linear combination of the  $s_i$ .

$$\mathbf{x} = \mathbf{A} \cdot \mathbf{s} \quad (64)$$

where  $\mathbf{A}$  is an unknown  $m$  by  $n$  mixing matrix. We wish to find  $\mathbf{s}$ , given  $\mathbf{x}$ , without knowing  $\mathbf{A}$ . To proceed, compute the scalar  $y$  by pre-multiplying (64) by some  $\mathbf{w}$

$$y = \mathbf{w} \cdot \mathbf{x} = [\mathbf{w} \cdot \mathbf{A}] \cdot \mathbf{s} = \mathbf{z} \cdot \mathbf{s} \quad (65)$$

By our assumptions, when  $y(f)$  is some mixture of the  $s_i$ , it will be more Gaussian over  $f$  than any of them alone. It will be least Gaussian when it corresponds to a single  $s_i(f)$ . Thus one performs an optimization in which different  $\mathbf{w}$  are tried until a Gaussianity minimum is found, deemed to correspond to a  $\mathbf{z}$  containing only a single non-zero element. In effect, the pre-multiplier  $\mathbf{w}$  is a trial un-mixing operator.

The classical measure of Gaussianity of a distribution is its kurtosis, defined as

$$kurt(y) = E\{y^4\} - 3(E\{y^2\})^2 \quad (66)$$

A perfectly Gaussian distribution has zero kurtosis. Spiky or uniform distributions have high kurtosis. Figure 38 shows representative cases.

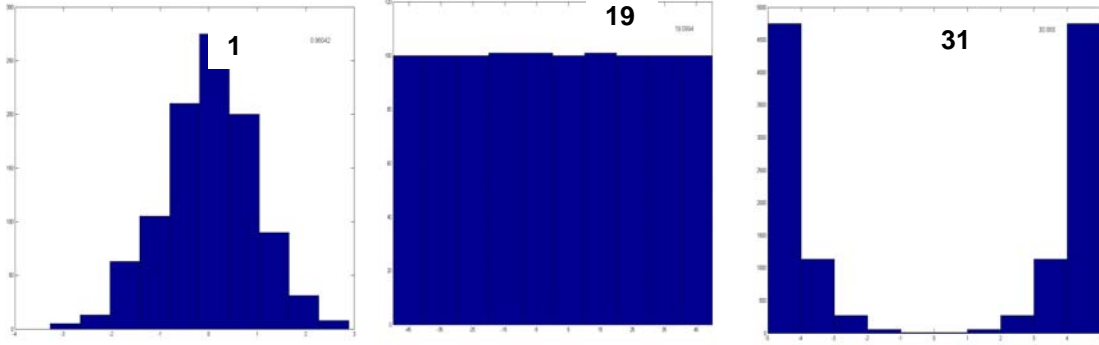


Figure 38. Three distributions with their respective kurtoses.

Kurtosis is relatively easily calculated, and for this reason it is used in the examples investigated as a handy indication of level of Gaussianity. However for ICA computations it is not a very robust indicator, being easily influenced by a few observations in the tails of a distribution. For this reason, in the computations Gaussianity is quantified using signal entropy considerations. With a suitable definition of signal entropy, it can be shown that Gaussian distributions have the largest entropy relative to all distributions of the same variance.

Entropy  $En$  (also known as “differential entropy”) is defined for a random variable  $y$  as

$$En = - \int p(y) \log p(y) dy \quad (67)$$

where  $p(y)$  is the probability density distribution for  $y$ . From information theory, a Gaussian random variable has the largest entropy of all random variables of the same variance [48]. Because optimization procedures typically seek minima, the ICA formulations uses “negentropy”  $J$ , defined as

$$J(y) = En(y_{gauss}) - En(y) \quad (68)$$

Where  $y_{\text{gauss}}$  is a Gaussian signal with the same covariance matrix as  $y$ . The more Gaussian-like a random variable is, the lower its negentropy. Calculating entropy or negentropy is difficult due to the unknown probability density functions (PDF) involved. One can estimate the PDF from empirical distributions of signal value itself. Alternately, approximations of  $J$  can be obtained from the signal using higher order moments [49]:

$$J(y) \approx \frac{1}{12} E\{y^3\}^2 + \frac{1}{48} kurt(y)^2 \quad (69)$$

Perhaps the most popular established software for performing ICA calculations, as exploited in [42], is the FastICA algorithm. The authors of FastICA go beyond (69) to other moment based approximations deemed more robust [50, 51]:

Crucial, and limiting assumptions of the method are *independence* of the sources, and the notion that *each source is invariant in all mixtures*, beyond a multiplicative factor. In general independence means that the occurrence of a particular value for  $s_1$  at a given frequency does not imply a particular probability for the value of  $s_2$  at that frequency. In the cocktail party analogy, invariance is tantamount to saying that a given speaker's voice is the same, or registers in the same way at all microphones within the room, though it may be louder or softer at different locations. In our UXO application, this implies that the signal from a UXO recorded at one vantage point is identical, exempt in magnitude, to its signal at any other vantage point. We know this to be false for a number of reasons - different signals caused by material heterogeneity of targets, when different parts of them are stimulated or observed in differing proportions; different responses to different direction of primary field, e.g. transverse vs axial excitation. To proceed, one must find a way to view a data set of EMI observations of a UXO as a superposition of invariant signals; and the BSS/ICA method must, in a sense, "share" that view of the signal composition.

It is clear from some popular examples and documented applications that the BSS/ICA approach can work. Below we consider two pictures, of Maxwell and Millikan (Figure 39). Each was decomposed into vectors of pixel values, random linear combinations of which then constituted the 400 mixtures  $\mathbf{x}$  to be analyzed. Using the program FastICA, we find 1) the method is remarkably capable of unmixing even these complex pictures; but 2) two different runs with the same input and same parameters can produce markedly different results and different degrees of success. Since the initial guess is random, different runs of ICA on the same data set (same mixtures, same sources, etc) can lead to greatly different solutions. While the second example in Figure 39 might simply be regarded as outright failure of the method, a more common malady might be seen as partial success, e.g. Figure 40. In the latter figure, the



signals extracted by FastICA indeed resemble the two non-noise input signals. However differences between the input and output signals are notable. Usually repeated runs of ICA are required and the most reasonable or appealing result is identified.

Section 7.2 investigates factors that affect the reliability of the ICA and its likelihood for success in particular in connection with UXO discrimination applications at highly contaminated sites (dispersed clutter, multiple sizable targets). First let us convince ourselves that there is some way to construe the signals that come from UXO's or other discrete metallic objects as coming from invariant sources. The anisotropic dipole idealization of an EMI target is used for this purpose in the work by the Duke group [42]. Figure 41 shows two possible objects serving as targets, on the left a clutter-like item and on the right a UXO. One can consider that each such scatterer behaves as a collection of infinitesimal dipoles, grouped in orthogonal sets of axial and transverse members, with magnitudes  $\beta_a$  and  $\beta_t$  respectively. The object on the left, being relatively small and homogeneous, only requires one such set. The one on the right contains two disparate sections, each of which produces its own sort of signal; hence each section requires its corresponding set of dipoles in the appropriate locations. In this viewpoint, a primary field striking the object produces the same signal as it would if it were striking such dipoles, while the dipoles respond independently of one another. The excitation field can always be decomposed into its axial and transverse components, and each of these will always produce the same response, scaled in proportion to the magnitude of the component.

Of course, the BSS/ICA is unaware of our idealizations. For this framework to succeed, the target model must produce a close enough rendering of actual behavior. In particular, in the frequency domain, the spectral characteristics of sources  $s_1(f)$ ,  $s_2(f)$ , ... will be those of  $\beta_{1,a}(f)$ ,  $\beta_{2,a}(f)$ , .... In the very least, this rendering of the scattering process must be successful enough so that there *are* some invariant  $s_1(f)$ ,  $s_2(f)$ , ... to be found. Section 2.3 notes some significant shortcomings of the dipole idealization for modeling UXO responses. We are content to pass over this point in order to get on to investigation of whether BSS via ICA can perform processing relevant to UXO's and EMI sensing when its most basic presupposition is fulfilled. After all, one can construct sensor-target arrangements that will in fact correspond closely to dipole scattering. We do this, in fact, in Section 7.2 below in order to move on to the most pertinent subsequent issues: *Given strict source invariance, how does each extracted component, determined from realistic signals under the requirements of independence and minimal Gaussianity, relate to the signals from physically different sources?* If we specifically construct signals comprised of responses by some realistic  $\beta_{1,a}(f)$ ,  $\beta_{2,a}(f)$ , will ICA identify sources with those spectra?

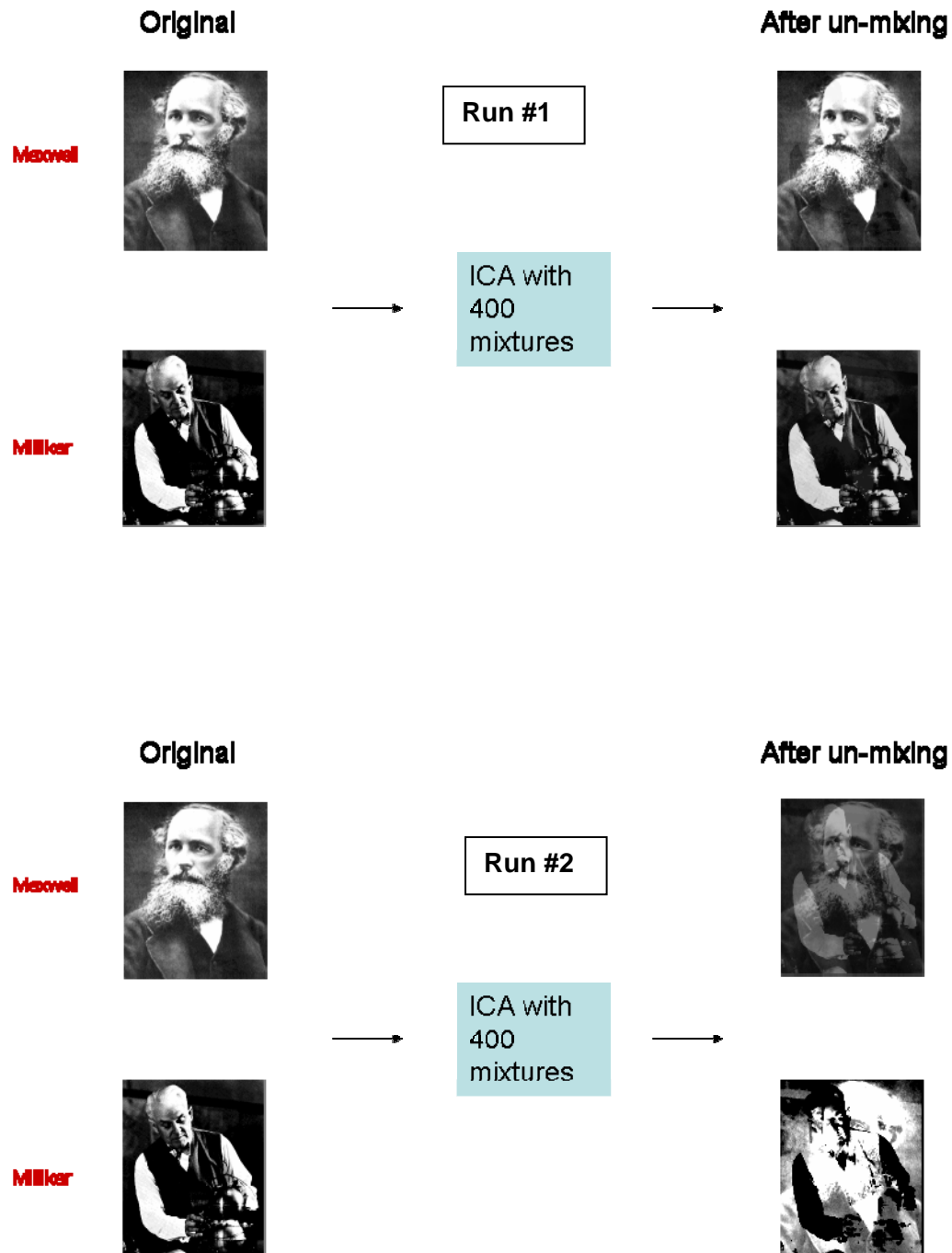


Figure 39. Results from two different ICA runs using FastICA to unmix pictures of Maxwell and Millikan.

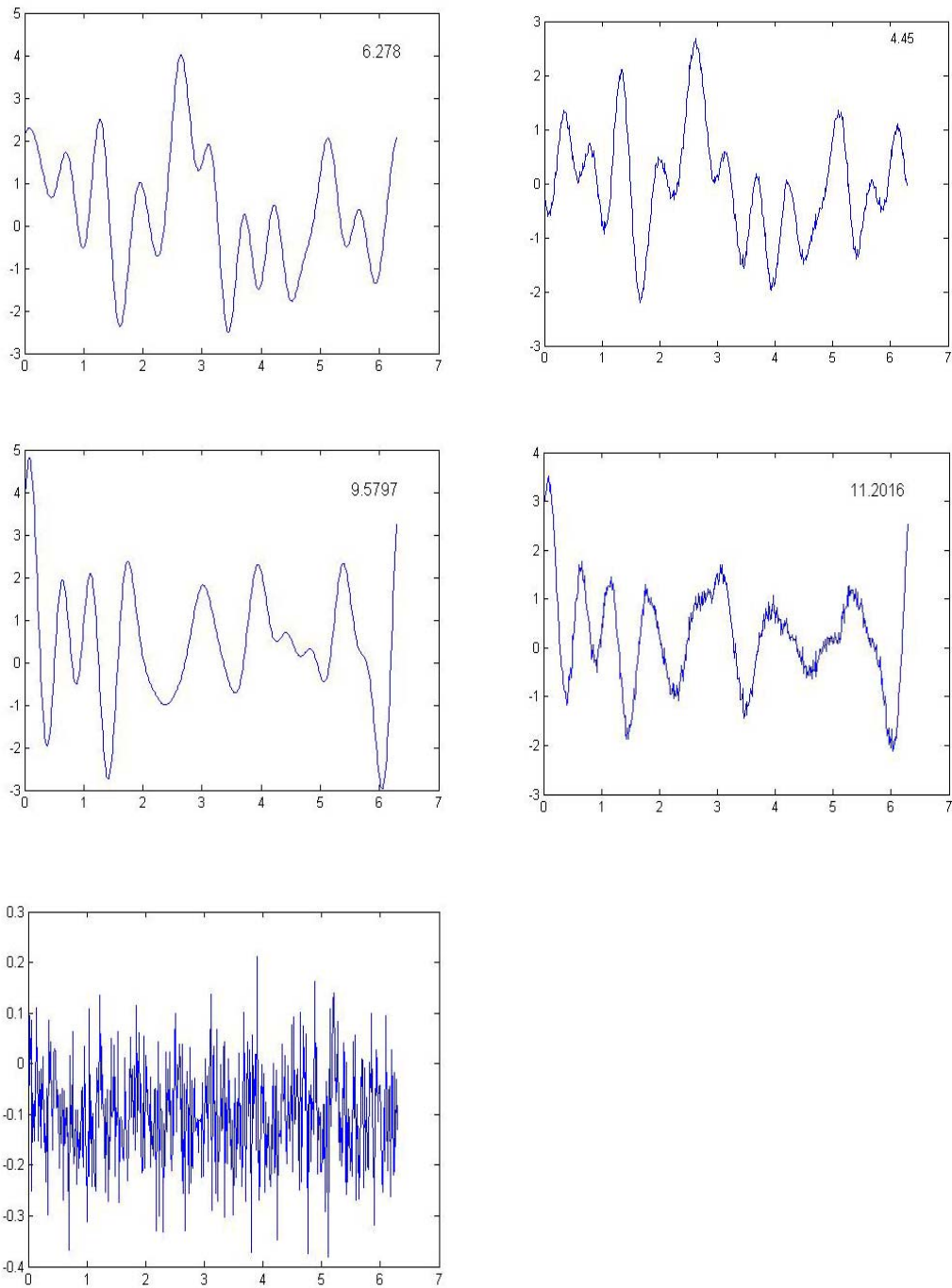


Figure 40. Low noise ICA test. Left: input signals, corresponding to two sources and (bottom) some added Gaussian noise. Right: IC's output by FastICA. Numbers in upper right of each plot are the respective signal kurtoses.

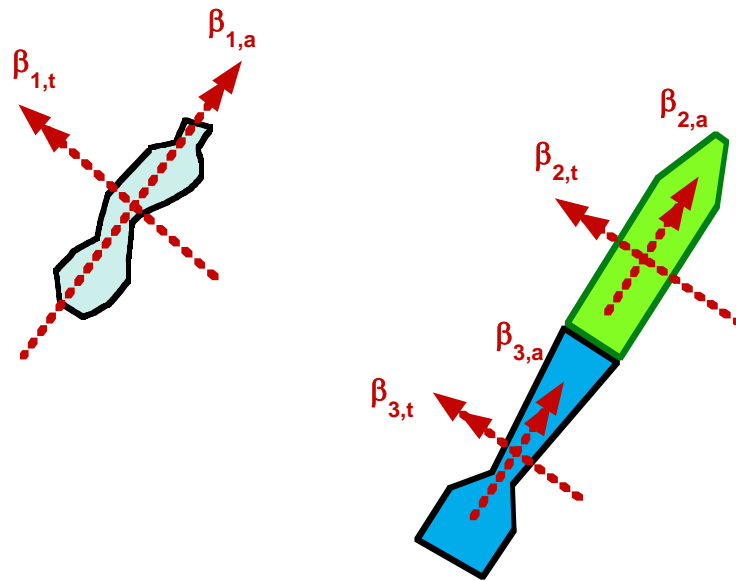


Figure 41. Two target types, and their representations by sets of orthogonal magnetic dipoles.

### 3. GROUND PENETRATING RADAR (GPR)

This section presents the basic parameter extraction system that was developed for processing of GPR signals for UXO discrimination. Basic tests in Section 3.2 show degrees of success in distinguishing the crucial parameters for contributing target when more than one is present. Prodded by these results, we developed a new, superior GPR, described briefly in the last part of this section and in Appendix B. Later sections describe the use of the new GPR together with EMI data under highly contaminated site conditions, including those at our testplots.

#### 3.1. GPR Parameter Extraction

With a downward look direction of the antenna, measured co- and cross-polarized radar reflections form a scattering matrix  $\mathbf{S}$  with elements  $S_{ij}$ .

$$\mathbf{S} = \begin{bmatrix} S_{11} & S_{12} \\ S_{21} & S_{22} \end{bmatrix} \quad (70)$$

When  $i = j$ , the return is co-polarized, corresponding to the reflection in the  $i^{\text{th}}$  direction (e.g. X axis) from transmission also polarized in that same direction. When  $i \neq j$ ,  $S_{ij}$  represents the cross polarized return, in which the polarization of the reflection in the  $i$  direction (e.g. X axis) is recorded, from transmission with the  $j$  polarization (e.g. Y direction). By the principal of electromagnetic reciprocity,  $S_{12} = S_{21}$ . If the coordinate axes are oriented in the principal directions of a scattering object, such as along and transverse to the axis of a cylinder, then we expect no significant cross-polarized return. The scattering matrix will be diagonal, with the only non-zero elements being the matrix eigenvalues. Overall, by obtaining the matrix  $\mathbf{S}$  for any orientation and performing an eigen-analysis, one obtains both the set of eigenvalues and the rotation matrices required to orient the coordinate system in the principal directions.

When struck by a radar pulse, an object such as a UXO will resonate after the initial, strong forced response. This resonance is caused by currents that run back and forth between the ends or across the sides of the object. Defining “late time” as the time after the initial response when lingering resonance dominates the signal, one sees a lower frequency and slower decay of currents running along the length of

the object as opposed to across it. With the axes oriented in the principal directions, the scattering matrix consists of

$$\mathbf{S} = \begin{bmatrix} \lambda_{//} & 0 \\ 0 & \lambda_{\perp} \end{bmatrix} \quad (71)$$

where  $\lambda_{\perp}$  and  $\lambda_{//}$  are the eigenvalues, corresponding to response in polarizations perpendicular to and parallel to the object's long axis, respectively.

Extraction of these eigenvalues allows one to calculate a number of revealing signal features. The first is the Estimated Linearity Function (ELF), defined as

$$\text{ELF} = \text{mean} \left| \frac{|\lambda_{//}(t)| - |\lambda_{\perp}(t)|}{|\lambda_{//}(t)| + |\lambda_{\perp}(t)|} \right| \quad t \in \text{late-time region} \quad (72)$$

If the object is elongated (“linear”), then as late time proceeds  $\lambda_{//}$  will predominate and the ELF will approach unity. If on the contrary the object is spherical or simply compact ( $\sim$  equi-dimensional), then the ELF will tend to zero. This parameter provides an indication of the elongation of the unseen scatterer.

If in late time one of the eigenvalues predominates, presumably  $\lambda_{//}$ , then the coordinate direction corresponding to it constitutes the Estimated Target Orientation (ETO). Also, because  $\lambda_{//}$  is the amplitude of a resonant signal, the fundamental frequency of that signal component is inversely proportional to the length of the object. In particular, the length of the object will be twice the dominant resonant electromagnetic wavelength in the soil. The fundamental (real-valued) resonant frequency and its exponential decay rate together define the estimated Complex Natural Resonance (CNR). At least under favorable circumstances, the recorded data will yield a reasonable estimate of all these parameters, on which classification decisions may be based.

Details of the parameter extraction algorithms are presented in the ESTCP Project 199902 Final Technical Report and in [43, 45, 46]. Here we summarize via Figure 42. The original transmission is in the frequency domain; after band selection this is translated to a time domain equivalent, e.g. equivalent of a pulse transmission, producing the kind of results typically shown in a GPR transect profile in which

the horizontal axis corresponds to position and the vertical axis to signal arrival time, approximately equivalent to distance from any reflectors. Using this space-time picture, the analyst performs adaptive smoothing and background removal. A late time region is selected in order to estimate a resonant frequency so this can be used to filter the data (step 7), de-emphasizing phenomena not associated with the resonating object. This presents a new TD picture which, following step 8, is smoothed and analyzed and a late time region presumably associated with the target is selected. Further processing extracts  $\lambda_{\perp}$  and  $\lambda_{//}$  and the quantities of interest derived from them in the late time regime.

Full GPR classification processing (as opposed to pre-processing for parameter extraction) is quite complex, and is detailed in the references. The discussion here proceeds on the basis of rather simple observations in connection with some or all of the three basic extracted parameters, ELF, ETO, and CNR.

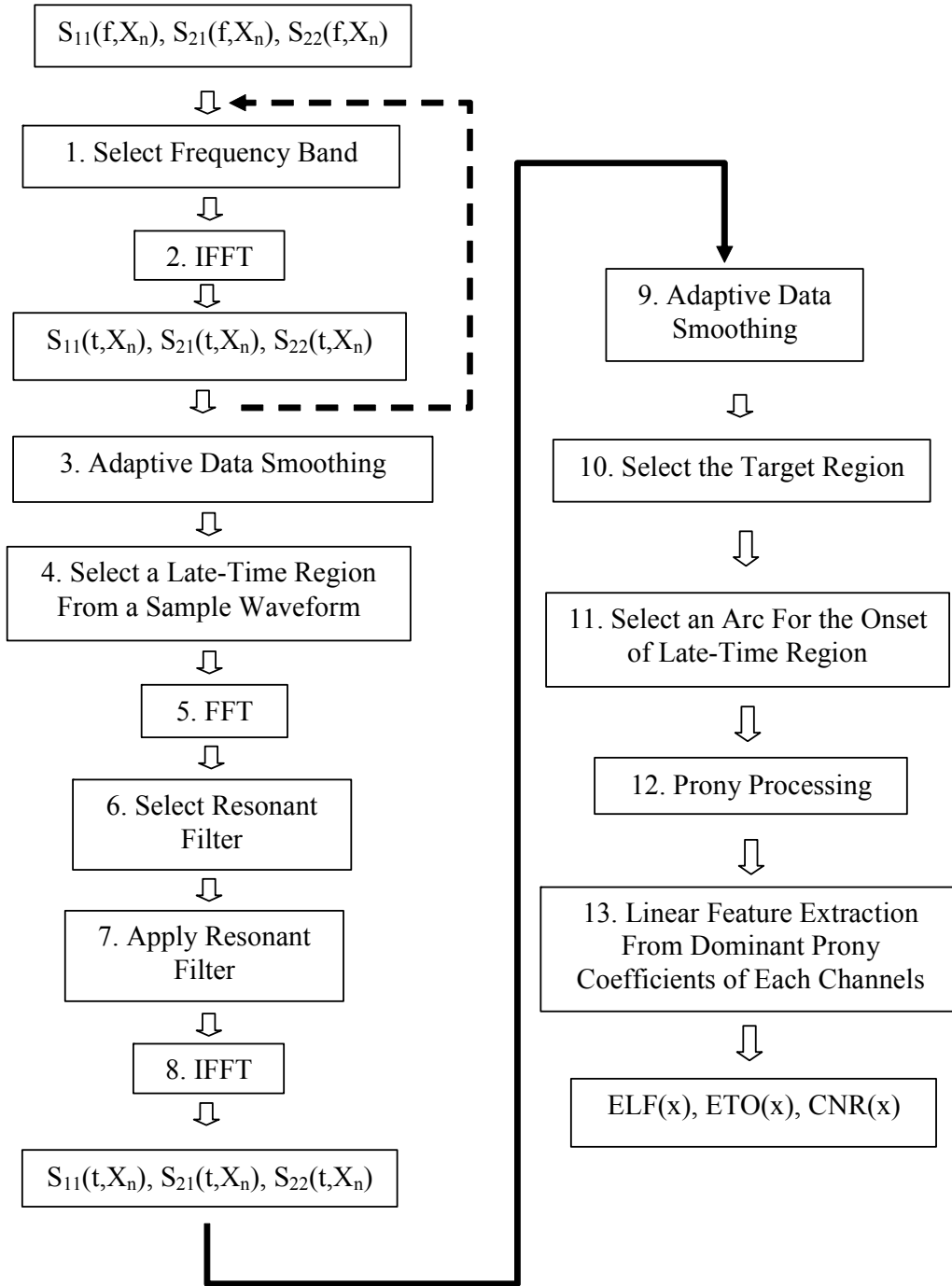


Figure 42. GPR parameter extraction flow chart.



## 3.2. UXO Classification by GPR Alone In Cases With Discrete Clutter

### 3.2.1. Setup and Signal Features of the UXO Alone

The main objective of this portion of the study is to explore the GPR capability in distinguishing and possibly characterize two closely spaced targets based on GPR's spatial, temporal and polarization resolution. Multi-pass GPR measurements using the pre-existing OSU-ESL GPR were conducted for a buried 105mm projectile inclined nose down at 45 degrees (Figure 43). The GPR was that developed for a recently completed ESTCP project [43-46]. The clutter consisted of a roughly 15" by 5" piece of thin ordnance scrap collected at a former firing range (Figure 44). The ordnance fragment was buried at the same depth and only one foot away from the UXO, as shown in the figure. The length of the projectile is approximately 20 inches. In one clutter configuration, the scrap is laid flat; in the other it is buried with long edge up. The UXO was angled either towards or away from the scrap. Different combinations of the two scrap orientations and two UXO orientations produced then four cases altogether.



Figure 43. A 105mm projectile (tail visible) buried at a depth of one foot and inclined 45 degrees.

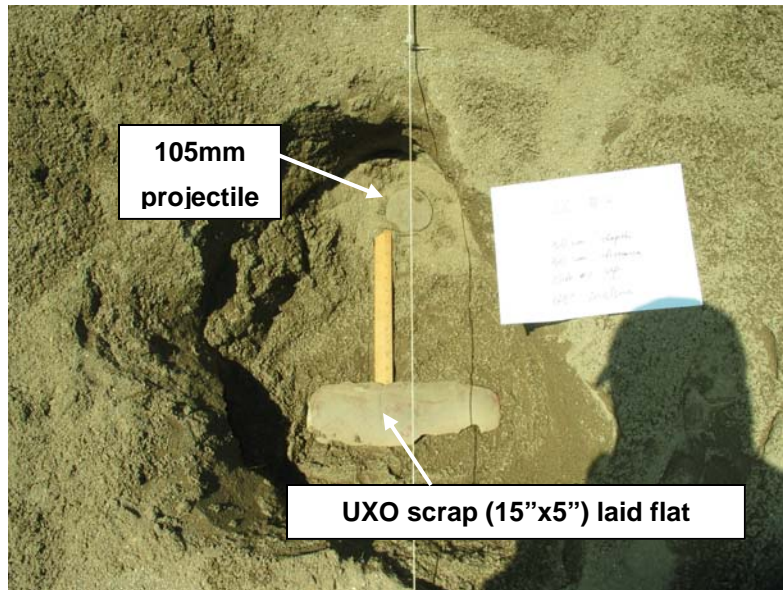


Figure 44. An elongated thin piece of ordnance scrap located close to a 45-degree inclined 105mm projectile.

All measurements were taken at an outdoor sand pit 18 feet in length, width and depth, at the Ohio State University ElectroScience Laboratory (OSU-ESL). The target items (UXO and clutter) were located around the center region. For each scenario, multiple linear GPR passes were made in different directions and with different offsets relative to the target locations. Along each pass, fully polarimetric swept-frequency data were collected from 10 to 810 MHz at 4 MHz frequency increments and at 3-inch position increments. Each scan was 10 feet in length. The  $S_{11}$  channel contains data from the transmitter and receiver polarizations parallel to pass direction, while for the  $S_{22}$  channel both Tx and Rx are polarized perpendicular to the direction of travel.

For reference, and to understand what might be produced by measurements from the more complicated scenarios, first we examine data from a case with the UXO alone. Figure 45 shows the relative position and orientation of the UXO from side view (a) and top view (b). The top end of the UXO is 30cm below the ground surface. The GPR passes are also indicated. Figure 46 shows background-removed GPR data in a typical time vs. position format as a result of pass #1. The gray scale indicates the voltage of the measured signal (signals in later time are amplified as a range gain is applied). Because the necessarily low frequency transmitted signal spreads out from the nominal look direction of the antenna, the receiver registers reflections when it is offset from the object, not just when it is directly above it. In a pass over a reflector, reflections will arrive in later time when the object is more distant and in earlier time when the

object is closer. Thus a scan passing over an object typically shows something of a hyperbola in the (horizontal) space- (vertical) time profiles such as those in Figure 46. The peak of the hyperbola represents the position at which the travel time to and from the object was a minimum. In this instance one sees two hyperbolas, indicating separate refractions off the two ends of the elongated object. Deeper below these initial reflections and harder to see in the figure are later time resonances characteristic of an elongated object.

Scattering from walls of the test pit is also present and contaminates the UXO responses in varying degrees, depending on time and position. For instance, the UXO responses collected around the center scan positions are less affected by the walls. This data demonstrates that different scattering events can be identified and grouped according to temporal-spatial distributions to provide information about target and clutter as well. In addition to this picture, data from other polarization ( $S_{22}$  and  $S_{21}$ ) also provide more information about each scattering event. In some situations the scattered signal from multiple targets or clutter can overlap. In this case, different measurement passes and different polarizations in each pass must be examined to try to distinguish separate scattering events. The intention of the investigation here is to see whether GPR's ability to record different arrival times, frequency and polarization sensitivities can assist in indicating the number of objects present and their character.

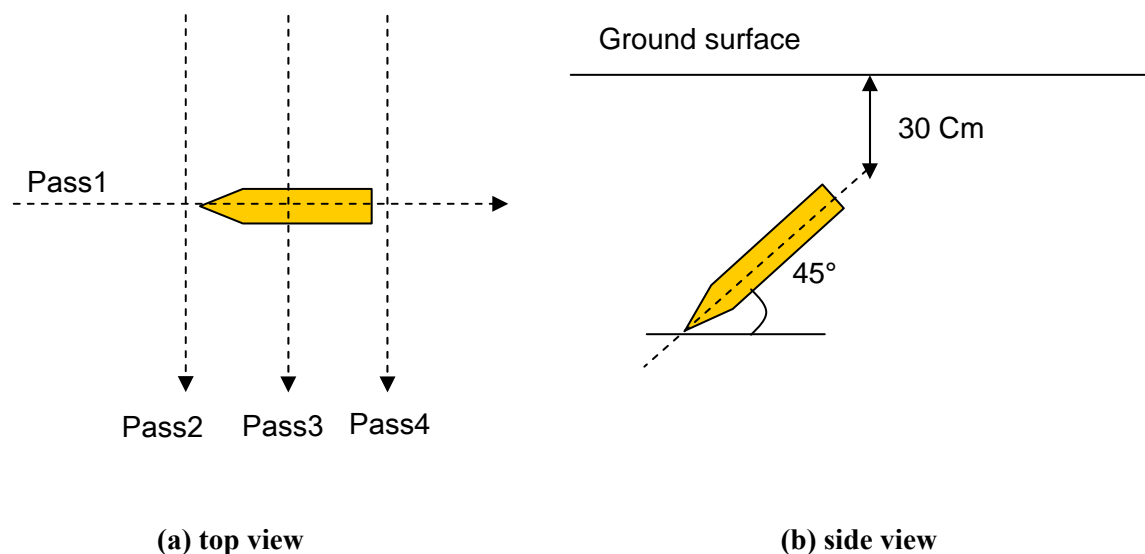


Figure 45. Site layout of a 45-degree inclined 105 mm projectile and GPR passes conducted for collecting UWB fully polarimetric data.

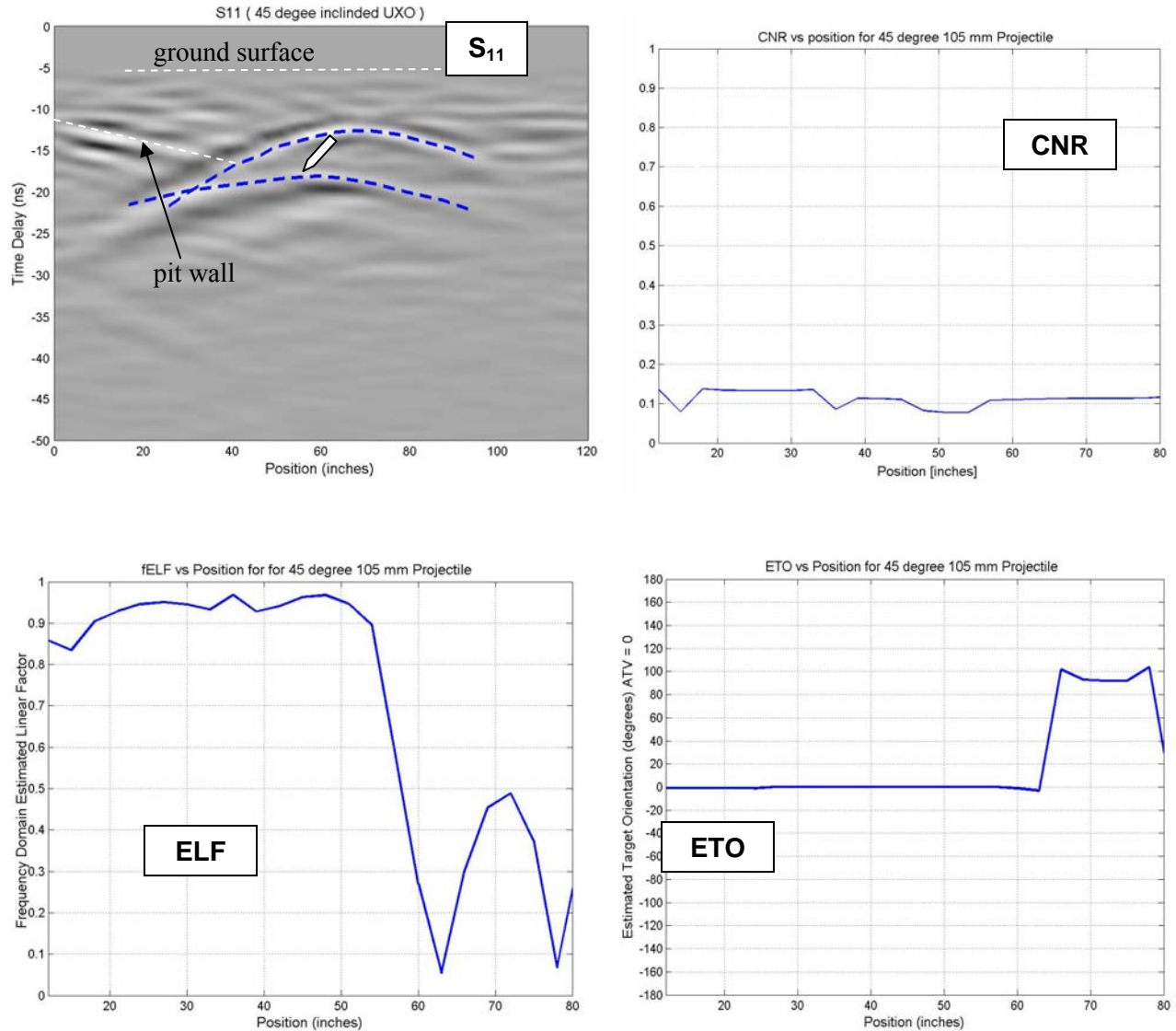


Figure 46. Background-removed S<sub>11</sub> data and extracted CNR, ELF and ETO for Pass #1 (parallel to UXO, filtered to extract 100~600 MHz).

If the dipping angle of an elongated object is small, the co-polarized reflection aligned with the axis of the body would be relatively strong (Figure 47, right) and late time resonances would appear. Such a reflection would also be inclined in the record, corresponding to the UXO's inclination (Figure 46). For more steeply inclined elongated objects, stronger end diffractions may appear, but side reflections and resonances will be reduced. End views of the object provide only small radar cross sections and less information regarding the elongation of the object and its late time resonances.

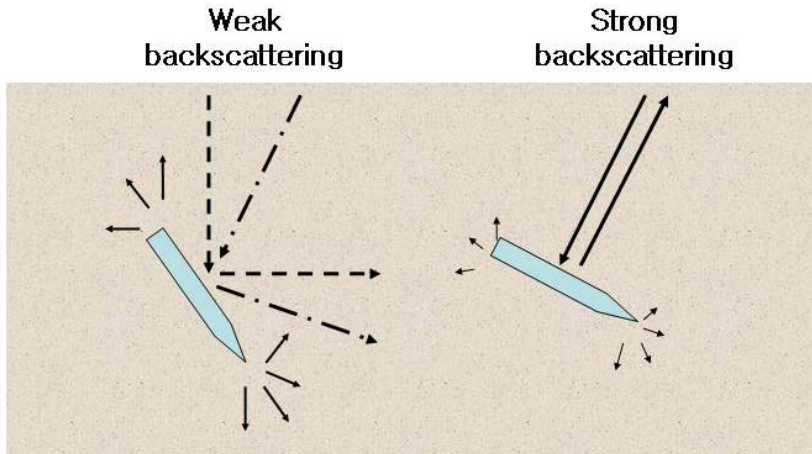


Figure 47. End diffractions and side reflections from an inclined UXO with different dipping angles. Left: steep; Right: slight.

In Figure 46, the real, center frequency of the CNR is approximately 100 MHz, corresponding to 26 inch length in soil with an estimated dielectric constant of 5. This could be longer than the actual length of the object's axis in part because the CNR-derived length reflects the path that electric currents must take from end to end over its curving surface. Additionally, the actual soil dielectric constant at depth could be greater than the estimated value of 5, which would produce a smaller length estimate. High ELF values are observed at positions offset to the left in the record, where the configuration produces nearly broadside incidence on the UXO, giving high linearity. The extracted ETO correctly indicates 0 degree UXO orientation with respect to the pass direction, as illustrated in Figure 45.

Figure 48 and Figure 49 plot the results obtained from Path-2 and Path-4 (see Figure 45). Since the polarization of  $S_{11}$  channel is transverse to the UXO, weak response is expected. On the other hand, the  $S_{22}$  direction is now aligned with the UXO and should show a stronger response, which it does. The ETO also correctly indicates 90-degree orientation with respect to the direction of travel (DOT). Notice the center dip in the ELF plot from pass #4. This is due to the fact that the radar is seeing the UXO from its end. The combination of rotational symmetry in this view and low cross section produce low signal linearity, as expected. This preliminary exercise indicates the kind of information that may be obtained from multiple, multiply oriented, fully polarimetric UWB GPR passes.



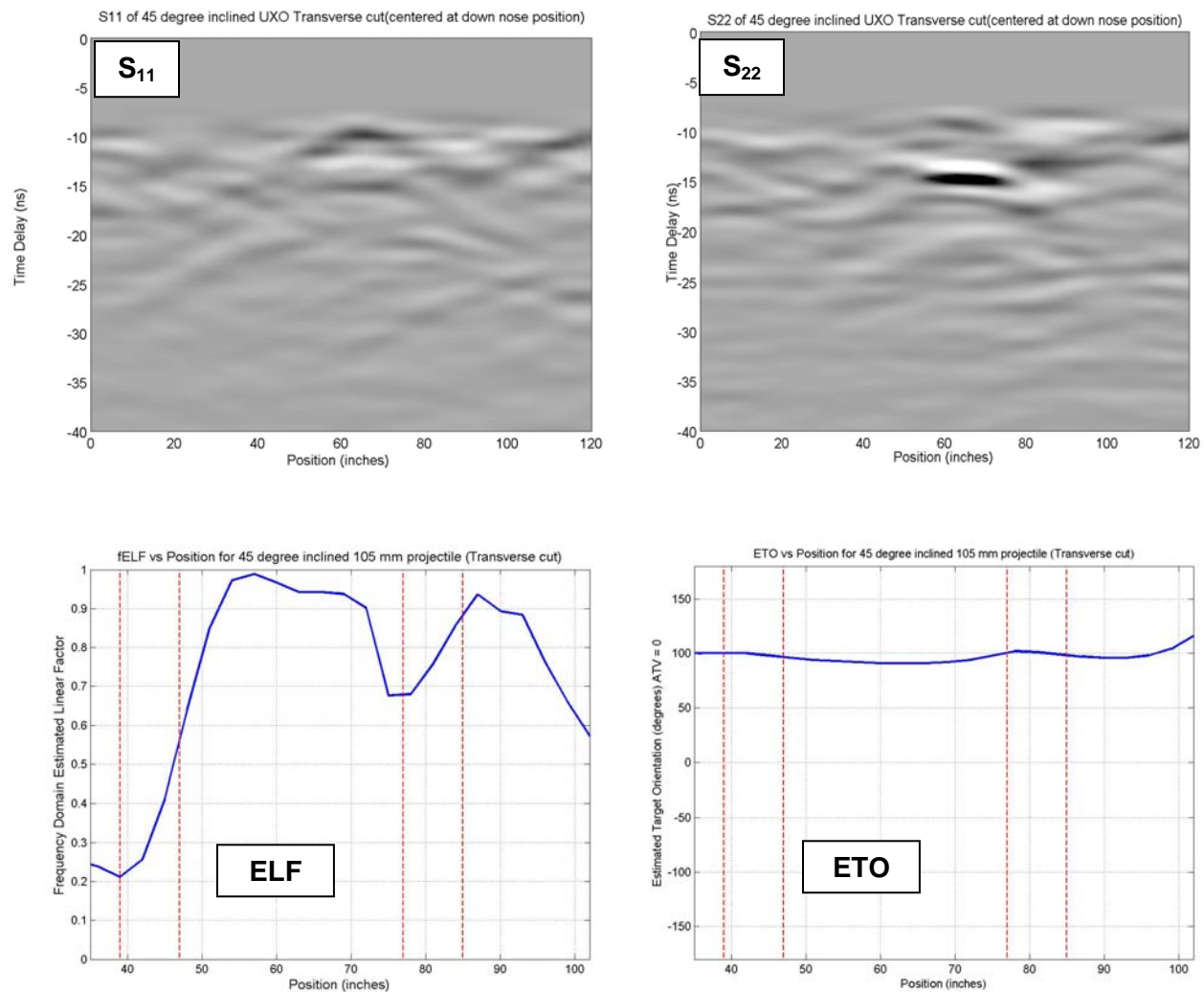


Figure 48. Background removed data ( $S_{11}$  &  $S_{22}$ ) and extracted ELF and ETO for Pass #2 (DOT is transverse to UXO, offset to the left, as per Figure 45).

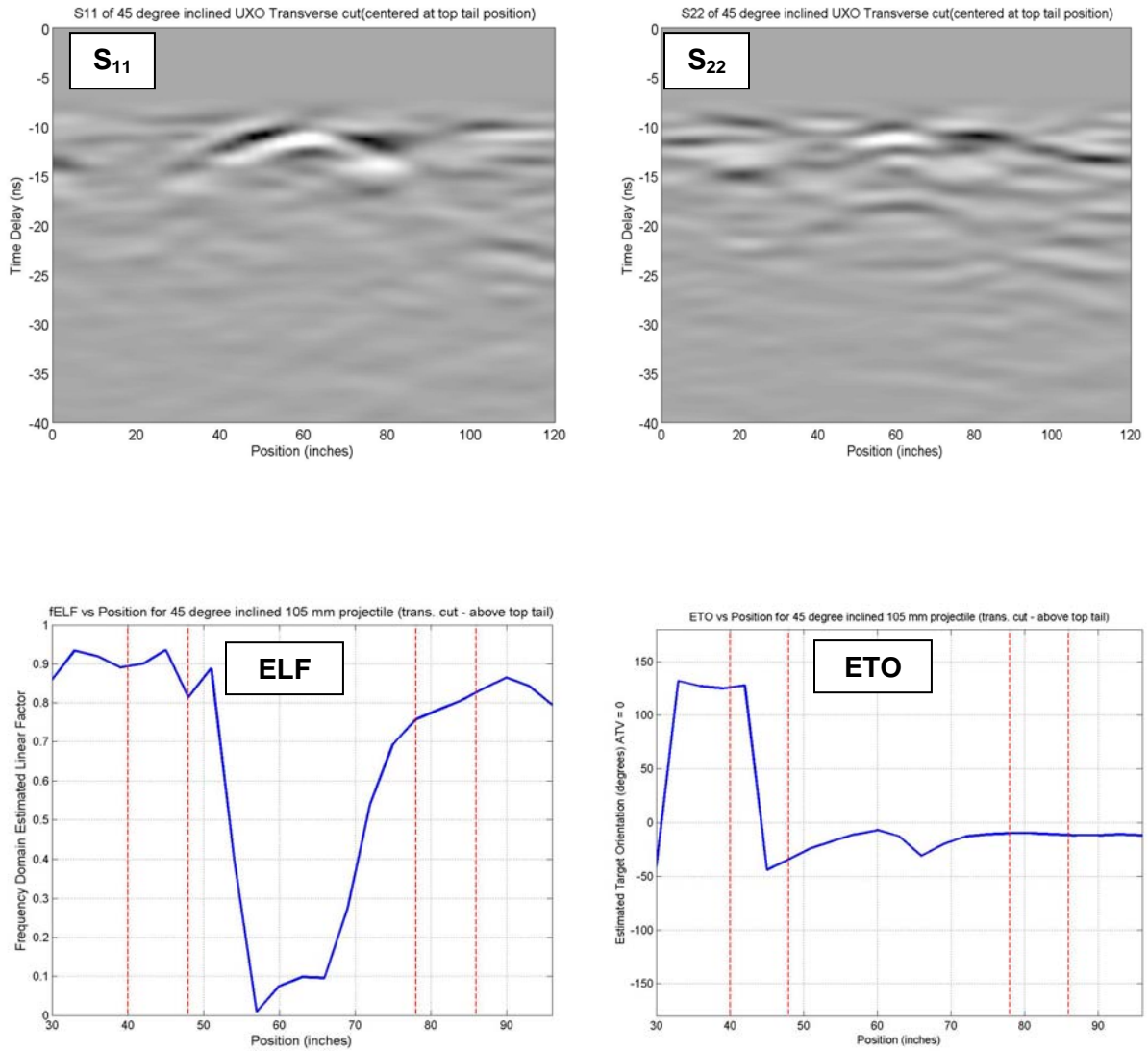


Figure 49 Background removed data ( $S_{11}$  &  $S_{22}$ ) and extracted ELF and ETO for Pass #4 (DOT is transverse to UXO, offset to the right, as per Figure 45).

### 3.2.2. **Scenario #1: Ordnance Scrap Edge-Up & 105 mm Projectile Tilted Outward**

The first scenario features a UXO and an elongated, thin shell scrap situated close to each other, as illustrated in Figure 50. The 6-pass GPR scan scheme is also shown in the right figure. Both objects are buried at a depth of 30 cm to the shallowest point and separated by 45 cm (nearest points). The nose of the 105 mm projectile is tilted downward 45 degrees away from the scrap. The long axes of the two objects are orthogonal to each other. The scrap is laid horizontally with one of its long edges facing up. In this configuration, path #2 is most useful to detect both objects from the scattering patterns. Once existence of multiple objects is recognized, better radar signatures such as ELF, ETO and CNR may be estimated for individual objects from passes going over each one, i.e. Path #4 and Path #6.

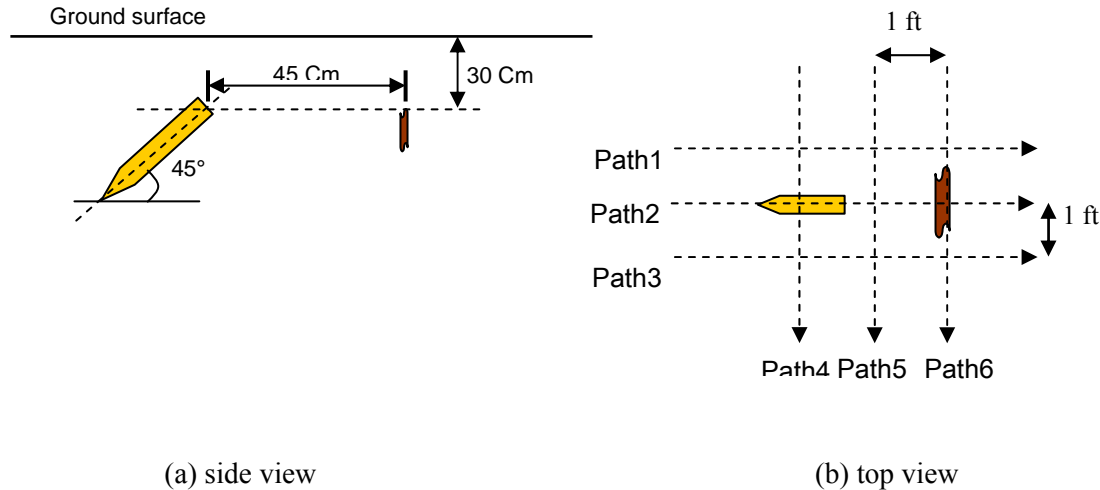


Figure 50. An edge-up, elongated piece of ordnance scrap buried with a 105 mm projectile tilted away from the scrap.

Figure 51 plots measured data ( $S_{11}$  &  $S_{22}$ ) from three of the passes. Horizontal scales have been shifted to be zero at the center position (60 inches). The  $S_{11}$  data in Path-2 shows response of an inclined target, similar to that observed in Figure 46. Overall complexity of responses observed from all six passes indicates that there is not just a single target below. Strong interference exists in most regions. Such interference is worsened by the large antenna footprint of this pre-existing GPR system. The left side of  $S_{11}$  data and the



right side of  $S_{22}$  data in Path #2 do indicate the presence of late-time resonance. If more comprehensive examination of the data (possibly together with EMI or magnetic data) indicates that the pass traveled more or less directly over the objects, then one should be able to extract reasonable ELF, ETO and CNR features and perform classification. If no additional information is available, at least one can extract the resonant frequency and estimate the lengths of the target(s). With the pre-existing large antenna, offset views from other passes suffer loss of polarization purity, making inferences murkier.

Figure 52 plots the extracted features for the right-side object with response peaking around the 70-inch position. It indicates good linearity,  $90^\circ$  orientation with respect to DOT and resonant frequency of 190 MHz, corresponding to approximately 14" in a medium with  $\epsilon_r = 5$ , close to the scrap's true length of  $\sim 15$ ". Figure 53 plots the extracted features for the left-side object with response peaking around the -40" position (unshifted 20" position). It indicates good linearity,  $0^\circ$  orientation with respect to DOT and resonant frequency of 100 MHz, corresponding to approximately 25" (true axis length  $\sim 20$ ") in a medium with  $\epsilon_r = 5$ .

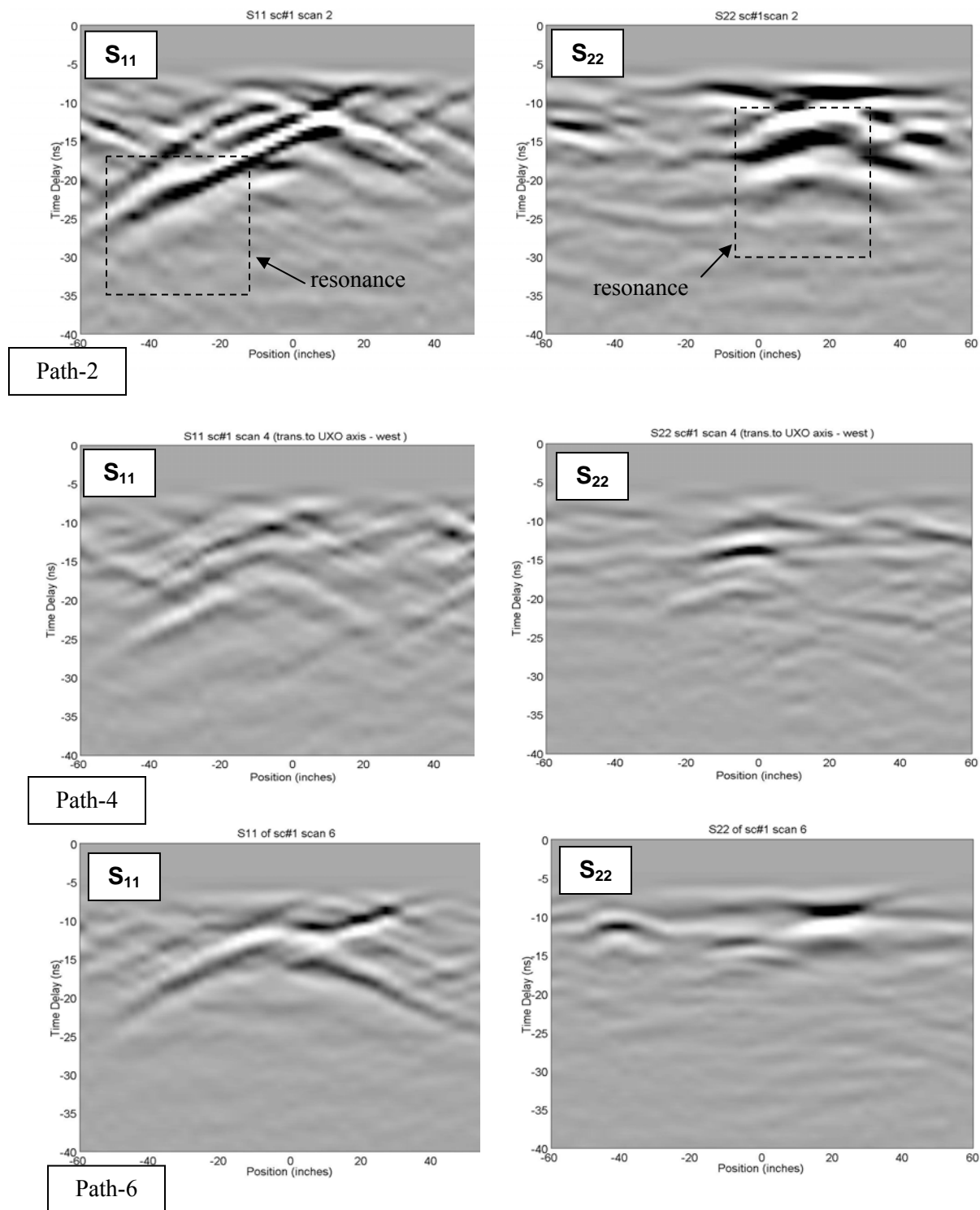


Figure 51. Measured GPR data from Scenario #1, for paths #2, #4, and #6.

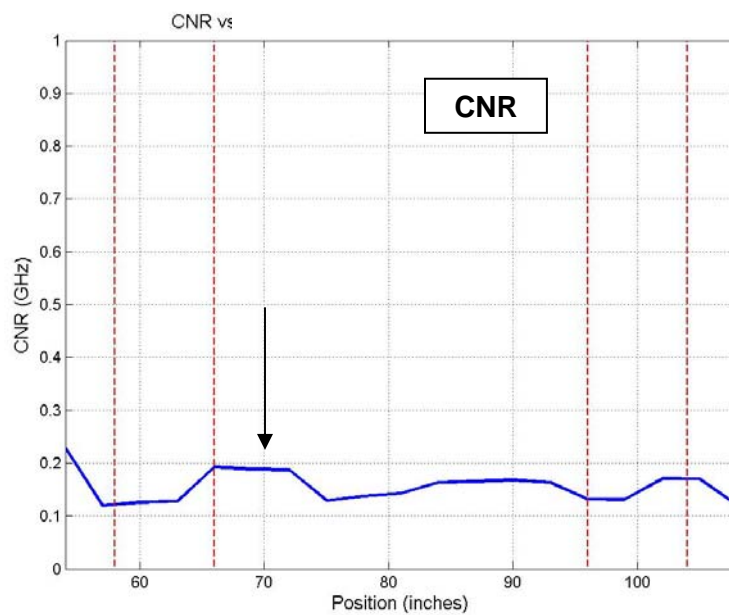
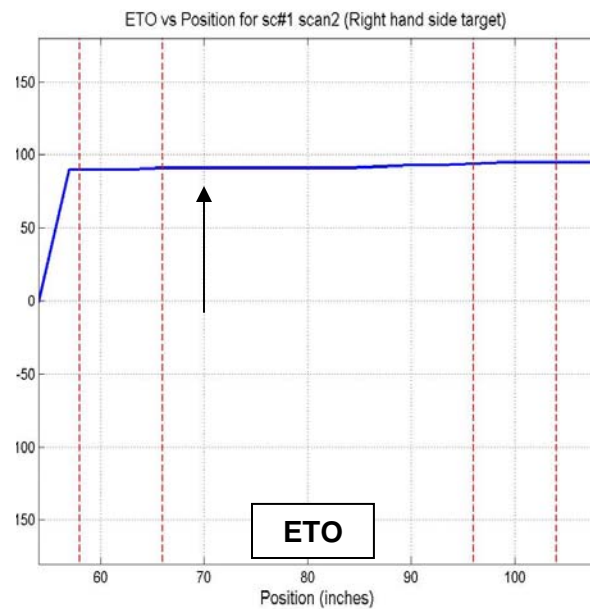
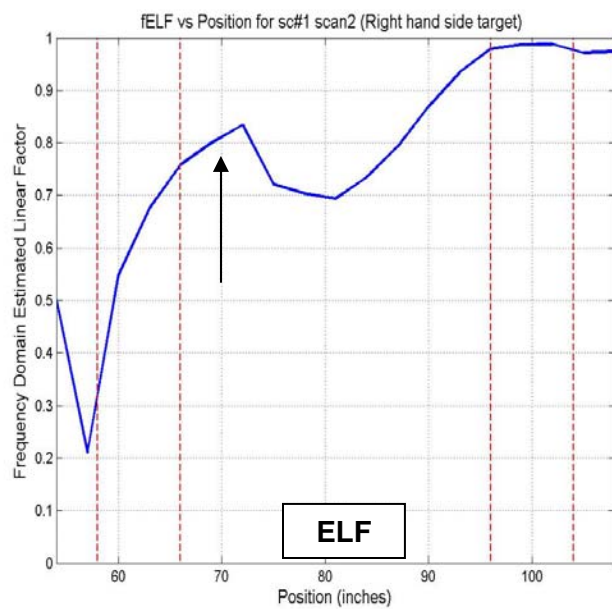


Figure 52. Extracted features for the RIGHT object (scrap) from Path #2 for Scenario #1.

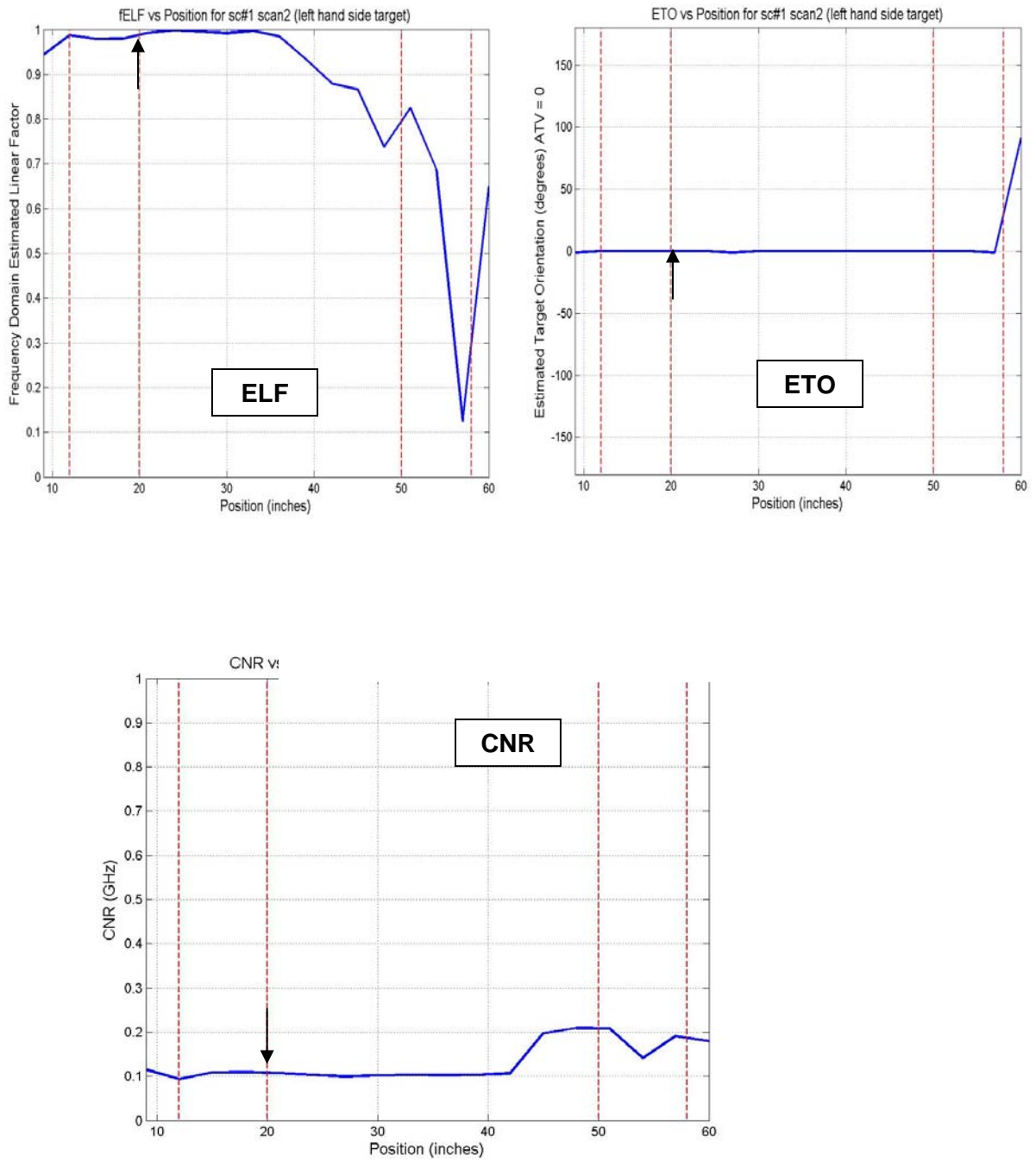


Figure 53. Extracted features for the LEFT object (UXO) from Path #2 for Scenario #1.

### 3.2.3. **Scenario #2: Ordnance Scrap Flat & 105 mm Projectile Tilted Outward**

The second scenario investigated contains the same two objects as in Scenario #1 except that the distance between the two is reduced to 30 cm and the scrap was laid flat to produce stronger scattering responses. This (Figure 54) represents a more challenging rendition of the first scenario.

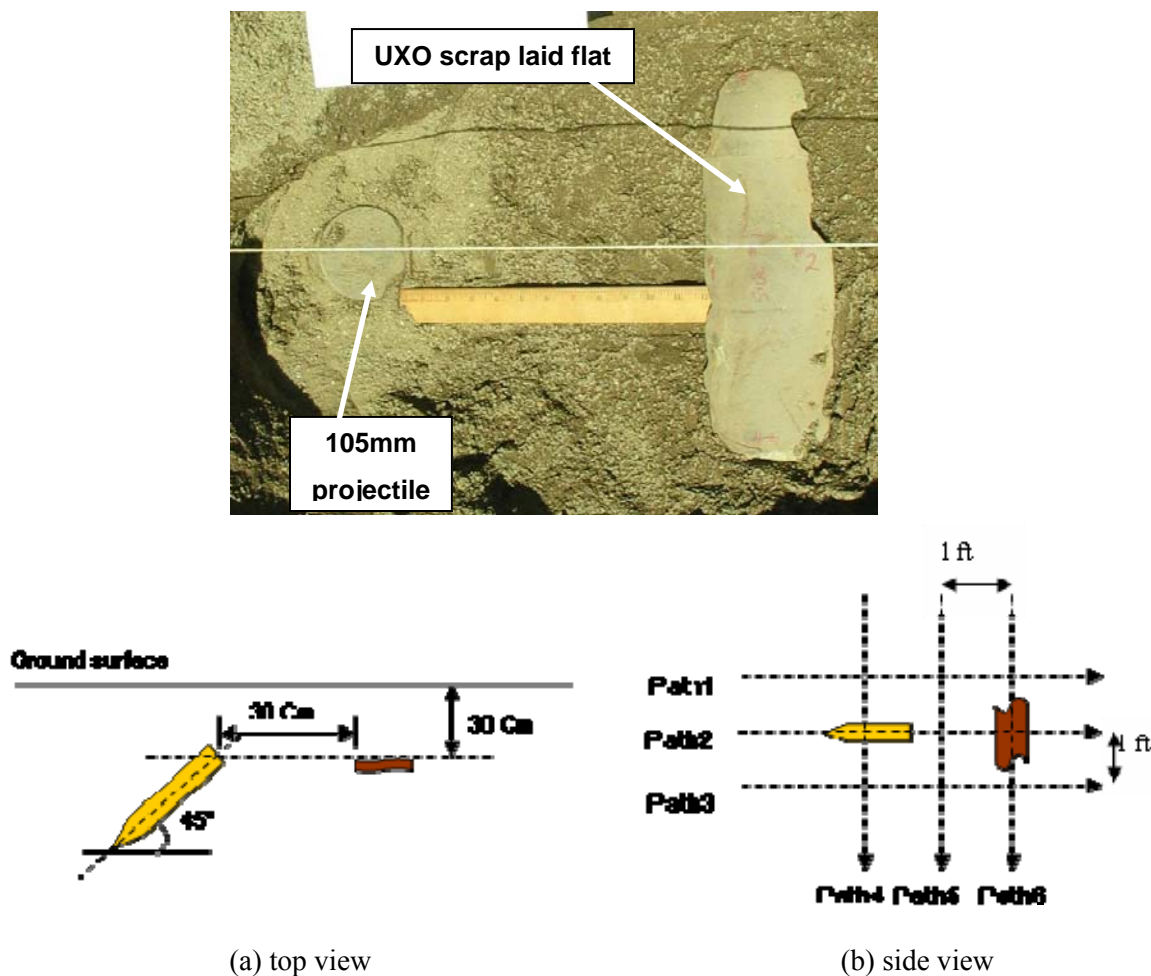


Figure 54. A flat, elongated piece of ordnance scrap is buried with a 105mm projectile tilted away from the scrap.

Figure 55 plots measured data ( $S_{11}$  &  $S_{22}$ ) from three of the passes. Here the center of the scan is located at the 60" position. Judging from the number of groups of hyperbolic arcs in all six passes, it is clear that there are two major targets in this area. With the different clutter orientation and closer spacing in this scenario, data from Path #4 reveals some severe interference. Responses from individual objects are co-located around center position with different delay time. At the same time, the scattering patterns still show good resonances in Path #2, as indicated in the dashed boxes. The good (least interference) feature region is around the 30-inch position for the left object and the 80-inch position for the right object.

Figure 56 plots the extracted features for the left target from data collected along Path #2. Around 20" it indicates high ELF,  $ETO=0^\circ$  with respect to DOT and a resonant frequency of approximately 105 MHz. All are correct features associated with ground truth of the projectile. Figure 57 plots the extracted features for the right-side target from data collected along Path #2. Around 80" it indicates high ELF,  $ETO=90^\circ$  with respect to DOT, and a resonant frequency of approximately 185 MHz. All are correct features associated with ground truth of the ordnance scrap.

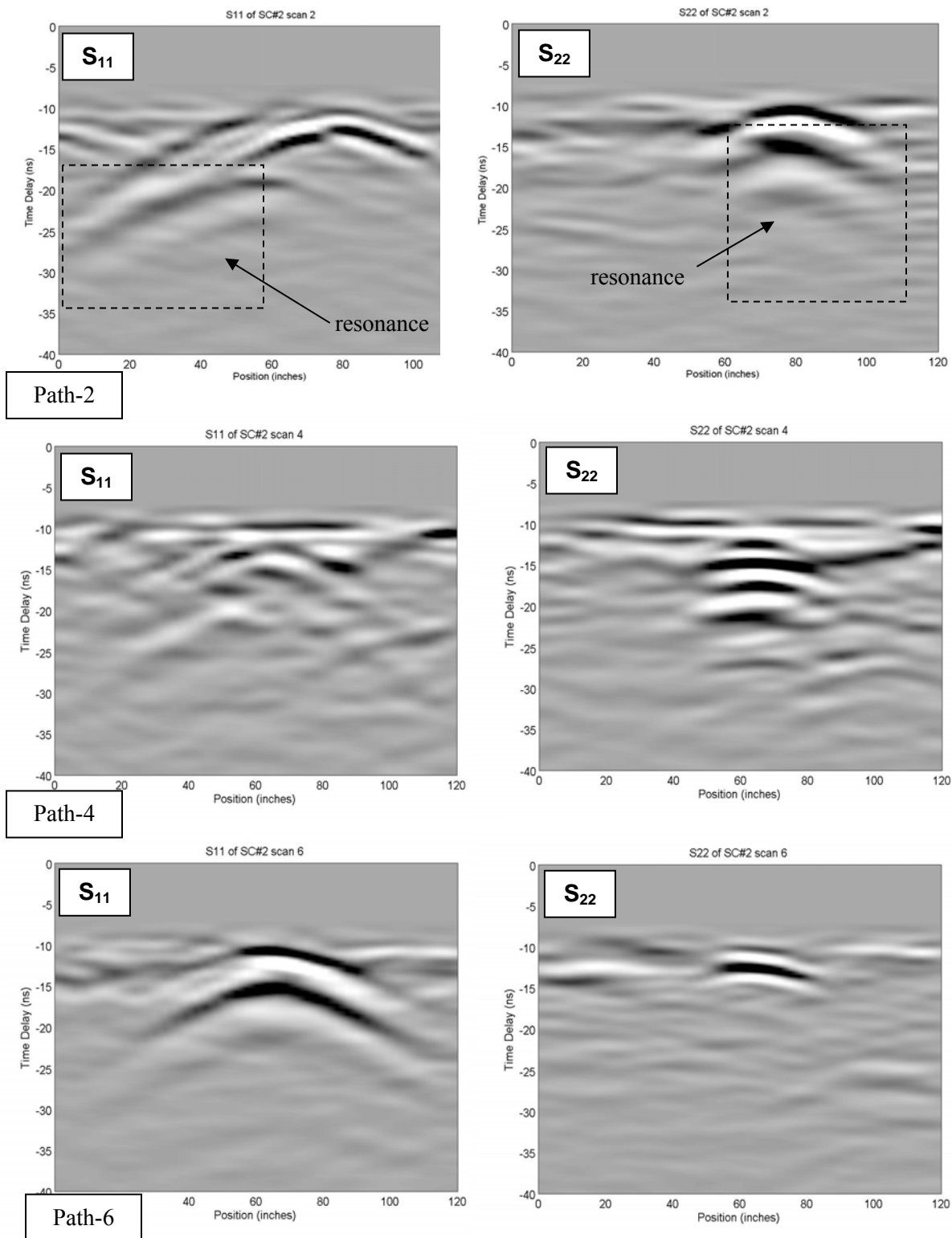


Figure 55. Measured GPR data from Scenario #2 for paths #2, #4, and #6.

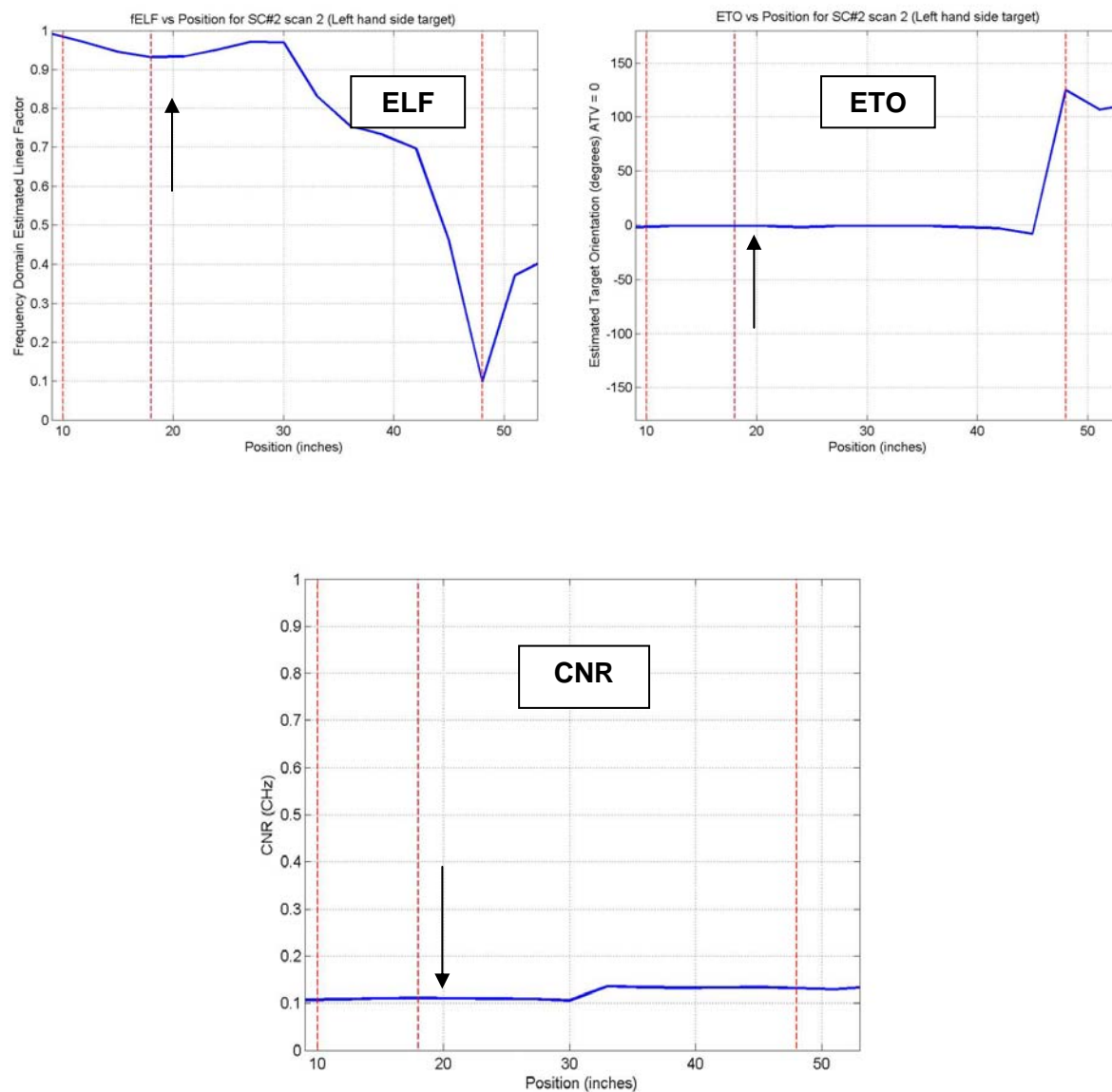


Figure 56. Extracted features for the LEFT object from pass #2 for Scenario #2.



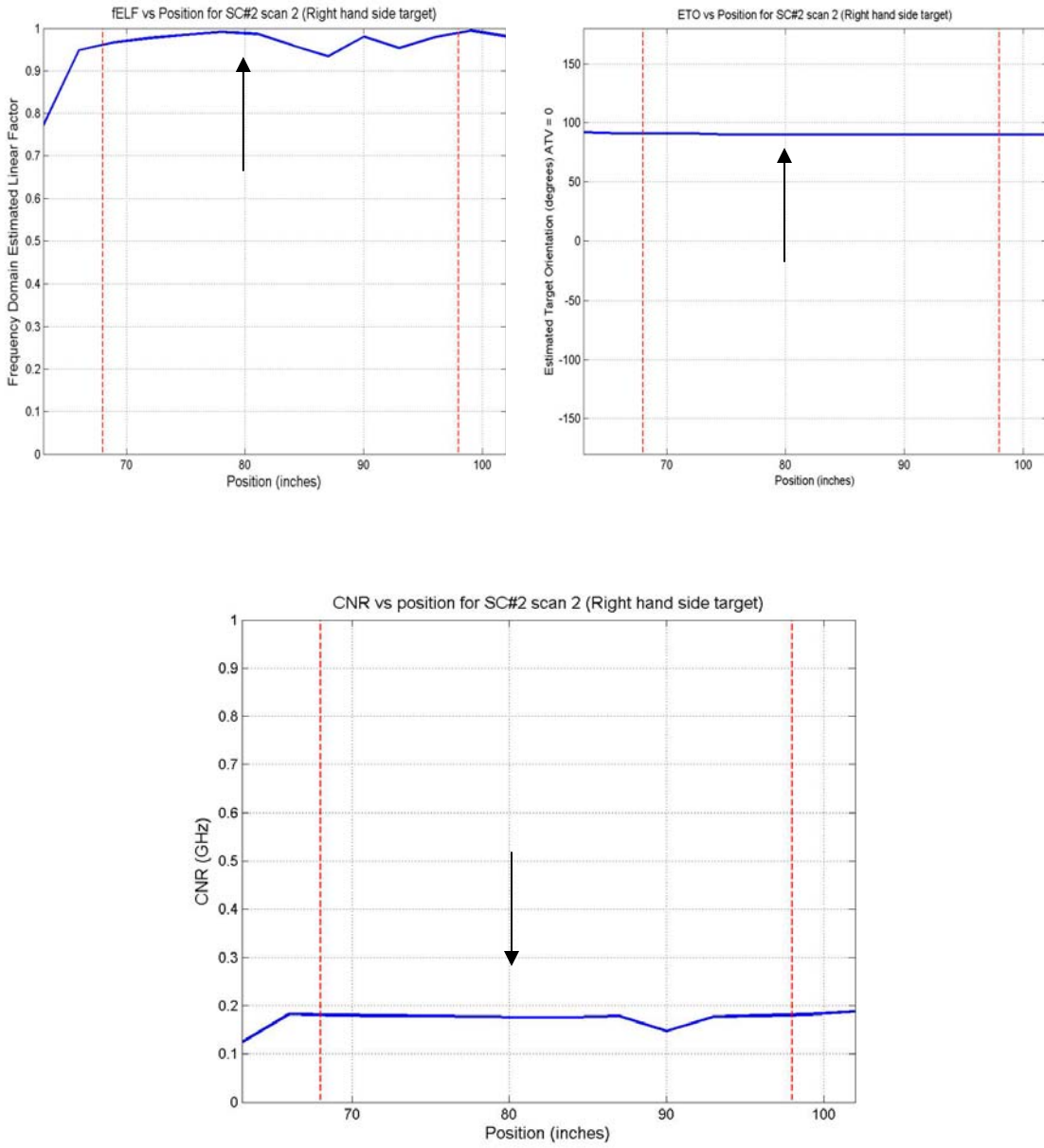


Figure 57. Extracted features for the RIGHT object from pass #2 for Scenario #2.

### 3.2.4. **Scenario #3: Edge-UP Ordnance Scrap & 105 mm Projectile Tilted Inward**

The configuration of Scenario #3 is shown in Figure 58. This is similar to Scenario #1 except that this is more challenging, with the projectile is inclined toward the scrap.

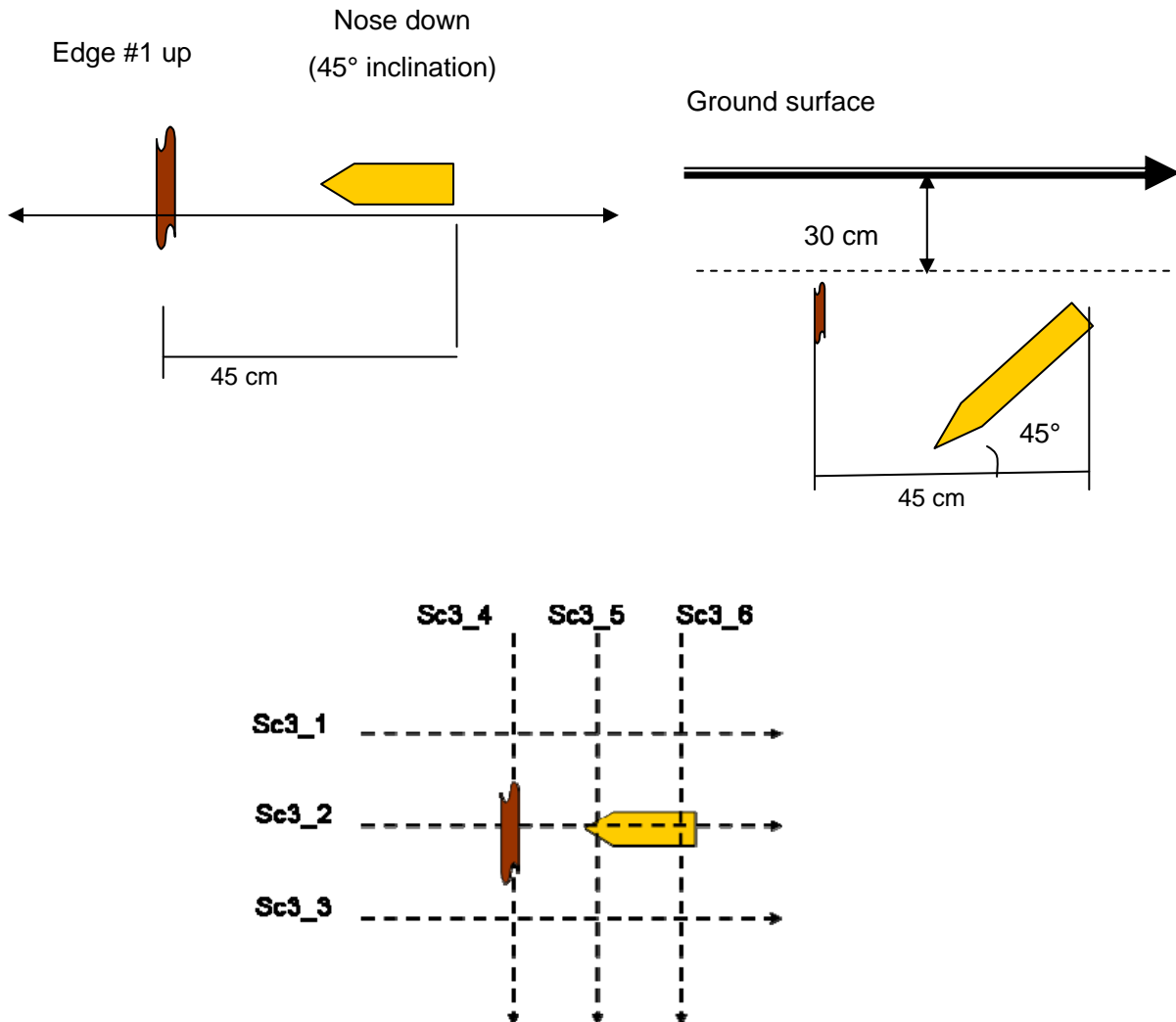


Figure 58. Target arrangement in Scenario #3 - An edge-up, elongated piece of ordnance scrap is buried with a 105mm projectile tilted away from the scrap.

This should cause the strongest UXO signal and resonance to occur at a antenna position nearly directly above the scrap, causing severe overlapping (interference) of GPR responses. As before, six GPR passes along Paths #1 through #6 were conducted.

Figure 59 shows the  $S_{11}$  and  $S_{22}$  data collected along three of the paths. Judging from complexity of the scattering patterns, it is not difficult to conclude that there is more than one object. Pass #3  $S_{22}$  data (not shown) indicates of two targets at different offsets.  $S_{11}$  data in pass #2 clearly shows signal overlap between the UXO and scrap, causing severe contamination in desired UXO signals when compared with Figure 46(a). The  $S_{22}$  response is mainly associated with the scrap since the polarization associated with channel 2 is transverse to the direction of travel, thus parallel to the long axis of the scrap. Observing these data from pass #2 alone, it would be difficult to tell whether there are multiple targets or not. Additional data from pass #4 and pass #6 reveal scattering patterns quite different from that for a single target. For example,  $S_{11}$  and  $S_{22}$  data from pass #4 indicate that the object below is quite linear (notice the strong late-time response in  $S_{11}$  but not  $S_{22}$ ) and oriented approximately along pass #4. The response in  $S_{22}$  is different from what a single target should produce in that its depth is different from that in  $S_{11}$  and it does not show hyperbolic arcs as a single fat target would do. In fact, the latter is due to the coupling between antenna-2 (transverse to the DOT) and a target that has a transverse offset. A similar situation is observed in pass #6.

On the basis of these scattering patterns, one might discern resonance in pass #2 in the indicated box area. The extracted features from this region are plotted in Figure 60. These results indicate good linearity, 90° orientation with respect to DOT and resonant frequency of approximately 145 MHz. The ELF and ETO correctly correspond to the features of the scrap but the resonant frequency is incorrect. The correct value should be 190 MHz. Note that 140 MHz happens to be between the resonant frequencies of the projectile (100 MHz) and the scrap (190 MHz). Therefore, the error is caused by the severe interference between these two objects.

In this scenario, the features of the projectile alone were not obtainable due to the interference. However the polarimetric responses do indicate the presence of two targets, along with their approximate positions and orientations.

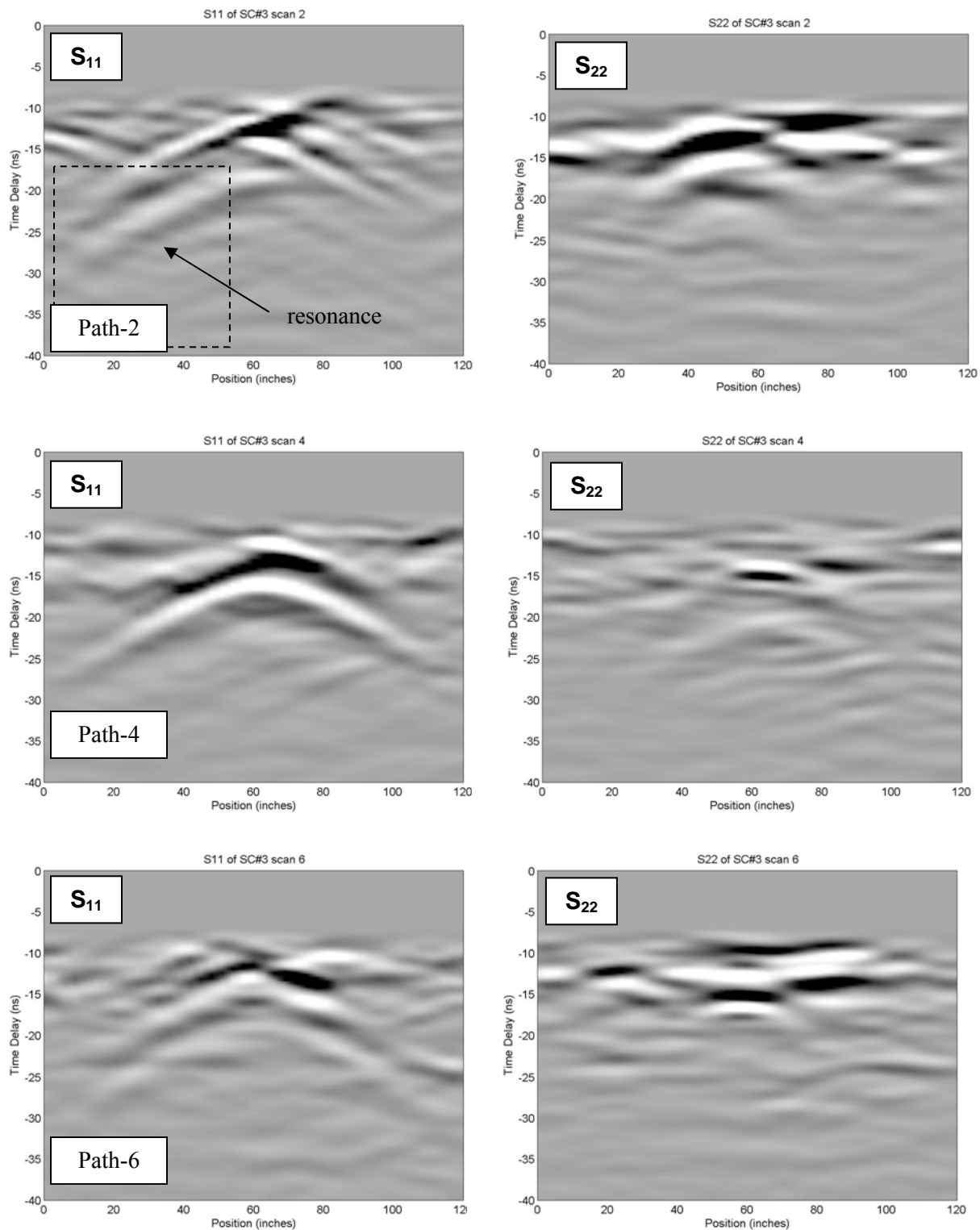


Figure 59. Measured GPR data from Scenario 3 for passes #2, #4, and #6.

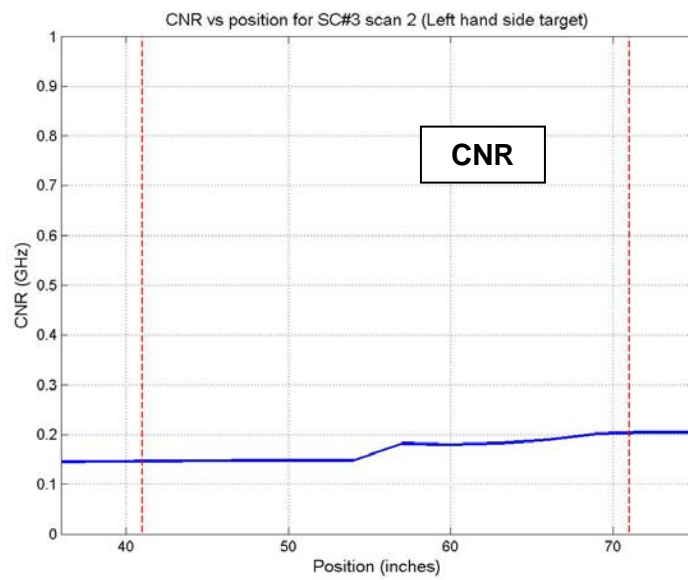
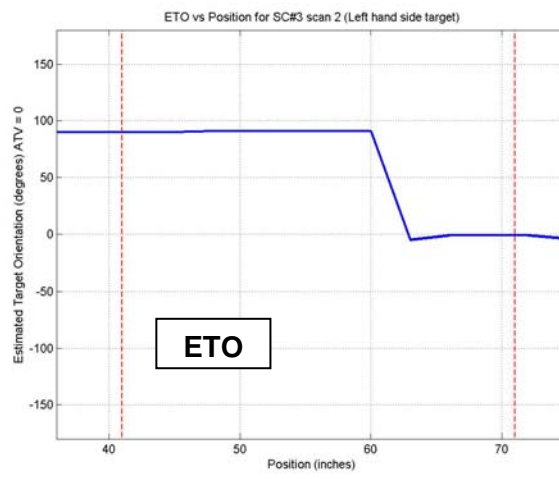
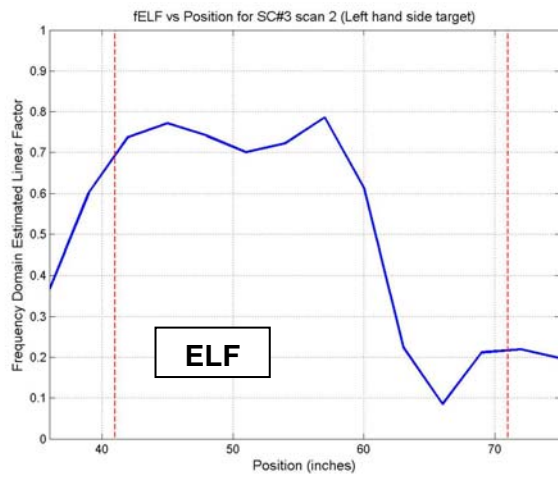


Figure 60. Extracted features for the LEFT object (scrap) from pass #2 for Scenario #3.

### 3.2.5. **Scenario #4: Ordnance Scrap Flat & 105 mm Projectile Tilted Inward**

Figure 61 shows the target arrangement in Scenario #4. This is the most challenging scenario in that the UXO is angled towards the scrap; and the scrap produces stronger responses in both  $S_{11}$  and  $S_{22}$  channels when it is laid flat compared to the edge-up case.

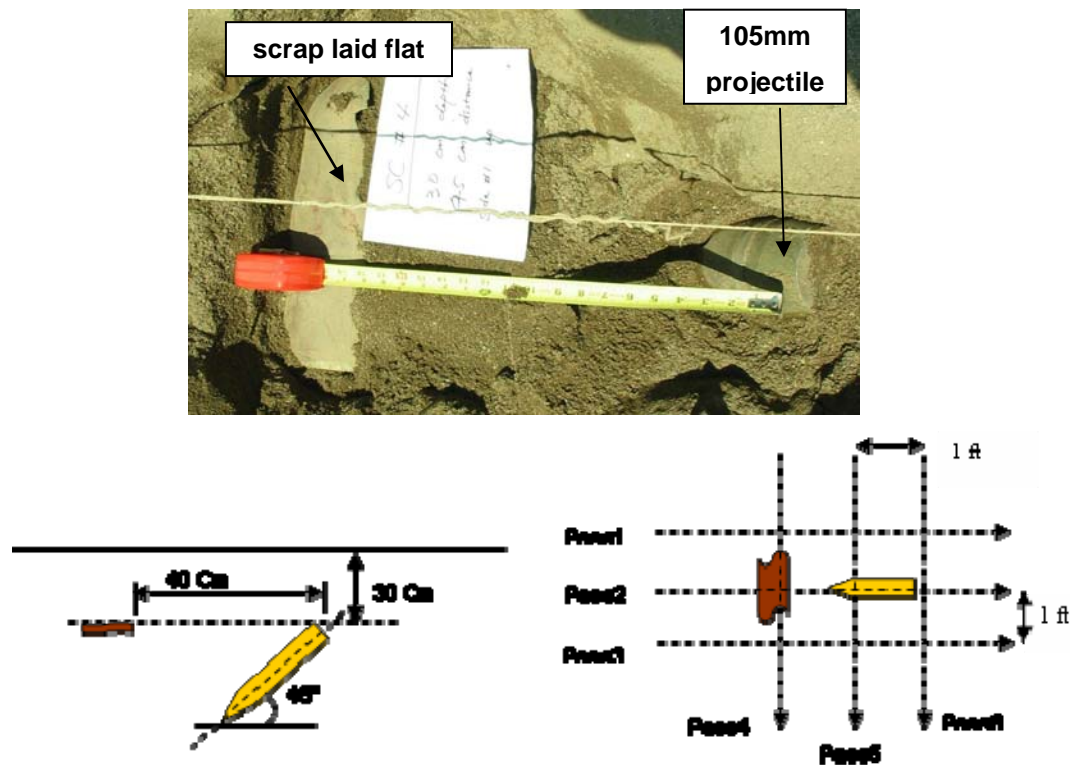


Figure 61. Target arrangement in Scenario #4 – A flat elongated ordnance scrap with a 105 mm projectile tilted towards the scrap

Figure 62 shows measured data ( $S_{11}$  &  $S_{22}$ ) from three of the passes. Judging from the number of groups of hyperbolic arcs in all six passes, it is clear that there is more than one target in this area with their responses overlapping severely. The findings from processed results are similar to those found in Scenario #3. Significantly, a large linear object is suggested on the left in path 2. That may be all one can infer from the data. Further attempts to interpret the extracted features will most likely result in misleading or insubstantial conclusions.

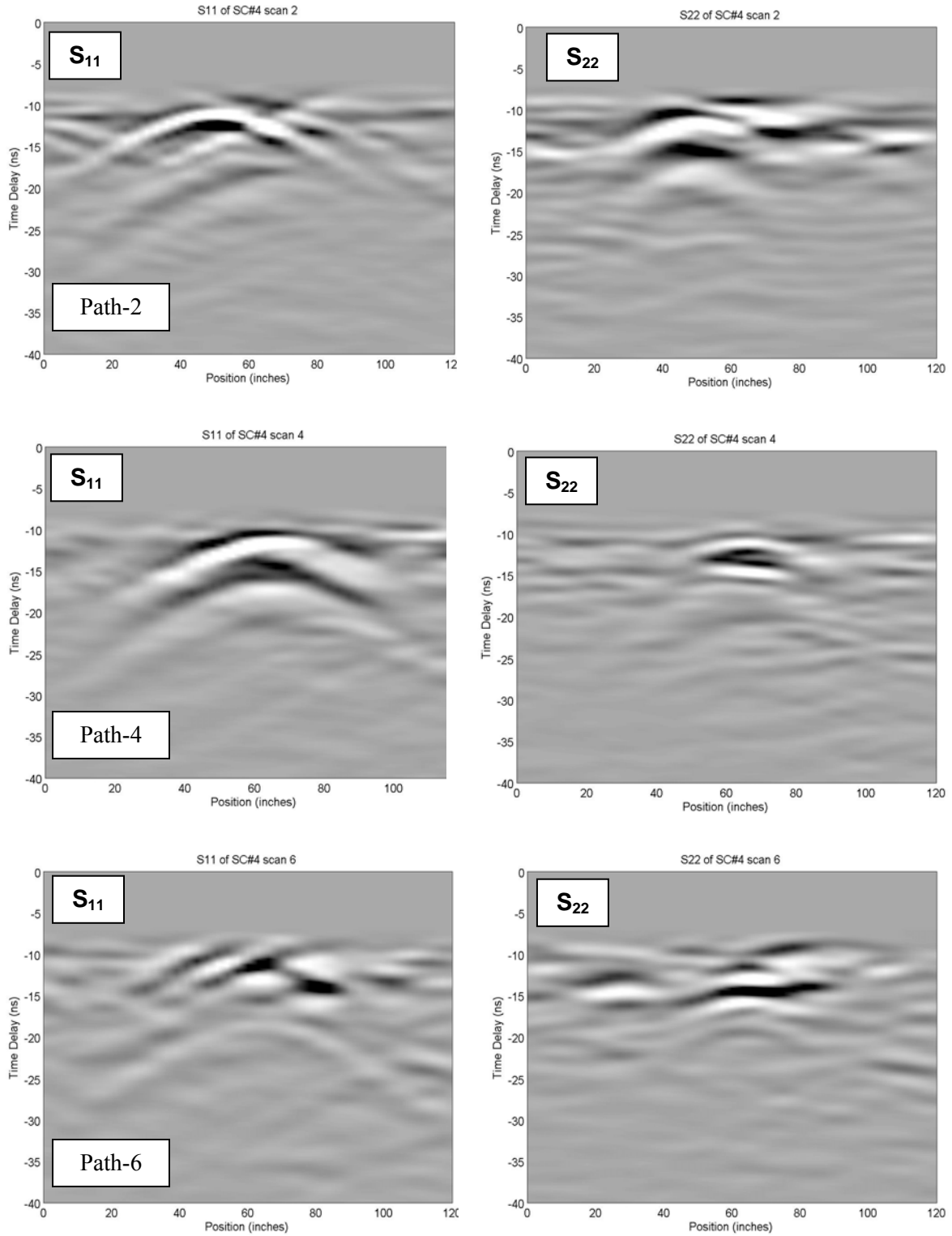


Figure 62. Measured GPR data from Scenario 4, for paths #2, #4, and #6.

### **3.2.6.                    *Conclusions***

The investigations in this section indicate that the presence of two objects separated by as little as 30 ~ 40 cm could still be detected. The utilization of scattering patterns from multiple and multiply oriented linear passes clearly helps decide the number and location of targets. Properly choosing the scan pass and response region during the feature extraction allowed at least some linear features of each target to be extracted correctly in most cases. The resonant frequency (related to the UXO length) appears to be more susceptible to interference than linearity. Scenarios #3 and #4 with UXO tilted toward the neighboring clutter appear to be the most difficult cases. While even the limited inferences from scenario #4 could guide or constrain EMI processing at the same site, more focused measurement could produce more discerning analysis. The capability of separating two nearby targets was limited here by the relatively large antenna footprint and can be improved with a smaller antenna design. Therefore in the course of this project a much more compact system was developed, allowing faster, denser, more localized data acquisition.

### **3.3.                    The New Improved GPR**

Inspired by the capabilities of the pre-existing UWB polarimetric OSU-ESL GPR but impressed with its limitations, we embarked in this project on a re-design, construction, and debugging of a new generation system. Overall, the new system is smaller, lighter, faster, easier to deploy, and more robust than the older one. Miniaturization of the antenna is made possible in large part by a dielectric fill in the horn, essentially eliminating the large “wings” that extended from the old antenna to accommodate the necessary lowest frequencies. At the same time, the new system covers approximately the same bandwidth as the old, from the neighborhood of 10 MHz up to ~ 800 MHz. Some details of the new system are given in Appendix A, with more available through the references [52]. To summarize here, in addition to the new smaller footprint antenna the new system incorporates an advanced digital down converter (DDC) and direct digital frequency synthesis (DDS). The new system was also outfitted with a convenient, user-friendly GUI, enabling the user to calibrate and control the system readily and to monitor data acquisition effectively.



For testing purposes no attempt was made to economize on computer monitor size, etc. All equipment could be mounted on a small cart that could be pulled along easily by a single person, with the horn fed bowtie (HFB) antenna dragged behind (Figure 63, Figure 147). During each measurement pass, a friction wheel mounted against the cart wheel automatically triggers measurements at some predetermined interval, here usually every 3 inches. Tests of the new system at Camp Lejeune illustrated considerable improvements in ease of measurement for greater data density and localization than was possible before [52]. While it is difficult to compare performance between different sites under different conditions, discrimination results also suggest some improvement over past experience with the older system. Therefore the new system was used in GPR measurements on the ERDC-CRREL outdoor testplots, which were then analyzed in conjunction with EMI data.

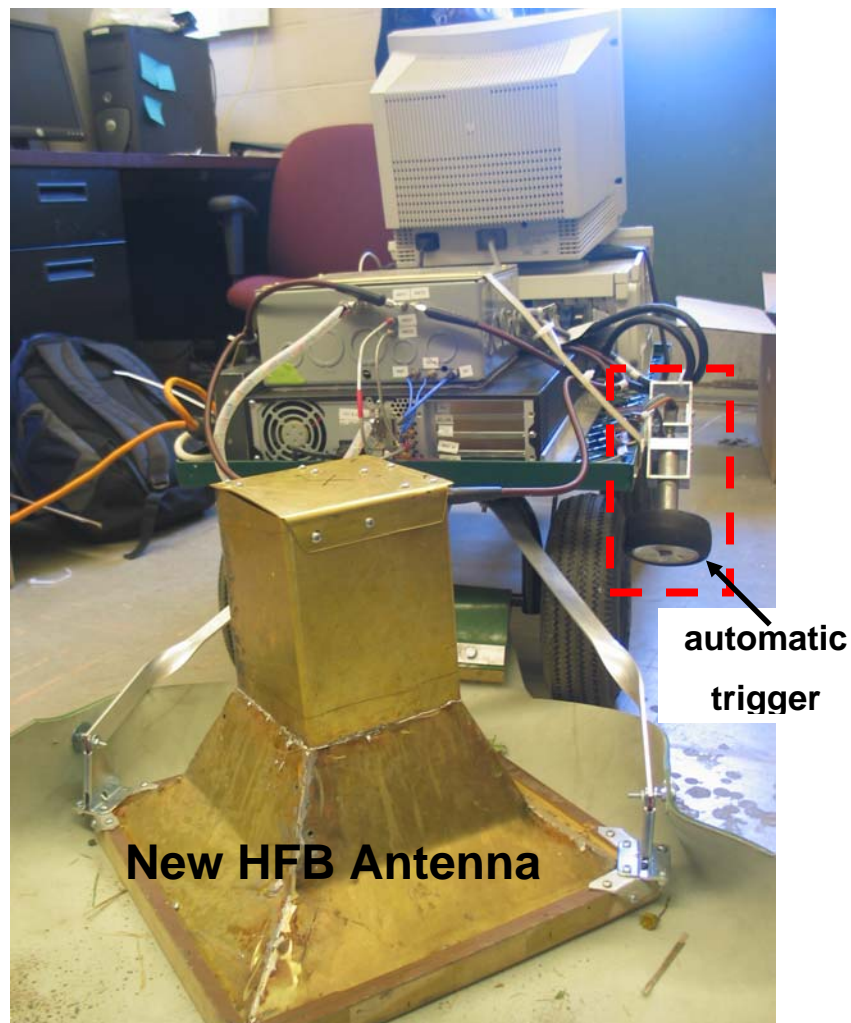


Figure 63. Integrated new dual-channel GPR radar with a miniaturated HFB antenna.

## 4. EMI INTERACTION BETWEEN OBJECTS NEAR ONE ANOTHER

In heavily contaminated sites, the possibility arises that a number of objects illuminated simultaneously by a sensor may interact. That is, the scattered field from each may impinge upon the other, creating a kind of secondary primary or incident field. In most contexts, it has been assumed that this interaction would be slight, and in any case would have a negligible effect on the received signals. "A negligible effect" means that the received signals will be about the same as one would get simply by superposing the responses of the individual targets, with each responding as if the other were not there. However, while some tests have seemed to show negligible interaction effects for certain degrees of proximity for particular objects, e.g. [53], other tests in our lab with different objects of comparable size and proximity appeared to show strong effects [54, 55]. In this section we pursue the matter of interaction effects, ultimately showing when this will be significant and showing how such significant effects arise.

First, we test our numerical model to make sure that it can model situations effectively when one object is very close to another. The MAS-TSA program (Section 2.1) was applied to GEM-3 measurements over a set of two cylinders. The program models the complete scattering problem with both items present, i.e. all interaction is included. A magnetic steel and a non-magnetic stainless steel cylinder, both with machined flat ends, were stacked upon one another end to end. Based on values in the literature and study of each  $L$  by  $a$  (half diam) cylinder separately, their parameters are: for the stainless steel,  $L_1 = 7.6$  cm,  $L_1/2 \ a_1 = 2$ ,  $\sigma = 1.4 \times 10^6$  S/m, ( $\mu_r = 1$ ); and for magnetic steel  $L_2 = 7.6$  cm,  $L_2/2 \ a_2 = 2$ ,  $\sigma = 4 \times 10^6$  S/m,  $\mu_r = 120$ . The ultimate observation point was 31 cm from the mid- point between the cylinders and the GEM-3 primary field was modeled in detail. In numerical calculations, the distance between cylinders was assumed to be 10 micrometers (repeated studies of this and other combinations indicated that there was no significant difference in results from assuming a microscopic gap or a solid connection between the two pieces). The numerical solutions match the measured data quite well (Figure 64), and thus we proceed with the model to investigate different geometries, material properties, and proximities for other cases. Parenthetically, note that from an observation point two characteristic lengths from the object one still sees a thoroughly different response, depending upon which end is facing the sensor. There is no single, unique axial response such as is presumed in analyses and processing based on the single, infinitesimal, anisotropic dipole model.

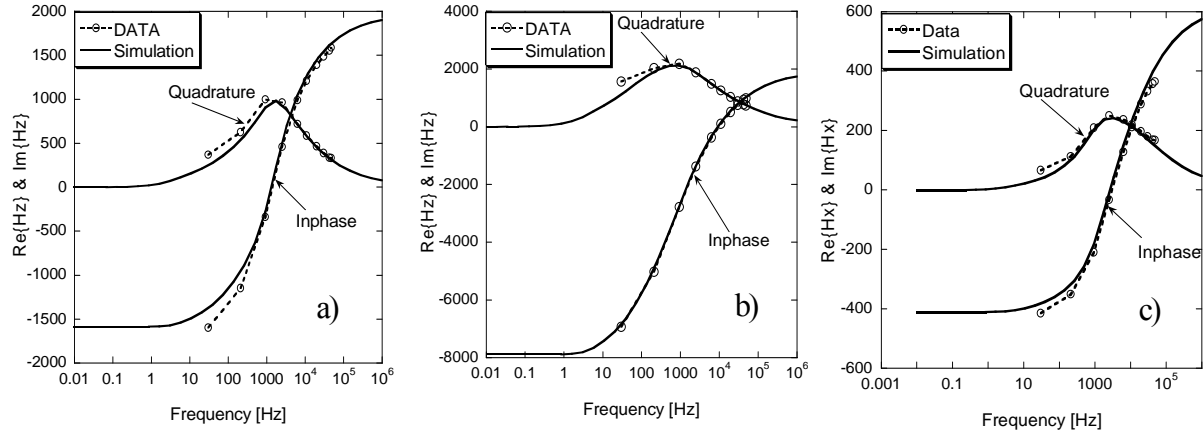


Figure 64. Measurement and modeled scattered fields from the two-cylinder combination with sensor above. a) stainless steel up, magnetic steel down; b) magnetic steel up, stainless steel down; c) horizontal.

Figure 65 shows calculated results for two cylinders under uniform axial excitation, placed again end to end but with various separations. One object is aluminum ( $\mu_r = 1$ ,  $\sigma = 2.8 \times 10^7$  S/m) and one is magnetic steel ( $\mu_r = 150$ ,  $\sigma = 4 \times 10^6$ ). Figure 66 shows the same test with the same materials, but performed with spheres instead of cylinders. Both figures show the same general phenomenon. For a combination of magnetic and non-magnetic objects (right column of plots), the calculation performed including all interactions produces essentially the same scattered field as simple superposition of separate solutions for each object, without any interactions included, but simply taking their locations into account. However for a combination of two magnetic objects, very strong interaction effects appear in the lower frequencies as the cylinders are placed closer to one another.

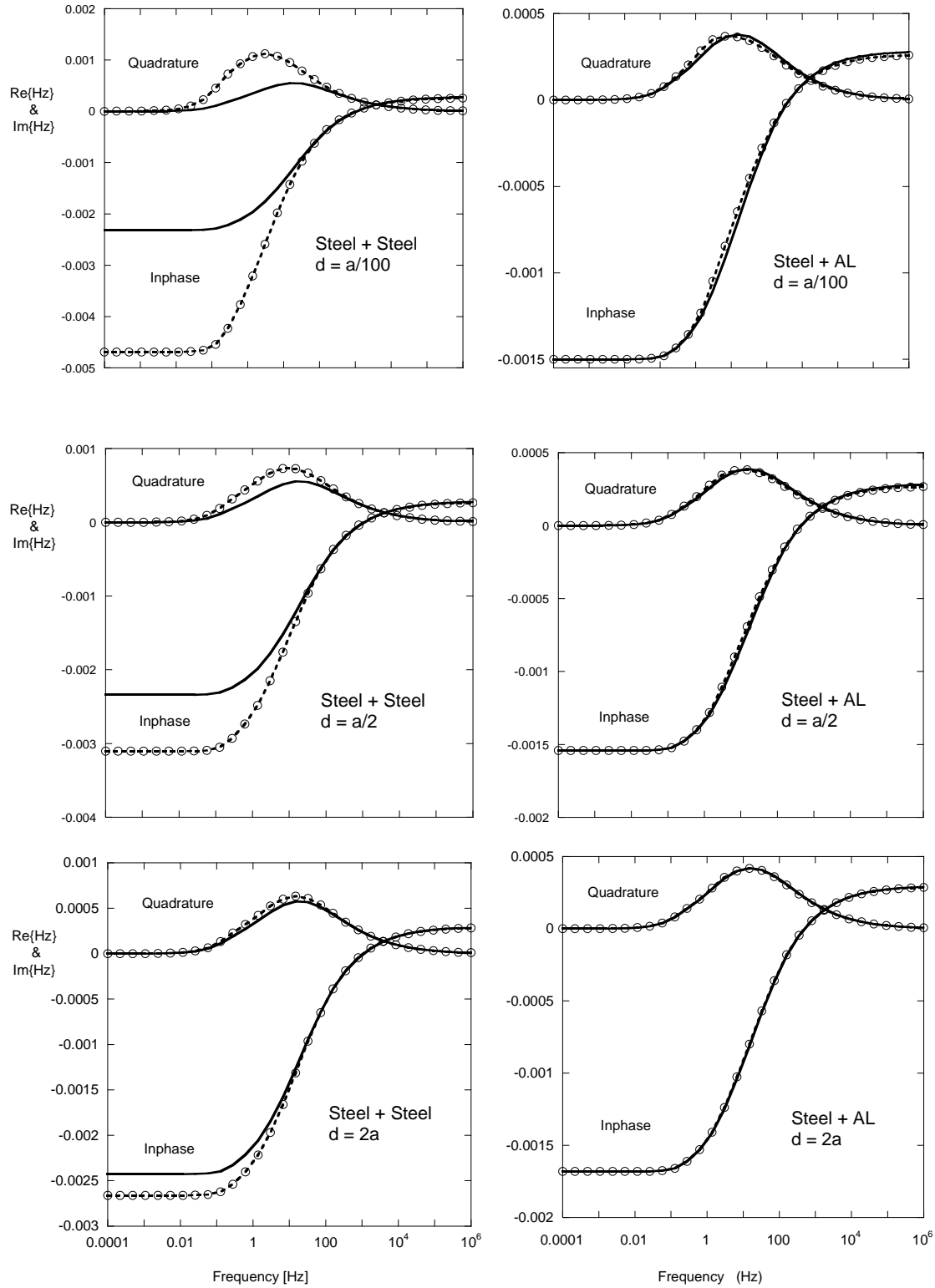


Figure 65. Scattered fields from axial excitation of two cylinders of diameter  $2a$ , placed end to end, at different separations  $d$ . Solid line = simple superposition; dashed markers = full interaction.

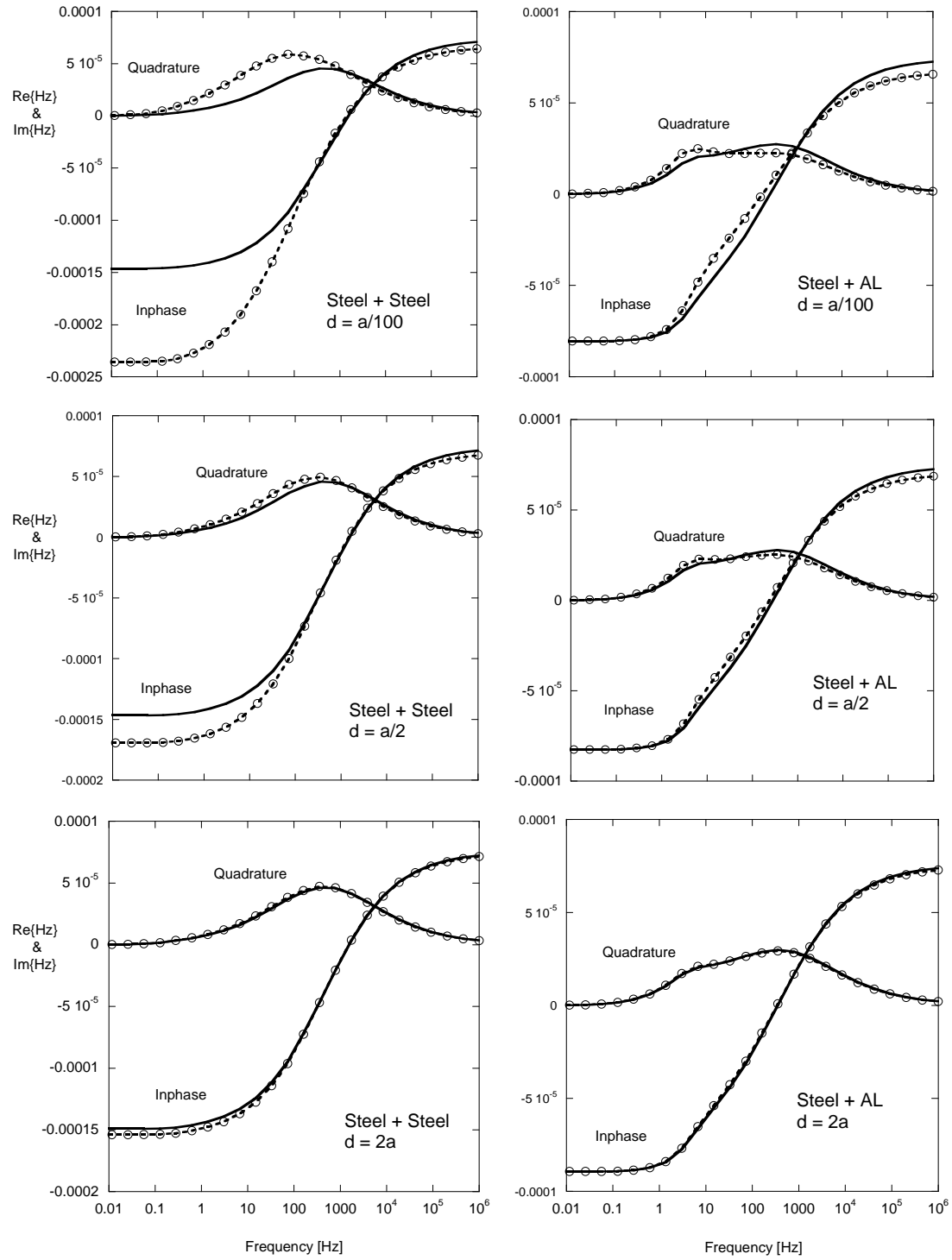


Figure 66. Same as Figure 65, but for spheres instead of cylinders.

To gain some perspective on this scattering behavior, let us examine the analytical solution for the scattered field from a sphere, alone, of radius  $a$ , subject to a uniform primary field oriented in the Z direction [56, 57].

$$H_z^{sc}(z) = H_0^{PR} 2(M - iN) \left(\frac{a}{z}\right)^3 \quad (73)$$

where  $M$  and  $N$  are frequency dependent. Expressing that dependency in terms of induction number  $|k|a$ , where  $k = \sqrt{i\omega\sigma\mu}$ , one obtains the “classical” plot in Figure 67. These curves include all effects of material properties  $\sigma$  and  $\mu$ , varied singly or together, between the low and high frequency limits of EMI. The total magnitude of  $2(M - iN)$  only varies between  $1 \sim 2$  under all conditions. This means that, at the object surface ( $z = a$  in (73)), the magnitude of the scattered field “saturates” at between 1 and 2 times that of the primary field, no matter how high  $\mu_r$  becomes.

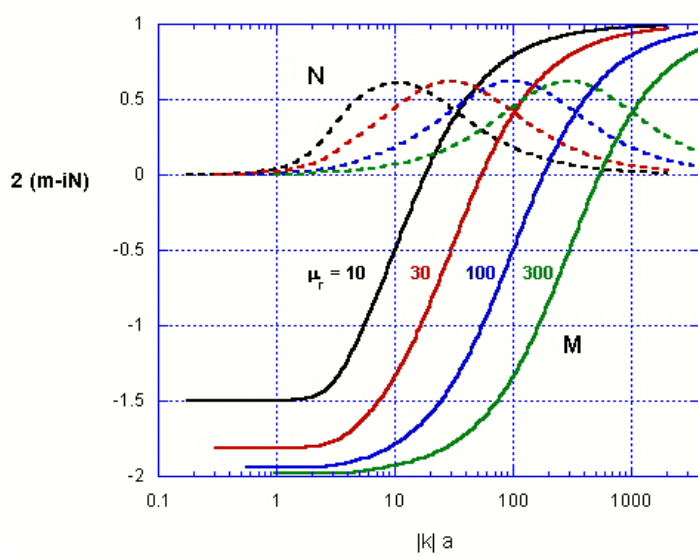


Figure 67. Inphase and quadrature components of the scattered field from a magnetic sphere.

Thus it is significant that the total fields in terms of  $\mu_r|\mathbf{H}|$  just inside and between magnetic objects in close proximity reach much higher values (Figure 68). Objects closer than those shown develop much more intense field concentrations, though that intensity seems largely confined to the region between them, limiting the effect on the scattered field at distant observation points. When the separation is increased, the intensification fades. The latter corresponds to cases with  $d > 2a$  (cf Figure 65 and Figure 66 showing far field effects).

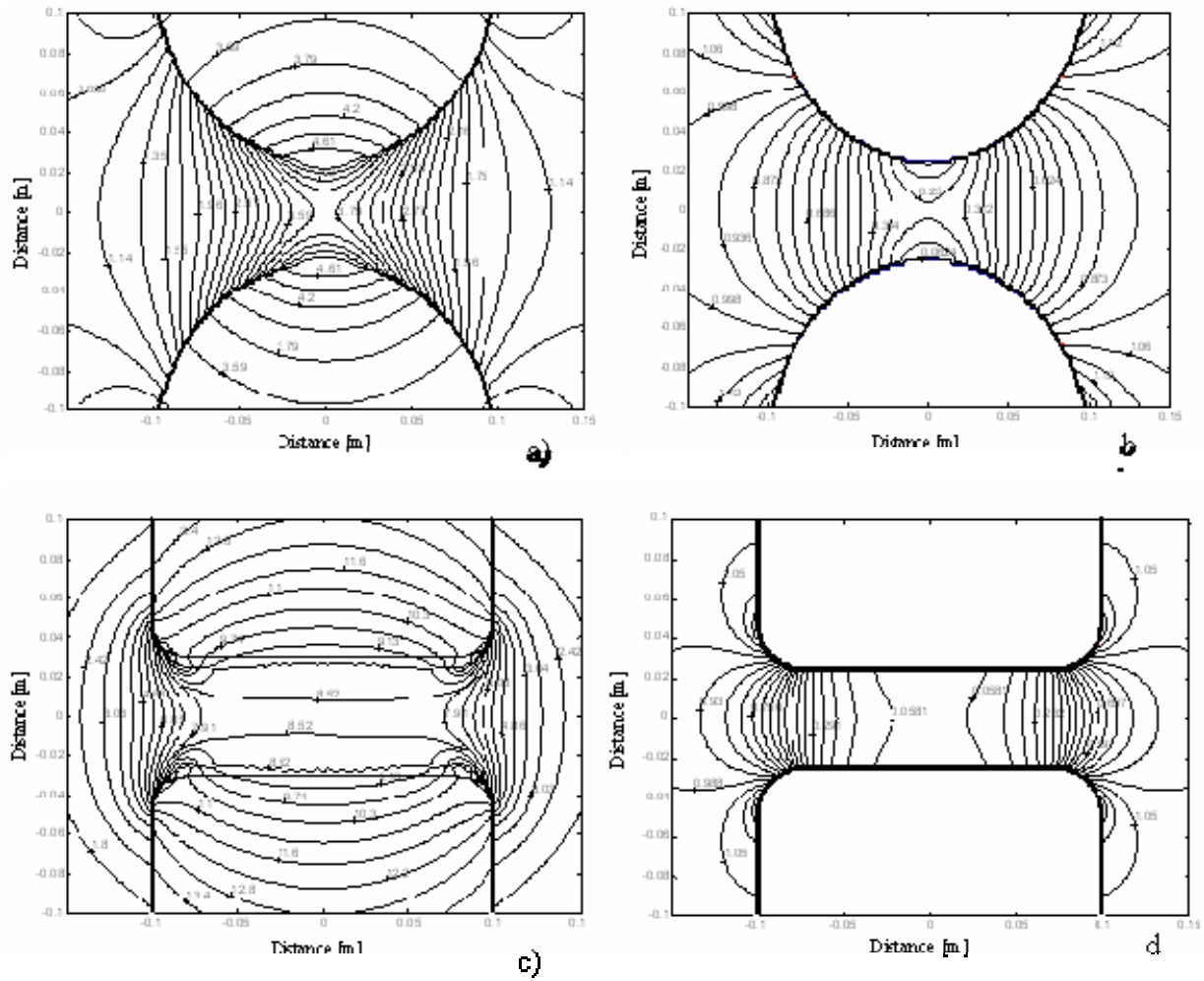


Figure 68. Near field responses  $\mu_r|\mathbf{H}|$  for  $d = a/2$ , when both objects are magnetic. Left: near low frequency limit; Right: near high frequency limit

The physical basis for the phenomena described in this section is reasonably clear. At low frequencies, *permeable* ( $\mu_r > 1$ ) scatterers magnetize, forming dipole-like structures that are aligned with the primary field. That is, in the regions near the poles of the object, the scattered field reinforces the primary field. Thus in the left column of plots in Figure 65 and Figure 66, each object increases the effective primary field on its neighbor above or below. The neighbor therefore scatters more strongly, further increasing the effective primary field on the first object, which in turn scatters more strongly, and so forth in a mutually reinforcing cycle. When the objects are quite close together this increase is quite intense and is not likely to be calculable by just iteratively treating the objects separately then attempting to correct for the interaction. In the figure above, with  $d = a/2$ , the fields between the cylinder ends and just inside those ends are about five times what they would be for the cylinder in isolation, substantially increasing the magnetic moment. Similar but less dramatic effects are evident in the low frequency permeable sphere case. This feedback loop between effective primary and secondary field will not occur if one of the bodies is non-permeable ( $\mu_r = 1$ , e.g. aluminum): Increasing the primary field upon the non-magnetic item has no effect at the lowest frequencies, because its response there is near null in any case.

At high frequencies, the scattered field at the object's poles tends to cancel the primary field, equaling it in magnitude and opposing it in direction (Lenz's Law). This occurs for both permeable and non-permeable objects, as all response is in the form of surface currents that are more or less indifferent to the body's composition. Note that between the objects in the right column of plots in Figure 68 the field is greatly diminished, relative to the background value of about unity. This makes the region between the objects similar in field values to the object interiors, where the primary field is essentially extinguished. Thus the assemblage of objects forms an overall construction resembling a single larger, elongated body, i.e. a superposition of the individual bodies. These results explain the disparate effects in seemingly similar but crucially different cases. Whether magnetic bodies of consequence will appear close enough to one another in highly contaminated sites to elicit this behavior will be case dependent. Overall, we imagine that this will not be a terribly common occurrence. Basically, objects must be very close together, relative to their diameters; and the diameters (region over which interaction takes place) must be a significant fraction of their lengths. Perhaps more consequential is the implication that multi-section UXOs with contiguous magnetic materials cannot be modeled by simply superposing the responses of the separate parts, as is done in models using multiple offset infinitesimal dipoles to represent inhomogeneous objects.



## 5. EMI SENSING IN CASES WITH DIFFUSE DISTRIBUTIONS OF SMALL CLUTTER

Here we pursue explicitly the signal behavior of a clutter environment consisting of widespread small metallic fragments. “Small” simply means that each object has dimensions significantly less than that of the overall problem geometry, including antenna height, depths of interest, and possible objects of interest. By contrast, the scatterer is assumed to be a larger scale, non-clutter body. “Widespread” means that a number of clutter items appear within the sensor's footprint at any time, and the clutter is distributed over the entire domain surveyed, though possibly only at a discrete depth. The clutter distributions are further divided into the classes of dense distributions or well-distributed assemblages, on the one hand, and sparse distributions on the other. In the former case, the items are small and widespread enough so that any surface or volume sub-region contains a statistically representative collection of them. That is, the sensor always registers the “average” behavior of the distribution from each such location. Sparse distributions produce more erratic signals, and for them the appropriate focus is on the statistics of response, drawing parallels to behavior of the well-distributed case.

Figure 69 illustrates dense distributions, showing manually randomized arrangements of spheres and small cylinders. A particular model of the GEM-3 UWB EMI sensor head that is 40 cm in diameter is shown with the sphere distribution [17]. This instrument was used for all measurements reported in this section. It operates between about 30 Hz and 50 kHz, consisting of concentric transmission and receiver coils all in the plane of the head. The electric currents in the two outer transmitting coils circulate in opposite directions. This produces a non-zero primary (transmitted) magnetic field  $H^{\text{PR}}$  at some distance from the head, while the two fields approximately cancel one another in the central cavity of the sensor head, around which is the receiver coil. The sensor responses are retained in the form of two components, one inphase with the transmitted field ("real" component) and the other in phase quadrature with the primary field ("imaginary" component). Given knowledge of the sensor coil geometry and currents, the primary field from this device is readily calculated. Figure 70 shows an example sparse clutter distribution, consisting of more diverse, widely scattered items. Referring to the marked points at 10 cm separation, one sees that the object separation is some significant fraction of the sensor head diameter.



Figure 69. Top: 40 cm diameter GEM-3 sensor head above a manually randomized dense surface distribution of steel spheres; Bottom: Similarly randomized dense distribution of short AL cylinders spread over approximately 1.2 m by 1.2 m.



Figure 70. A sparse distribution of clutter items, some collected from firing ranges, relative to 10 cm spacing of grid marks.

The question arises: should we expect a cloud of small clutter items to produce a strong enough signal to matter, relative to that from a much more massive object of interest? Other things being equal, small items will produce much smaller EMI responses. A quite approximate but still useful rule of thumb is that, at least from some reasonable range, compact objects with comparable composition subject to the same excitation will produce responses in proportion to their volume. By this standard, an item with, say, one-tenth the diameter of another would only produce  $1/1000$  as strong a response. Nevertheless, clouds of small items can still pose problems because 1) there may be many, possibly very many small items, the extreme being nearly invisible but densely distributed micro-fragmentation; and 2) clutter items may be near the surface, much closer to the sensor. EMI sensors for close interrogation, i.e. discrimination, typically transmit from wire loops which we may approximate as infinitesimal magnetic dipoles. The transmitted signal decays as  $1/R^3$ , where  $R$  is the distance from the sensor to a scatterer. Similarly, the impinging primary field induces dipole type response in the scatterer, and the scattered field also decays as  $1/R^3$  as it returns to the sensor. (We assume here and in what follows that the sensor operates in monostatic mode). Altogether, this produces the commonly used EMI  $1/R^6$  signal decay rule of thumb for dipole type sensors. This rule implies that a near-surface object one-tenth as far from the sensor as a deeper object will produce one million times the signal magnitude, other things being equal. Thus a distribution of small clutter items near the surface may

obscure a larger, deeper item of interest, even though the inherent response of each clutter item is very much smaller.

## 5.1. Overall Scenario, Assumptions, and Basic Relations

Assume that an EMI sensor resides at the origin of an  $(x,y,z)$  coordinate system, with  $z$  positive downward, into the ground (Figure 71). A clutter layer begins at  $z = h$ , which may or may not coincide with the surface of the ground. As noted above, because currents in the metallic scatterers are approximately nine orders of magnitude greater than those in the soil and only a small volume of soil is illuminated in any case, we may assume that received fields are dominated by the scatterers. That is, we assume that the ground itself is transparent to the sensor.

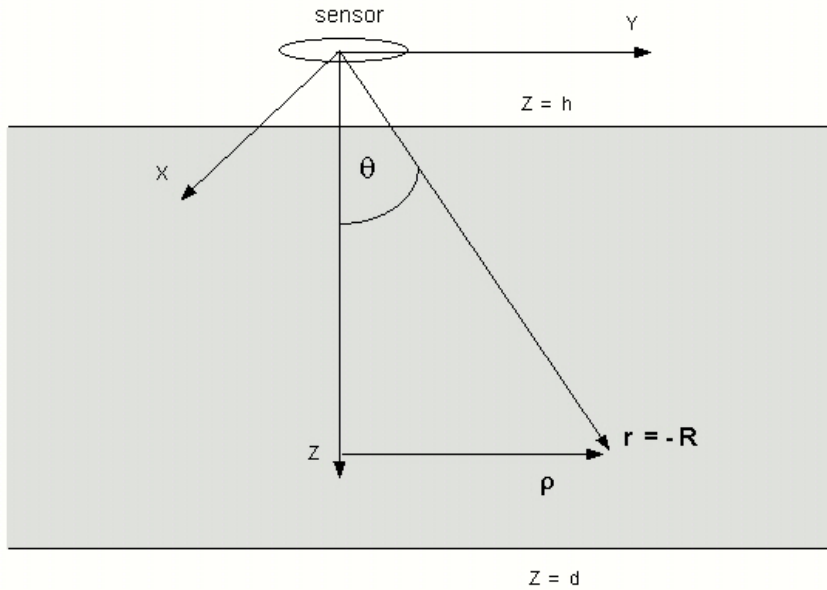


Figure 71. A sensor resides at the origin, above the ground surface. A clutter layer extends from  $z = h$  to  $z = d$ .

In terms of its scattering behavior, when each small metallic clutter object is subjected to the primary (transmitted) magnetic field  $\mathbf{H}^{\text{PR}}$  (A./m), it behaves like an anisotropic magnetic dipole with induced

magnetic dipole moment  $\mathbf{m}$  ( $\text{A m}^2$ ). For the  $i^{\text{th}}$  object located at  $\mathbf{r}_i$  with magnetic polarizability matrix  $\mathbf{M}_i$  ( $\text{m}^3$ )

$$\mathbf{m}_i = \mathbf{M}_i \cdot \mathbf{H}^{\text{ex}}(\mathbf{r}_i) \quad (74)$$

where  $\mathbf{H}^{\text{ex}}$  is the total excitation field acting on the  $i^{\text{th}}$  object. As noted in Section 2.3.1, under the infinitesimal dipole idealization the scattered magnetic field  $\mathbf{H}_i^{\text{s}}$  from the  $i^{\text{th}}$  object measured at the sensor location  $\mathbf{r}_o$  (below, the origin) is

$$\mathbf{H}_i^{\text{s}}(\mathbf{r}_o) = \frac{\mathbf{I} - 3\hat{\mathbf{R}}_{io}\hat{\mathbf{R}}_{io}}{4\pi R_{io}^3} \cdot \mathbf{M}_i \cdot \mathbf{H}_i^{\text{ex}} \quad (75)$$

where

$$\mathbf{R}_{io} = \mathbf{r}_o - \mathbf{r}_i, \quad R_{io} = |\mathbf{R}_{io}|, \quad \hat{\mathbf{R}}_{io} = \frac{\mathbf{R}_{io}}{R_{io}} \quad (76)$$

Most EMI sensors transmit from horizontal loop antennas. In that case the cylindrical  $(\rho, z, \phi)$  coordinate system is often most suitable for expressing the primary field. Also, a magnetic dipole is a good representative source for testing basic sensitivities, when the sensor loop is small relative to the scale of observation. For use in the expressions below, the expression in cylindrical coordinates for the primary field transmitted by an infinitesimal dipole antenna at the origin is

$$\mathbf{H}^{\text{PR}} = \hat{\rho} \frac{3\rho z}{4\pi R^5} + \hat{z} \frac{2z^2 - \rho^2}{4\pi R^5} \quad (77)$$

where  $R = \sqrt{\rho^2 + z^2}$  is the distance from the location of the dipole. For some very large loop transmitters, the primary field is uniform at the scale of the geometry in Figure 71 and only  $H_z^{\text{PR}}$  is present.

Based on the results in Section 4, the interaction between scattering particles will be negligible except in cases with quite dense (spatial) distributions. To cover all eventualities, the excitation field acting on the  $i^{\text{th}}$  particle is expressed as

$$\mathbf{H}_i^{\text{ex}} = \mathbf{H}^{\text{PR}}(\mathbf{r}_i) + \sum_{j \neq i} \mathbf{H}_{ji}^{\text{s}}(\mathbf{r}_i) = \mathbf{H}^{\text{PR}}(\mathbf{r}_i) + \sum_{j \neq i} \frac{\mathbf{I} - 3\hat{\mathbf{R}}_{ji}\hat{\mathbf{R}}_{ji}}{4\pi R_{ji}^3} \cdot \mathbf{M}_j \cdot \mathbf{H}_j^{\text{ex}} \quad (78)$$

where  $R_{ij}$  is the distance between the  $i^{\text{th}}$  and  $j^{\text{th}}$  particles and the summation term represents the action of surrounding particles on the  $i^{\text{th}}$  object [53]. If the primary field is uniform and fixed, then all factors in (78) remain fixed as the observation distance (sensor's  $h$ ) increases. The concomitant decline in the measured response will depend on  $h$  only through  $R$  as it appears explicitly in (75), for each  $i^{\text{th}}$  particle. For a dipole antenna, the spatially non-uniform excitation field on the  $i^{\text{th}}$  object and its neighbors declines as  $h$  increases. However the results in Section 4 reveal that the  $i^{\text{th}}$  object will only be influenced by its very nearest neighbors. Thus the distance of the sensor from the cluster consisting of particle  $i$  and its nearest neighbors is  $\sim R_{i0}$ . Both the direct excitation of the  $i^{\text{th}}$  object through

$\mathbf{H}^{\text{PR}}(\mathbf{r}_i)$  and its indirect excitation by the action of  $\mathbf{H}_j^{\text{ex}}$  on its neighbors will be essentially the same function of  $R_{i0}$ . Otherwise put, because the arrangement of the particles remains fixed as the antenna recedes, both the strength of their direct stimulation and of their interaction will fade by the same factor. Particularly because the details of the clutter items are typically unknown, we are concerned here primarily with patterns of response from the clutter, e.g. pattern of  $h$  dependency, and not on prediction of precise magnitudes at some particular observation point. For such purposes, then, we may generally proceed as if coupling were insignificant, *i.e.* as if  $\mathbf{H}_i^{\text{ex}}$  in (75) were simply  $\mathbf{H}_i^{\text{PR}}$ ; and in any case the effect of coupling can in principle be accounted for by adjustments of the effective values within  $\mathbf{M}$  without alteration of the general response patterns. That is, instead of accounting for nearest neighbors by including coupling through  $\mathbf{H}_i^{\text{ex}} = (1+\alpha)\mathbf{H}_i^{\text{PR}}$  for some  $\alpha$ , we can proceed formally by treating  $\mathbf{H}_i^{\text{ex}}$  uniformly as  $\mathbf{H}_i^{\text{PR}}$  and assuming that the (generally unknown)  $\beta_i$  is effectively  $(1+\alpha)\beta_i$ .

Subject to these understandings, the response to  $\mathbf{H}^{\text{PR}}$  from many well distributed clutter particles can be written as

$$\mathbf{H}^{\text{s}} = \int dV p(z) \frac{3\hat{\mathbf{R}}\hat{\mathbf{R}} - \mathbf{I}}{4\pi R^3} \cdot \mathbf{M}(\mathbf{r}) \cdot \mathbf{H}^{\text{PR}}(\mathbf{r}) \quad (79)$$

where  $\hat{\mathbf{R}}$  is now the vector between each  $dV$  and the observation point (origin), and the density function  $p(z)$  specifies the spatial distribution of the clutter particles as a function of depth. Two general kinds of clutter distributions will be distinguished for treatment here:

1. Well distributed, dense clutter, in which  $p(z)$  is assumed (statistically) uniform in any horizontal plane, and every  $dV$  contains a large sample of particles.  $\mathbf{M}$  is construed as a continuous function of  $\mathbf{r}$ , though its value may be a random variable, e.g. containing particle orientation distributions. The only (potentially) random variable is  $\mathbf{M}$ .
2. Sparse distributions, in which  $\mathbf{M}(\mathbf{r}) = 0$  for most  $\mathbf{r}$  and may otherwise be regarded as a delta function at some finite collection of points. Particle positions as well as their characteristics may be random variables.

The second case will be treated separately below via Monte Carlo simulations. In the analytical formulation we concentrate on the first case, considering two particle density distributions explicitly:

$$p(z) = \begin{cases} 0, & z < h \\ n_v, & d \geq z \geq h \end{cases} \text{ volume layer} \quad (80)$$

$$p(z) = n_s \delta(z - h) \text{ surface layer}$$

where  $n_v$  and  $n_s$  are the number of scatterers per unit volume or per unit surface area, respectively. Note that the statistical properties of  $\mathbf{M}$  are not a function of  $\mathbf{r}$  beyond what is specified in the density distribution  $p(z)$ . Combinations of statistically different classes of clutter items may still be treated by superposition.

## 5.2. Orientation Distributions

Under the assumptions above  $\mathbf{M}$  may be expressed as a diagonal matrix,  $\text{diag} \{\beta_1, \beta_2, \beta_3\}$  of the eigenvalues of  $\mathbf{M}$ . This implies a view aligned with the particles' principal scattering axes, which for simple shapes coincides with principal geometrical axes. This suffices for our purposes here, in that random combinations of different  $\beta_i$  will still ultimately produce dipole moments in arbitrary directions. As representative anisotropic objects, we will only consider bodies of revolution (BOR). The two

transverse eigenvalues  $\beta_2$  and  $\beta_3$  are equal, denoted hereafter  $\beta_b$ , and  $\beta_1$  equals the polarizability  $\beta_a$  along the principal axis (“axial” polarizability). The orientation of each scatterer is expressed relative to a local coordinate system  $(x_t, y_t, z_t)$  with origin at the centroid of the clutter item, where the  $z_t$  axis is aligned with the global  $z$  axis and  $x_t$  is aligned with the global cylindrical  $\rho$  axis (Figure 72). The axis of the subject scatterer points in some direction  $\hat{\mathbf{a}}$ , the orientation of which is expressed in terms of local polar and azimuthal angles and their associated unit basis vectors,  $\hat{\boldsymbol{\theta}}_t$  and  $\hat{\boldsymbol{\phi}}_t$ , respectively.

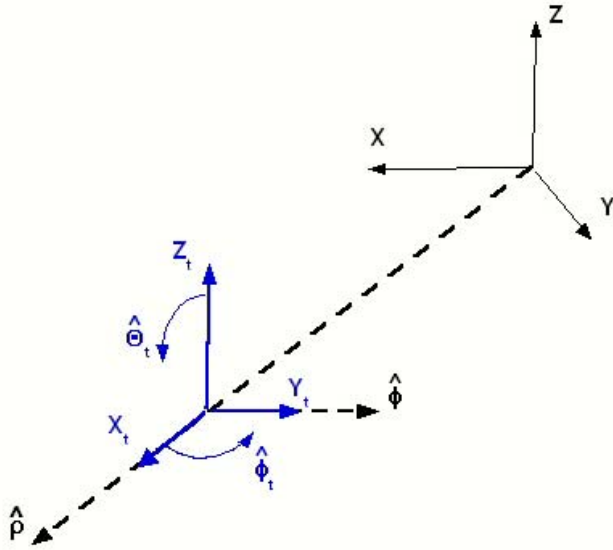


Figure 72. Local scatterer axes  $(x_t, y_t, z_t)$  and associated rotation angles, in relation to the global system.

In terms of these quantities

$$\mathbf{m} = \beta_a \hat{\mathbf{a}} H_a^{\text{PR}} + \beta_b \hat{\boldsymbol{\theta}}_t H_{\theta_t}^{\text{PR}} + \beta_b \hat{\boldsymbol{\phi}}_t H_{\phi_t}^{\text{PR}} \quad (81)$$

where local and global coordinate directions are linked by

$$\begin{aligned} \hat{\mathbf{a}} &= \hat{\mathbf{z}} \cos \theta_t + \hat{\boldsymbol{\rho}} \sin \theta_t \cos \phi_t + \hat{\boldsymbol{\phi}} \sin \theta_t \sin \phi_t \\ \hat{\boldsymbol{\theta}}_t &= \hat{\mathbf{z}} \sin(-\theta_t) + \hat{\boldsymbol{\rho}} \cos \theta_t \cos \phi_t + \hat{\boldsymbol{\phi}} \cos \theta_t \sin \phi_t \\ \hat{\boldsymbol{\phi}}_t &= \hat{\boldsymbol{\rho}} \sin(-\phi_t) + \hat{\boldsymbol{\phi}} \cos \phi_t \end{aligned} \quad (82)$$



so that

$$\begin{aligned}
H_a^{\text{PR}} &= H_z^{\text{PR}} \cos \theta_t + H_\rho^{\text{PR}} \sin \theta_t \cos \phi_t \\
H_{\theta_t}^{\text{PR}} &= H_z^{\text{PR}} \sin(-\theta_t) + H_\rho^{\text{PR}} \cos \theta_t \cos \phi_t \\
H_{\phi_t}^{\text{PR}} &= H_\rho^{\text{PR}} \sin(-\phi_t)
\end{aligned} \tag{83}$$

To preserve sign consistency between the local coordinates and the global sign of  $\mathbf{m}$ , the range of local scatterer angles is  $0 \leq \theta_t \leq \pi/2$ ,  $0 \leq \phi_t \leq 2\pi$ . This describes every possible scatterer orientation, given the symmetries of the BOR particles.

In general, the clutter items are randomly oriented according to some distribution  $P(\theta_t, \phi_t) = P_\theta(\theta_t) P_\phi(\phi_t)$ . Denoting the ensemble average of a function  $F$  as  $\langle F \rangle$

$$\langle F \rangle \equiv \int_0^{\pi/2} d\theta_t \int_0^{2\pi} d\phi_t F(\theta_t, \phi_t) P(\theta_t, \phi_t) \tag{84}$$

one obtains the average or resultant  $\mathbf{H}^s$  from (79) and the relations above simply as

$$\langle \mathbf{H}^s \rangle = \int dV p(z) \frac{3\hat{\mathbf{R}}\hat{\mathbf{R}} - \mathbf{I}}{4\pi R^3} \cdot \langle \mathbf{m} \rangle \tag{85}$$

In typical field practice only  $H_z$  is measured, for which the relations above produce

$$\begin{aligned}
\langle H_z^s \rangle &= \int dV \frac{p(z)}{4\pi R^3} \left\{ (3\cos^2 \theta - 1) \langle F_z \rangle + 3\cos \theta \sin \theta \langle F_\rho \rangle \right\} \\
&= \int_{z=h}^d dz p(z) \int_S \frac{1}{4\pi R^3} \left\{ (3\cos^2 \theta - 1) \langle F_z \rangle + 3\cos \theta \sin \theta \langle F_\rho \rangle \right\}
\end{aligned} \tag{86}$$

where

$$\begin{aligned}
F_z = & \beta_a \left[ H_z^{\text{PR}} \cos^2 \theta_t + H_\rho^{\text{PR}} \cos \theta_t \sin \theta_t \cos \phi_t \right] \\
& + \beta_b \left[ H_z^{\text{PR}} \sin^2 \theta_t - H_\rho^{\text{PR}} \cos \theta_t \sin \theta_t \cos \phi_t \right]
\end{aligned} \tag{87}$$

and

$$\begin{aligned}
F_\rho = & \beta_a \left[ H_z^{\text{PR}} \cos \theta_t \sin \theta_t \cos \phi_t + H_\rho^{\text{PR}} \sin^2 \theta_t \cos^2 \phi_t \right] \\
& + \beta_b \left[ H_z^{\text{PR}} \cos \theta_t \sin(-\theta_t) \cos \phi_t + H_\rho^{\text{PR}} \left( \cos^2 \theta_t \cos^2 \phi_t + \sin^2 \phi_t \right) \right]
\end{aligned} \tag{88}$$

Illustrative examples of  $P_\theta(\theta_t)$  and  $P_\phi(\phi_t)$  are:

$$P_\theta(\theta_t) = \left\{ \begin{array}{l} \frac{2}{\pi}, \text{ omni-directional (uniform) over polar angle} \\ \delta(\theta_t), \text{ vertical} \\ \delta(\theta_t - \pi/2), \text{ horizontal} \end{array} \right\} \tag{89}$$

and

$$P_\phi(\phi_t) = \left\{ \begin{array}{l} \frac{1}{2\pi}, \text{ uniform over azimuthal angle} \\ \frac{1}{2} \{ \delta(\phi_t) + \delta(\phi_t - \pi) \}, \text{ radial } (\hat{\rho}) \\ \frac{1}{2} \{ \delta(\phi_t + \phi) + \delta(\phi_t + \phi - \pi) \}, \text{ horizontally uni-directional } (\hat{\mathbf{x}}) \end{array} \right\} \tag{90}$$

Execution of the averaging operations in (86) based on (89) and (90) produces the following table:

Vertically and horizontally omni-directional	$\langle F_z \rangle = \frac{1}{2} [\beta_a + \beta_b] H_z^{\text{PR}}, \quad \langle F_\rho \rangle = \frac{1}{4} [\beta_a + 3\beta_b] H_\rho^{\text{PR}}$
Vertical	$\langle F_z \rangle = \beta_a H_z^{\text{PR}}, \quad \langle F_\rho \rangle = \beta_b H_\rho^{\text{PR}}$
Omni-directional within horizontal layer	$\langle F_z \rangle = \beta_b H_z^{\text{PR}}, \quad \langle F_\rho \rangle = \frac{1}{2} [\beta_a + \beta_b] H_\rho^{\text{PR}}$
Radially oriented within horizontal layer	$\langle F_z \rangle = \beta_b H_z^{\text{PR}}, \quad \langle F_\rho \rangle = \beta_a H_\rho^{\text{PR}}$
Uni-directional horizontal layer	$\langle F_z \rangle = \beta_b H_z^{\text{PR}}, \quad \langle F_\rho \rangle = [\beta_a \cos^2 \phi + \beta_b \sin^2 \phi] H_\rho^{\text{PR}}$

### 5.3. Effect of Sensor Elevation $h$

All the results in the table above imply the solution for spherical clutter particles, for which  $\beta_a = \beta_b = \beta$ :

$$\langle H_z^s \rangle = \beta \int_{z=h}^d dz p(z) \int_S dS \frac{1}{4\pi R^3} \left\{ (3\cos^2 \theta - 1) H_z^{\text{PR}} + 3\cos \theta \sin \theta H_\rho^{\text{PR}} \right\} \quad (91)$$

As pursued more specifically below, the different orientation distributions for anisotropic clutter items, as expressed through (86), simply weight the participation of  $H_z^{\text{PR}}$  and  $H_\rho^{\text{PR}}$  differently relative to their roles in (91). In particular, in each case the  $h$  dependence of the terms on the right in (86) and (91) will be the same; therefore we will study the consequences of the latter, simpler equation explicitly.

To carry out the integrations in (91) note that, over each horizontal surface  $S$ ,  $z$  is constant,  $R = z/\cos(\theta)$ , and  $dS = d\rho \rho d\phi$ , where  $\rho = z \tan(\theta)$ , and  $d\rho = z d\theta/\cos(\theta)$ . Thus the integration over  $S$  becomes an integration over  $\theta$  and  $\phi$ . If the primary fields from our loop antennas are axi-symmetric, then all the values of  $\langle F_z \rangle$  and  $\langle F_\rho \rangle$  are constant over the integration with respect to  $\phi$  except in the case of the uni-directional horizontal layer. However the latter integrates over  $\phi$  to produce the same result

as for the omni-directional horizontal layer, for which  $\langle F_z \rangle$  and  $\langle F_p \rangle$  are constant with respect to  $\phi$ . This all emphasizes what is apparent if one considers the implications of (85) directly: Clutter orientation distributions that are statistically independent of position simply imply how much different axes of the scatterers interact with each primary field component. However, even for non-uniform primary fields, *the orientation distributions do not affect the dependency of  $\langle H_z^s \rangle$  on sensor elevation, beyond a scaling factor applicable uniformly for all values of  $h$ .* Thus, as indicated above, we will investigate the basic sensitivities of  $\langle H_z^s \rangle$  to  $h$  using (91), with the understanding the results may simply be scaled for anisotropic clutter items.

Analytically, we consider below two specific types of excitation, namely a uniform primary field  $\mathbf{H}^{\text{PR}}$  ( $H_z^{\text{PR}} = 1$ ,  $H_p^{\text{PR}} = 0$ ) and a magnetic dipole excitation field (77). In practice, a small number of infinitesimal magnetic dipoles is often a good fundamental representation of the kinds of sources in existing instrumentation, provided the scatterers are a sufficient distance away (see measurement tests below).

For a uniform primary field (91) becomes

$$H_z^s = \frac{\beta}{2} \int_{z=h}^d dz p(z) \int_{\rho=0}^{\infty} \rho d\rho \frac{3 \cos(\theta) - 1}{(z / \cos(\theta))^3} \quad (92)$$

or

$$H_z^s = \frac{\beta}{2} \int_{z=h}^d dz \frac{p(z)}{z} \int_{\theta=0}^{\pi/2} d\theta \sin(\theta) (3 \cos^2(\theta) - 1) = 0 \quad (93)$$

Thus, when subjected to a uniform primary field, a distribution of particles that is perfectly uniform statistically will produce null response in a localized receiver. This is true for both of the  $p(z)$  distributions in (80); that is, it is the zero value of the integration with respect to  $\theta$ , at each  $Z$  value, that nullifies the entire integration.

This suggests that a very large excitation loop, as required for a uniform primary field, will minimize the response of widespread clutter relative to an object of interest, as long as the clutter is

well distributed at least over the footprint of the sensor. Realistically, the clutter may not be sufficiently uniform in its horizontal distribution for this result to hold, *i.e.* the integration with respect to  $\theta$  for any actual realization may produce some nonzero value, say  $V$ . Then, under a uniform primary field, the surface layer produces

$$H_z^s = V \frac{n_s \beta}{2} \frac{1}{h} \quad (94)$$

and the volume layer produces

$$H_z^s = V \frac{n_v \beta}{2} \ell n \left( \frac{d}{h} \right) \quad (95)$$

Thus when the clutter is spread entirely over a surface, any effect on the received signal will decline only in inverse proportion to the height of the antenna. When the clutter is spread over a volume layer, the signal will be inversely proportional to the log of antenna height, scaled by the depth to which the clutter is found. Equation (95) does not converge to (94) as  $d \rightarrow h$  only because, in the former, we assume that the scatterers are volumetrically distributed with  $n_v$  per unit volume, so that a layer of zero thickness contains zero scatterers. Note that the signal from the volume layer declines as the antenna is raised because, while both  $d$  and  $h$  increase,  $d/h \rightarrow 1$ . Relative to all other cases considered, this decline is very slow.

When the primary field can be approximated by that emitted by an infinitesimal magnetic dipole then, with the various geometrical relations above, all integrations can be carried out by elementary methods, yielding

$$H_z^s = \frac{11\beta}{140} \int_{z=h}^d dz \frac{p(z)}{z^4} \quad (96)$$

so that

$$\begin{aligned}
H_z^s &= \frac{11\beta n_s}{140} \frac{1}{h^4}, & \text{surface layer} \\
H_z^s &= \frac{11\beta n_v}{420} \frac{1}{h^3}, & \text{volume layer } (d \rightarrow \infty)
\end{aligned} \tag{97}$$

In these cases, as the sensor is elevated, the signal received from the clutter declines much more rapidly than for the uniform primary field, as does the signal from a larger object of interest.

Specialized for the primary field produced by a real sensor, the relations above will be tested against data from manual randomizations of the dense, relatively well-distributed clutter in Figure 69. These same clutter distributions will then be used to evaluate strategies for dealing with the screening problem, in which distributions of small clutter items may obscure an underlying larger object's signal.

#### 5.4. Tests of Basic Formulation Against Measurements

To validate (91) and its basis, measurements were made over the two dense surface clutter distributions in Figure 69 using the GEM-3 sensor. No attempt was made to estimate  $\beta$  or  $n_s$ , because these quantities only introduce a scaling factor into the results. Rather, patterns were compared by subjecting the theoretical and experimental curves to the normalization produced by matching them at a single point (usually the strongest). Similarly, comparisons to data for sensor elevation effect can be carried out using any convenient single frequency. In measurements over the clutter layer in Figure 69, as illustrated in Figure 73, except for a small amount of low amplitude, high frequency drift, the same relative magnitudes apply to all frequencies across the band.

Selecting the frequency of the quadrature component peak for the short AL cylinders and the other indicated frequencies for the other clutter layers produces the results in Figure 74. The numerical result is obtained from (91) by simple quadrature integration, using numerical expressions for the GEM-3 primary field based on the law of Bio-Savart [11]. The analytical result (straight dashed line) is obtained when the GEM-3 is modeled as an infinitesimal dipole using (97). This dipole representation of the GEM-3 is simple to apply and is reasonably accurate, on this log-log scale, for antenna elevations above about

20 or 30 cm. In general, the GEM-3 field can be represented arbitrarily accurately and very efficiently with a collection of dipoles or fictitious magnetic charges, usually modest in number. No explicit measures were taken to include orientation distribution effects for the AL cylinders; rather, as discussed above, that is accomplished by the normalization. The curve for the calculated GEM-3 response was not used for elevations less than 10 cm, because the primary field is highly non-uniform in that region, and the accuracy of the numerical model of the antenna is questionable there. The evident good agreement between theory and measurement validates the formulation leading to (91).

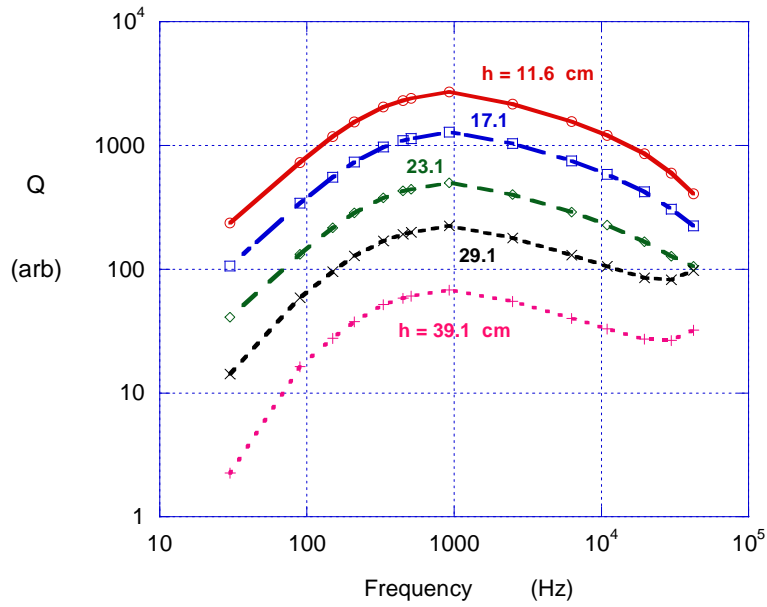


Figure 73. GEM-3 quadrature response vs frequency, for different sensor elevations over the clutter layer in Figure 69.

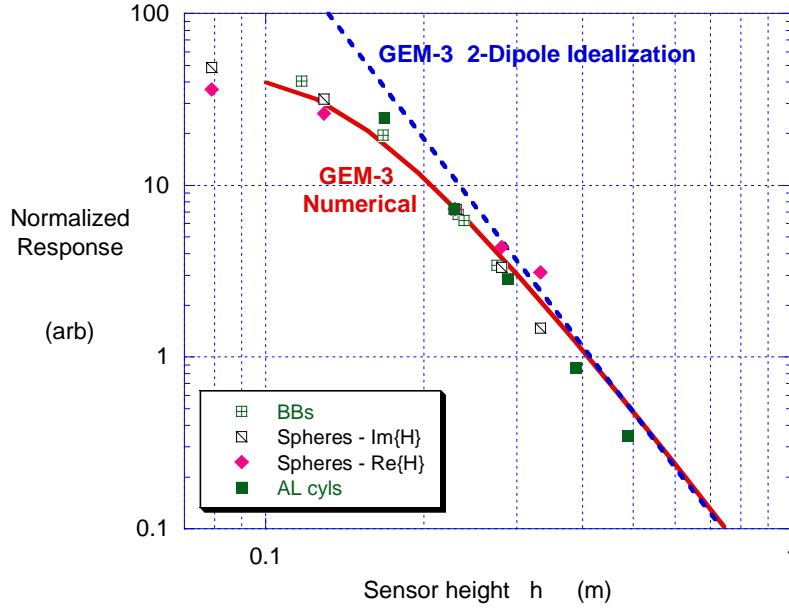


Figure 74. Markers: GEM-3 response magnitude vs antenna height above a dense surface distribution of randomly dispersed pellets, “BB’s” (30 Hz) and of the steel spheres (11 kHz) and of the AL cylinders in Figure 69 (930 Hz).

## 5.5. Layers of Finite Thickness

Equation (97) indicates that a dipole sensor signal from a half space of well-distributed clutter will decay as  $\sim 1/h^3$ . Figure 75 shows computed responses from the GEM-3 for layers of various finite thicknesses that are otherwise identical ( $\beta n_v = 1$ ). The primary field values are obtained numerically by the Bio-Savart law and in all cases are normalized by the same factor. Thus the normalization does not alter the relative magnitudes of responses to be expected from different layers. The 40 cm width of the sensor head provides some degree of spatial scale. Overall, increase in layer thickness  $t$  by a factor of 8 increases the response by about a factor of 3. With repeated doubling of  $t$ , the curves clearly converge on a limiting behavior, paralleling the  $\sim 1/h^3$  line in the mid-range values of  $h$ . The curves for smaller values of  $t$  shift to a steeper slope at higher values of  $h$ , moving in the direction of the  $\sim 1/h^4$  relation that applies to an infinitely thin (“surface”) layer. That is, from greater height the thinner layers appear more like surface distributions than the thicker ones. Overall, for the higher values of  $h$  for which we



expect dipole-like sensor behavior, the pattern for the 40 cm layer resembles that of a half space; the 5 and 10 cm layer patterns tend towards that for a surface distribution, with the 20 cm result in between.

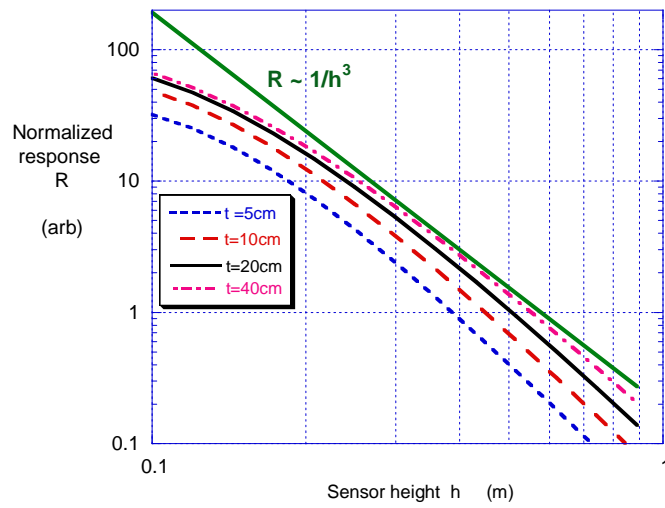


Figure 75. Calculated GEM-3 responses  $R$  from well-distributed clutter in layers of various thicknesses  $t$ , compared to a line with log-log slope of  $-3$  for  $R \sim 1/h^3$ .

## 5.6. Monte Carlo Analysis of Signal Statistics vs Sensor Elevation for Sparse Distributions

All the cases considered above involved well-distributed clutter. That is, the density of the clutter and similarity of the individual scatterers was such that essentially every horizontal sensor position received about the same response. Otherwise put: each contributing sub-domain of cluttered surface could be assumed to produce a fairly close approximation of the average behavior, and variance of the received signal across observation points at the same height is small. A more realistic, or at least more common scenario is one in which the clutter items are more various in themselves and are more sparsely distributed.

Figure 76 shows a collection of firing range clutter items, “randomly” distributed over a surface. The grid, drawn for scale, has lines 10 cm apart, and that is roughly the characteristic separation of the individual items. When the GEM-3 sensor passes over this clutter distribution at an elevation of 10 cm, pausing to record at each grid line intersection on a 7 by 7 point central segment of the grid, the signal contours in Figure 77 result. The signals are much smoother than they would be for independently random point by point variation. Data are clearly highly correlated between neighboring spatial points and between different frequency values. Despite the evident disorderliness in the visual patterns, from a processing standpoint the signals in Figure 76 are uncomfortably “target-like” and less obviously noise-like. As pointed out above (Section 2.6.2), in Bayesian-inspired processing of EMI signals, practitioners minimize objective functions containing squared error weighted by estimated signal variances. The form of the objective function assumes Gaussian *uncorrelated* noise. Because this is far from the reality, one must recognize that such formulations are at best guided by the forms that appear in Bayesian analysis, but do not really meet the statistical pre-suppositions of the theory, even approximately. This section first investigates the actual statistical character of some clutter signals. Then we proceed with Bayesian type formulations – better termed statistically weighted least squares (SWLS) – to see if these forms at least offer some frameworks that may be beneficial in actual application, even if they cannot be justified rigorously in detail.



Figure 76. Sparse clutter example used in measurements, on 10 cm grid

To assess the overall magnitude of the clutter signals and its significance, note that the maximum range of signal variation in Figure 77 is  $\sim 500$  to  $700$  ppm (in GEM-3 units). Experience shows that signals from targets of interest at some depth are very frequently less than  $1000$  ppm. Also, although the contributing items are small, their response is clearly not restricted to the higher frequencies, and in fact is worst at the lowest. This illustrates the potentially devastating on EMI signals from near surface items that are quite small relative to UXO's. Below we investigate levels of clutter signal intensity associated with different distributions of small ordnance fragments collected at firing ranges during cleanup of the former Ft Ord. Data illustrates the signal effects when mats of such clutter are placed over buried ordnance; processing shows the extent to which clear classification can still be achieved.

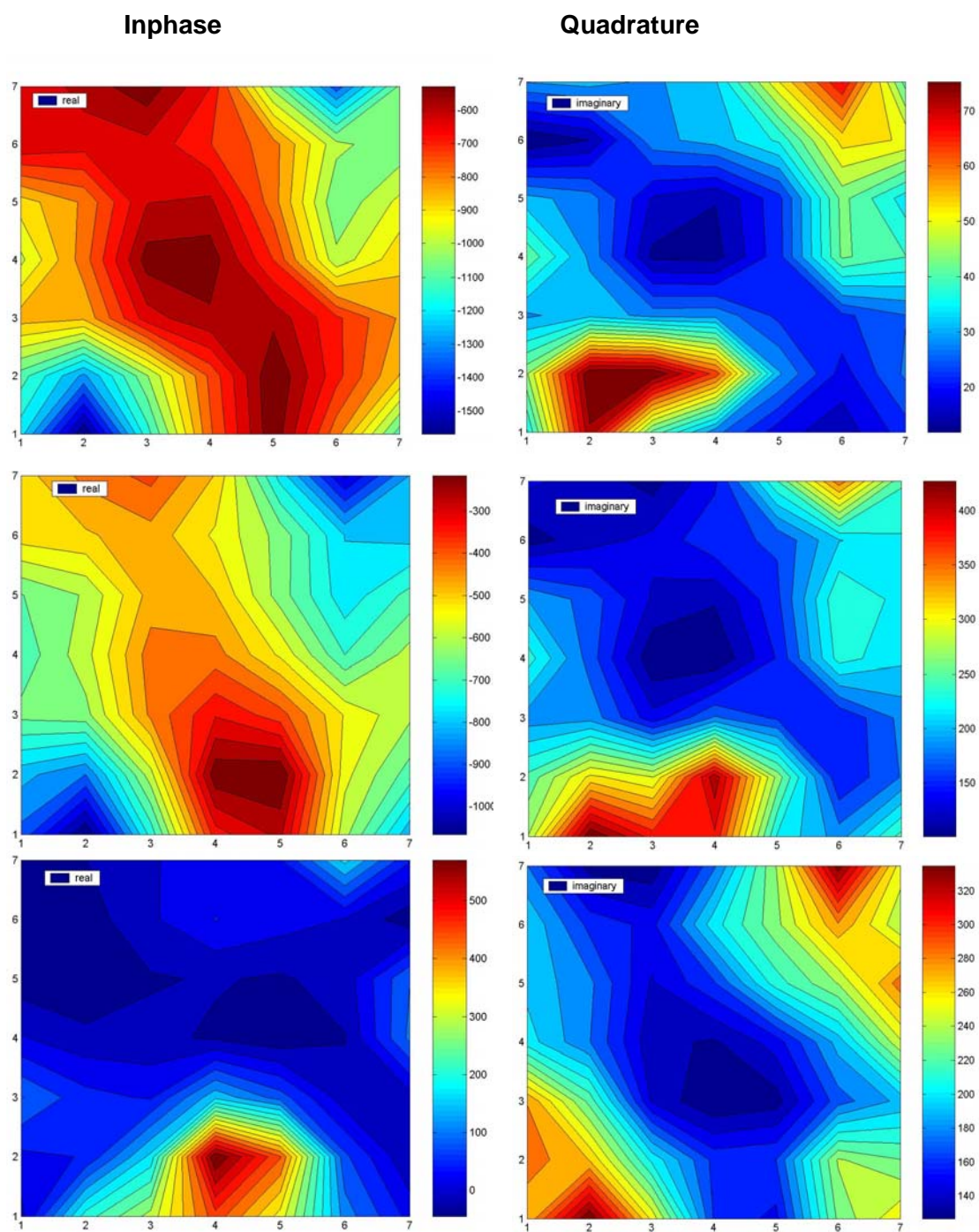


Figure 77. GEM-3 signal contours 10 cm above the sparse clutter distribution. Top: 30 Hz; Middle: 930 Hz; Bottom: 47.8 kHz.

Monte Carlo simulations constitute a way to determine the statistics of response from classes of clutter layers consisting of particles assumed to respond as tri-axial point dipoles. In the approach used here, a random number generator produces both the positions of the particles as well as their principal polarizabilities  $\beta_i$ . For the polarizabilities, a flat distribution of magnitudes between 0 and 1 is applied. For the clutter items,  $N_p$  particles are spread over  $4 \text{ m}^2$  and distributions are rejected with fewer than  $N_{\min}$  particles within the central square meter, i.e within the area directly under the observation point. Constrained by  $(N_p, N_{\min})$ , this process produces some number  $N_c$  of particles in the central square meter, differing from the ensemble average  $\langle N_c \rangle$  by  $\text{StdDev}\{N_c\}$ . The program runs 1000 cases for each sensor height and records the statistics of the received field, for both dipole and uniform primary fields. Figure 78 shows the results for the dipole primary field, where the solid line is the ensemble average of scattered  $|H_z|$ , and the dashed lines indicate one standard deviation above and below the average. As in measurements over the clutter in Figure 70, shown in a section below, at the lowest antenna position the standard deviation is on the order of 100% of the value of the average. Observations for smaller  $N_{\min}$  show that the deviation increases markedly.

Reassuringly, the height dependence of  $\langle |H_z| \rangle$  adheres reasonably closely to the  $1/h^4$  rule. Perhaps most notable for statistical processing is the relation between  $\text{StdDev}\{|H_z|\}$  and  $\langle |H_z| \rangle$ , as a function of  $h$  (Figure 79). The standard deviation declines more rapidly with  $h$  than  $\langle |H_z| \rangle$ , in particular  $\text{StdDev}\{|H_z|\} \sim 1/h^5$ . A uniform  $H^{\text{PR}}$  over the same test ensemble produces comparatively little change in  $\langle |H_z| \rangle$  as  $h$  increases (Figure 80). This is in line with the results derived analytically for the dense, well-distributed layers, i.e. (92) - (95). Those results indicate that any non-zero value should merely be the wavering residue of imperfect cancellation during the averaging, as opposed to a systematically finite value, and on average it should decline quite slowly with  $h$  (i.e.  $\sim 1/h$ ). The  $\text{StdDev}\{|H_z|\}$  for the uniform  $H^{\text{PR}}$  case also shows commensurately less change with antenna elevation. As in the dipole case, the standard deviation declines an order of magnitude more rapidly than does  $\langle |H_z| \rangle$ , i.e. roughly proportional to  $\sim 1/h^2$  for the uniform primary field as opposed to  $\sim 1/h^5$  for the dipole source (Figure 81).

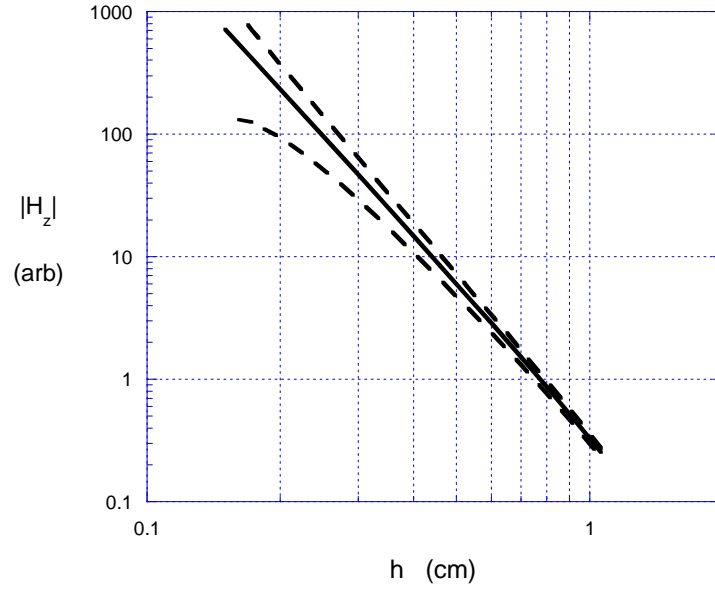


Figure 78. Simulations of response vs height from randomized 4 m<sup>2</sup> surface layers of anisotropic clutter items beneath a dipole source, with  $N_p = 100$ ,  $N_{\min} = 20$ ,  $\langle N_c \rangle = 26$  and  $\text{StdDev}\{N_c\} = 3.7$ , showing (dashed) envelope of one standard deviation about  $\langle |H_z| \rangle$ .

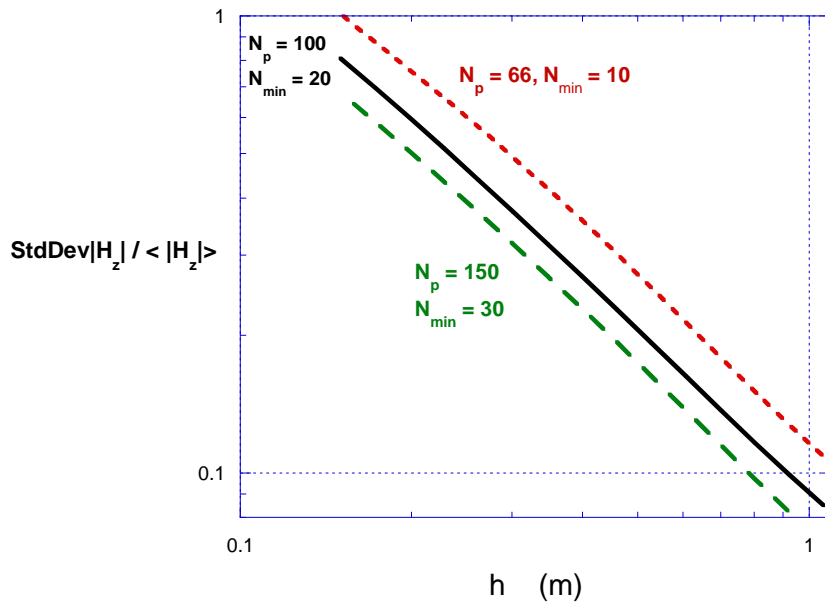


Figure 79. The percent StdDev of  $|H_z|$  is approximately proportional to  $1/h$ .

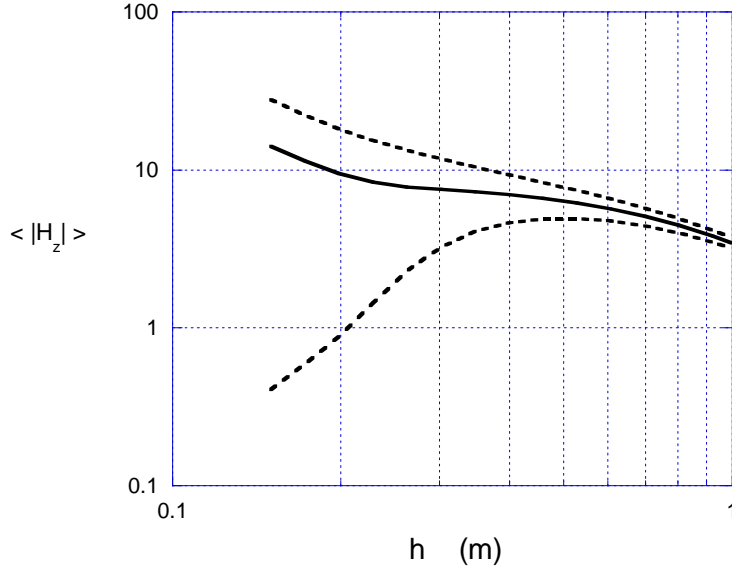


Figure 80.  $N_p = 150$ ,  $N_{\min} = 30$ ,  $\langle N_c \rangle = 37$  and std dev  $N_c = 8$

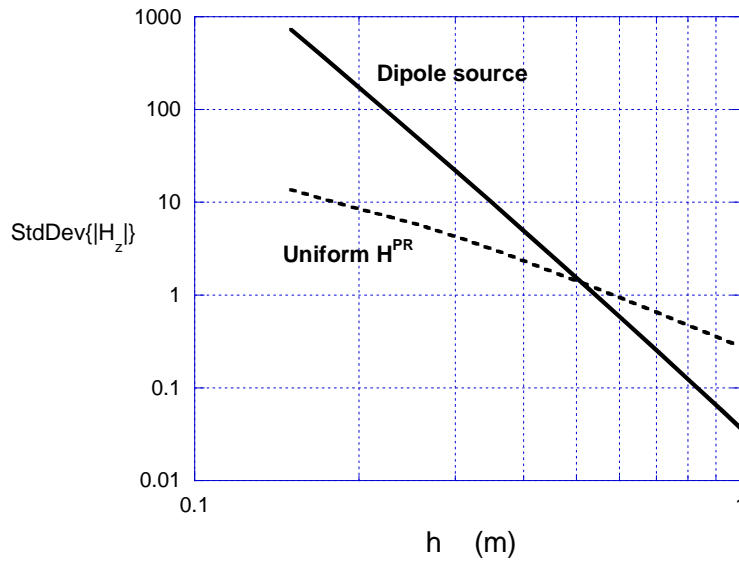


Figure 81.  $\text{StdDev}\{|H_z|\}$  for  $N_p = 150$ ,  $N_{\min} = 30$ ,  $\langle N_c \rangle = 37$  and  $\text{StdDev}\{N_c\} = 8$  as in case of Figure 80, for both dipole source and uniform excitation field.

The preceding addresses the question of how responses for individual realizations ( $\sim$  positions on the landscape) compare statistically to the ensemble (field) average. Alternatively, and perhaps more relevant to survey practice, one may query the statistics of signal behavior as a function of height over individual positions (realizations) with respect to the  $1/h^4$  power law. That is, for each realization of

particle characteristics and arrangements, how closely will the signals follow  $\sim A/h^4$  for some  $A$ , however different any one  $A$  may be from that for the ensemble average? This may furnish better guidance on the question of whether it is beneficial or not to change antenna elevation in any given instance.

Over a given realization, we only expect some close approximation of the  $A/h^4$  for sensor elevations that are great enough so that a number of particles are contributing. Therefore, for each realization in the 1000 Monte Carlo simulations, a SLS best fit  $A$  is determined for the  $A/h^4$  rule, for  $h > 50$  cm. The signals for all  $h$  values  $> 10$  cm are then compared to those predicted by the resulting local  $A/h^4$  rule. One might say that the signal fade over each realization (location) is compared to "its own"  $1/h^4$  rule, as opposed to the field average. Figure 82 shows the statistical behavior of the deviation of signals from that predicted by the "local"  $1/h^4$  rule. While here a linear log-log relation does not appear as in Figure 79, because the fit was forced for  $h > 50$  cm, still the overall patterns in the global and local statistics are similar. Based on the magnitudes in the deviations, Figure 82 is somewhat more encouraging than Figure 79, in that the variation from the ideal behavior is somewhat less: One has more reason to believe that the order of magnitude of clutter signals will fade as  $1/h^4$  relative to the predominating local values than to some field average.

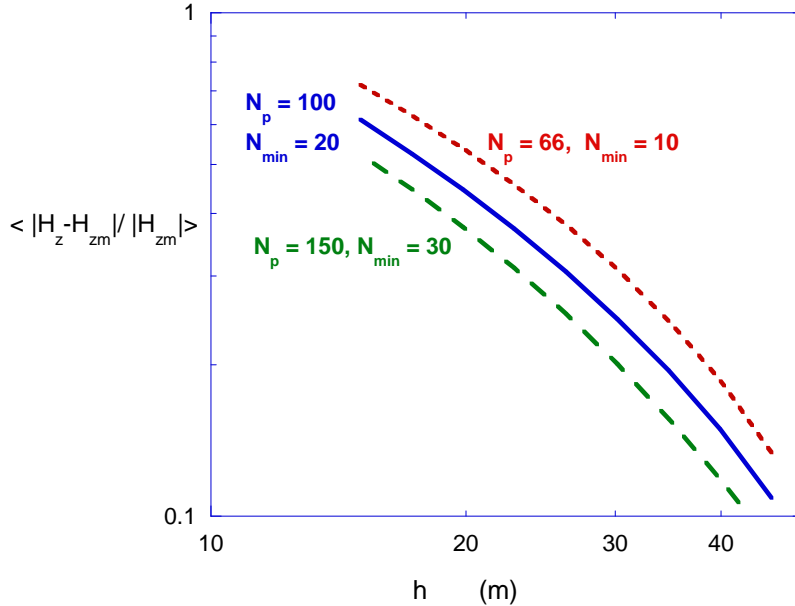


Figure 82. Average magnitude of deviation of received  $H_z$  from the locally modeled value  $H_{zm} = A/h^4$  for different clutter densities.



## 5.7. Sensor Elevation in the Screening Problem

To explore the effects on object visibility relative to smaller clutter, consider the setup shown in Figure 83 with a dipole antenna. The object is assumed to respond as a point scatterer with signal decaying as  $1/d^6$  while surface and volume layers of well-distributed clutter obey the power laws (97) above. Figure 84 shows signal strengths from both clutter and object, separately, when all responses are normalized so that they are the same at the initial antenna height (0.1 m). As the antenna is raised from 0.1 m to 1 m, the various clutter layer signals decline between about 3 and 4 orders of magnitude. How the scatterer's signal behaves relative to this is completely dependent on its depth. The shallowest object fades at about the same rate as the surface layer signal. The intermediate depth object fades in much the same way as the volume layer. However the most important observation is that the signal from the object at intermediate depth fades much less rapidly than that from the shallow surface layer, and the deepest object fades much less rapidly than either of the clutter distributions. While the fading power law ( $1/d^6$ ) for the scatterer is more severe than those for the clutter ( $1/h^3$  or  $1/h^4$ ), the smaller change in  $d$  relative to its initial value more than compensates, at least initially.

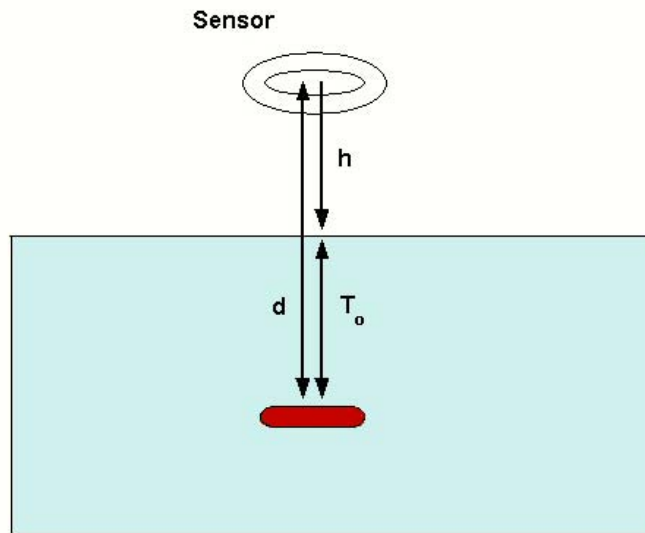


Figure 83. Setup for analysis of SCR vs sensor height, with target (red) below surface.

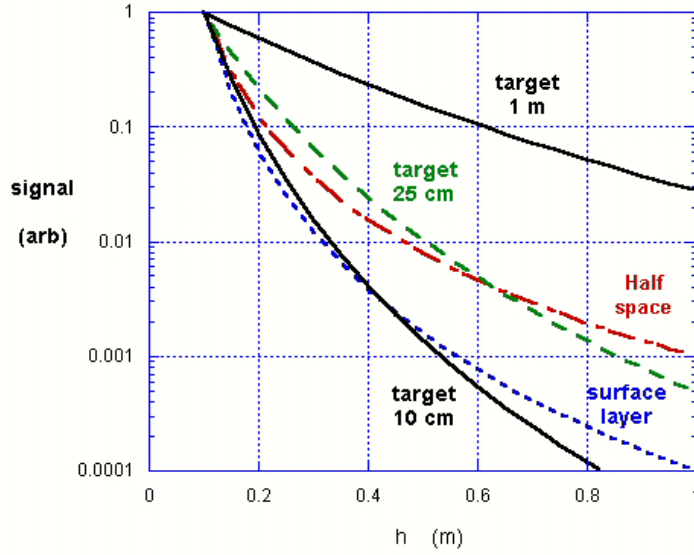


Figure 84. Received signals as a function of antenna height under a dipole primary field, for surface and half space clutter layers, and from a discrete object at indicated depths below ground surface.

These observations can be generalized using the analytical expressions above. The depth of the object below the surface is expressed as  $T_o = n h_o$  where  $h_o$  is the initial elevation of the sensor above the ground surface. As the antenna is raised, the signal  $s$  from the object declines according to

$$\frac{s}{s_o} = \left( \frac{d_o}{d} \right)^{mt} = \left( \frac{1+n}{h_r+n} \right)^{mt} \quad (98)$$

where  $h_r = h/h_o$ ,  $mt$  is 3 for the uniform primary field, and is 6 for the dipole primary field. The clutter signal  $C$  declines as the antenna is raised according to

$$\frac{C}{C_o} = \left( \frac{1}{h_r} \right)^{mc} \quad (99)$$

where  $mc$  is 1 for the uniform primary field and a surface layer of clutter; is 3 for the half space of clutter below a dipole primary field; and is 4 for the surface layer of clutter with dipole primary field. Thus the relative change in signal to clutter ratio (SCR) will be given by

$$\frac{SCR}{SCR_0} = \left( \frac{1+n}{1+n/h_r} \right)^{mt} h_r^{mc-mt} \quad (100)$$

As  $h_r$  increases, at some point the expression in brackets will cease to change significantly and the SCR will only decline indefinitely with further elevation of the sensor, in proportion to  $h_r^{mc-mt}$ . However, for the relevant range of about  $1 < h_r < 10$ , gains in SCR are often seen. Figure 85 shows how the SCR changes for different relative object depths,  $n$ . For a uniform primary field, little is accomplished by raising the antenna. For the dipole primary field, elevation helps, more so for deeper objects. Note that there will be a maximum benefit at intermediate  $h/h_0$  values for all but the shallowest object depths.

Of course, a real scatterer, sizable compared to the problem dimensions, will not behave as an ideal infinitesimal dipole at a discrete depth. To pursue this and to support the conclusions above, GEM-3 measurements were made with the antenna above the surface clutter layer in Figure 69 (top). An 18 in by 3 in steel cylinder was placed vertically with its end a few inches below the surface. Figure 86 shows the independently normalized quadrature components of the steel spheres and also of the large steel cylinder, when each is alone. This is encouraging from the point of discrimination in that they show completely contrasting trends, with that for the cylinder falling monotonically with frequency, and that for the spheres generally rising into the higher frequencies. This is the kind of relation we may often expect in the contrast between large and small object responses. Figure 87 shows the Q component magnitude measured with the steel cylinder beneath the clutter layer, for different sensor heights above the surface. The figure shows a distinct progression as the antenna is raised. At the lowest elevation ( $h_1$ ), the Q curve does not resemble the pattern for either target very closely, but is generally more similar to that for the surface clutter, which is proportionally much closer to the antenna. (Note log-log scale in Figure 87 in comparison to the semi-log scales in Figure 86). At the maximum height  $h_4$  the mix of signals has changed. In particular, as the antenna is raised the cylinder achieves stronger participation, strengthening the lower frequency portion of the curve. Thus, despite the complexity of the GEM-3 primary field and the fact that the cylinder extends over a large depth range, one sees the kinds of effects predicted on the basis of (100). Raising the antenna has produced a partial segregation of the signals from the two scatterer classes, into different regions of the spectrum.

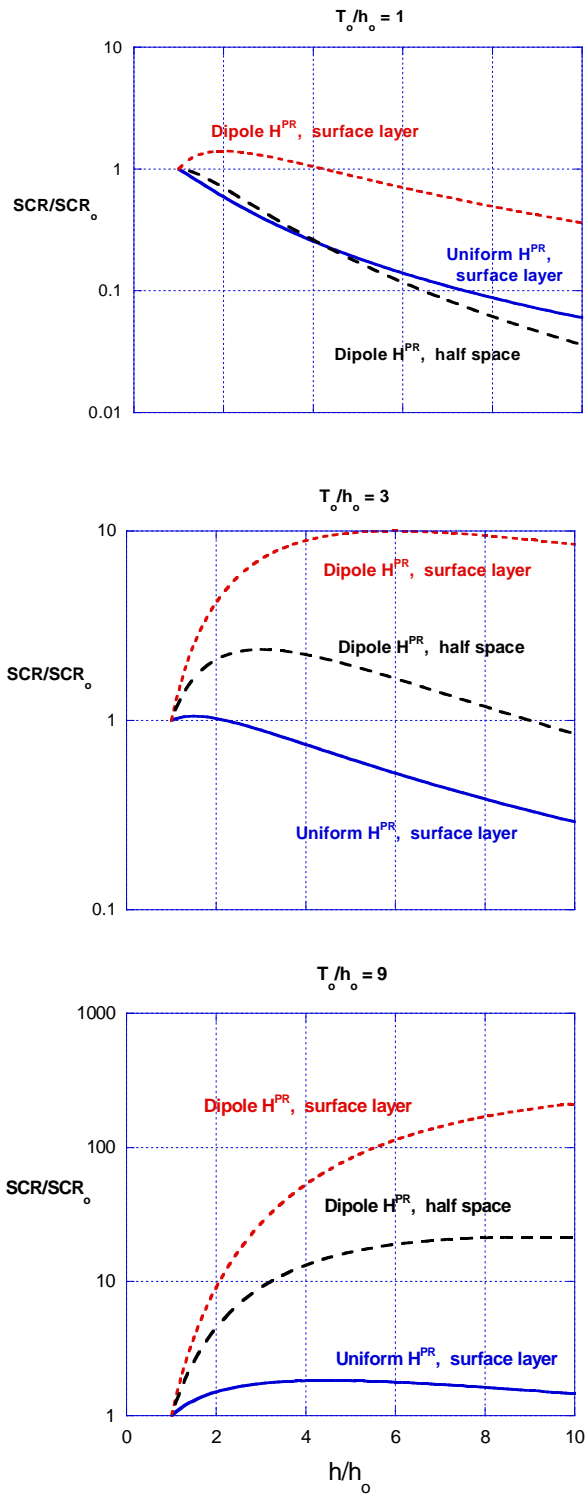


Figure 85. SCR relative to its value at the initial sensor height  $h_0$ , as a function of  $h/h_0$ .

It is important to note that Figure 87 contains results that have all been normalized relative to a single reference value, then displayed relative to a log scale in the vertical axis. The patterns would have been more vivid if signals had been normalized separately and then shown relative to the same linear scale. However the scaling in Figure 87 is used to emphasize the principal caveat attached to any strategies in which one raises a dipole type antenna, namely, the drop in absolute signal magnitude. Raising the antenna very much will reduce signals to background values, limiting the range of applicability of this approach. In Figure 87, clutter and target signals decline about 1 to 2 orders of magnitude. As indicated in Figure 74, raising the antenna some 10's of cm beyond the maximum height for the data shown in Figure 87, but still less than 1 m, would likely reduce signals to the level of background noise.

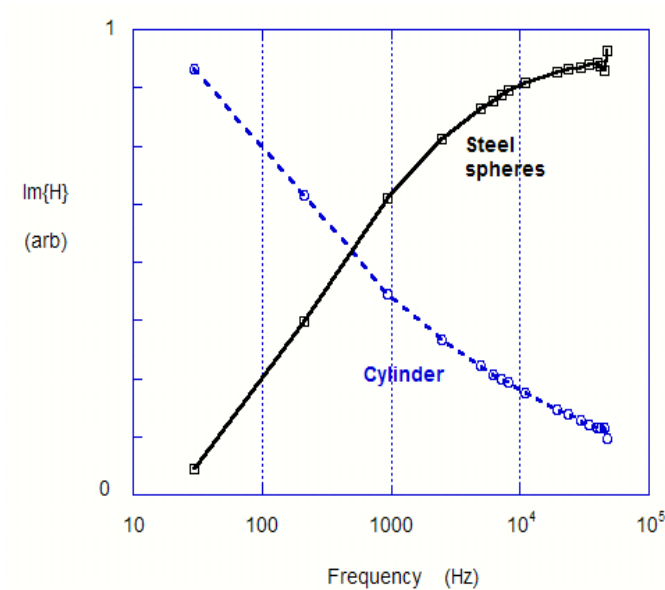


Figure 86. Independently normalized quadrature components measured with the GEM-3, for the surface layer of steel spheres and for the vertical large steel cylinder, each alone.

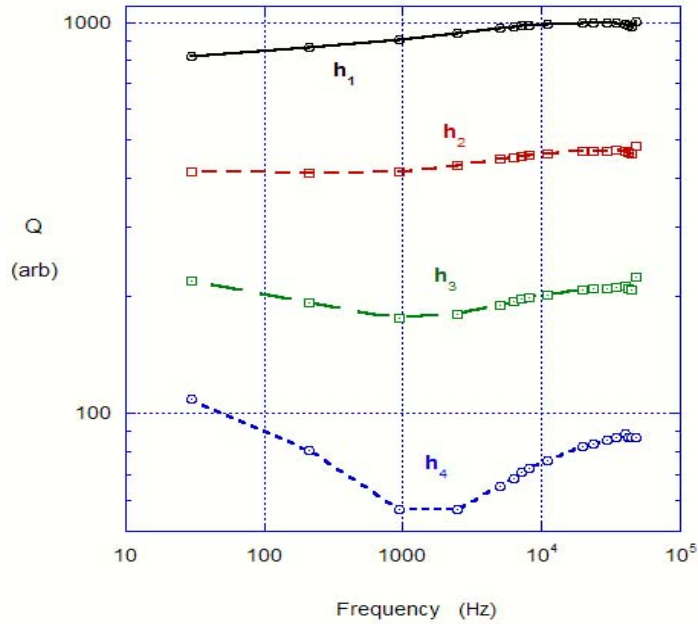


Figure 87. Response from randomized surface layer of steel spheres with the large vertical steel cylinder beneath, for successive antenna heights above the surface between  $h_1 \sim 18.3$  cm and  $h_4 \sim 33.5$  cm

## 5.8. Pattern Matching EMI Discrimination with Diffuse Clutter

The most direct approach to discrimination processing in EMI is magnetic field “pattern matching.” That is, the measured signals correspond in some way to magnetic field patterns in space and/or time and frequency, as those are apprehended by the sensor. The processing contains some kind of forward model to predict such field patterns, assuming that they are produced by any member of an inventory of possible UXO “candidates.” A sequence of optimizations is performed in which each candidate is tested for possible positions and orientations that produce the best match between the measured and modeled magnetic fields. The UXO that produces the best match is judged the most likely candidate to be present. Some absolute measure of goodness of fit is typically examined to see how good a match the best candidate achieves, and a UXO/non-UXO decision (or likelihood judgment) follows.

A crucial decision in any variant of pattern matching is what measure of goodness of fit should be employed, tantamount to what sort of objective function should be minimized during the optimization search. The next section presents some UXO discrimination tests in which simple least squares (SLS) objective functions are used to treat data in which substantial signal clutter is present from dispersed small items. This is followed by a demonstration of the inclusion of clutter statistics in the objective function, with examination of the relative benefits of doing so.

### 5.8.1. *Simple Least Squares (SLS)*

A simulation and then a measurement experiment are conducted to investigate SLS effectiveness in pattern matching when substantial dispersed clutter is present. Both assume negligible ground effects. For the simulation experiment, a data set  $\mathbf{H}^d$  is constructed containing signals from an 81 mm mortar (Target #1 in Figure 88) as well as those from a scattering of ideal dipoles. The calculations assume that the GEM-3 instrument produces the data over a grid above the UXO, and its transmitted field is modeled rigorously. The SEA produces a high-fidelity rendering of the UXO response, while the dipoles are adequate as a source of small, irregular, dispersed clutter items. The analyst assumes that any of the six UXO's in Figure 88 might be present, and tries to determine by a simple least squares best fit which object is most likely, in some disposition as determined by the optimization. With the SEA forward model available to produce the modeled fields  $\mathbf{H}^m$  for each prospective UXO, without clutter, the analyst minimizes the objective function  $\Phi$

$$\Phi = \sum_i^{N_f} \sum_j^{N_p} \left| H_j^d(f_i) - H_j^m(f_i) \right|^2 \quad (101)$$

where  $j$  indicates position on the grid and  $i$  the frequency index, superscript  $d$  indicates data and  $m$  indicates modeled quantities. Figure 89 furnishes some idea of SCR by showing spectra of the signals at each point on the 5 by 5 points measurement grid, with and without the clutter. Overall, where the UXO signal is strongest, the SCR is good; where the UXO signal is weaker, the SCR is poor. Results of the pattern matching optimization appear in Figure 89.



Figure 88. Target #1 (correct answer) and others sought by pattern matching in signals contaminated by diffuse clutter.

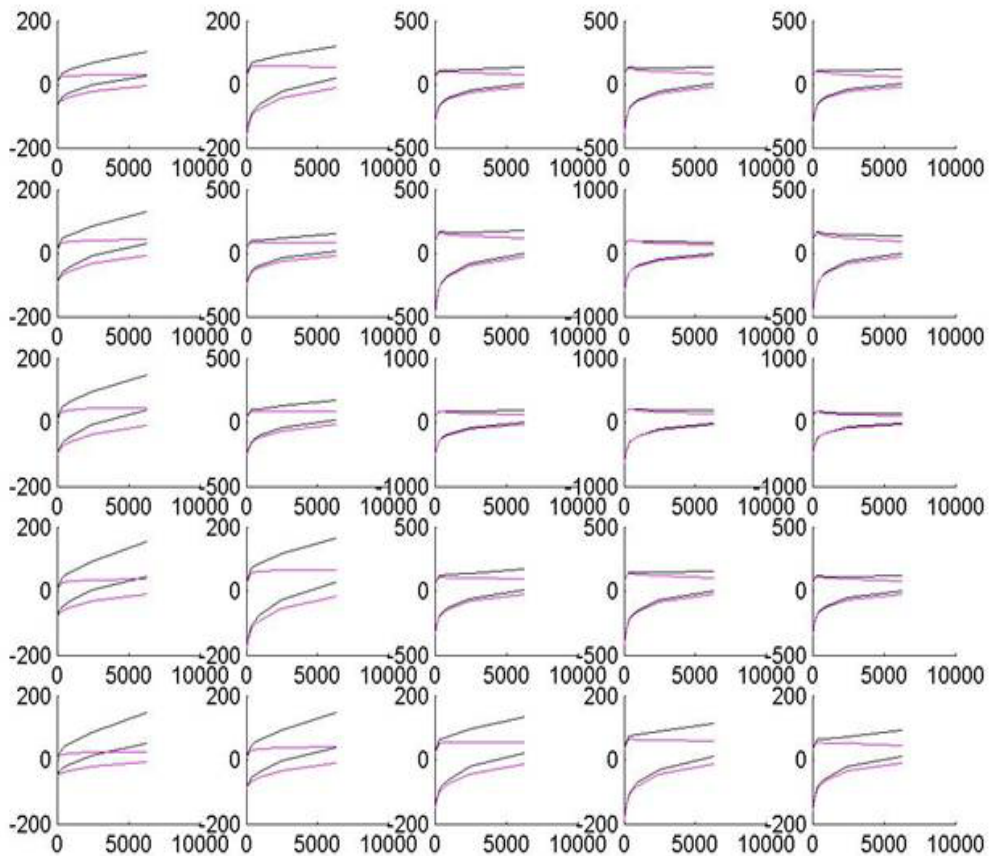


Figure 89. Simulated spectra over a 5 by 5 grid for 81 mm UXO buried in magnetic soil, with (blue) and without clutter (magenta) from a scattering of dipoles.



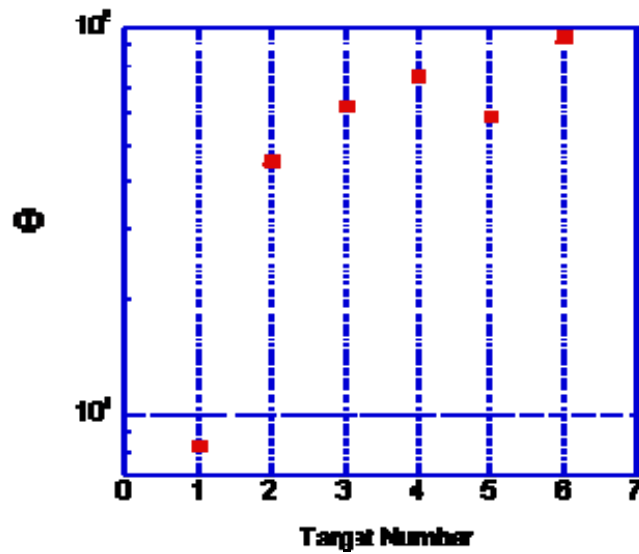


Figure 90. Residual mismatch (objective function value) at convergence when different possible targets are sought in cluttered synthetic signals. The 81 mm UXO correctly produces the lowest mismatch.

Despite a substantial SCR the method identifies correctly which UXO is present. As a parallel experiment based entirely on data, the 105 mm projectile (ATC 188 in Figure 91) is placed below the layer of clutter in Figure 76. GEM-3 data were taken over a measurement grid 10 cm above the clutter layer. The setup was such as to produce a SCR somewhat more challenging than that in the simulation test. The analyst assumed that any of the three UXO's in Figure 91 might be present, and performed competing optimizations on that basis. Results in Figure 92 show that the correct target produces the lowest mismatch. Other UXO's produce worse matches to the signal from the actual UXO plus clutter; and the correct target matches the signal with UXO plus clutter better than it matches the clutter signal alone. All this is encouraging. However it leaves open the large question of absolute degree of likelihood. The method correctly indicates what the most likely case is, but because of the noise floor produced by the clutter one cannot quantify how likely that is. Further work is needed to find systematic ways to estimate the degree of matching that optimization can produce between UXO's and pure clutter signals, under any particular circumstances. Ideally this would quantify the effects of a noise floor on the measure of goodness of fit. It would guide judgments as to when any degree of match with a UXO signal departed from this enough to warrant a judgment that the UXO was present.

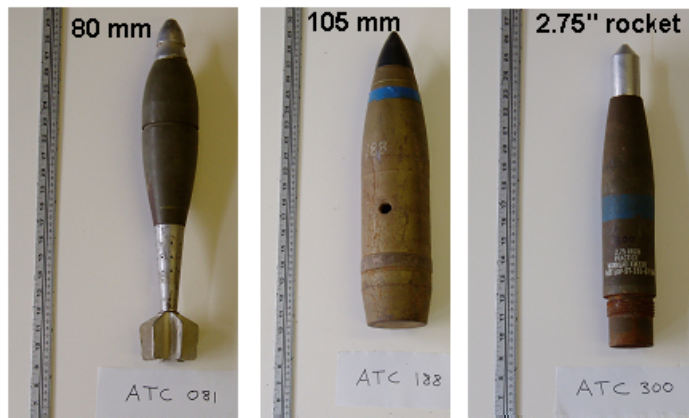


Figure 91. Three possible UXO's sought in the actual cluttered signal, using spheroidal mode based SEA to find best match with observed (scalar) magnetic fields

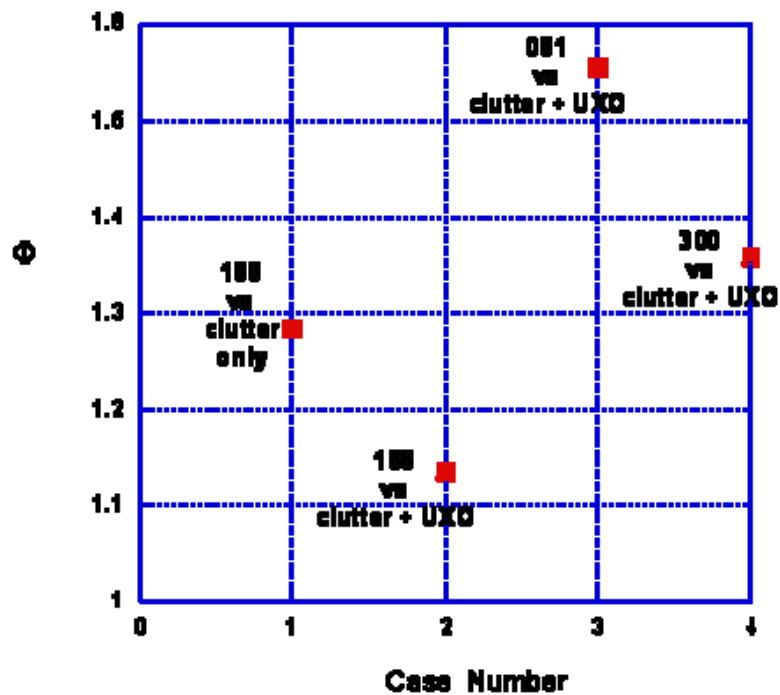


Figure 92. Correct target (188) produces the lowest mismatch with the case that includes its signal plus clutter.

### **5.8.2.                    *Statistically Weighted Least Squares (SWLS) with Limited Data***

To explore the utility of the clutter statistics in UXO discrimination, experiments were performed based on measurements over the clutter layer in Figure 70. Broadband GEM-3 data were recorded over a 5 by 5 grid of positions, with the clutter items rearranged three times for each grid. Each measurement position was typically more than 10 cm from the next nearest (see position marks in the figure), with an antenna elevation of 10 cm. Mean and standard deviation were calculated over these samples, for each of the 17 frequencies used, for both inphase and quadrature components of response (Figure 93). A target of interest is represented by a prolate spheroid. We have shown that spheroids can sometimes be used effectively to represent the EMI responses of more complicated object geometries (Section 2.3.2). Modeling a UXO as a prolate spheroid is particularly convenient because an analytical solution can easily be evaluated, at least for high permeability materials, even for realistic sensor primary fields. To match the response of a particular small UXO in either horizontal or nose up position, the spheroid here is assigned minor semi-axis  $a_0 = 3.8$  cm, major semi-axis  $b_0 = 18$  cm, electrical conductivity  $\sigma = 4 \times 10^6$  S/m, and relative magnetic permeability  $\mu_r = 287$ . It is situated with its nose at depth  $z_0$  below the clutter surface and tilted at  $45^\circ$  relative to vertical. Data for testing alternative inversion approaches at selected SCR values is obtained by assuming that the target is located at some chosen position, then superposing the recorded GEM-3 clutter signals at each  $(\mathbf{r}, f)$ , after scaling it to achieve a selected maximum SCR.

Note that the statistics shown in Figure 93 result from a number of rearrangement of the clutter items; however they are not really ensemble averages in the statistical sense presupposed in the rigorous statistical formulations (Section 2.6.2). They were obtained at each frequency by averaging over the spatial points of the three rearrangements of items considered together. If the statistics were true ensemble averages, then any one arrangement of the items analyzed would represent a particular realization amongst a great many from which collectively the averages had ultimately been obtained. The approach taken here is a convenience necessitated by a limited amount of data. As such it is closer to the reality of how one must operate with actual field data. Even if one has field data from sampling over a large region, it is likely that only the clutter sampling from a limited area near a point of concern will be statistically relevant.

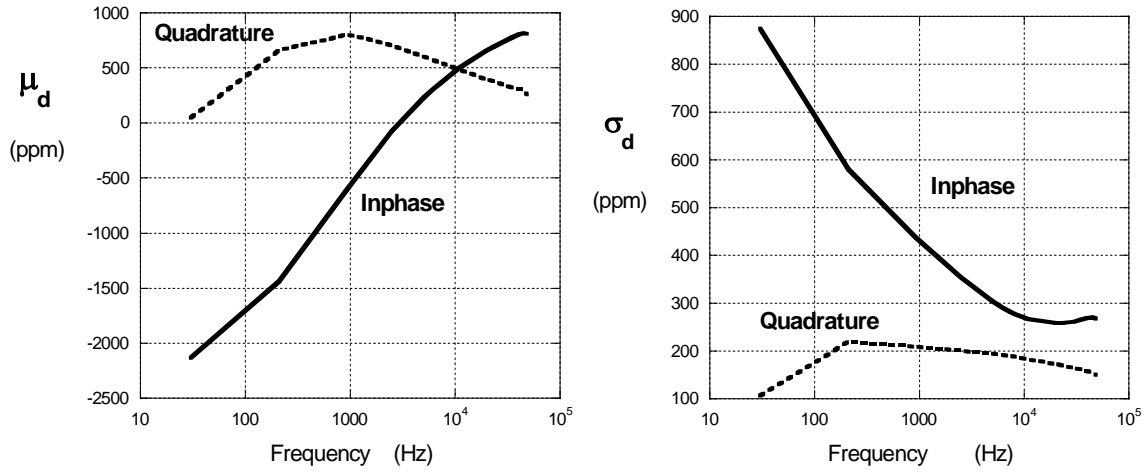


Figure 93. Mean (left) and standard deviation (right) of measurements over the clutter in Figure 70, as functions of frequency.

In the first set of test cases, the clutter and antenna are fixed and we consider the effects of different possible  $z_0$ . Using the synthesized, cluttered observations of the target from all spatial positions on the measurement grid, the SLS and SWLS systems invert the data for values of  $a$  and  $b$ . No statistical information is used in the SLS processing. In the SWLS calculations, the (frequency dependent) ensemble value of  $\sigma_d$  is used for  $\sigma_{d,i}$  at each observation point, and the ensemble  $\mu_d(f)$  is subtracted from each  $H_d$  value (see (57) and the related discussion). Here and in what follows  $\sigma_a$  and  $\sigma_b$  equal 0.5 cm and 2 cm, respectively. Figure 94 shows that, when the target is shallow and the SCR is thus at its maximum, both the SLS and SWLS approaches do well. Greater target depths decrease the SCR, in the face of which the SWLS approach produces generally more consistent and more accurate results. Alternatively, one may perform the same kind of test but keep the target at a fixed depth (20cm from the center of target to the surface clutter layer), while elevating the sensor. Here we scale  $\mu_d$  and  $\sigma_d$  according to the  $1/h_r^4$  and  $1/h_r^5$  rules, respectively, where  $h_r$  is depth relative to the initial value. The  $H_d$  values themselves are assumed to scale by  $1/h_r^4$ . Again (Figure 95), the SWLS approach produces more accurate and more stable results.

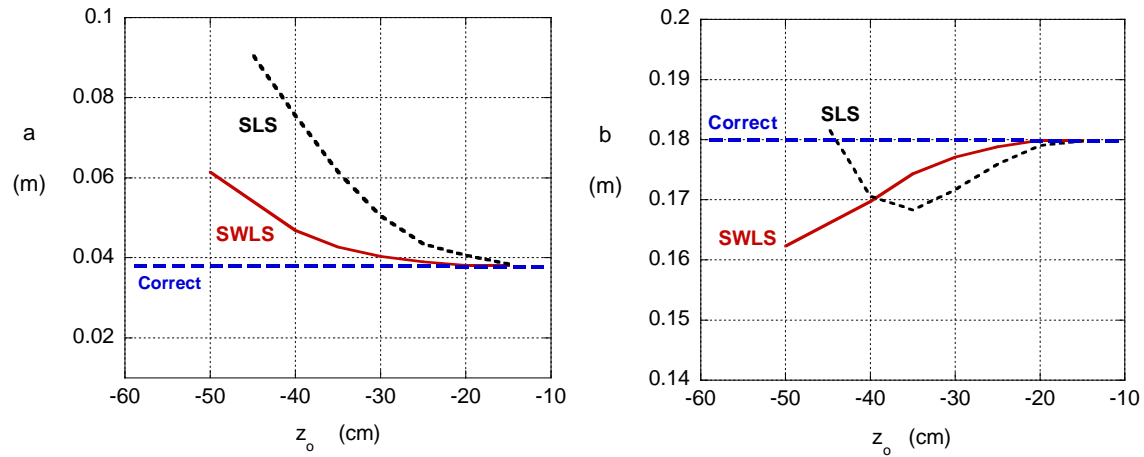


Figure 94. Values of target  $a$  and  $b$  obtained from inversion for different depths of target below the clutter, using the SLS and SWLS optimization formulations.

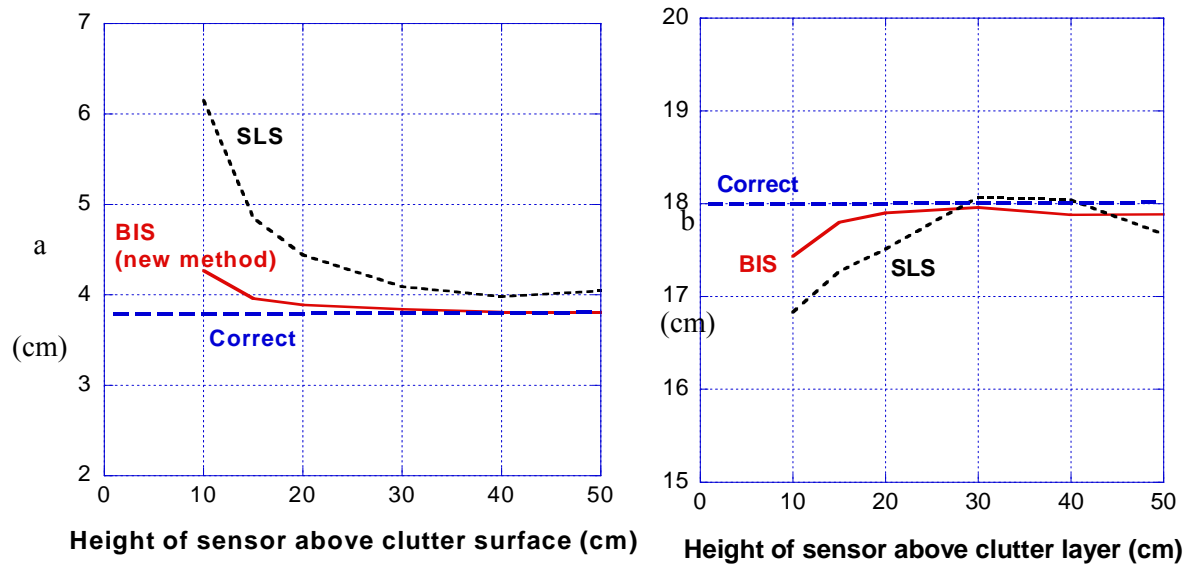


Figure 95. Performance of the Bayesian inspired system (BIS = SWLS) vs SLS for characterizing a UXO-sized object beneath the clutter in Figure 70.

To extend the testing of the Bayesian inspired SWLS vs SLS approaches beyond the clutter data provided by the treatment above, further Monte Carlo runs were performed with clutter signals generated analytically by surface assemblages of small spheroids with assigned, randomized properties, locations, and orientations. Here the 36 cm long spheroidal target was located 40 cm (to center) under the clutter layer and tilted at a  $45^\circ$  angle.  $H_d$  was obtained directly from analytical calculation of scattered fields produced by the clutter particles and target, for the GEM-3 sensor at different elevations. To generate the signal clutter, 200 small spheroids ( $a=0.005\text{m}$ ,  $b=0.03\text{m}$ ,  $\mu_r=200$ ,  $\sigma=10^7 \text{ s/m}$ ) were distributed on a 2m by 2m square area, with random location and orientation for each spheroid. One hundred random realizations of clutter distribution and orientation were calculated with several different sensor heights for each realization. For each realization data were obtained over a 5x5 grid with 10 cm (synthetic) measurement spacing, with both target and clutter present. Values of  $a$  and  $b$  were then inferred from the cluttered data. For each height, the signal mean value and standard deviation were calculated for the 100 realizations. Not surprisingly, the mean values of  $a$  and  $b$  from both SLS and SWLS approaches are accurate, when  $H_d$  is "de-meaned" and a sufficient number of realizations is considered. However, the plot for standard deviation of  $a$  and  $b$  (Figure 96) shows that the results from the SWLS approach are more stable and generally closer to the true value. For both approaches, raising the sensor reduces the standard deviation. This produces more accurate values of the parameters but in reality would likely engender signal magnitudes too faint to apprehend securely against other kinds of background noise, beyond a modest elevation above the initial 10 cm.

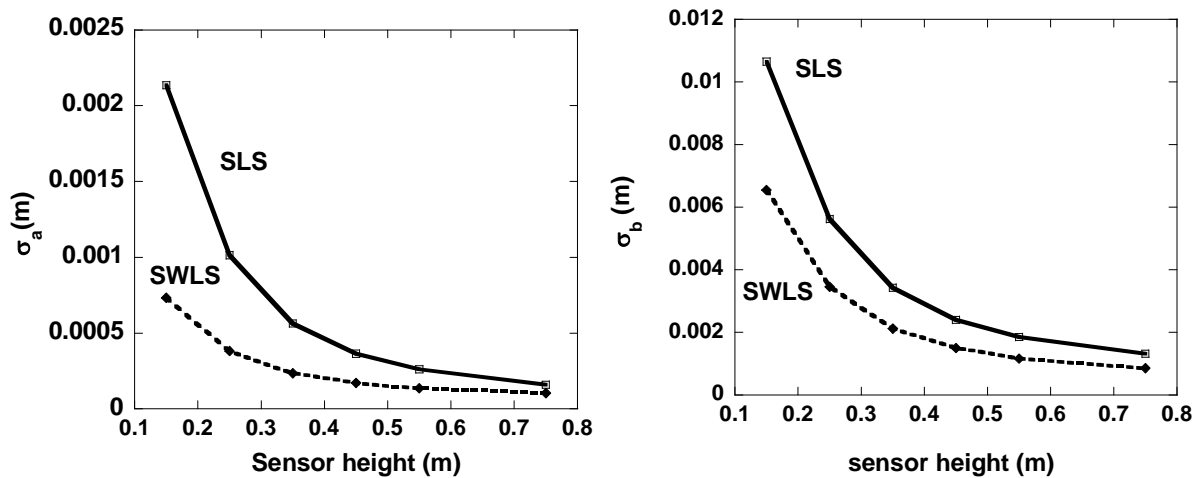


Figure 96. Standard deviation of inferred  $a$  and  $b$  from 100 random realizations

### 5.8.3. *Pattern Matching SWLS for UXO Signals in Large Ensembles with Ideal Noise*

Here we explore the potential role of clutter statistics in pattern matching optimization, for cases including diffuse clutter and signals from specific UXO's. Rigorous, detailed UXO signals are provided by SEA modeling (Section 2.4). For cases with no significant noise present, the goodness-of-fit is determined by optimizing the target disposition  $(x_0, y_0, z_0, \theta_0, \phi_0)$  to minimize  $F_{obj}$ ,

$$F_{obj}(x_0, y_0, z_0, \theta_0, \phi_0) = \frac{\sum_f \sum_j |H_m^j(f) - H_d^j(f)|^2 (w(f))^2}{\sum_f \sum_j |H_d^j(f)|^2 (w(f))^2} \quad (102)$$

where  $j$  is the spatial point index,  $f$  indicates frequency, subscripts  $m =$  modeled and  $d =$  data. The weights  $w$  are defined as

$$w(i, j) = \frac{1}{|H_d(i, j)|^{1/2} + \varepsilon} \quad (103)$$

and the “floor” for frequency domain GEM-3 data  $\varepsilon$  is 10 ppm. This weighting of the objective function is designed to restrain the influence of large amplitude data when the sensor is very close to the target, as small position errors can cause large signal excursions; and at the same time to de-emphasize weak signals near or below the noise floor from distant positions .

The benchmark case is that of a 105 mm projectile with about 25 cm below the sensor, with data obtained over a 7 by 7 point grid of measurement points with 10 cm spacing. The parameters inferred from optimization of data with no additional noise introduced are

$$\text{Target center } (x_0, y_0, z_0) = (0.1928, 0.0037, -0.2548) m$$

$$\text{Target orientation } (\theta_0, \phi_0) = (2.3429, -0.8231)$$

$$\text{Matching factor } f_{match} = 1 - F_{obj} = 0.9964$$

Those values produce the detailed picture of measured and modeled  $H_z$  shown in Figure 97. The peaked structure of the data results from the fact that the sensor was swept over lines on a grid, passing closest to the target at some point in the interior of each line. The data display in the figure lists the data points in segments of 49 spatial points, each segment corresponding either to the inphase (I) or quadrature (Q) part of the signal for one of the frequencies used. As the response changes very gradually over frequency, the exact frequencies used are not important. Suffice it to say that the ten frequencies were spaced roughly equally in log space between 30 Hz (“f<sub>1</sub>”) and some 10’s of kHz (“f<sub>10</sub>”). Clearly the model works very well. The optimization processing produces quite a good match with the data, not just overall (statistically) but point by point in weaker as well as stronger signal regions.

To introduce clutter, assume that it follows a normal distribution  $n \sim N(\mu_c, \sigma_c^2)$ . For the case with diffuse clutter distributed over the target, (102) and (103) are modified to include clutter statistics:

$$F_{\text{obj}}(x_0, y_0, z_0, \theta_0, \phi_0) = \frac{\sum_f \sum_j |H_m^j(f) - H_d^j(f) - \mu_c(f)|^2 (w(f))^2}{\sum_f \sum_j |H_d^j(f) - \mu_c(f)|^2 (w(f))^2} \quad (104)$$

with

$$w(i, j) = \frac{1}{|H_d(i, j)|^{1/2} + \sigma_c + \varepsilon} \quad \varepsilon = 10 \text{ ppm} \quad (105)$$

Rerunning the optimization over an ensemble of cases produces a comparison of results with no noise (clutter), and with clutter treated alternatively by the SLS and SWLS. Figure 98 provides a vivid picture of the case by case variation of results. Table 2 summarizes the statistics of the results. Use of different definitions of the matching factor do not allow direct comparisons of the goodness of fit between the SLS and SWLS. However overall the results show that the SWLS averages are more accurate than SLS results in that they are closer to the no-noise case parameters. The SWLS results are more stable case by case, producing smaller standard deviations. The substantial variation realization by realization illustrates the danger of comparing different approaches by viewing individual cluttered cases.



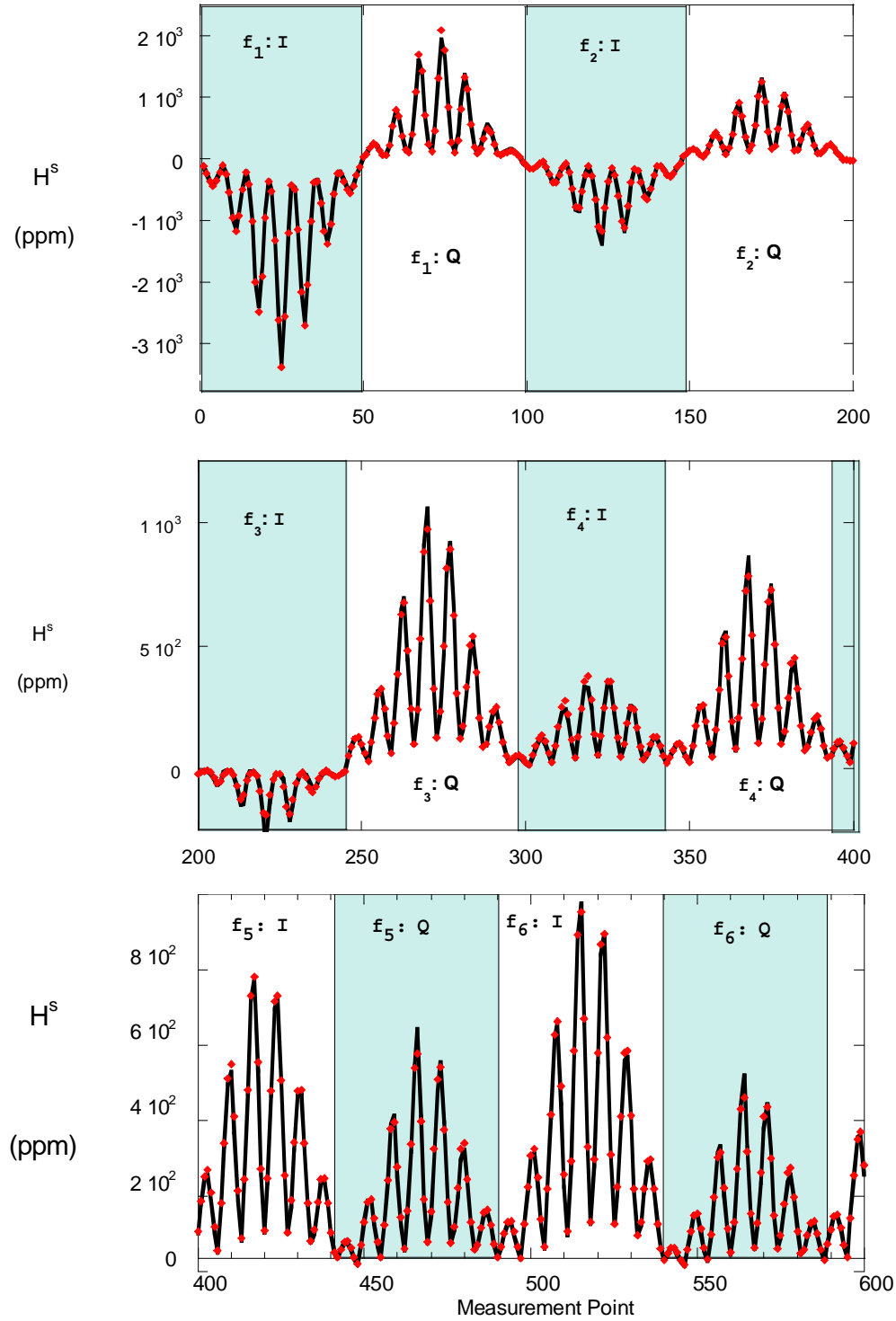


Figure 97. Comparison of SEA modeled (line) and measured response (markers) for 105 mm projectile. Each of the alternating shaded/clear panels shows either inphase (I) or quadrature response (Q) response over 49 positions, at the  $n^{\text{th}}$  frequency  $f_n$ .

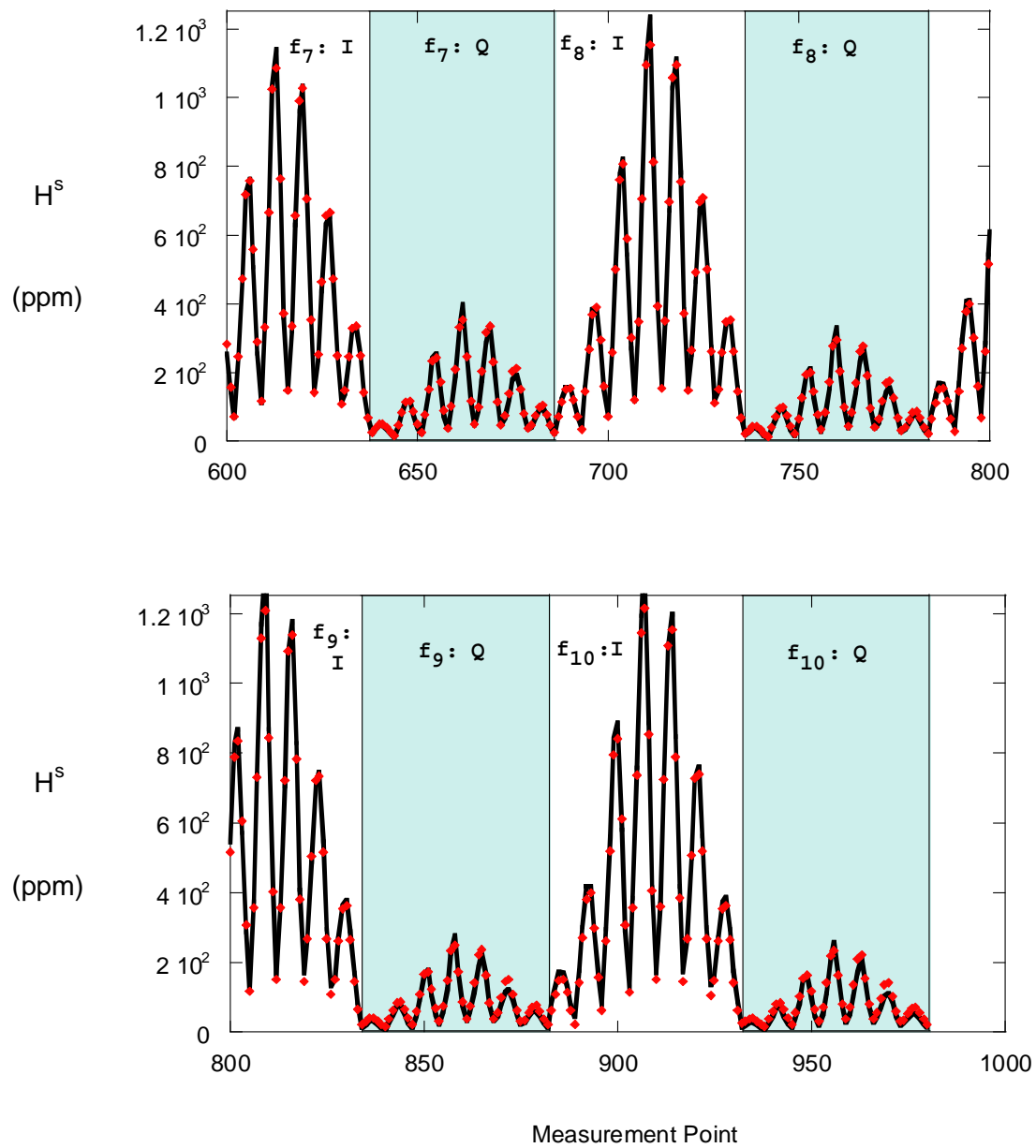


Figure 97 continued and concluded.

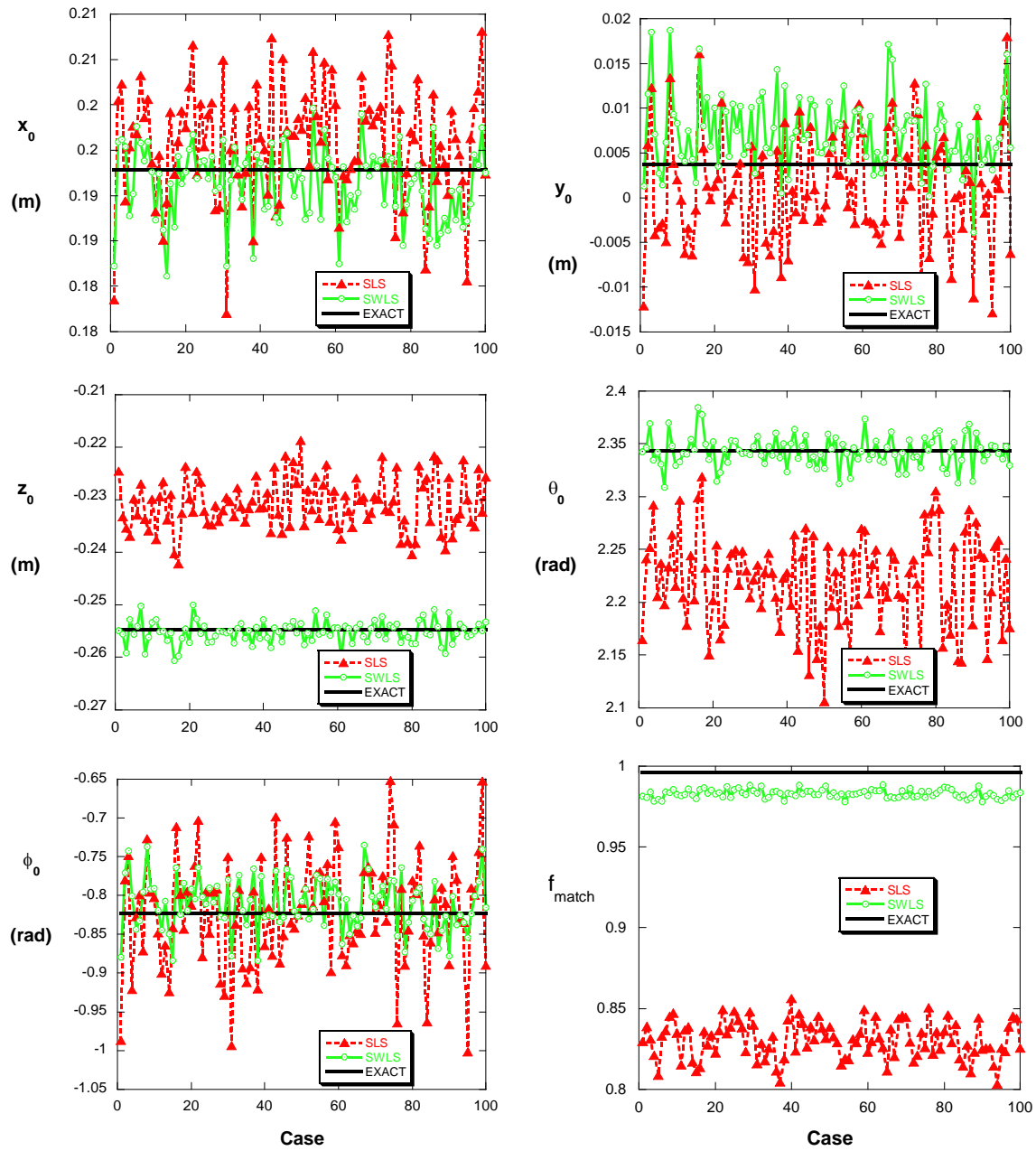


Figure 98. Variation of inferred parameters in sequence of optimization cases, comparing simple least squares (SLS) and statistically weighted least squares (SWLS) objective function performances.

Table 2. Statistics of the results of SLS, SWLS, and no noise runs for the UXO within statistically ideal signal clutter.

	Mean (SLS/SWLS)	Standard deviation(SLS/SWLS)	No clutter
$x_0$ (m)	0.1957 / 0.1914	0.0063 / 0.0041	0.1928
$y_0$ (m)	0.0008 / 0.0073	0.0063 / 0.0041	0.0037
$z_0$ (m)	-0.2309 / -0.2552	0.0050 / 0.0021	-0.2548
$\theta_0$	2.2201 / 2.3426	0.0444 / 0.0146	2.3429
$\phi_0$	-0.8214 / -0.8106	0.0710 / 0.0336	-0.8231
$f_{match}$	0.8306 / 0.9830	0.0117 / 0.0025	0.9964

## 5.9. Summary Discussion

While the specific strength and spectrum of EMI scattering from small, widely dispersed clutter items will depend on the particulars of the items and their distribution, simple power laws work well in describing the decline of received signal with antenna elevation. That pattern of decline is different from the sort produced by larger discrete objects, i.e. targets of interest such as UXO. For dense, well-distributed clutter, direct application of the power laws works quite well. For sparse, heterogeneous clutter the theory also works but in a statistical sense, on average over the measurement field. For a statistically homogeneous field, the deviation between data over an individual location and the ideal power laws declines as the sensor is elevated. Overall, raising the antenna should increase the signal to clutter ratio for all but the shallowest targets beneath a layer of clutter. Bayesian inspired statistical processing that takes advantage of these clutter statistics, including their elevation dependency, appears to be superior to simple least squares processing in discerning the properties of larger objects below a layer of clutter.

A few crucial concerns must enter into any treatment of data that attempts to exploit the results presented here. For sparse clutter, elevating the sensor causes the clutter signal variance to decrease faster than the average magnitude of the clutter signal itself. While this is desirable overall, it can serve to amplify the role of weaker signals from higher elevations when the variance is used to weight factors in the framework of statistical processing. The absolute diminution of signal strength with antenna elevation is itself a concern. EMI signals from dipole type antennas decline very rapidly with sensor elevation. The elevation at which the signal fades to the level of background clutter and system noise depends on the specific sensor and the application considered. Future tests on specific sensors will illuminate this problem.

## **6. DISCRETE CLUTTER AND UXO OBSCURATION IN EMI**

### **6.1. Phenomenology: Modeling Results**

This section investigates the setup depicted in Figure 99, in which a piece of flattened scrap lies between the UXO and the sensor. The tests alternate between considering one to be aluminum-like and the other steel-like, and then v.v. Although the simulation program can model any combination of BOR shapes under general excitation, for ease in geometrical description the objects are assumed to be aligned spheroids with the sensor directly above. The objective of the computational experiments is to investigate the extent to which the shallower object obscures the larger, deeper item.

The first point to be made is a note on physical mechanism. Both the results in Section 4 as well as close examination of simulations such as those in this section show that the shallower object does not obscure the UXO by blocking its signal in the sense that might apply in wave problems, as opposed to the potential problem at hand. Section 4 shows that no interaction of such objects is evident in the received signal even when they are much closer together than in the example here. This means that, for all practical purposes, the field transmitted by the sensor reaches the UXO virtually as if the scrap were not there; and the field coming back from the UXO “goes around” the scrap with negligible disturbance on its way back to the sensor. Variations on the configurations considered in this section and examination of the contribution of each object also reveals that no real blockage by the scrap occurs. As the diameter of the scrap is increased there is ultimately a limit to this, as that diameter becomes many times greater than the UXO and some “shadowing” of the latter occurs. However this requires scrap diameters or coverage well in excess of anything that is reasonable to consider here, if the shallower piece is truly scrap. The ultimate point is that any obscuration of the UXO occurs overwhelmingly because the magnitude of the response from the shallower object is greater, not from shadowing or signal blockage. For completeness and to remove any questions about interaction, blockage, or shadowing, the tests in this section use the full multi-object MAS formulation, including all interactions between the objects, significant or not.

The “scrap” in these tests consists of a flattened shape (oblate spheroid), 14 cm across and 3 cm thick, while the “UXO” is a prolate spheroid, 40 cm long and 10 cm in diameter (roughly the size of a 105

mm projectile). The electromagnetic properties for steel objects are  $\mu_r = 90$ ,  $\sigma = 4.0 \times 10^6$  S/m and for aluminum  $\mu_r = 1$ ,  $\sigma = 2.0 \times 10^7$  S/m. Whichever of the two objects is steel/AL, the combination of materials and objects was chosen because, other things being equal, 1) the UXO has an inherently stronger response, only moderately so when the scrap is steel, but over an order of magnitude stronger when the scrap is AL (see below); and 2) the two items have sufficiently distinct spectra so that one can tell whether one or the other predominates or whether both are in evidence.

The three sensor locations considered are  $h = 20, 53$ , and  $87$  cm (33, 66, and 100 cm above the midpoint between the two objects). In the full suite of tests (FY03 annual report, only summarized here), excitations are provided by a uniform vertical field, by a GEM-3 device, and by an infinitesimal magnetic dipole. This list of sensors proceeds from the least to the most localized. One expects a much greater excitation of the scrap relative to the UXO for the dipole transmitter than with the uniform field, with the GEM-3 somewhere in between. For this reason only the uniform field and dipole sensor results are shown here, as they bracket the sensor possibilities.

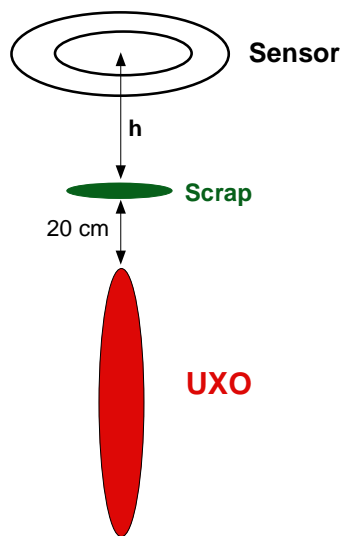


Figure 99. Model for flattened scrap above a UXO-sized target.

### 6.1.1. AL Scrap above Steel UXO

The first set of tests pursues cases in which the shallower scrap object is aluminum while the deeper UXO is assigned the steel-like material characteristics. The inherent response spectra of each item is shown in Figure 100. Interestingly, while quite dissimilar, both objects have quadrature (Q) peaks in the same very low frequency locale. This is presumably because, while the AL scrap is much smaller overall, it is roughly as wide as the UXO. One depends on the inphase (I) and its relation to the quadrature component to distinguish the responses of the two objects.

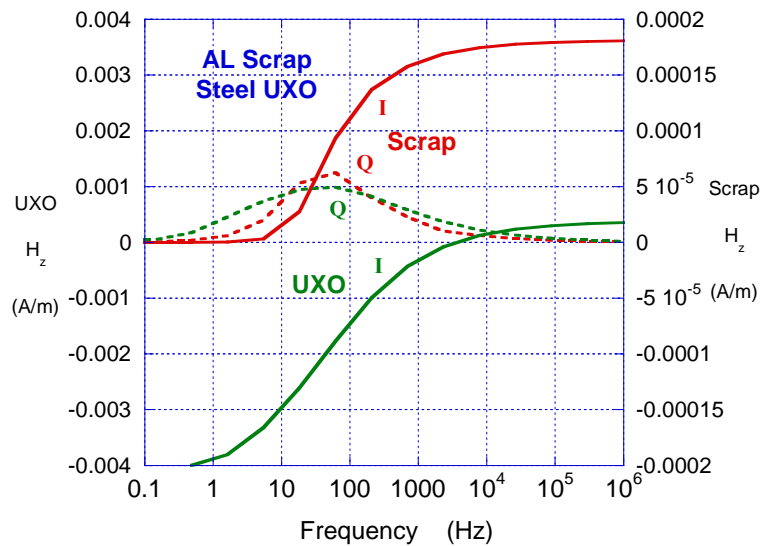


Figure 100. Response spectra for flattened AL scrap and steel UXO-like target, separately, under unit magnitude axial primary field and an observation point 1 m from the center of each target.

The figure shows that, other things being equal, the piece of scrap produces responses over an order of magnitude smaller than the UXO. However in the setup in Figure 99 things are not equal. They are particularly unequal when the transmitter is an ideal dipole (Figure 101). When the sensor is quite close to the shallower scrap ( $h = 20$  cm), the scrap dominates the combined signal virtually entirely. As the sensor is raised to  $h = 87$  cm the ratio of the different distances from the sensor to the objects diminishes and the presence of the UXO is felt more strongly. Even so, at  $h = 87$  cm the observed spectrum still does not resemble that of the UXO alone closely enough for unambiguous identification. In addition, the



magnitude of response drops by over two orders of magnitude as the sensor is raised. To gain the advantage suggested by the raised-antenna calculations, one would have to use a powerful enough transmitter to overcome SNR problems associated with the relative drop off in received signal strength.

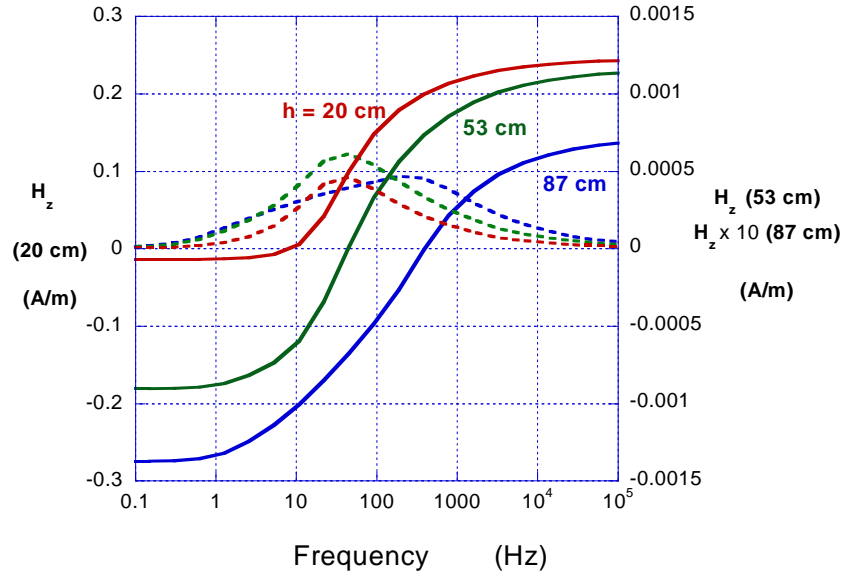


Figure 101. Signal when AL scrap is located above a steel UXO-like target, with dipole sensor at various elevations  $h$ . Solid lines are inphase component, dashed quadrature.

In the time domain, results are only significantly better in “turn on” cases, with significant sensor elevation. In typical TD EMI sensing, the sensor transmits a steady or at least slowly varying magnetic field which is then abruptly shut off, after which ( $t > 0$ ) the object’s response is recorded. By convolving the impulse responses in Figure 101 with a step down function

$$h(t) = \begin{cases} 1, & t < 0 \\ 0, & t \geq 0 \end{cases} \quad (106)$$

and inverting into the time domain, one obtains time domain equivalents to the above, for an ideal step shut off excitation (Figure 102). The picture is not encouraging: one can hardly distinguish different shapes in the time trajectories for the different cases of clutter alone vs clutter with UXO at the extremes of the standoff range.

Matters improve somewhat if one considers a time domain strategy consisting of a step up excitation instead of a step down input. That is, the primary field is manipulated to behave like

$$h(t) = \begin{cases} 0, & t < 0 \\ 1, & t \geq 0 \end{cases} \quad (107)$$

In this scenario, the abrupt increase in the primary field causes transient responses much like those for the turn off case, except that here a magnetic target's response converges to some non-zero long time value. This is lost in the turn off case, in which all object responses tend to zero over long time. The rarity of the turn on case is a result of the difficulty of recording secondary field signals while the typically much larger primary field is simultaneously present. In fact, avoidance of this problem is one of the principal motivations of the TD sensing mode overall, with its common turn-off excitation mode. Nevertheless, the turn on TD case can be engineered. Using the bucking system of the GEM-3 to produce a "cavity" at the receiver coil in both FD and TD versions of the instrument, Geophex Ltd has accomplished this, and others have apparently done similar exercises.

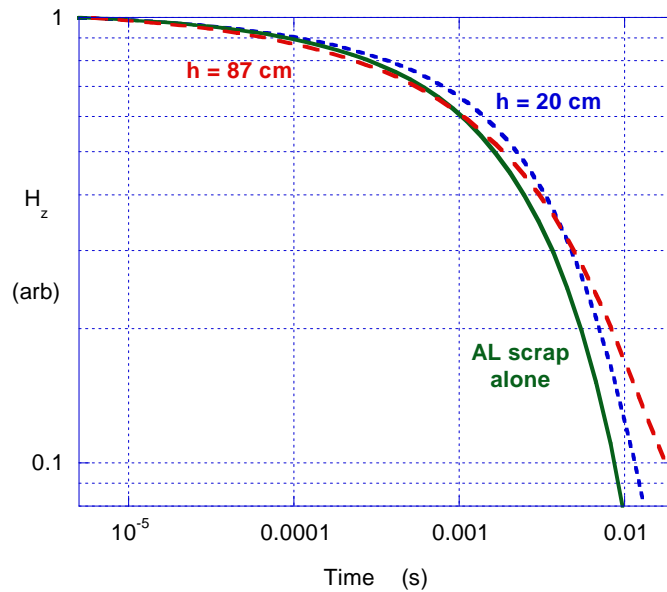


Figure 102. Normalized time domain solutions for the same case as in Figure 101, translated to the time domain for a perfect step shutoff of the primary field.

Figure 103 shows the computed turn-on case responses of the AL scrap and steel UXO when each is in isolation. While the field in and from each object is initially ( $t < 0$ ) zero, when the transmitted field is suddenly activated each object produces a jump in response, displacing its signal from zero. Initially this is negative, opposing the imposed change in the direction of the primary field's alteration (Lenz's law), after which the field in and from the object is pulled in the direction of the imposed positive change. Most notably, after declining from its initial jump, the non-permeable AL scrap maintains no long time response to a steady magnetic field while the steel does. When the AL scrap and steel UXO are present together as per Figure 99, with a dipole transmitter in turn-on TD mode, the trajectories in Figure 104 are obtained. As long as the antenna is sufficiently elevated ( $h$  significantly greater than 20 cm), the UXO time history stands out from that of the scrap over a good range of recordable time ( $t < 10$  ms). Again, at this elevation for a concentrated sensor, SNR issues may arise.

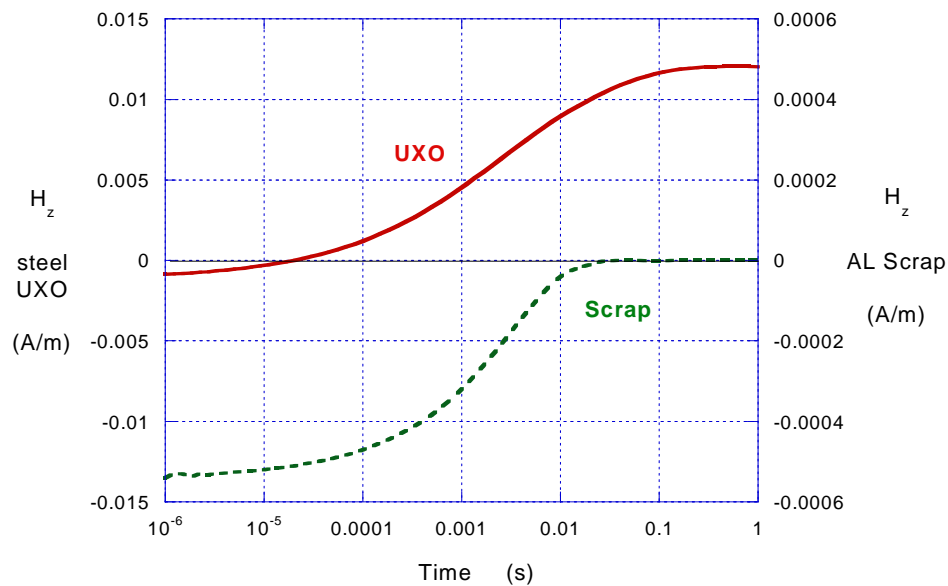


Figure 103. Steel UXO and AL scrap, each responding alone in the TD to sudden turn on of a uniform primary magnetic field at time = 0, observed from 1 m away.

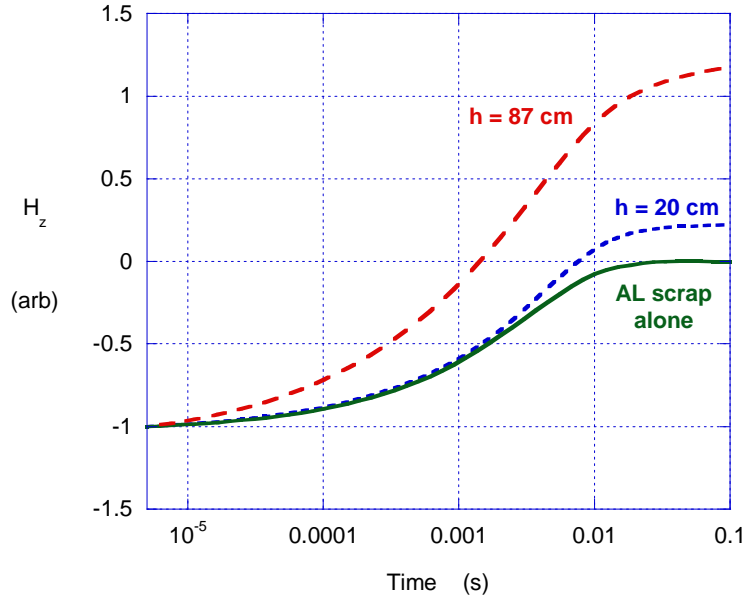


Figure 104. Same as in Figure 102, but for a perfect step turn-on of the primary field (dipole source), with curves normalized to the same initial magnitude.

The picture also improves if one considers a uniform primary field. While this is rare in EMI sensing above the static limit (magnetometry), systems exist that approximate this very well. Even short of the virtually completely uniform primary field applied in that system, any system with a transmitter loop that is large relative to the standoff from the target approximates this to some degree. The uniform field thus represents a limiting case in this direction, relative to the infinitely concentrated ideal dipole treated above.

Figure 105 shows results obtained for the same configuration considered above, i.e. Figure 99 with AL scrap and steel UXO, but under a uniform vertical primary field. Note that the left vertical axis pertains to the  $h = 20$  cm case, while the right vertical axis pertains to the other two. Response for the lowest  $h$  is ambiguous in that it is a blend of the two spectra, looking like neither that of an AL target (of any shape) or an elongated vertical steel object. (It does resemble that of either a transverse elongated steel object or a compact i.e.  $\sim$  equi-dimensional steel object. See e.g. [2] for basic spectral sensitivity studies relative to shape and material composition). By the intermediate antenna elevation the pattern shows strong indication of vertical elongated steel, in particular crossing of inphase and quadrature components, at low magnitude, far out into the frequency range. By the highest  $h$  the UXO pattern is clearly dominant. As the signal magnitude only declines about 1 to 2 orders of magnitude over this

increase in  $h$ , one may speculate that profitable analysis of the more distant observations may still be possible, under a uniform primary field.

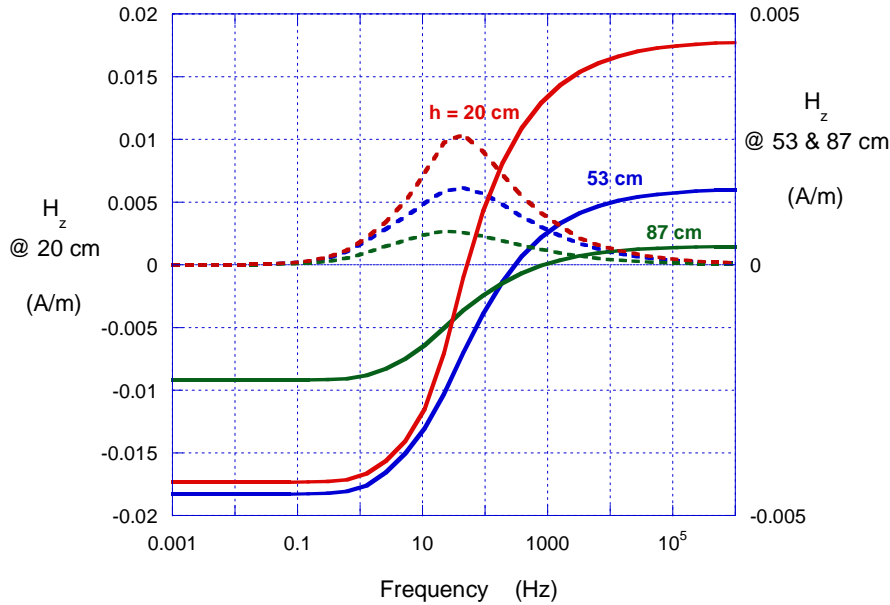


Figure 105. Response from AL oblate scrap over steel UXO, under uniform primary field, observed at various elevations  $h$ . Solid lines are inphase component, dashed quadrature.

In the time domain, advantages are obtained comparable to those between Figure 105 and Figure 101 in the frequency domain. Figure 106 shows the normalized signal histories computed for the AL scrap and steel UXO, subjected to a uniform primary field that is suddenly turned off. The objects are considered alone and in combination as per Figure 99. Other things being equal, i.e. with the signals scaled to begin at the same magnitude, one sees the difference in response caused by the presence of the UXO after about 1 ms, more so if the sensor is more elevated. An instrument would have to record up until some time near or beyond 10 ms for the clearest evidence of difference in pattern, and would have to approximate the 87 cm elevation to isolate the UXO signal in late time. This could be a challenge for many existing TD sensing systems, either by their design or because of SNR problems in late time that are difficult to avoid. Note that the difference in normalization required to equalize the signals from  $h$  at 20 cm and 87 cm is a factor of 13. This is not so bad. That is, under a uniform primary field one could gain clearer evidence of the UXO by raising the receiving antenna, with only about an order of magnitude

fade in overall signal magnitude. Figure 107 shows TD results for the turn on case under uniform primary field, again plotted in semi-log form because of the change in sign of the signal. The difference in scale relative to the log-log plots for the shutoff cases makes the turn on cases a bit difficult to compare. Nevertheless, relative to Figure 104 for the dipole case turn-on case, Figure 107 for the uniform field turn-on case shows distinct advantages from the more uniform excitation. Distinct evidence of the UXO appears after only  $\sim 1$  ms, at  $h$  only raised to 20 cm.

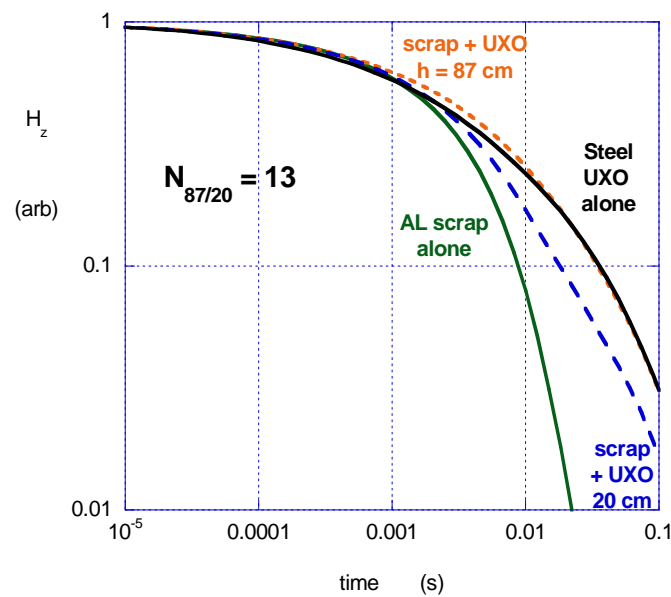


Figure 106. Normalized TD responses for oblate AL scrap and steel UXO, under a uniform primary field, each observed alone from a large distance or in combination at various elevations  $h$  above the scrap.

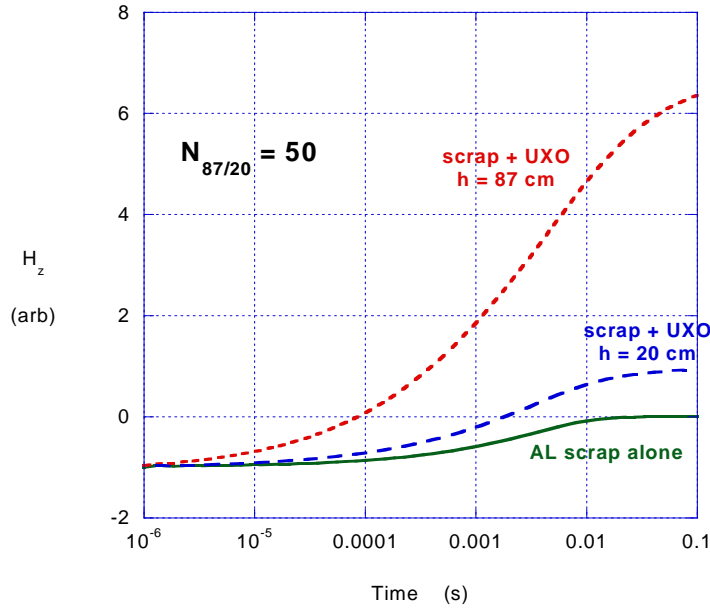


Figure 107. Turn on case for flattened AL scrap over steel UXO under uniform primary field, with all responses normalized to be the same magnitude at earliest time.

### 6.1.2. *Steel Scrap above AL UXO*

To see the effects of a “role reversal” of the two sets of material properties used above, consider the same setup as shown in Figure 99, with the same shapes and dimensions but with steel scrap above an AL UXO-like object. While steel scrap is common, a non-ferrous UXO is much less so. In any case, non-magnetic UXO’s do exist; and similar results might be observed for a UXO with a large AL tail, such as an 81 mm mortar, oriented vertical nose down and located below the scrap. Figure 108 shows the applicable response spectra for the steel scrap and AL UXO in isolation. Figure 109 shows the spectral response when a uniform vertical primary field is applied to the setup in Figure 99, as the sensor (receiver) moves through various elevations  $h$  relative to the upper surface of the scrap. Again, the observation position is directly above the aligned objects.

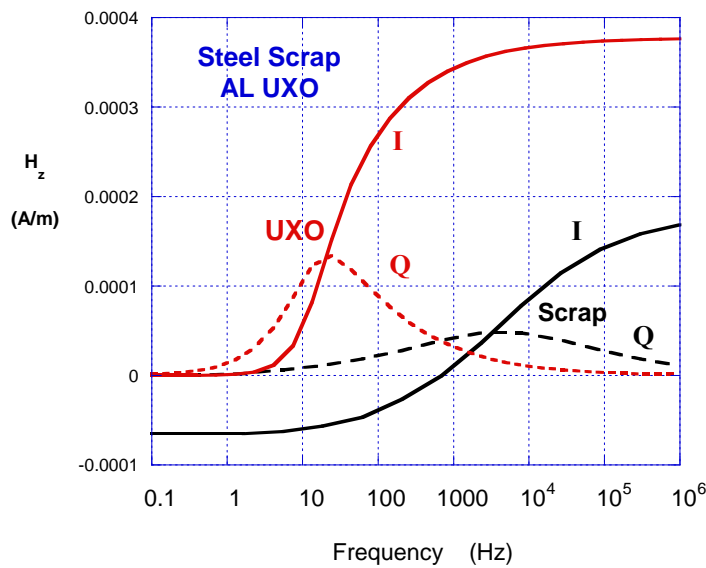


Figure 108. Reference response spectra of oblate steel scrap and an AL "UXO" alone, for a uniform, unit magnitude axial primary field and an observation point 1 m from the center of each target.

At the lowest elevation the spectrum looks very much like that of the scrap alone. Based on a knowledge of the spectrum of the UXO and an examination of this combined signal, one would not be inspired to look further for the deeper UXO. At the intermediate elevation some indication of the underlying UXO begins to emerge, both in terms of relation of the I and Q components to one another and in the existence of a lower frequency bump in the Q component. At the highest  $h$  we see clearly a bi-modal response, with a strong, if not dominant part of the Q component due to the UXO. This serves to emphasize the potential benefits of changing the sensor elevation. At the same time, note that signals in the more revealing pattern at  $h = 87$  cm are about two orders of magnitude weaker than that from close observation ( $h = 20$  cm). As we shall see below, this effect is considerably worse for more localized, dipole type EMI sensors.



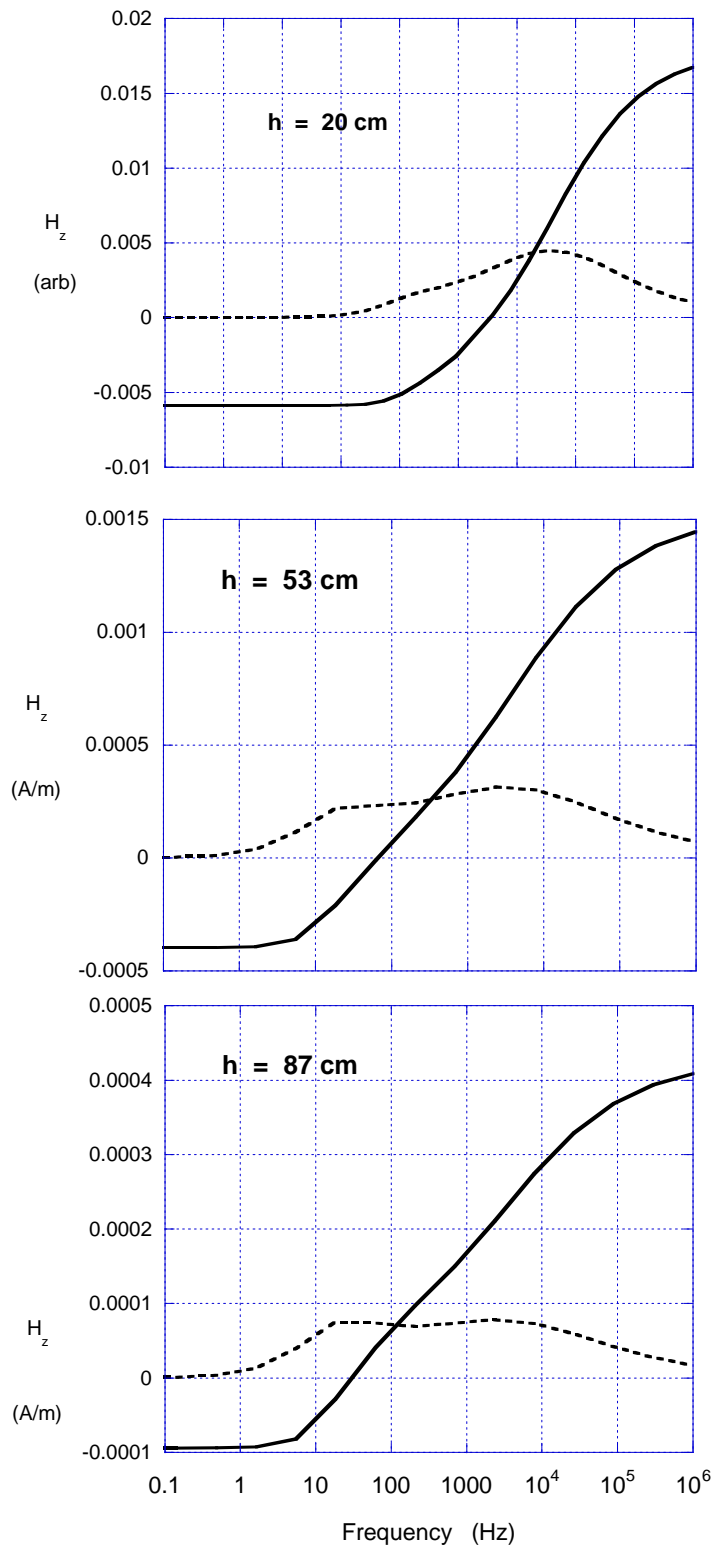


Figure 109. Response from the combination of steel scrap above an AL UXO, at various observation elevations  $h$ , under a uniform primary field.

Figure 110 shows results for the same case as in Figure 109, except that here the source is a magnetic dipole of unit amplitude moment. In a general way, one sees the same pattern as before. However here the emergence of the pattern alterations with increasing  $h$  is considerably weaker, as is the signal at higher  $h$ . The signal fall off between the lowest and highest observation point is over four orders of magnitude, and the evidence of the UXO only appears significantly at the highest elevation. It is questionable whether one could succeed in analyzing such a weak signal. We expect coil-based antennas like the GEM-3 to behave somewhat like this at the lower elevations and very much like this at the higher elevations. Overall, the relative strengths of the scrap UXO signals in the TD will again be comparable to those seen in the FD. In addition, for the dipole antenna case, the TD UXO response will be weaker here compared to the scrap, just as FD response is in Figure 110 relative to that in Figure 109.

Figure 111 shows results computed in the time domain by inverse Fourier transforming computations performed by the multi-object MAS program. Here the responses of the AL UXO and steel scrap are calculated for the each object alone but positioned as per Figure 99 relative to the sensor. Because in the turn-on case only the response of the steel scrap would persist as time proceeded, no scenarios such those in Figure 107 are explored here. The scrap items are, alternatively, sphere #1 with a 2 cm in radius, made of the same material as the original flattened scrap; sphere #2 with 4 cm radius and with both  $\mu$  and  $\sigma$  increased 50% relative to the original material; and a third sphere in which  $\mu_r$  is reduced from 90 to 65 and  $\sigma$  is increased from  $4 \times 10^6$  to  $8 \times 10^6$  S/m. (We have shown elsewhere that, for highly permeable bodies, the response spectrum depends only on the ratio of  $\sigma$  and  $\mu$ , not their individual values, [6]). Relative to its initial (early time) value, the smaller sphere #1 response decays somewhat more rapidly than the original flattened scrap, but still approximately parallels the history of the latter. That is, many such spheres that are significantly closer to the sensor than the UXO will effect about the same amount of TD obscuration as the larger flattened piece of the same metal. Shape is apparently not a vital factor, relative to sheer volume of metal. Sphere #2 is larger than the first sphere, producing signals comparable in magnitude to the original flattened scrap. While its material (electromagnetic) parameters have been changed, the ratio  $\mu/\sigma$  has been maintained relative to the original and its time history is very similar to the original's. Notably, even when the parameters are changed significantly, the shapes of the decay trajectories are rather similar.

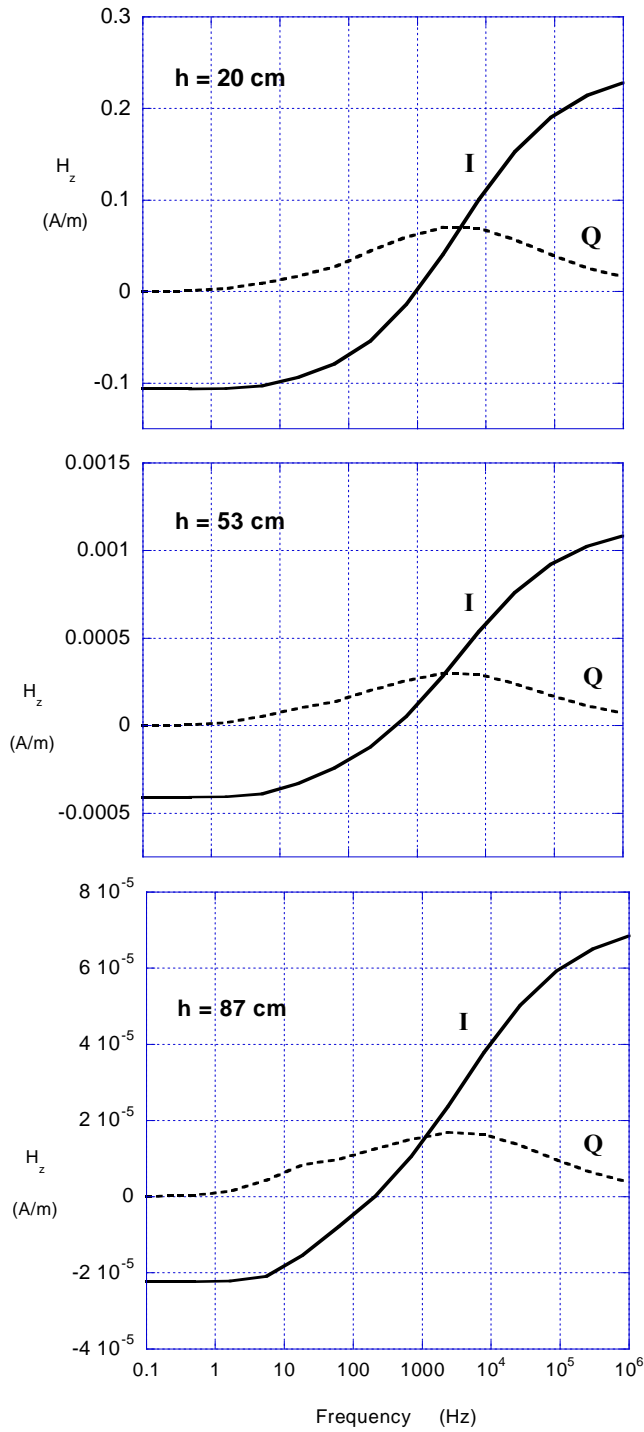


Figure 110. FD response of flattened steel scrap over the AL UXO, with dipole source and observation point at various elevations  $h$ .

Overall, if both ferrous scrap and AL UXO were present simultaneously with their signals more or less additive, the following picture emerges: If the initial (early time) response of ferrous scrap of a variety of shapes is on the same order of magnitude as that of the AL UXO (scrap curves shifted upwards on the plot), then the record must proceed beyond at least past  $\sim 1$  to  $10$  ms before the scrap signal declines by about an order of magnitude. Only then might the different shape of the pattern contributed by the UXO be distinguished. By a time of  $1$  ms the signal from the smallest sphere has already decayed about an order of magnitude. Thus clutter consisting of a number of items of this size that produced signal comparable in strength to the UXO in early time would most likely permit visibility of the UXO before its sharp falloff between  $1$  and  $10$  ms. Beyond that, with comparable early time scrap and UXO amplitudes, any change in the AL UXO's properties that caused its sharp drop off in response to occur earlier would likely render it invisible (e.g. reduction in size). If the signals from any of these scrap choices began at a significantly higher amplitude than the UXO, then it is doubtful that the different shape of the UXO decay curve would ever emerge.

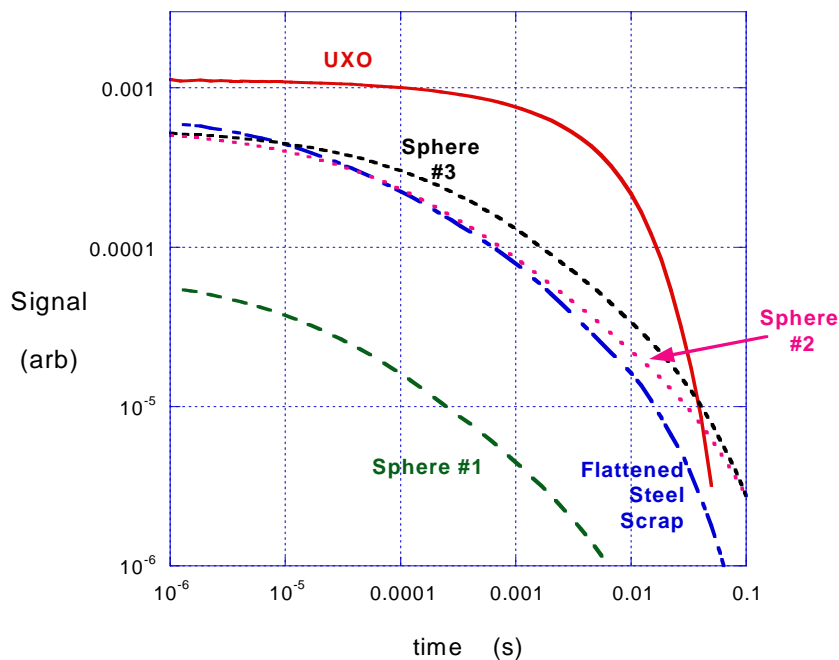


Figure 111. TD decay curves for the AL UXO and various steel scrap items described in the text, each alone under a uniform primary field, observed in the positions in Figure 99 with  $h = 87$  cm.

## 6.2. Phenomenology: Measurement Examples

This section considers the example of a heat round positioned vertically nose downward. A small horizontal steel plate is also located nearby at the same depth as the tail of the UXO (Figure 112). Grids of GEM-3 data were taken in air, about 17 to 23 cm above the tail, producing the signal contours shown in the figure. The UXO, separation between plate and UXO, and edge-view size of the plate in the figure are approximately to scale. While the plate is not very large (14 cm square), this example is nevertheless somewhat “loaded” in that the tail of the UXO used produces quite a weak EMI response; the bulk of the strongly responding material is thus deeper than the plate and the GEM-3 is more sensitive to closer objects than an instrument would be with larger loops. Be that as it may, the results are representative of what one would inevitably obtain with any other handheld-sized sensor. They are also at least suggestive of what would be obtained with a larger sensor that tended to “see further” more easily; see Section 6.1 immediately above.

The data obtained at low, medium, and high EMI frequencies are quite sobering. In each of the contour plots, signal concentration on the left side may be attributed primarily to the UXO while concentrations on the right are caused predominately by the clutter plate. At most frequencies the clutter dominates the picture in both components, despite its much smaller size/volume. Its upward facing flat size and depth no greater than the UXO tail easily produces a comparable or greater signal. Locating the plate deeper raises the relative response of the UXO considerably. If the center of each object is the same depth, then both contribute but one can still isolate and analyze the separate contributions by the methods discussed here ( see e.g. Sections 2, 7, and 8.3). If the plate is shallower it essentially dominates the picture to the point where the SCR is beyond what any processing can deal with. In the case in the figure, one can at least say that multi-component, UWB data demonstrates its advantages: while the UXO is almost completely obscured for individual components at some frequencies, using both components and all frequencies shows that something is indeed present in the left portion of plot. The UWB data alerts one to the effect that there is more than one object present and the case must be processed accordingly.

Figure 113 shows results that are obtained when the plate location is shifted horizontally until it is partly over the UXO tail. Its signals cannot be distinguished spatially from those produced by the UXO. Essentially, it completely dominates the observed spectrum of the received signal.

These results emphasize the conclusions drawn from the modeling exercises in the previous section, namely, very little shallow clutter can thoroughly obscure the EMI signal of a deeper UXO.

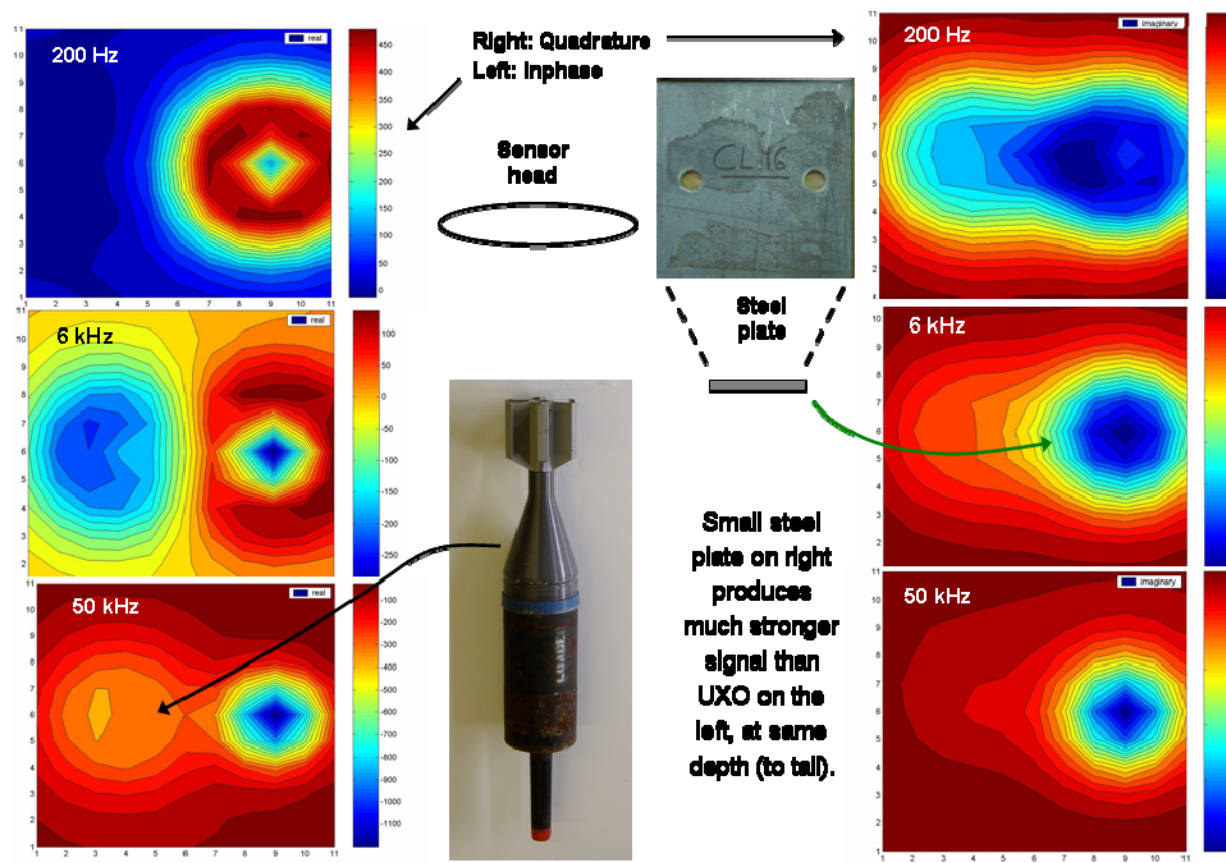


Figure 112. Signal contours at low, medium, and high frequency, on a plane over the vertical UXO and offset horizontal steel plate. Left column: Inphase component; Right: Quadrature component.

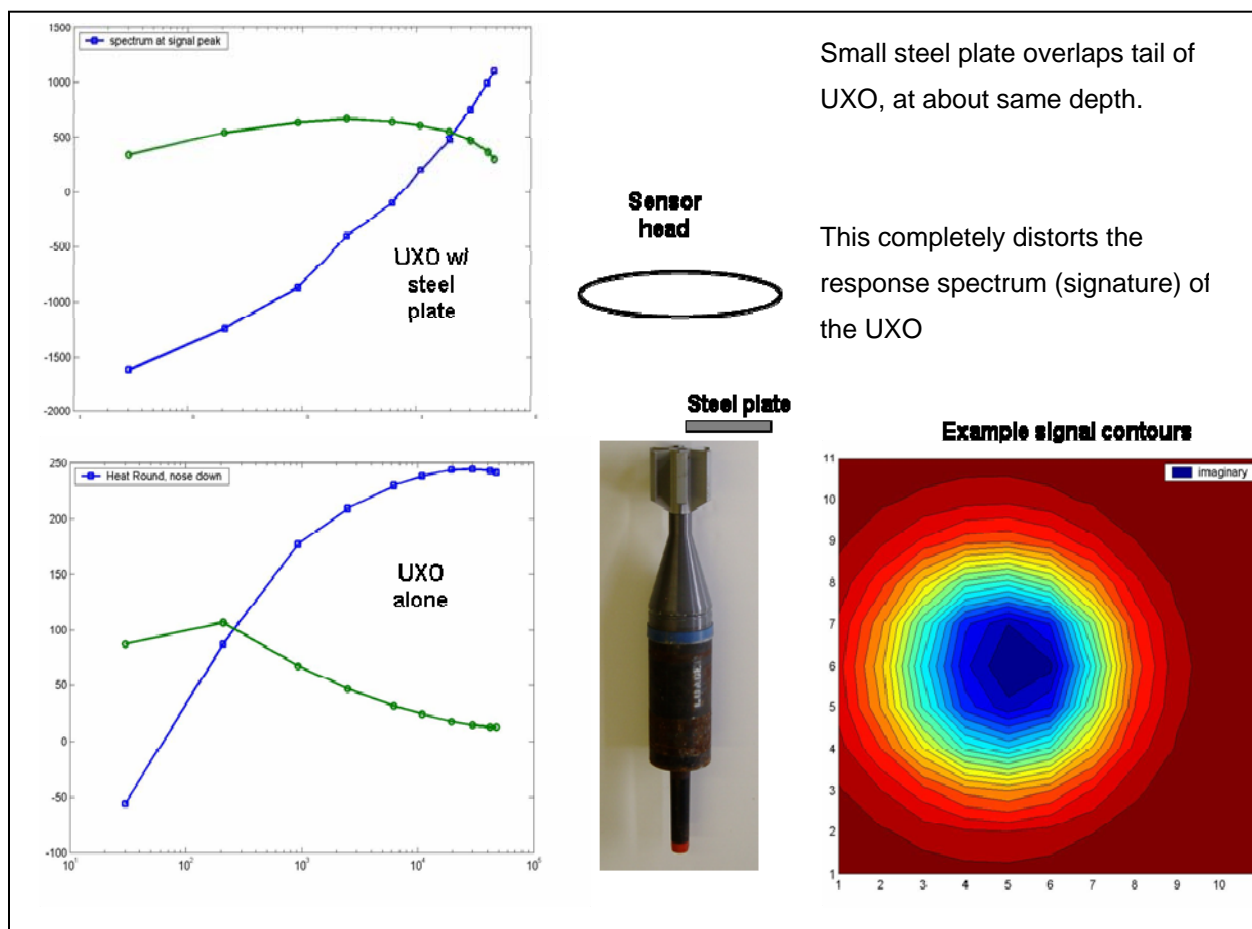


Figure 113. Left column: Response spectra with (top) and without (bottom) the steel plate in the position shown by the UXO's tail.

## 7. DISCRIMINATION OF MULTIPLE OBJECTS VIA EMI ALONE

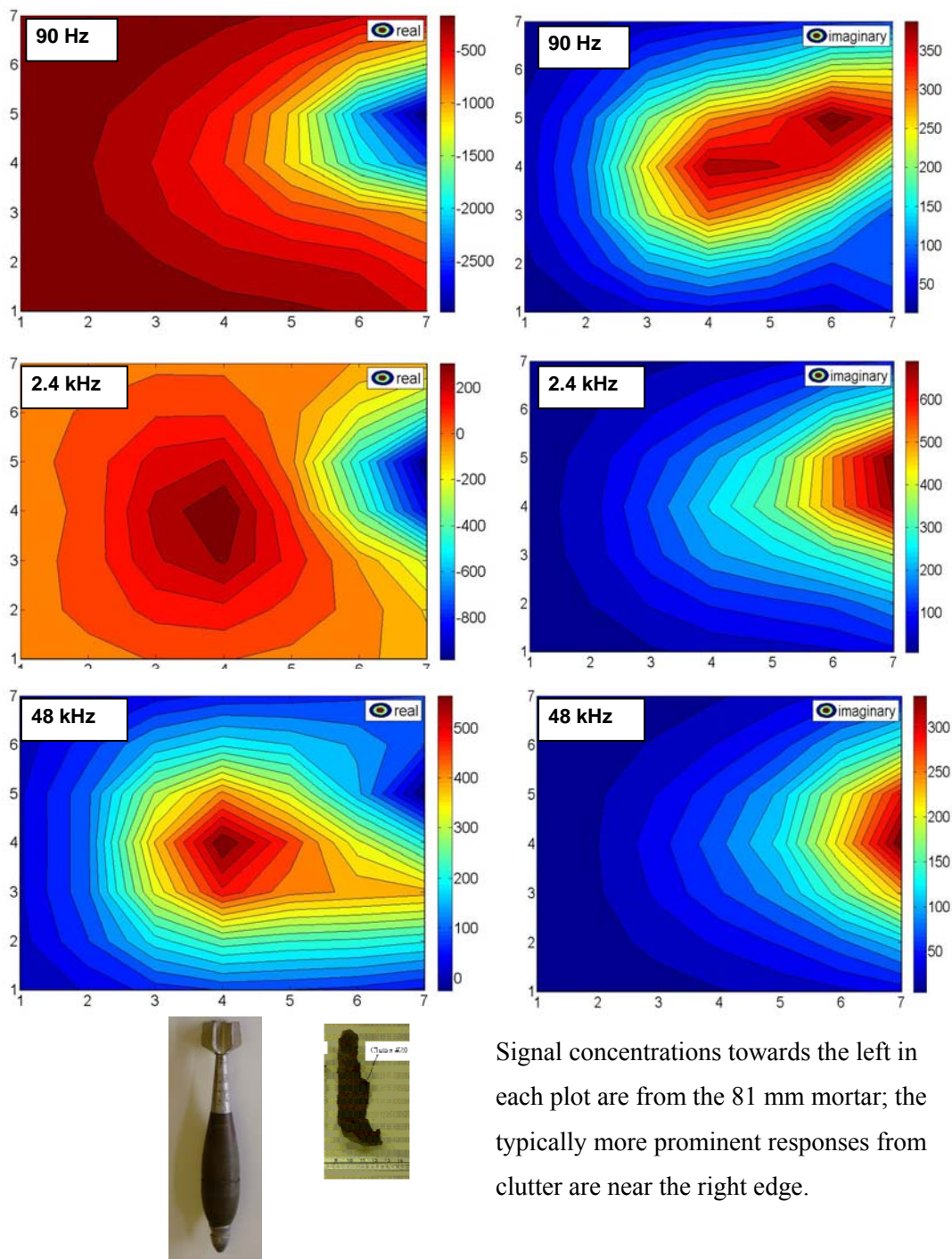
### 7.1. Multiple Object Discrimination Using the NSMC

#### 7.1.1. *Cases with Unknown Number of Objects*

In the cases considered in this section, discrete clutter enters more as a source of ambiguity than direct obscuration. That is, in each case the clutter does not greatly overshadow the UXO's signal as often was the case in previous sections. Rather its signal simply competes with or accompanies that of the UXO, frequently overlapping with it spatially, as in Figure 114. Discrimination was accomplished by assuming an essentially arbitrary spheroidal surface corresponding to each object on which equivalent NSMC sources were solved for. The DE optimization algorithm was applied to both objects simultaneously to determine amplitudes of the responding sources for each object, together with their orientations and positions and to isolate one object from the other automatically. On convergence, the  $Q(f)$  patterns were examined (Sections 2.4.3 and 2.4.4) and compared to those for known UXO types. An alternative is to first assume that only a single object is present and to compute  $Q(f)$ ; then to perform a second run assuming two possible objects, comparing goodness of fit or other measures of reasonableness to distinguish the more likely case. However the NSMC based method is fast enough so that there is little computational penalty for just proceeding on the assumption of two objects.

Always assuming the presence of two objects raises the question of what the optimization will produce when only one is present. At least in the tests reported here the answer appears to be that shown in Figure 115. The computational system inferred one  $Q(f)$  that corresponds closely to a UXO that was present and for the other object it simply produces an extremely faint presence. The latter corresponds more to signal clutter than physical clutter, with  $Q$  values that are so low that it may be considered a "null object." This pleasing result may not always be replicated in other cases. One may have to constrain the optimization in some way, e.g. to make sure that it does not approximate one object by using two overlapping or very close ones or by doing something else that corresponds to "splitting the difference." For the present, we take the method's inference of a null object as its way of indicating that only one object is present when it begins with the assumption of two.





Signal concentrations towards the left in each plot are from the 81 mm mortar; the typically more prominent responses from clutter are near the right edge.

Figure 114. GEM-3 signal profiles over a measurement grid above a vertical 81 mm mortar and a nearby piece of ordnance scrap.

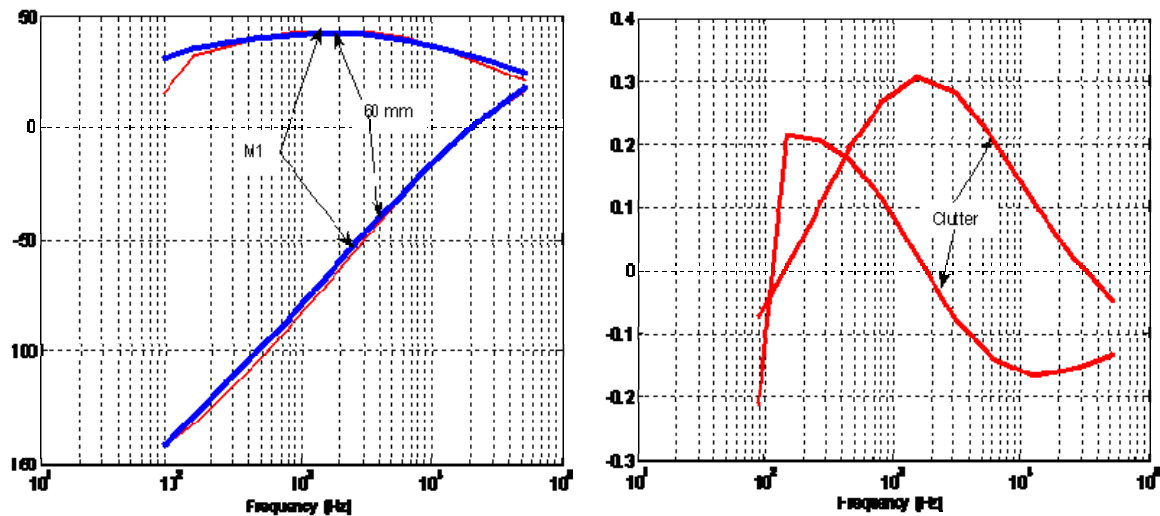


Figure 115. Left: Match of  $Q(f)$  to UXO that was present. Right: Inferred null object for second object, when none was present

### 7.1.2. NSMC Blind Tests for One or Two Objects – UXO and/or Discrete Clutter

In these tests the analyst worked at a different institution (Dartmouth) from that where the data were taken (ERDC-CRREL), and did not encounter the ground truth until after processing was done. Three UXO's familiar to the analysts were used as unknowns in this test: an 81 mm mortar, a 2.75" rocket, and a 105 mm projectile (Figure 116); the analyst sought others as well. Discrete clutter items were selected from those in Figure 117. In some cases only a UXO was present; in others a UXO with a piece of clutter was situated so that it produced significant signal in the data. Two 7 by 7 grids of GEM-3 data with 10 cm point spacing were taken over each set of objects, in the lab in air, with an elevation change of 5 cm between the two grids.

Results of the test are shown in Table 3. In each case the inversion correctly classified one object as a UXO. In only one case did it infer a clutter item when there was none (UC-6), an error with minimal consequences. In a minority of cases a different UXO was identified from the one actually present. However results in terms of the ultimate criterion of "dig" or "no-dig," and the number of objects is

extremely good. Some of the challenges of this data set were traced to relatively sparse data. Interpolation that produced a denser sampling of values plus 20-20 hindsight eliminated all short-comings of the analysis. In any case, this lab test provided confidence in the method, which was then applied to our outdoor testplots, where soil effects complicate matters considerably (Sections 2.5 and 8.4).



Figure 116. The three UXO's used as unknowns in the NSCM multi-object blind test.



Figure 117. Left to right: clutter items 16, 12, and 20 used in the NSCM multi-object blind test..

Table 3. Results for NSMC blind test with one or two objects in air, when either of the objects may be discrete clutter.

Unknown	Actual	Processing	
		Object #1	Object #2
UC-1	2.75" rocket alone	UXO	<none>
UC-2	2.75" rocket + CL12	UXO	Clutter
UC-3	80 mm + CL20	UXO	Clutter
UC-4	80 mm alone	UXO	<none>
UC-5	80 mm + CL20	UXO	Clutter
UC-6	80 mm alone	UXO	Clutter
UC-7	80 mm + CL20	UXO	Clutter
UC-8	80 mm + CL20	UXO	Clutter
UC-9	105 mm + CL16	UXO	Clutter
UC-10	105 mm alone	UXO	<none>
UC-11	105 mm + CL16	UXO	Clutter
UC-12	105 mm + CL16	UXO	Clutter

## 7.2. ICA Tests

The program FastICA has been used in other work directed at discriminating UXO's [42]. As noted above, in our experience the results of IC analysis using FastICA are highly variable for a given problem. Because the initial guess is random, different runs of ICA on the same data set can lead to thoroughly different solutions. The most reliable results were obtained when the signals sought are substantially non-Gaussian, ideally with all except one having kurtosis on the order of 10 or greater. This may or may not be fulfilled by signals of actual interest to us here. In what follows, the algorithm FastICA is applied to various test cases to ascertain the relevant limits on performance of the method, given this popular and highly regarded implementation.

### **7.2.1.        *Effects of Gaussianity, constant and variable noise***

Beginning with noiseless cases, we simply mix together two signals so as to produce an ensemble of randomized mixtures. The signals themselves are obtained by randomizing the Fourier transforms of base signals, then inverting into the sample domain. Figure 118 shows two signals obtained in this way, together with the distributions of their values. Although each signal features a vaguely bell-shaped curve of value distributions, the corresponding kurtoses are still reasonably high from our point of view, so that they might be distinguished from signals with Gaussian distributions. Five hundred mixtures of these two signals are obtained simply by forming different linear combinations of them, i.e. superpositions, each of which contains the originals multiplied respectively by different random numbers. FastICA clearly succeeds in extracting the two constituent signals from mixtures, using only three mixtures (Figure 119 ). Results from the complete ensemble of 500 mixtures were insignificantly different.

Figure 120 illustrates the effect on results when one of the signals of interest is insufficiently non-Gaussian. While the top signal has rather high kurtosis, the bottom one does not. The result is that the IC obtained that corresponds to the top signal suffers some distortion, despite its own credentials; and the second IC only resembles the low-kurtosis contributor in a general sort of way, at best. In short, separation of the signals is incomplete. As observed above, different runs will produce variations on this theme. However the principal observation here shows through the variability of many examples. In general, the more Gaussian signals are, the more difficulty ICA seems to have correctly identifying them, i.e. isolating them.. Empirically, in terms of kurtosis, useful thresholds were found to be: “very non-Gaussian,” meaning kurtosis greater than about 10; and very Gaussian, meaning kurtosis less than about three. In terms of performance, the distinctly worst cases occurred when two signals to be separated both met the “very Gaussian” criterion above. Further, when one of the signals classes as very Gaussian, the other signal must have a kurtosis of greater than 10 or else the solutions cannot be identifiable as corresponding to the original sources.

Perhaps the most revealing tests are those in which noise is added. From the point of view of ICA, “noise” is just another added signal. When the noise signal is always the same in all mixtures, i.e. the same set of values in the same sequence, within a multiplicative factor, the method succeeds as well as otherwise, by the same (kurtosis) criteria (Figure 121). Both coherent signals possess somewhat marginal kurtosis, but the higher kurtosis contributor comes through relatively clearly, and the other is at least

reminiscent of its original form. By its very nature, however, noise is rarely constant in this way. If instead one adds different random noise to each mixture, with on average the same SNR as in the previous example, then the results in Figure 122 are obtained. The method fails completely.

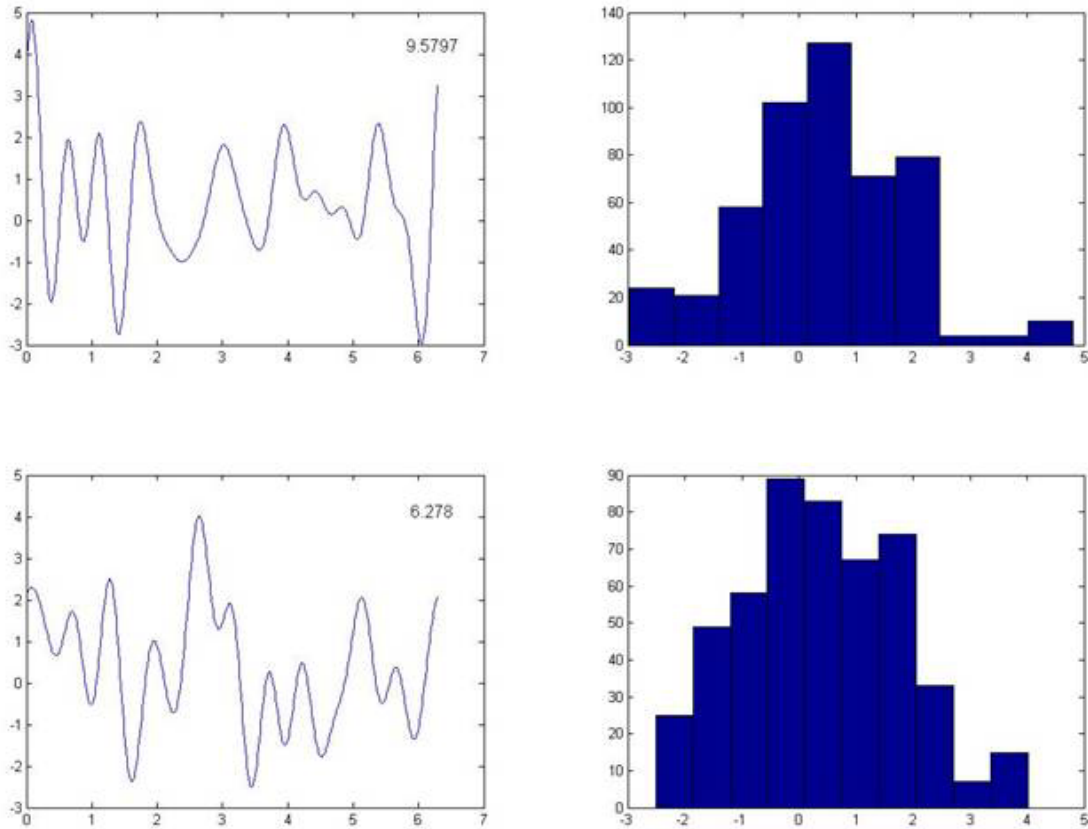


Figure 118. Signals to be mixed, with their respective kurtoses (left); value distributions for each (right).

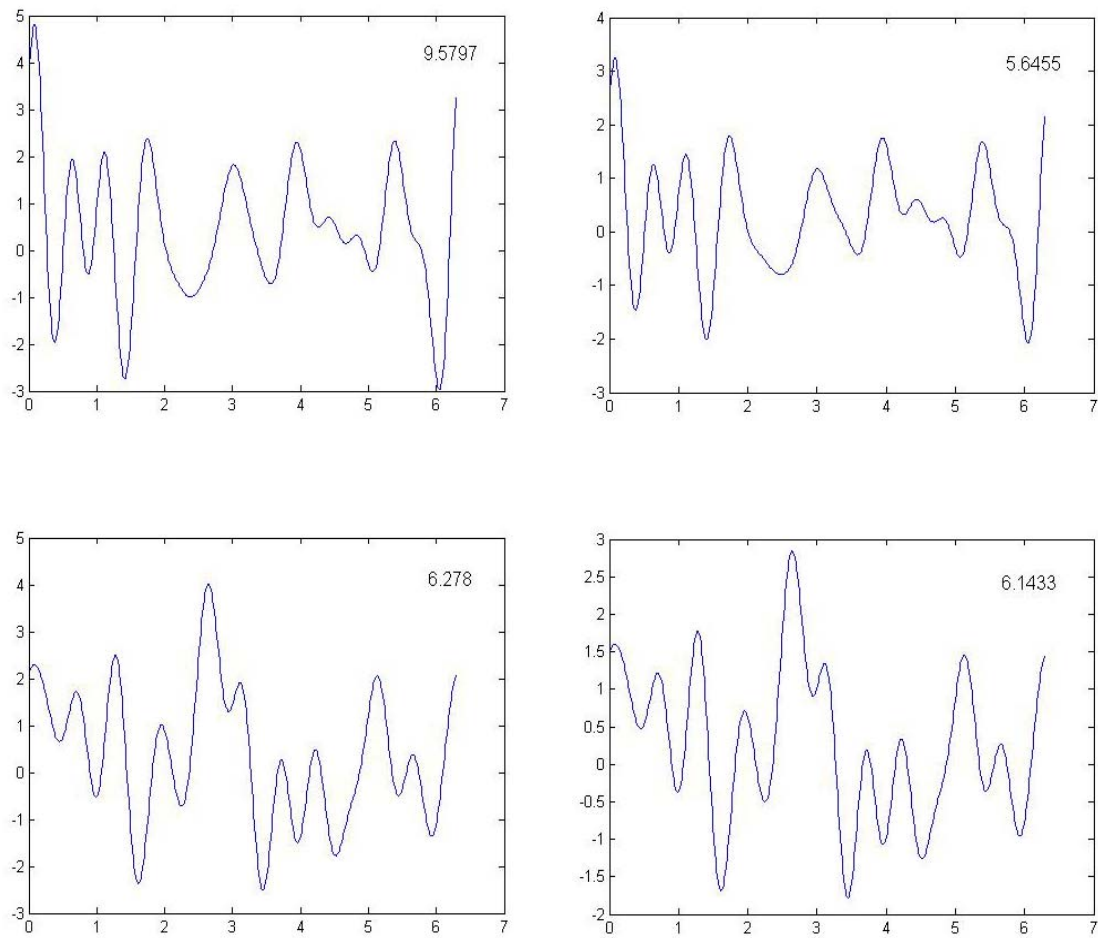


Figure 119. Signals to be mixed, with their respective kurtoses (left); IC's obtained from processing of three mixtures (right).

..

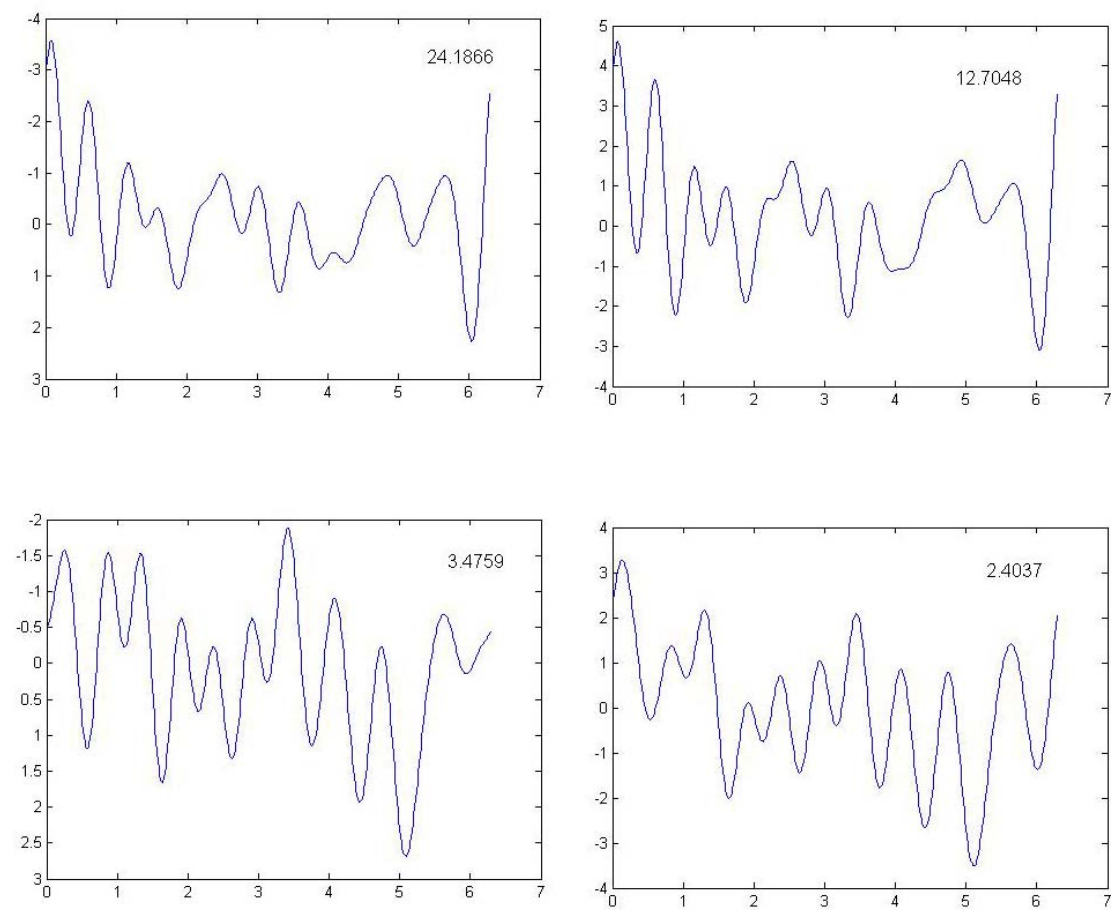


Figure 120. Signals to be mixed, with their respective kurtoses (left); IC's obtained from processing of 500 mixtures (right)



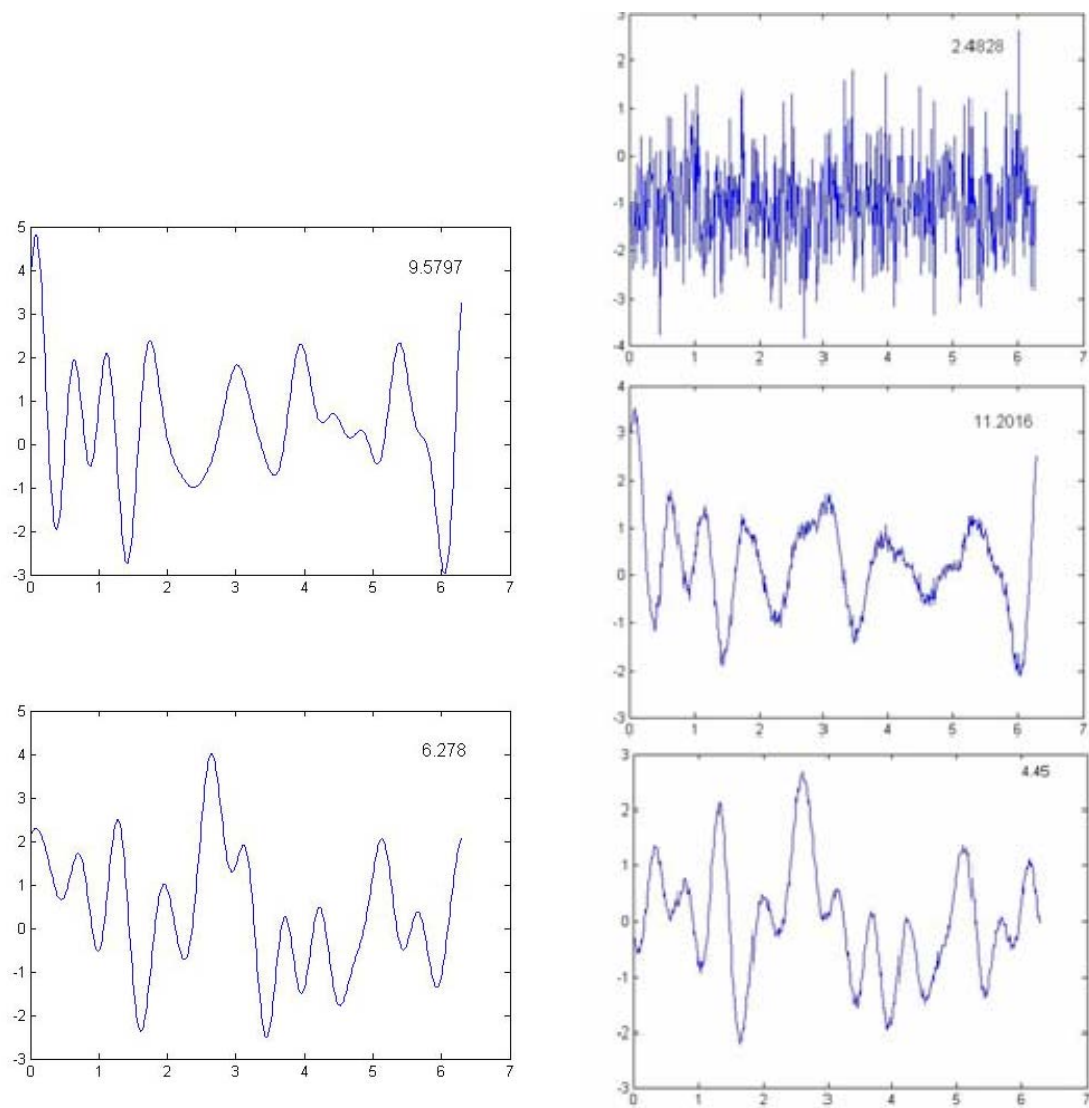


Figure 121. Signals to be mixed, with their respective kurtoses (left); IC's obtained from processing of 500 mixtures with invariant noise just added at different percentages (right)

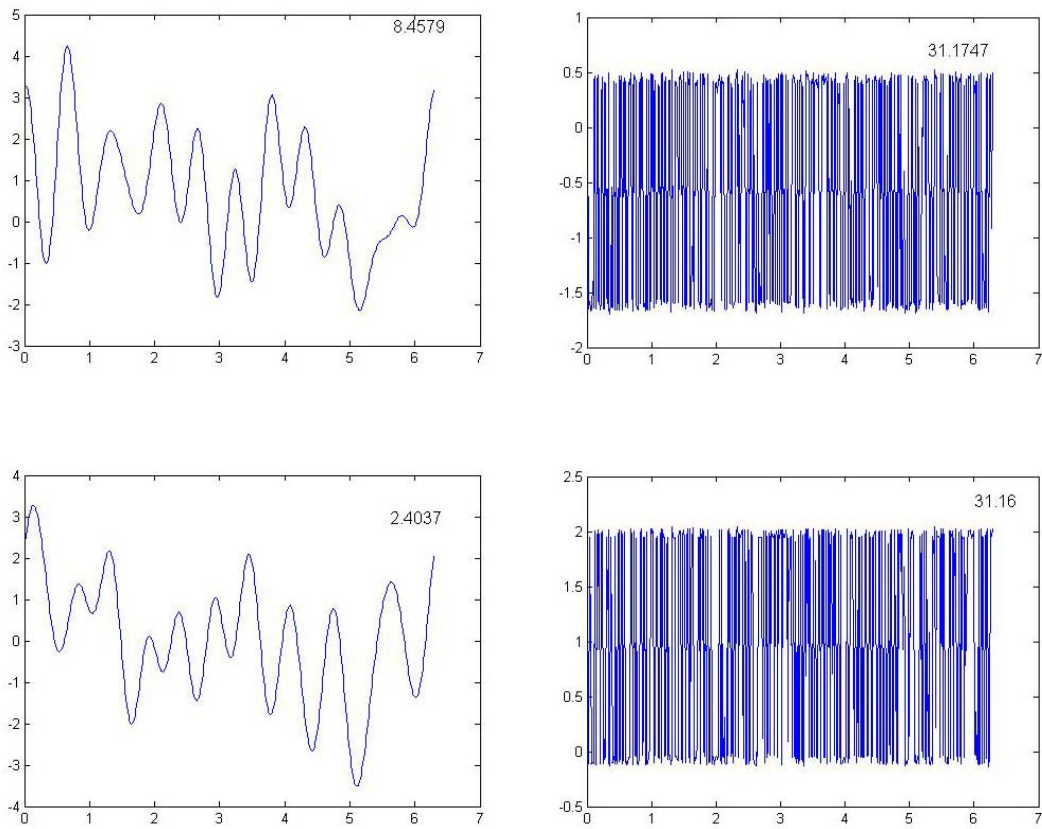


Figure 122. Same as previous figure, but with results (right) when different noise is added to each mixture.

### **7.2.2. ICA using EMI spectra for metallic objects**

The Gaussianity and noise sensitivity observed here are serious concerns for application of the method in realistic situations. An even greater concern however resides in the question of what the relation is between the IC's that the method extracts and the physically distinct sources of signal. Otherwise put, the examples reported thus far may be tests more of Gaussianity and invariance than of effects of the constraint that different contributors be independent. To pursue cases more relevant to EMI discrimination of UXO's, we construct signal mixtures consisting of analytically determined EMI responses from different homogeneous spheroids. For simplicity, we only consider contributions from the axial moments of the two items. Note that this is already considerably simpler than the setup in Section 2.6.5 in that here each contributor would likely only require a single dipole to produce its signal. Figure 123 shows the real (inphase) and imaginary (phase quadrature) portion of the moments (magnetic polarizabilities) of the two bodies. Note: we are proceeding here in the frequency domain in the sense that signals will consist directly of mixtures of these spectra. All components have desirably high kurtosis, the lowest standing out a bit with a value around 6 (second object, imaginary component). Based on rigorous analytical solutions for the shapes postulated, of relevant size and material types, these are realistic and relevant example FD input signals.

Figure 124 and Figure 125 show results typical of many tests involving noise free mixtures of the two complex-valued source signals in Figure 123. Recall that the computed IC's will differ from the inputs by a scaling factor. This means that the output may appear with a sign opposite to that of the input. This is not significant. Depending on how strict one's criteria are, some parts of the results are tolerable (e.g. top signal in Figure 124; possibly top signal in Figure 125). However the other two extracted components show large distortions relative to the inputs. Suffice it to say that the results are quite unreliable, even with these relatively high kurtosis inputs. This may be due to the very simplicity or smoothness of EMI signals from the broad class of objects of interest. The signals in the tests in the previous section oscillate substantially over the domain of observation. The constraint of independence – a value observed at some point in one does not imply any value at the same point in the other – can more readily be approximated. However, inevitably, the components in our realistic signals tend to have somewhat similar shapes. Inphase components reach high and low plateaus at each end of the spectrum; phase quadrature components both tend to zero at the extremes of the domain, with a peak in the middle, and so forth. Perhaps most significant, each component aligns on a particular value only once, or perhaps twice. All this means that there is some manner of systematic relation between the value occurrences in

the two components. This compromises the constraint of independence, while the solution algorithm is designed to select independent components, per force. It is doubtful that UXO and clutter EMI signals in other domains – time, space – will be substantially more independent.

One may not warm to the explanation here that insufficient signal independence may be undercutting the method's performance with realistic signals. However, the performance is indeed as observed, even in the absence of kurtosis and SNR challenges. Overall, we conclude that the applicability of BSS/ICA to the UXO EMI sensing problem remains to be shown.

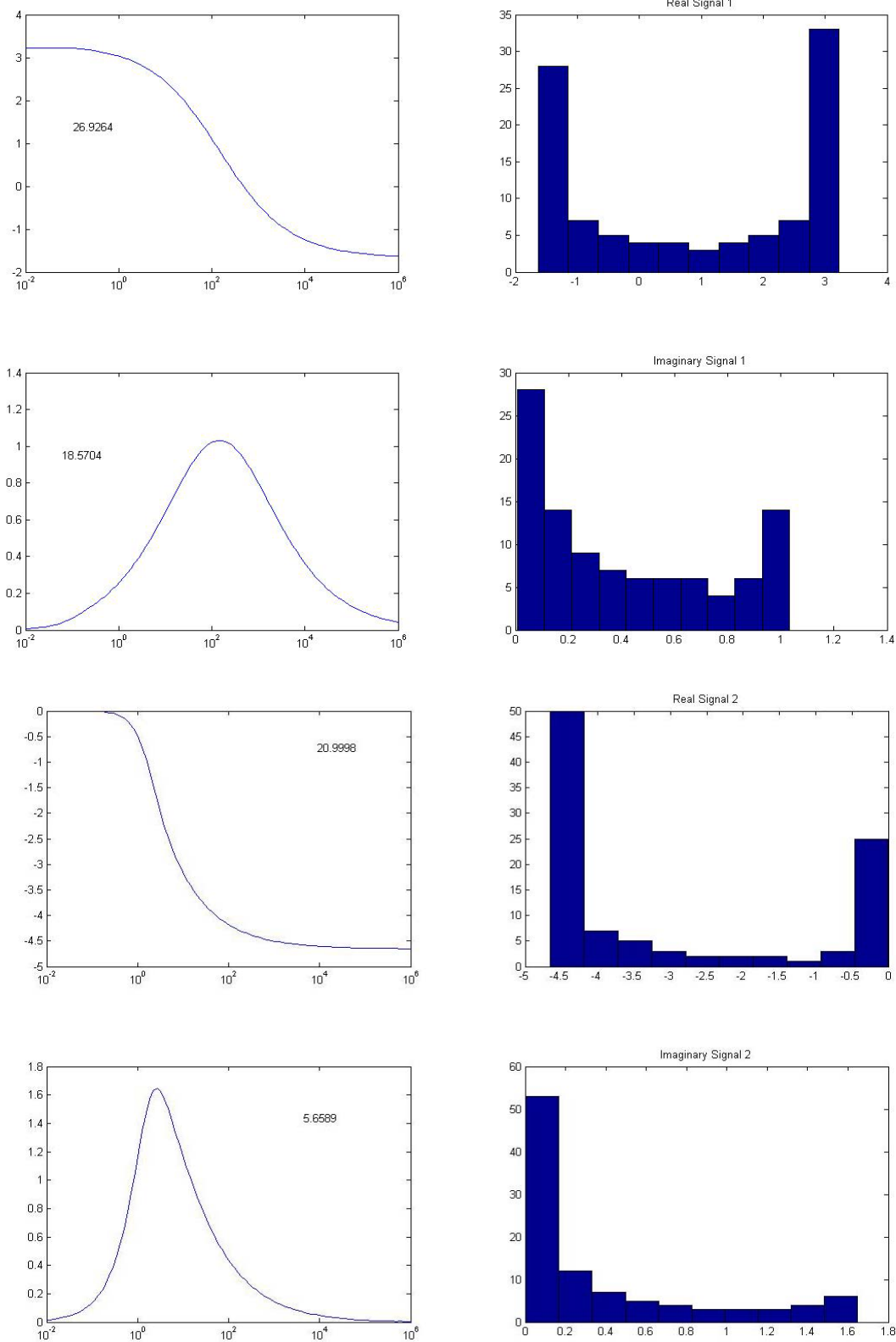


Figure 123. Real and imaginary parts of signals vs frequency, from spheroids 1 and 2 (left), with their distributions of value over frequency (right).

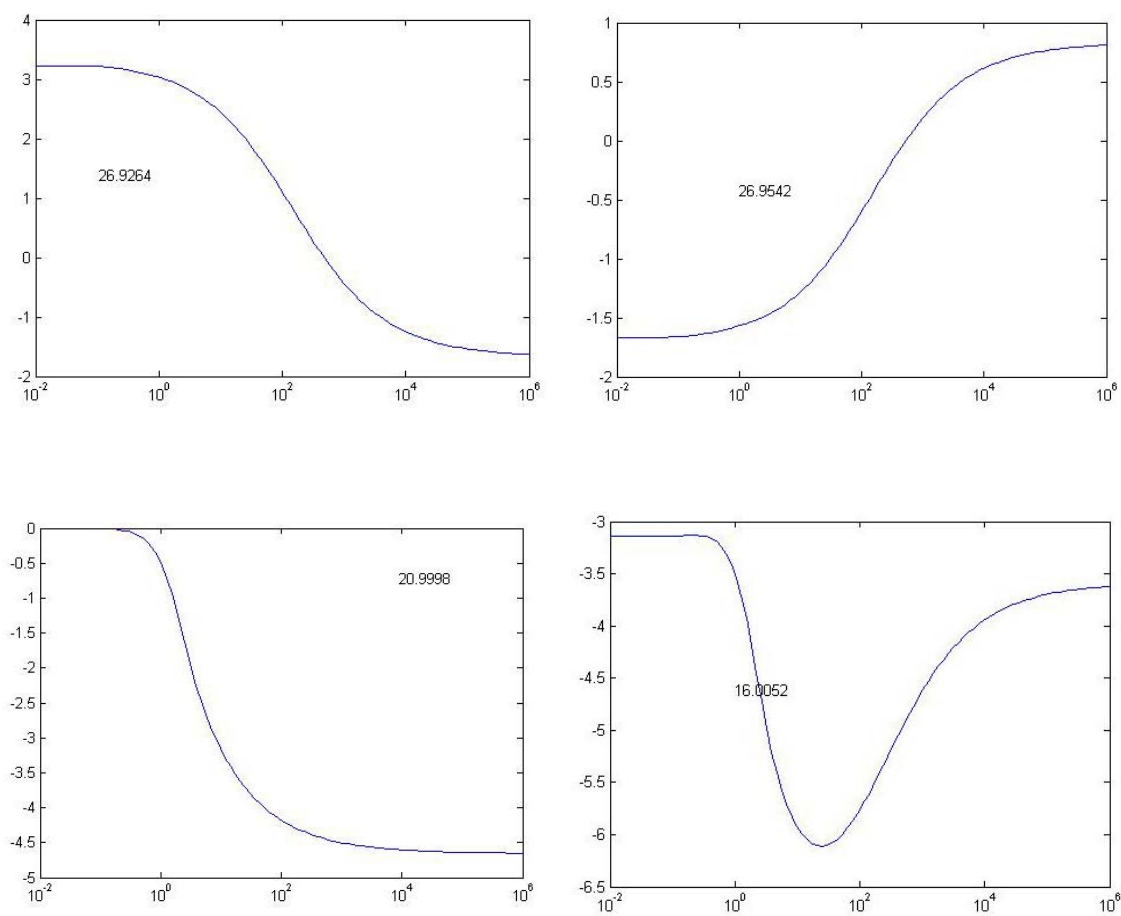


Figure 124. Real (inphase) components of the two spheroidal contributors. Left: original signals. Right: Corresponding extracted IC's.

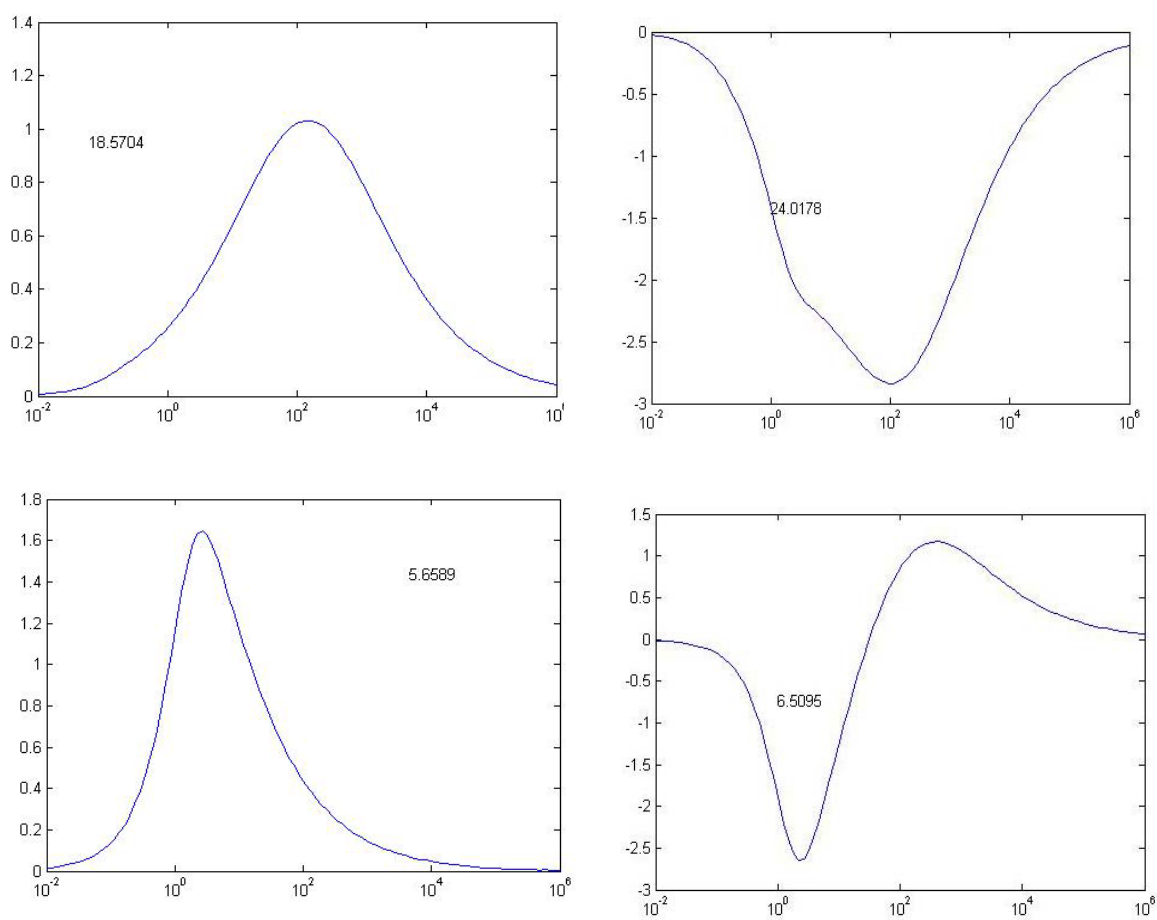


Figure 125. Imaginary (phase quadrature) components of the two spheroidal contributors. Left: original signals. Right: Extracted IC's

## 8. GPR AND EMI

One of the attractions of EMI over GPR as a subsurface UXO sensing technology is that the soil is more or less transparent to the former. While EMI suffers somewhat from clutter or shift in values due to soil responses, the signals do not suffer the very substantial diminution that radar waves do, as a result of the lossiness ( $\sim$  energy absorbency) of the soil. GPR may suffer strong responses by soil heterogeneities and dielectric clutter, adding further obscuration in the face of substantial signal decay in moist soil. How much the radar waves decay depends on many factors, including level of moisture saturation, salinity, temperature, and soil composition. The worst cases are those with cold, wet, very fine grained soil such as fine silt or clay. In such cases GPR may be all but useless; or, in the least, be relegated to the lowest GPR frequencies ( $\sim 10$ 's of MHz to perhaps a couple 100 MHz), with attendant loss of resolution.

A cause of signal diminution that both EMI and GPR have in common may be termed geometrical spreading. This is essentially the only cause of signal attenuation for EMI; for GPR it is an approximately multiplicative effect, exacerbating the diminution caused by soil absorption. Geometrical spreading means the distribution of a given transmitted field over a larger and larger area as one moves farther and farther from the source. It is easiest to grasp in connection with GPR, in which waves propagate outwards from a source. If one imagines a given signal (field pattern) radiating outwards through a given segment of solid angle, clearly the radiated field's energy will be spread out over a greater and greater area as distance from the source increases. Even in a lossless medium this causes signal magnitude attenuation  $\sim 1/r$ . While at our scale of observation EMI fields do not consist of propagating waves, similar considerations apply in that the concentration of energy maintained around a concentrated source must diminish with distance from that source. Virtually all EMI transmitters consist of electric current loops tantamount to magnetic dipole structures. Beyond the very near field ( $r \sim$  loop diameter) magnetic dipole fields decay as  $\sim 1/r^3$ . This is due purely to the geometry of field, and not to any interaction with surrounding media. The  $1/r^3$  decay is quite a severe effect, given that both transmitter and responding object act approximately like dipoles, producing a net signal diminution at worst of  $\sim 1/r^6$ . This may be mitigated by large transmitter loops that transmit more uniform fields, or by being in the very near field of the responding object. Be that as it may, in the least one may assume an EMI signal decay on orders somewhere between  $1/r^3$  and  $1/r^6$ , usually closer to the latter.



The point to be considered here is that, despite its other signal loss vulnerabilities, GPR may sometimes have advantages over EMI because of much milder geometrical spreading. Beyond the fact that the inherent geometrical spreading of GPR signals from both sensor and target is much less, radar beams can be concentrated directionally by the transmitting antennas. Section 6 above shows potent EMI examples in which discrete shallow targets can obscure deeper ones. Section 8.1 below pursues a testplot example with a deeper and a shallower UXO in which EMI and GPR responses are compared. Section 5 above analyzes the EMI effects of widely dispersed small clutter items, indicating that, while small, they may cause intense signal clutter, primarily due to the different  $\sim 1/r^6$  geometrical spreading effects between target and clutter. Section 8.2 below examines a testplot example with a relatively large buried UXO beneath various densities of ordnance clutter collected at a live site; GPR and EMI responses are compared.

Other features of GPR may also make it worth considering in the UXO discrimination sensor mix. Because radars record different arrival times for objects at different distances, in principle the reflections from different objects may be distinguished. Even for objects whose signals overlap, polarimetric analysis of the reflections may reveal distinct contributors to a total response. Both the presence of a time record and polarization sensitivity are absent in EMI, and therefore GPR may serve to complement induction surveying at a site where both can be employed. In what follows, Section 8.3 provides an example of multi stage processing in which GPR information and different levels of EMI processing are enlisted for a multi-target discrimination case. Lastly, Section 8.4 presents results of blind discrimination tests using both EMI and GPR data from our outdoor testplots.

## **8.1.           Obscuration by Shallow Targets: GPR vs EMI**

The scenario constructed in one of the testplots consisted of two UXO's, one 81 mm mortar, inclined at about 45 deg and buried about 30 cm deep, and a much larger 155 mm UXO approximately 40 cm deeper. The soil was moist, probably about half saturated. The relative positions of the buried targets are apparent in the GPR profile in Figure 126, which shows a grayscale image tantamount to a vertical slice through the ground in a plane containing both targets. By contrast, the images on the right in the figure show GEM-3 EMI signal contours over horizontal planes at the ground level. The quadrature component at 210 Hz is shown because that component avoids a fatal level of clutter due to ground response, and that frequency featured a strong response from both targets. The upper right plot shows

signal contours obtained with both targets present. The shallower target was then excavated and the plot resurveyed, with new background subtraction. Given that the lower right plot only shows responses from the deeper, larger target (155 mm), it is clear that the upper right plot is strongly dominated by responses from the shallower target alone, despite the fact that it is much smaller. (The tilt in the shallower mortar displaces its strongest response to the left in the image.) The essential point here is that while the inherently weaker but closer target can virtually completely obscure the larger target beneath for EMI, both targets are clear in the GPR data. This is because GPR suffers substantially less geometrical spreading, and the technology can both focus the transmitted radar beam and amplify the received response as a function of time (apply range gain).

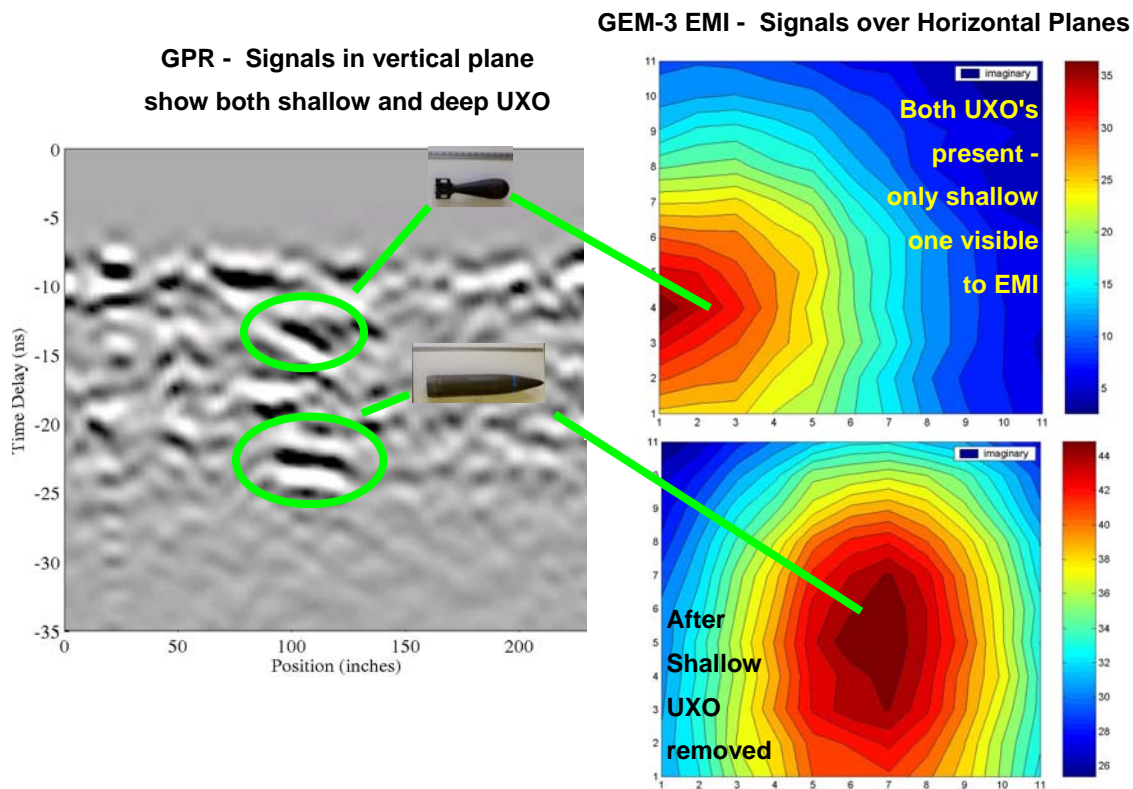


Figure 126. Left: GPR profile along a survey line (horizontal axis) over two UXO's, one shallow and the other deeper. Vertical time axis corresponds approximately to depth. Right: EMI signal contours over a horizontal surface on the testplot above the location of the targets.

## 8.2. GPR, EMI, and Obscuration by Diffuse Clutter

Section 5 above presents an analysis of the effects of diffuse small clutter items on EMI signals, including their relative effects on obscuration of larger discrete targets. This section examines a case from the testplots in which a relatively large UXO (105 mm projectile) is buried with or without a layer of ordnance clutter scattered about the surface. GPR and EMI surveys in both cases contrast the level of obscuration imposed by the surface clutter. Figure 127 shows the plot of ground without the clutter, including the survey line; the UXO in question; and the GPR profile from a survey along a line parallel to the UXO axis. (The ordnance was buried with a 45° inclination, distorted by the different scales on the vertical and horizontal axes in the grayscale profile). The ground surface is visible at about -7 ns delay and a strong indication of the target appears at about -22 ns.

Figure 128 shows the effect on the GPR survey when it is repeated with the addition of clutter mat on the ground surface. Clutter items were collected by team members from a live cleanup site at the former Ft. Ord, from an area deemed remediated in the sense that all targets of concern had been dug. This ordnance clutter was left after a cleanup of obvious surface and near-surface clutter by the cleanup crew; it was obtained from a spot of at least one square meter between the holes dug. It may thus be taken as representative of the residual background clutter with which the digital geophysics had to contend. Our team member excavated to the depth of about one shovel head and then sifted the soil. Different spots sampled showed different levels of residual clutter contamination. Based on the field worker's observation, the density and size of pieces on the mat at the top of Figure 128 rate as moderate, for this highly contaminated site at Ft Ord. The GPR profile at the bottom of Figure 128, taken in the testplot along the same line as in Figure 127 but now with the clutter mat, shows no noticeable reduction in clarity of response from UXO. Essentially, the GPR system sees right through the clutter, without any additional notable responses from the clutter location (surface at ~ -7 ns). Further, given the delay between the near surface responses and those from the deeper object, any scattering of the transmitted signal from the clutter pieces fades long before the reflection arrives from the UXO.

Next, the same experiment was performed with the EMI sensor. GEM-3 surveys were performed over grids of points near the ground surface, with and without this same clutter mat. Figure 129 shows responses for the buried UXO alone at three (low, medium, high) frequencies, including both inphase and quadrature components. The inphase plot at the middle frequency shows primarily background and clutter from soil response, occurring at a frequency where the real part of the spectrum from the UXO passes through zero. The quadrature response is clear throughout, also showing reasonable sensitivities: Ferrous

objects such as the 105 mm projectile show stronger axial responses at low frequencies, and stronger transverse responses at higher frequencies. Because the UXO is tilted, this causes the shift in location of the maximum in the contours as frequency increases. Also, the quadrature signal at the highest frequency is the weakest.

Figure 130 shows the results of an identical GEM-3 survey but with the moderate clutter mat in place on the ground surface above the UXO. Signal contours are distorted beyond recognition for both components at all frequencies, except possibly for quadrature response at 30 Hz. A positive view of this is that a sufficiently broadband EMI device may sometimes dodge the response of small clutter to some degree because its quadrature response will frequently appear predominately at higher frequencies. If the UXO has a strong low frequency quadrature response, it will show through. The signal plotted in the upper right of Figure 130 is dominated by the axial response of a rather large ferrous object – from experience we expect a notable, if not maximal response here. The darker view is that the small surface clutter produces an essentially disabling level of signal clutter at most frequencies in both components, leaving little for analysis. Repeating this experiment but with a lighter clutter concentration showed a reduction in the distortions, but still a poor SCR. A heavier but still realistic clutter intensity was comprehensively fatal for any analyzable target signal.

This case study illustrates that, while GPR is vulnerable to many signal clutter problems in subsurface surveying that do not affect EMI, it is insensitive to surface clutter effects that can easily cripple EMI.



**105 mm  
Projectile  
at  
45°  
inclination**



**GPR reflection is  
also clear  
(vertical plane)**

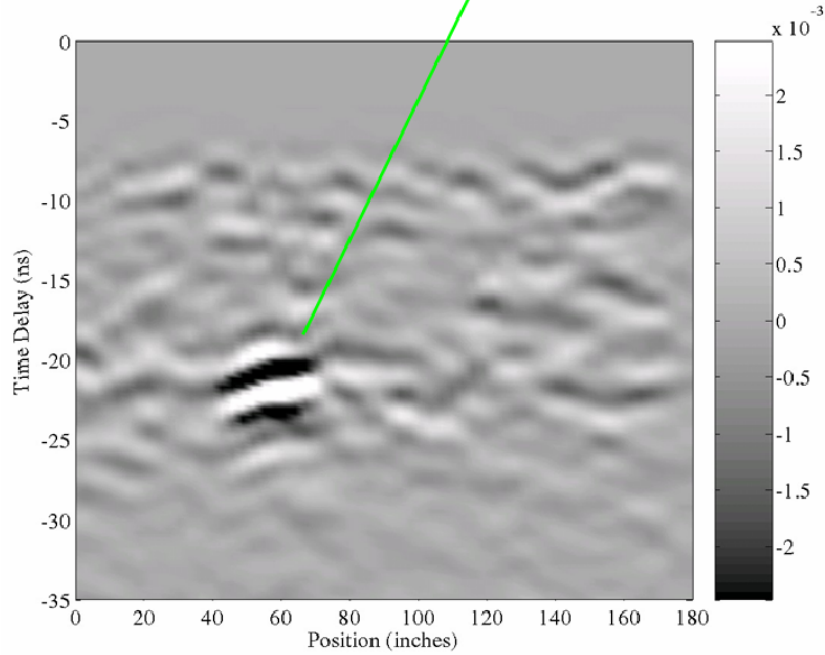


Figure 127. Top: plot of ground under which 105 mm projectile (middle) is buried. Bottom: GPR profile of measurements along the string across the plot.



**GPR reflection  
remains clear,  
unaffected by  
dispersed clutter on  
the surface**

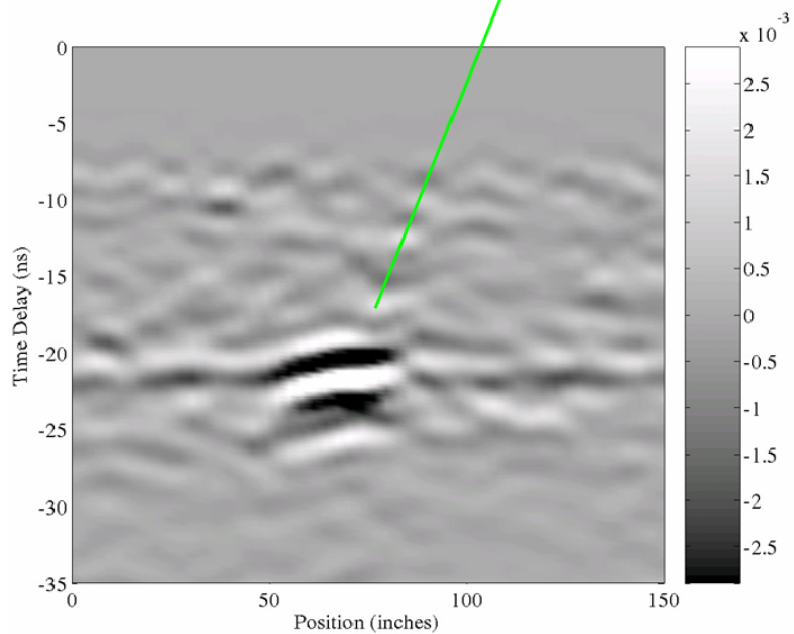


Figure 128. GPR profile (bottom), along same measurement transect as in the previous figure, but with the medium intensity clutter mat emplaced above the target.



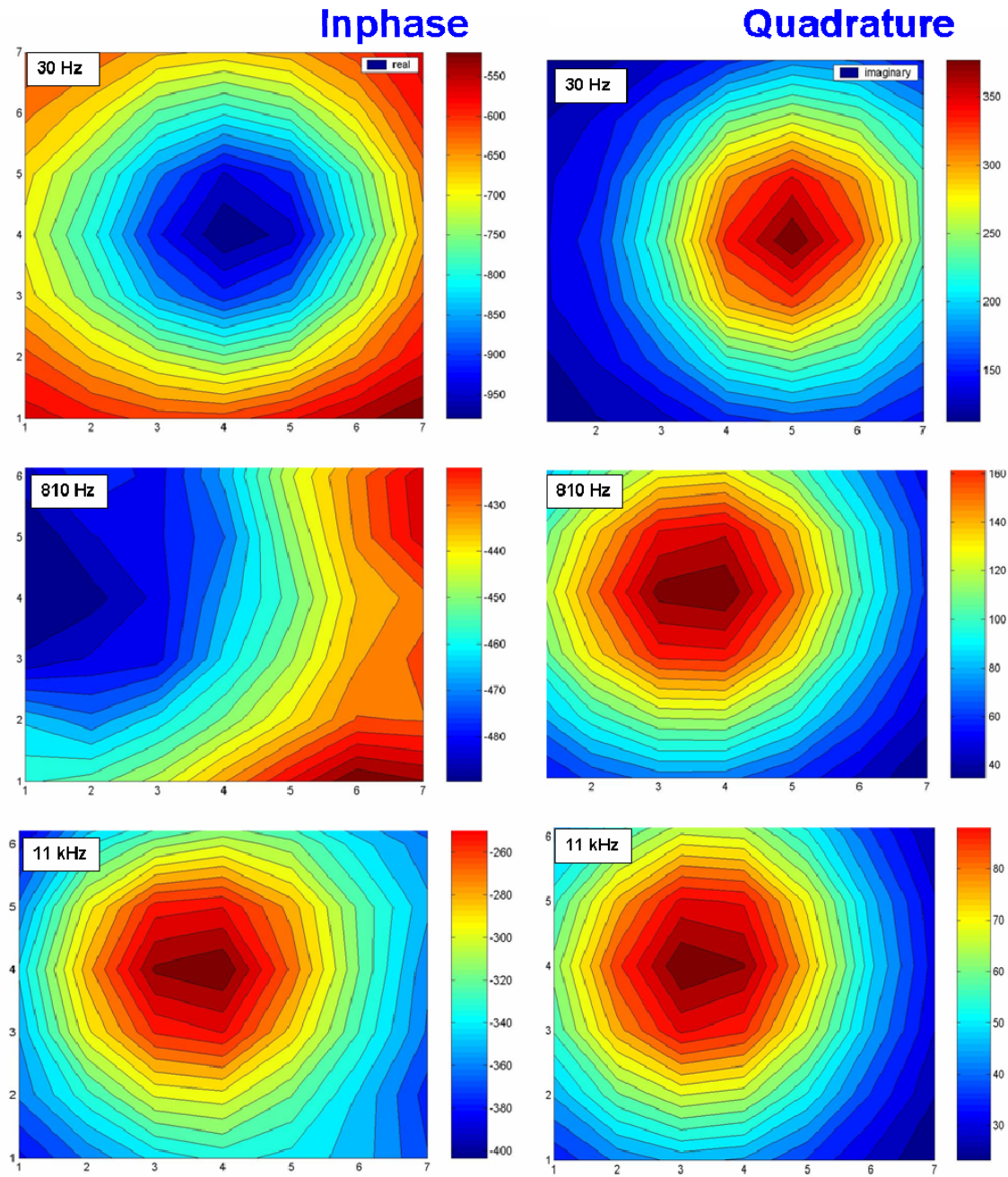


Figure 129. EMI signal contours measured over the 105 mm UXO, as emplaced for measurements in Figure 127 and Figure 128.

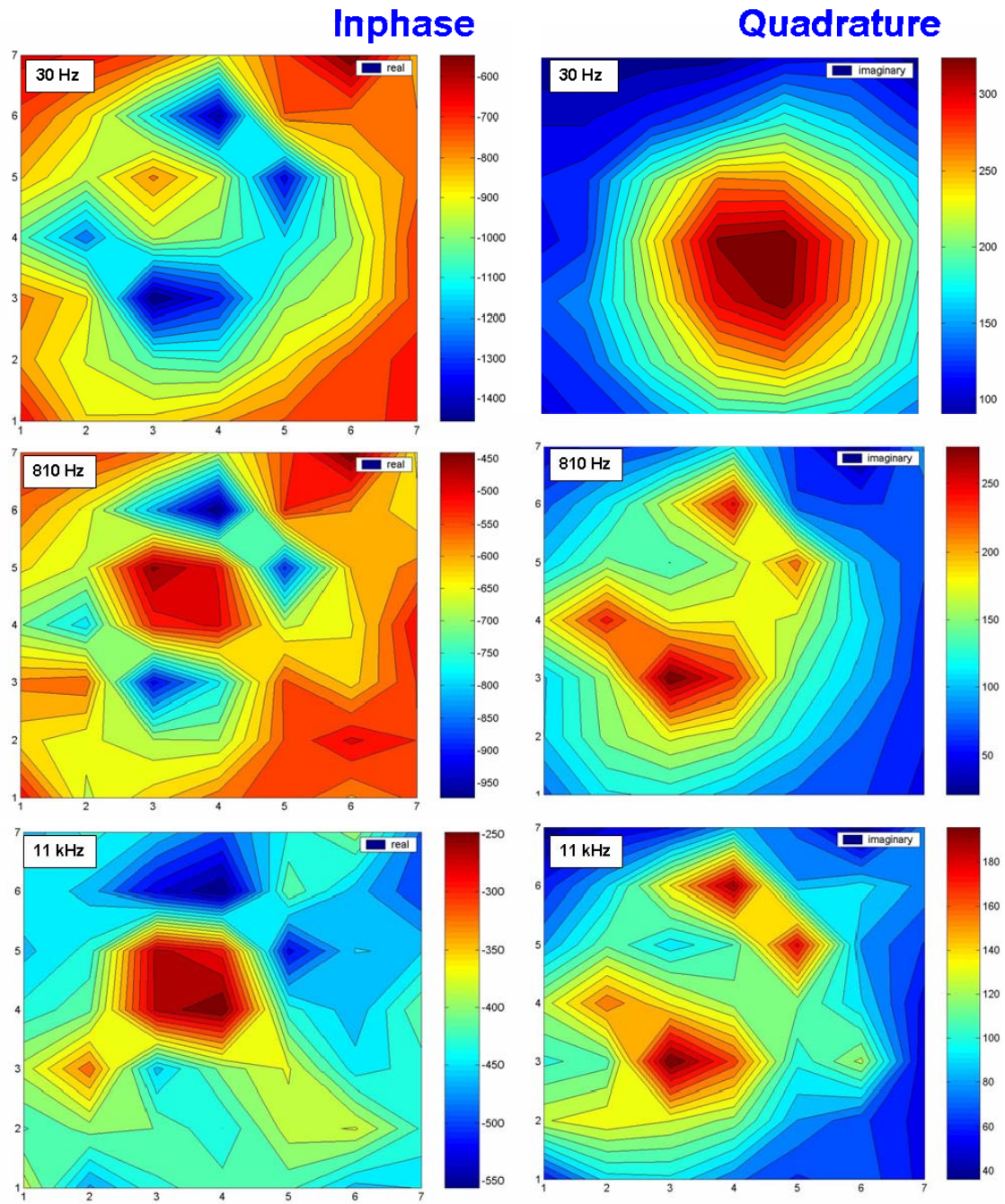


Figure 130. Same case as in previous figure, but after addition of the clutter mat on the ground surface.



### 8.3. Multi-stage Collaborative Processing Example

This section presents an example of multi-stage processing in which both GPR and EMI data are exploited together. The data from the two technologies can be exploited together in a variety of ways and in a variety of orders – preliminary EMI can be fed into or constrain GPR processing, or vice versa. Here the GPR analysis is performed first and its results are used to guide the EMI analysis. That latter proceeds itself through a number of stages, from an essential but conceptually simple dipole decomposition of the signal contributors, to an SEA-based pattern matching exercise.

GPR measurements were carried out with an ultra-wideband ( $\sim 10$  MHz to  $\sim 800$  MHz) fully polarimetric GPR developed by the Ohio State University Electroscience Laboratory (OSU/ESL). Data taken for blind tests at our testplots (Section 8.4) derived from a new, improved GPR developed in the course of this project (Section 3). The measurements discussed in this section were taken with an antecedent instrument developed during ESTCP sponsorship [44]. Methods of parameter extraction are given in that and in preceding references, and are sketched in Section 3.1 above. Data were taken on a backyard sand pit at the OSU-ESL along a grid with lines parallel and perpendicular to the axis of a buried 105 mm projectile, which was buried together with a piece of ordnance scrap (Figure 132). Path 2 was parallel to the axis of the UXO, perpendicular to the clutter orientation, and passed directly over the objects. Elements of the scattering matrix are shown in the figure, including  $S_{11}$  (both transmitted and received fields parallel to the direction of the path), and  $S_{22}$  (both transmitted and received fields perpendicular to the direction of the path). The horizontal axis corresponds to position along the survey transect while the vertical axis shows arrival time of the signals, loosely corresponding to (round trip) depth or distance to a reflector. A significant, linearly elongated response appears in the  $S_{11}$  data, but not in  $S_{22}$ , at around  $x = 40$  inches (the UXO). Another response is found around  $x$ -position 80 inches but only in  $S_{22}$  (the clutter). Each object responded most strongly to the component oriented in its principal direction. Thus this data set indicates that there is more than one object present. This is not uniformly evident in the EMI data, in which the signals from the two objects overlap, as illustrated in Figure 131.

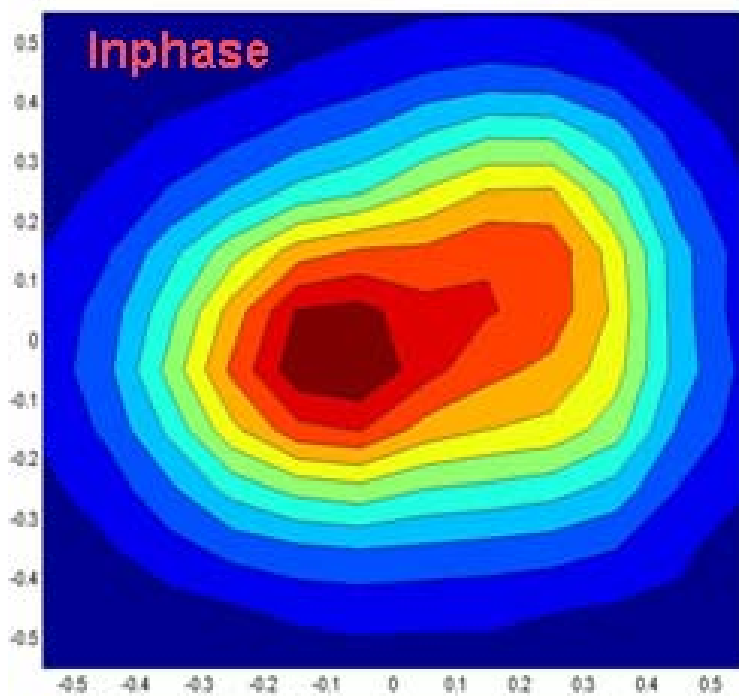


Figure 131. Example EMI signal contours over the scrap plus 105 mm combination, on a 1 m by 1 m grid.

Examination of this GPR data along with that particularly from paths 4 and 6 suggests that there are two objects at the centers of paths 4 and 6. Once the number of targets is determined, some of their positional details may be inferred. Based on measured dielectric constants, timing of closest response, and the centers of the various responses in the profile, we may estimate that relative to the path 2 midpoint  $x \sim -15$  cm,  $y \sim 0$ , and  $z \sim -53$  cm for the first object (UXO); and  $x \sim 30$  cm,  $y \sim 0$ , and  $z \sim -44$  cm for the second one (clutter).

For this simple configuration, azimuthal orientation ( $\phi$ ) can be estimated from the scattered field responses in terms of  $S_{11}$  and  $S_{22}$ , and more particularly from analyses of the direction in the horizontal plane of the dominant, late time resonances. Figure 132 suggests that the left target is inclined at roughly  $\theta \sim \frac{3}{4}\pi$  from the horizontal; the second pattern looks more or less level  $\theta \sim 0$ . The target length and linearity feature of the targets can also be estimated from GPR data (Figure 133). Late time resonance (visible in processing but not in the gray scale profiles in the figure) indicated that both objects are elongated. The target length is estimated from late time resonant frequencies, for a soil dielectric constant estimated to be about 9. In this case, the resonant peaks for the two objects are around 100 MHz and 170

MHz, which suggest 50 cm and 30 cm lengths, respectively. We use these values as going estimates, to feed into the analysis in later steps as a first guess.

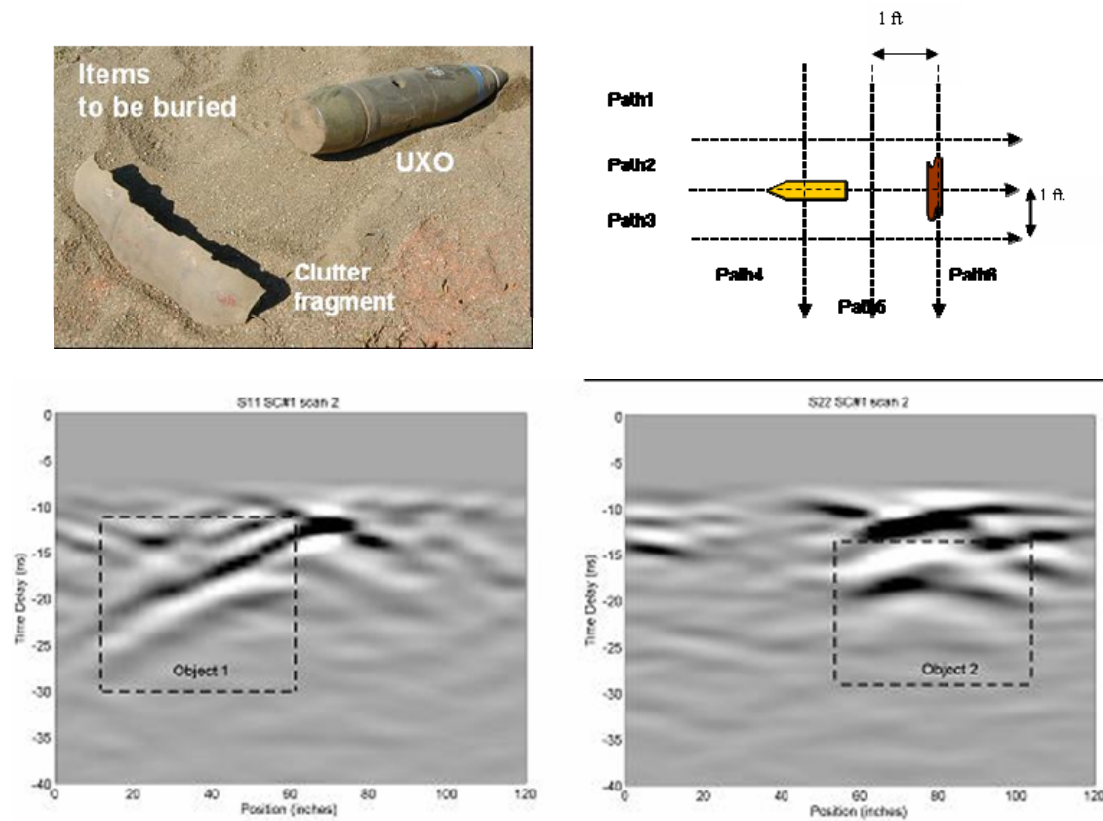


Figure 132. Upper left: Ordnance scrap and 105 mm projectile, in approximately the relationship in which they are to be buried. Upper right: survey path geometry.  $S_{11}$  (lower left) and  $S_{22}$  (lower right) signal profiles along path 2.

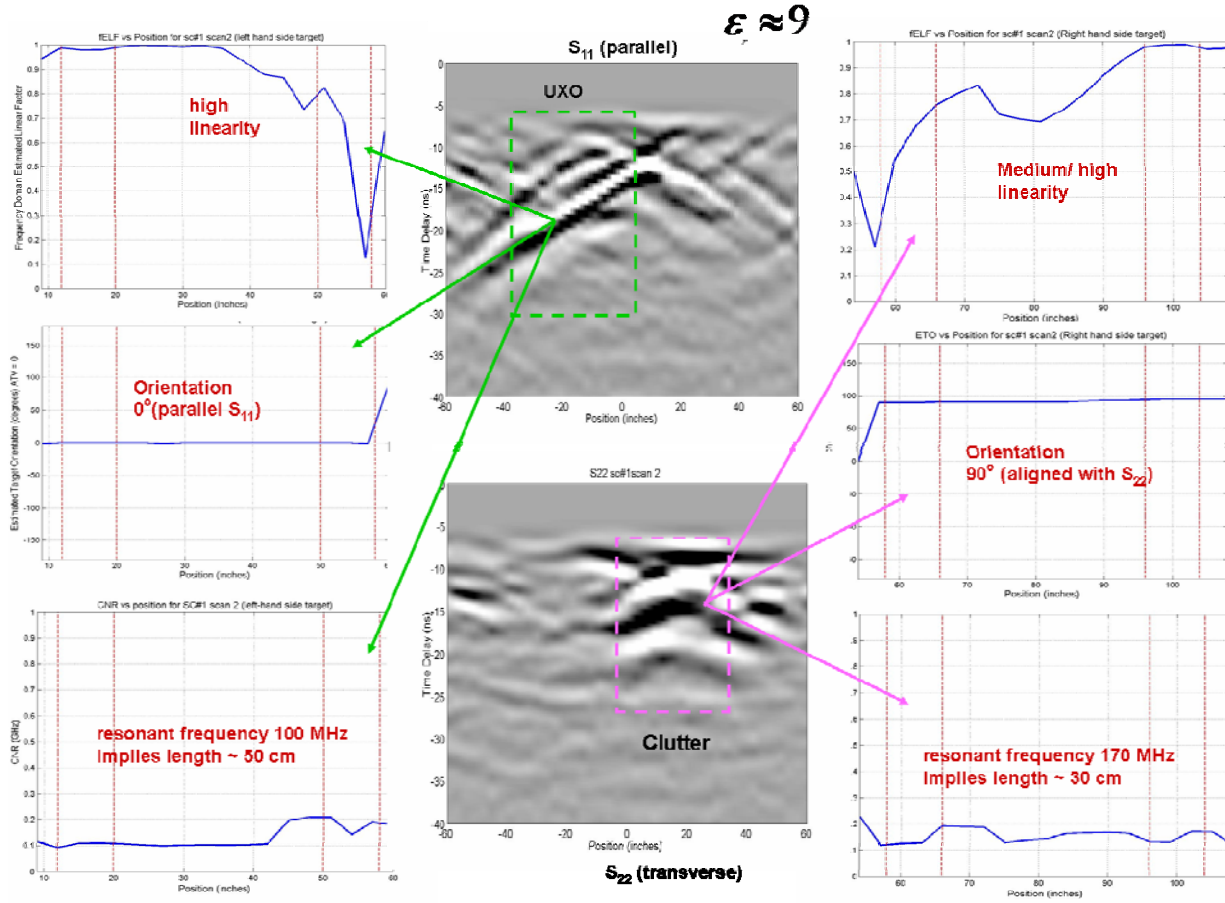


Figure 133. Different polarizations in the same GPR profile indicate two objects. Analysis of GPR processing parameters produces estimates of object properties.

The next stage of analysis consists of dipole decomposition of the EMI data. That is, optimization calculations determine two tri-axial dipoles, with their positions and orientations, which together reproduce the data (Section 2.6.4). The eigenvalues  $\beta_i$  of the magnetic polarizability matrix for each object is then examined. Figure 134 shows the results of such an optimization, obtained with the position and orientation values from the GPR analysis fed in as initial guesses, with reasonable bands around the values as search constraints.

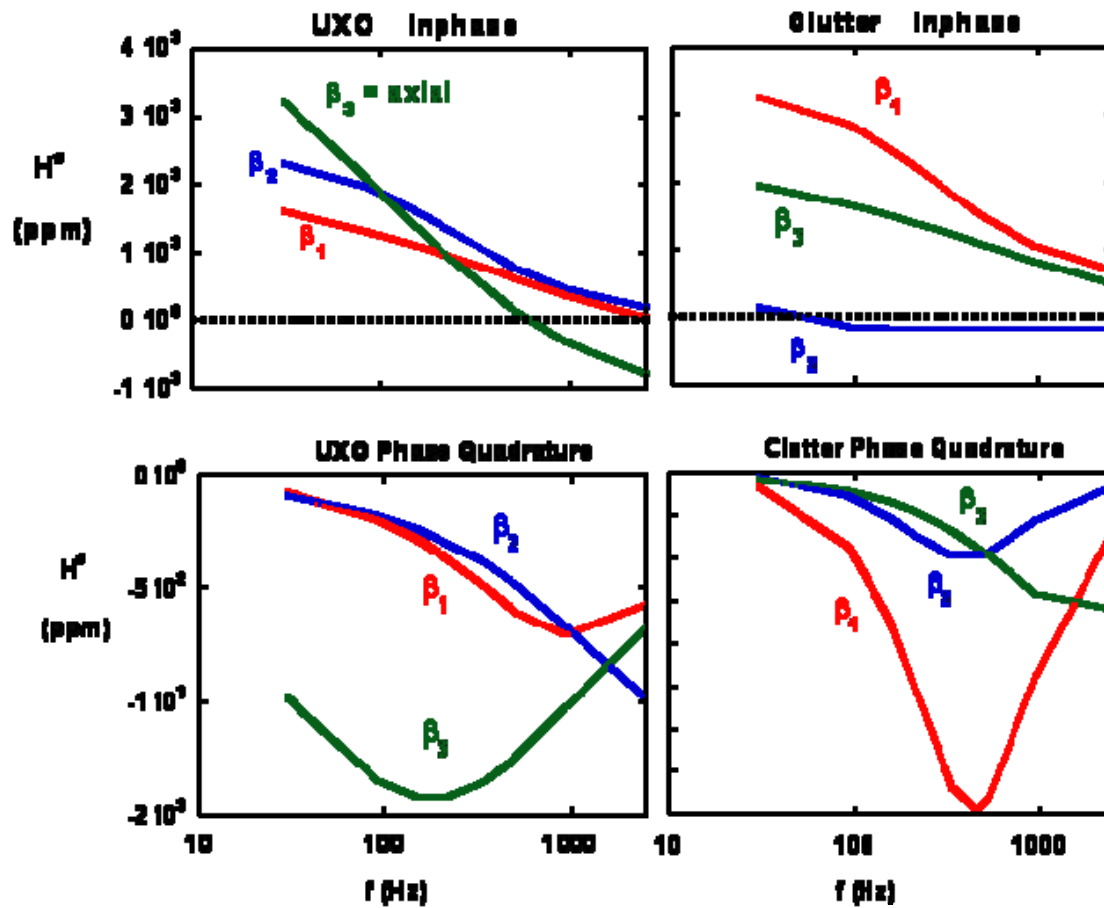


Figure 134. Magnetic polarizability values obtained for the two objects by optimization.

The  $\beta_{ii}$  spectra for the two objects suggests that the first one is a BOR with one dominant polarizability eigenvalue; the other object is probably a non-BOR and thus is ruled clutter.

In the next step, data for the “suspicious” object #1 alone is extracted by using its inferred dipole representation in standard expressions (Section 2.6.4). This data is then subjected to pattern matching tests for known UXO types. Only two UXO’s in the library of candidates have lengths of about 50 cm, namely a 105 mm projectile and 81 mm mortar (Figure 135), for which SEA models were previously established and tested independently. The pattern matching optimization reports a matching factor,  $\alpha$

$$\alpha = 1 - \frac{\sum_f \sum_i |H_i^m(f) - H_i^d(f)|^2 w_i(f)}{\sum_f \sum_i |H_i^m(f)|^2 w_i(f)}, \quad w_i(f) = \frac{1}{|H_i^d(f)| + 10} \quad (108)$$

where  $H_i^m$  is a value from the model,  $H_i^d$  is from the data,  $w$  is a weighting function, and summation is over measurement grid position ( $i$ ) and frequency ( $f$ ). This weighting function is intended to reduce the contribution of measurements at points too far or too close to the sensor because those are most vulnerable to high noise levels or position error.

The optimization produces a best match of 90.3% for the 105 mm projectile and 65.6% for the mortar, suggesting correctly that object 1 is the 105 mm UXO.



Figure 135. Two UXO's and their matching factor  $\alpha$  values, for object #1.

Altogether, the multi-stage processing procedure combining GPR and EMI information can be outlined as follows:

### **Step 1. Discrimination with GPR Data**

GPR analysis estimates, where possible, the number of objects, their positions, orientations, lengths, and “linearity” (evidence of elongation).

### **Step 2. Simple Dipole Model**

Take advantage of GPR results to substantially minimize optimization time and risk. Divide the process into two subtasks:

1. Apply a two-dipole model with specified location and orientation, according to the GPR estimates: The problem entails only the real and imaginary parts of 6 unknowns, i.e. 3  $\beta_{ii}$  for each object
2. Apply a general, relatively unconstrained two-dipole model: Speed convergence by using the estimated geometrical and  $\beta$  values from the previous steps as a first guess.

### **Step 3. SEA Pattern Matching**

Use the dipole model result of a “suspicious” item to extract its signal. Then perform pattern matching for a library of possible UXO’s, using the SEA as a forward model. The quality of the best match is examined.

#### **8.4. GPR and EMI Blind Processing of Testplot Data**

For multi-target blind discrimination tests with the added element of troublesome soil conditions, outdoor tests were performed on testplots constructed at ERDC-CRREL in Hanover NH. Isolated targets or clusters of two items were buried at shallow depths in designated cells in each plot. Both EMI (GEM-3) and GPR surveys were performed. Each of the soils used showed significant EMI magnetic response, illustrated in Section 2.5.3. One or more of each of the items from the selection of UXO's shown in Figure 136 were emplaced, as were items from the clutter collection in Figure 137. As explained below, for the purposes of the test the 57 mm shell was considered to be below the size level considered significant. It is also minimally elongated. Therefore it was used as a clutter item. Clutter plate LG-22, while not very large, was also emplaced edge up so that in cross section it would be unlikely to resemble a UXO. Two steel spheres were also emplaced as clutter and calibration items, labeled SP-1 (diam ~ 4 in, not shown) and S-1 (diam ~ 3.5 in, Figure 24).

The test site consisted of a row of testplots (Figure 138), each with reinforced concrete walls and floors, 28 feet square and about 6.5 feet deep. These were filled with selected soils from outside the site, as available from local suppliers (Figure 138, bottom). For the tests reported here, plots #2, #3, and #4 were used. Overall, an effort was made to create different soil conditions in the different plots, constructing some combination of environments that might occur naturally. Plot #2 contained a medium, unwashed bank run sand capable of holding some moisture but also draining significantly better than the silts and clays in the other plots. The other two plots were purposely layered, with lower layers (Figure 139) that tended strongly to hold moisture. Note the silt and clay grain size distributions in the bases of these plots (Figure 141 and Figure 142). Naturalistic heterogeneity was also introduced by using unsifted supplies in some of the layers (Figure 140), including the top level of plot #3. As only five target clusters were placed in each plot, in order to avoid positions near the walls, it is not possible to draw meaningful statistical inferences as to correlation between soil type and effects on surveying. Suffice it to say that wet, heterogeneous, distinctly non-ideal conditions prevailed in each plot. Heterogeneity was worsened, especially for GPR, by the plentiful soil disturbances caused by site preparation and target burial.

Figure 143 through Figure 145 show the target cluster arrangements within each plot. Orientation abbreviations include:



NUS(N) 45 = angled nose up at 45 deg from the horizontal, facing south (north);  
NDN 45 = angled nose down at 45 deg from the horizontal, facing to the north;  
HNN = horizontal, nose north;  
VND(U) = vertical, nose down (up);  
HNE(W) = horizontal, nose east (west);  
CHEW = clutter horizontal east-west;  
VNW = vertical (edge up) running east-west.

Table 4 shows how the ground truth was sorted into discrimination classes. When only a single object was present and processing indicated either no second object or a second object consisting of clutter, this was considered a correct classification. This was motivated in large part by an environment that produced substantial signal clutter. If signal processing classed a return as clutter, it was considered a matter of indifference whether the source was a discrete clutter object or more irregular or diffuse clutter sources in the environment.

EMI surveying was performed over grids (Figure 146) laid on the ground and also elevated a few cm, so that all related processing could access two levels of observation. With rare exceptions, the grid was centered over the reference position for each cluster, as indicated by the red dots on Figure 143 through Figure 145. GPR surveying used a wheeled cart with antenna dragged behind (Figure 147), pulled manually by one of the survey crew. Recording, positioning, and controls as described in Section 3. Sets of survey lines followed the pattern shown in Figure 148, with 30 cm line spacing.

Measurements were taken at these testplots by CRREL personnel. Except for the PI, no measurement personnel had contact with the analysts, who resided at Dartmouth (EMI) and Ohio State University (GPR). The analysts were told the approximate locations of the target clusters (i.e. red dots on Figure 143 through Figure 145) with the indication that there were at most two in each cluster; however, they were given no other information on position, orientation, arrangement, or identity of targets. The EMI analysts were familiar with all the targets in Figure 136 but did not know how many of each might be included and did not know if others were included from a larger set they had been studying.



Figure 136. UXO selection used in the testplots, with more than one of some types used.



Figure 137. Clutter items used in the testplot scenarios, in addition to two steel spheres.



Figure 138. Different soil conditions were established in each concrete walled testplot.





Figure 139. Plots #3 and #4 base layers.



Figure 140. Heterogeneous material in Plot #3: Left: base; right: added top layer.

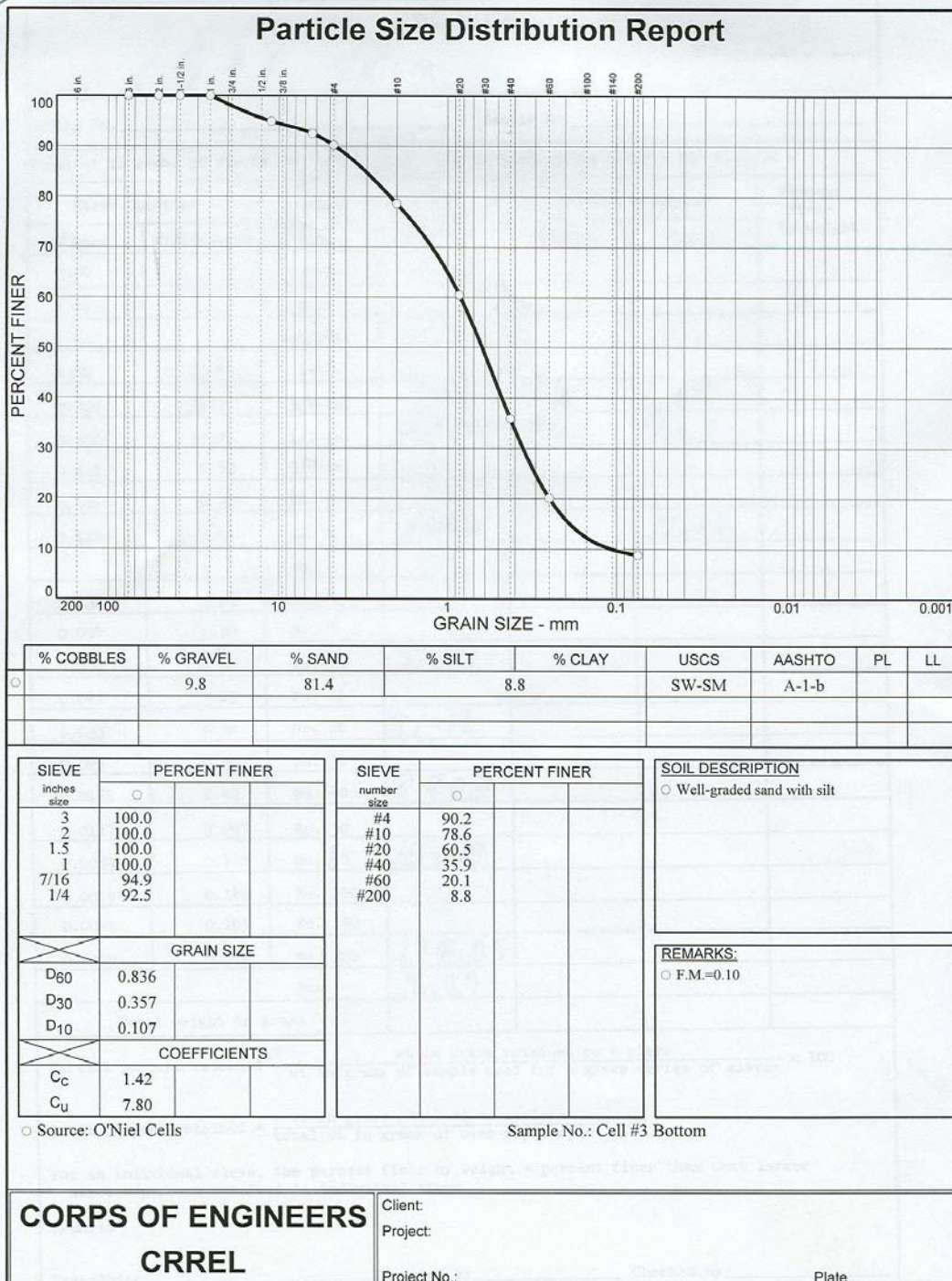


Figure 141. Grain size distribution for base of Plot #3, containing predominately New England Silt.

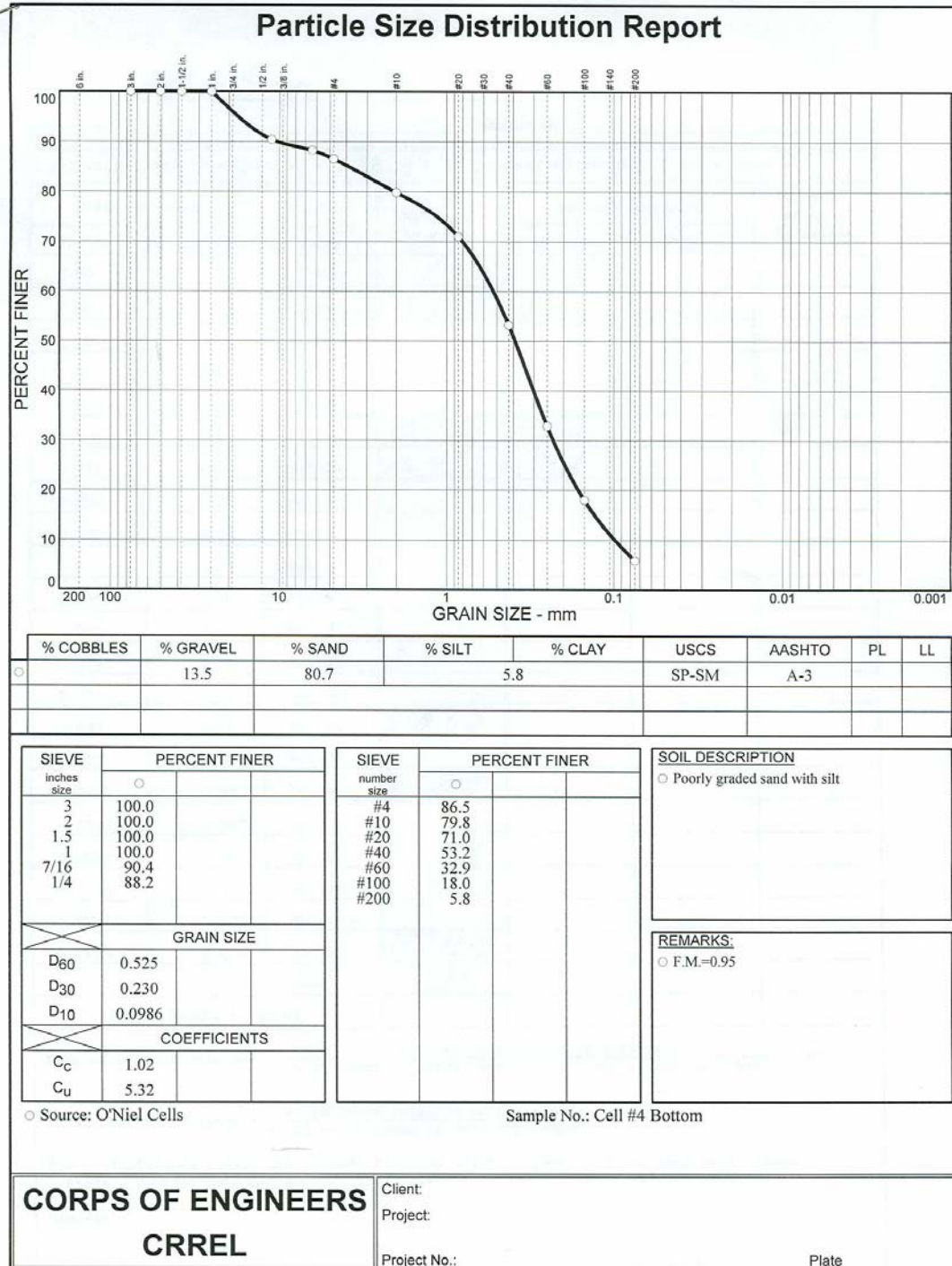


Figure 142. Grain size distribution for base of Plot #4 and top of Plot #3, showing strong silt and clay fractions.



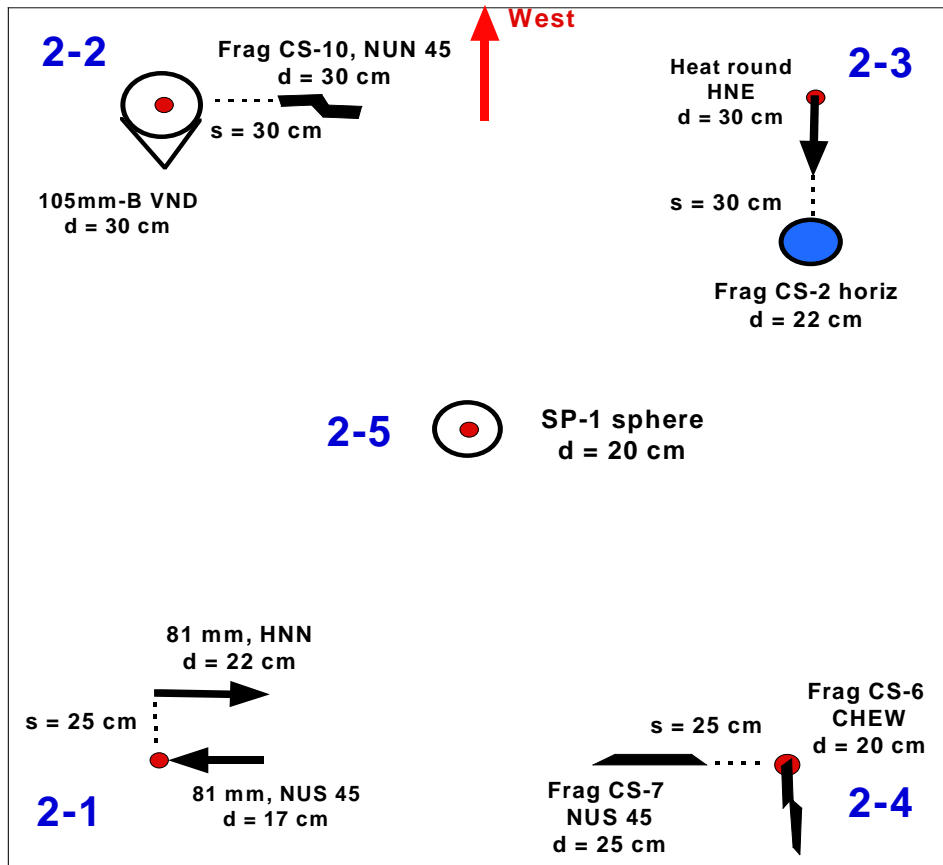


Figure 143. Testplot #2 target arrangements.  $s$  = separation of target edges;  $d$  = depth to shallowest point.



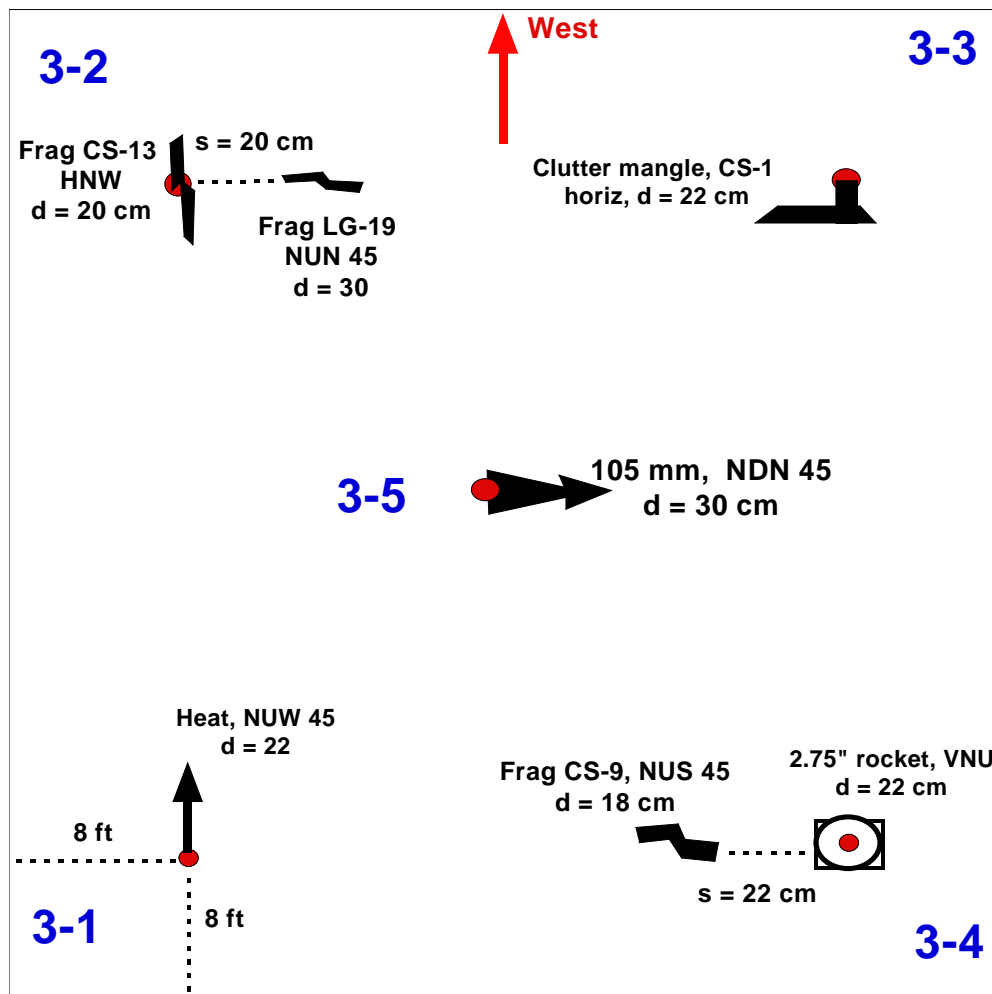


Figure 144. Testplot #3 target arrangements

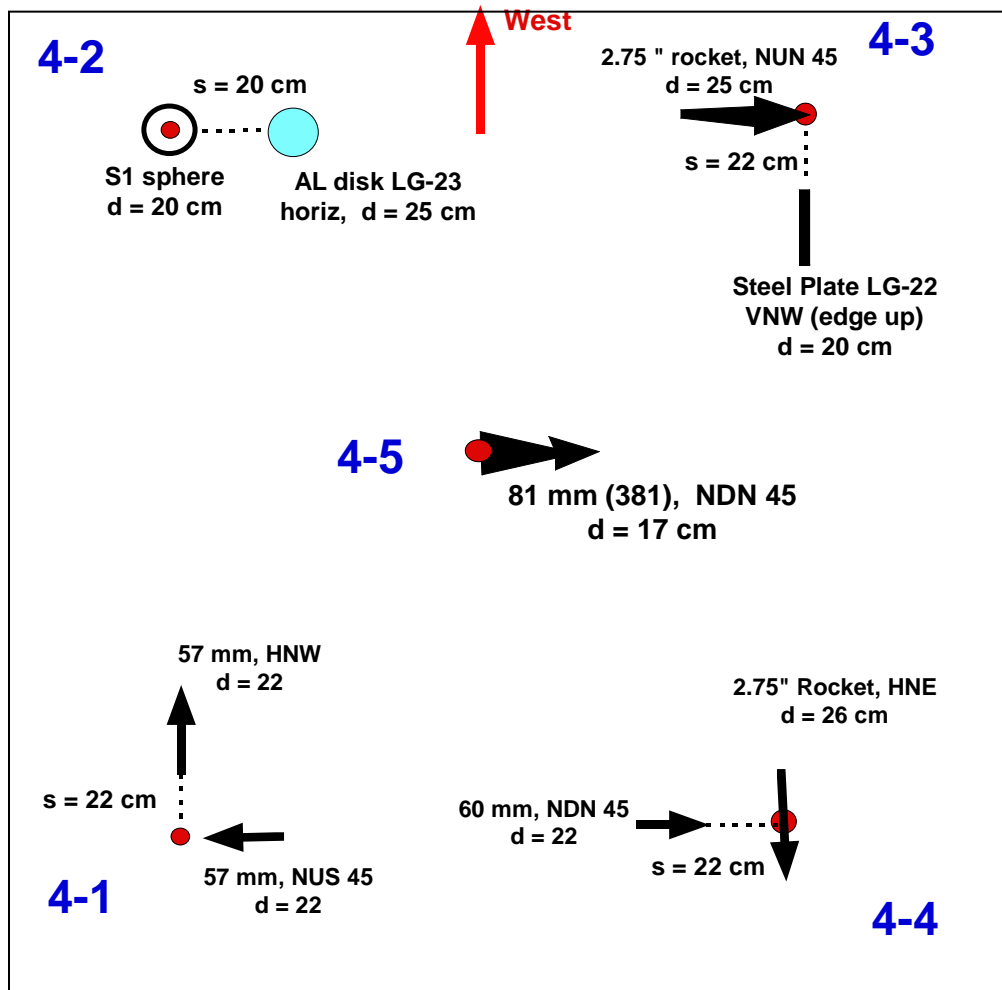


Figure 145. Testplot #4 target arrangements

Table 4. Ground truth for each cluster cell, with corresponding discrimination classes  
CL = clutter; \*\*\* = no target. Note discussion of items 3-2 in text.

location	ground	truth	Discrimination	class
2-1	81 mm	81 mm	UXO	UXO
2-2	105b VND	frag	UXO	CL
2-3	Heat HNE	horiz frag	UXO	CL
2-4	EW frag	NS frag	CL	CL
2-5	Steel sphere	***	CL	CL
3-1	Heat NUW	***	UXO	CL
3-2	EW frag	NS frag	CL	CL
3-3	clutter mangle	***	CL	CL
3-4	2.75" VNU	NS frag	UXO	CL
3-5	105mm NDN	***	UXO	CL
4-1	57mm NUS	57mm HNW	CL	CL
4-2	Steel sphere	AL disk	CL	CL
4-3	2.75" NUN	EW plate edge	UXO	CL
4-4	2.75" HNE	60mm NDN	UXO	UXO
4-5	381 NDN	***	UXO	CL

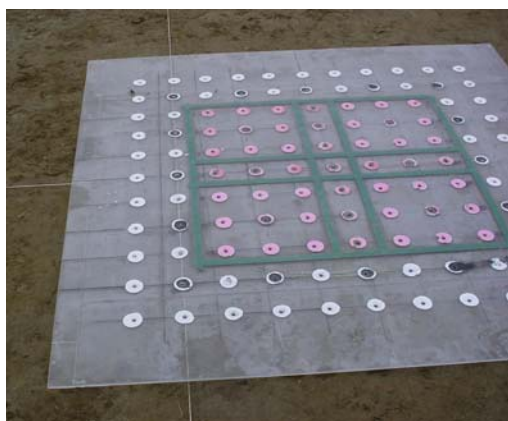


Figure 146. Top: GEM-3 surveys were performed over grids over each target cluster within plots #2, #3, and #4. Bottom, left: Grid of points at 10 cm increments for survey at soil level; right, same for raised grid. The peg at the center of the sensor head fits into holes at each designated position.



Figure 147. GPR cart with antenna pulled behind.

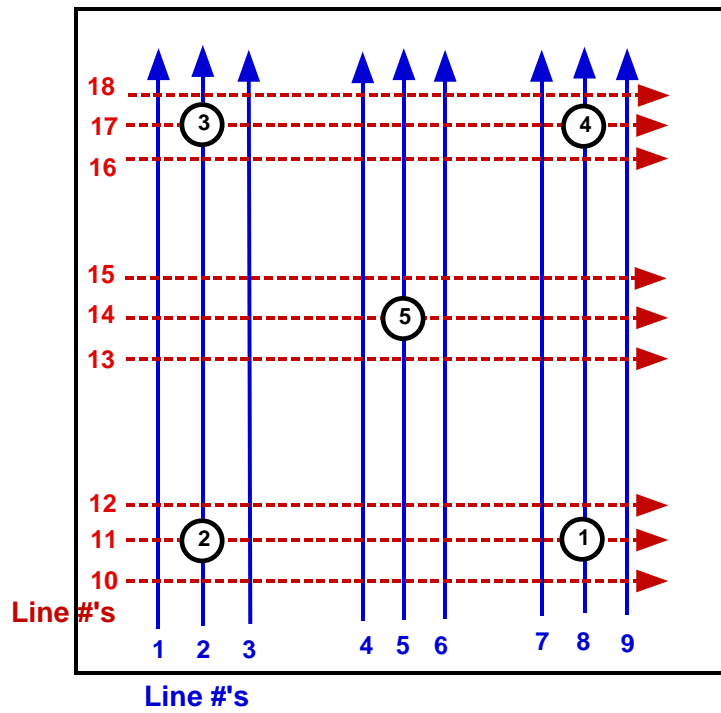


Figure 148. GPR survey pass pattern on testplots, with 30 cm spacing between lines.

### **8.4.1. Processing Results**

In addition to sorting the ground truth into effectively UXO and clutter items, Table 5 classes each cell (cluster) as representing either a “dig” or “no-dig” scenario. A “dig” scenario is one in which at least one of the items present is a UXO (excluding the 57 mm shells). Cases 3-2 represents something of a quandary in that the two pieces of clutter present were both distinctly larger than the UXO size cutoff (labeled “LG CL” above, being CS-13 and LG-19 in Figure 137). For the purposes of Dig/No-Dig judgments, one can consider them as clutter (“criterion 1”) or UXO-like (“criterion 2”).

The NSMC-based EMI processing is described above (Sections 2.4.3, 2.4.4, 2.6.3 and 7.1). Here, to obtain values for background subtraction including soil response, the analyst had to try various samplings of “quiet” areas in the data on grids around the targets. While this was probably the best that could be done, it definitely introduced significant uncertainty in the inphase component, in the form of a probably inaccurate constant shift (Section 2.5). First the processing computed the total NSMC  $Q(f)$  for each of two possible objects contributing to the generally overlapping signal distributions on each grid, expecting a “null object” or noise-like  $Q(f)$  for each insubstantial target. When a  $Q(f)$  resembled one or more of those from UXO’s in the size ranged classed as UXO in the ground truth, the processing deemed the corresponding object to be a UXO. With these criteria, the EMI processing by itself produced the results in Table 6.

On a target-by-target basis (Table 6), this EMI processing correctly detected UXO’s in a strong majority of the cases, under both criterion #1 and criterion #2 (73% to 77%). The false alarm rate ranged from 12% to 21%, depending on the criterion. Especially in view of the difficult soil conditions, this is a good performance. Perhaps more important is the EMI processing performance on a scenario by scenario basis, in terms of correctness of a dig/no-dig judgment. We view a dig judgment as correct is at least one object in the ground truth is in the UXO class. A no-dig judgment is correct only if neither of the objects is in the UXO class. Table 7 shows the performance of the EMI processing alone under these two criteria. Correct detection of dig scenarios is very good, with only a single one missed under either criterion. In the no-dig cases, the processing produced false alarms (FA) in 40% ~ 50% of (this small number of) cases. While the performance is quite good where it is perhaps most crucial, with few missed dig judgments, this is tarnished by the substantial FA rate. We look the GPR for possible help in suppressing the latter.

The GPR processing was not used alone to make decisions on UXO-likeness per se. Rather the results were examined for evidence of key factors, most notably the ELF determined for each object that the GPR processing perceived. A high (near unity) ELF indicates an elongated object with a dominant direction. In 3-4 GPR suggests the presence of two elongated objects, one of which has a resonant frequency (not shown) in the range seen elsewhere for sizable UXO's. This could help steer EMI reprocessing. Beyond that, however, the GPR processing would not have helped EMI in the other cases with missed UXO's: In scenario 2-1 GPR indicates the presence of one elongated object, but EMI has already detected at least one such. In 4-4 GPR completely misses the conclusion of any possible UXO's present.

GPR could be more useful for suppressing false alarms in the two cases where they appear unequivocally (both criteria). In both 3-3 and 4-2 GPR sees nothing at all resembling a UXO type response. For the ambiguous case 3-2, GPR agrees with EMI that two UXO-like objects are present. Therefore the EMI data were re-processed for scenarios 3-3 and 4-2, with only an indication to the EMI analyst that the GPR processing disagreed with the EMI conclusions. This time only the quadrature component of the EMI signal was used because it generally escapes ground effects. Table 8 shows that reprocessing removed the erroneous EMI classifications in both cases. The second run reclassified both objects in cell 3-3 as inconsequential from the point of view of our classification system. In cell 4-2, the first run correctly recognized that one of the objects was a small steel sphere but classified the other non-ferrous object as a non-magnetic rockeye UXO. On reprocessing with EMI quadrature part only, the system recognized that the non-permeable item was not UXO-like (it is an AL disk, LG-23 in Figure 137), while the second object was again small, ferrous, and minimally directional. Thus, in terms of our classification system, both reprocessings produced corrected results, eliminating all false alarms that would cause unnecessary digs under criterion #2.

Table 5. EMI and GPR First Round Processing Results. For EMI, Det = correctly identified as UXO class, CL = correctly classed as non-UXO.

	GT 57 mm size cutoff			EMI		obj#1	GPR		
	Ground	Truth	Class	ID#1	ID#2		ELF	obj#2	ELF
2-1	UXO	UXO	Dig	Det	miss-uxo	UXO	0.8	***	
2-2	UXO	CL	Dig	Det	CL	N/A		N/A	
2-3	UXO	CL	Dig	Det	CL	CL	0.2	CL	0.3
2-4	CL	CL	No-Dig	CL	CL	UXO	0.8	UXO	0.8
2-5	CL	CL	No-Dig	CL	CL	CL	0.3	***	
3-1	UXO	CL	Dig	Det	CL	UXO	0.7	***	
3-2	LG CL	LG CL	Dig/No	UXO	UXO	UXO	0.9	UXO	0.7
3-3	CL	CL	No-Dig	FA	CL	CL	0.2	***	
3-4	UXO	CL	Dig	miss-uxo	CL	UXO	0.9	UXO	0.8
3-5	UXO	CL	Dig	Det	CL	CL	0.3 !!	***	
4-1	CL	CL	No-Dig	CL	CL	poor data			
4-2	CL	CL	No-Dig	CL	FA	CL	0.3		
4-3	UXO	CL	Dig	Det	CL	UXO	0.65		
4-4	UXO	UXO	Dig	Det	miss-uxo	CL	0.3		
4-5	UXO	CL	Dig	Det	CL	UXO	0.5	low confidence	









Table 6. Target by target performance of testplot data processing by EMI alone.

	Criterion 1		Criterion 2	
Truth	11 UXO	19 CL	13 UXO	17 CL
EMI proc	8 Det	4 FA	10 Det	2 FA

Table 7. Scenario by scenario performance of testplot data processing by EMI alone.

	Criterion 1		Criterion 2	
Truth	9 Dig	6 No-Dig	10 Dig	5 No-Dig
EMI proc	8 Dig	3 FA	9 Dig	2 FA

Table 8. EMI reprocessing results for two FA cases

Cell 3-3 (Second run, only quadrature part)		 Or <b>Clutter: obscure signature</b>
Cell 3-3 (First run, both inphase and quadrature parts)		<b>Clutter</b>
Cell 4-2 (Second run, only quadrature part)	<b>Non-permeable clutter</b>	
Cell 4-2 (First run, both inphase and quadrature parts)		

## 9. REFERENCES

1. F. Shubitidze, K. O'Neill, S. A. Haider, K. Sun and K. D. Paulsen (2002). Application of the method of auxiliary sources to the wideband electromagnetic induction problem, *IEEE Trans. Geosci. Rem. Sens.*, 40 (4), 928-942.
2. F. Shubitidze, K. O'Neill, K. Sun, and K.D. Paulsen (2004). Investigation of broadband electromagnetic induction scattering by highly conductive, permeable, arbitrarily shaped 3-D objects, *TGARS*, Vol 42, No. 3, pp 540-556.
3. F. Shubitidze, K O'Neill, I. Shamatava, K. Sun and K.D. Paulsen (2003). Analysis of EMI scattering to support UXO discrimination: heterogeneous and multiple objects, *Proc. SPIE AeroSense: Detection and Remediation Technologies for Mines and Minelike Targets VIII*, 21–25 April 2003, Orlando.
4. C.D. Moss, T.M Grzegorzczuk, K. O'Neill, and J.A. Kong (2006). A hybrid time domain model of electromagnetic induction from conducting, permeable targets, *IEEE Trans. Geosci. Remote Sens.*, Vol 44, No. 10, 2916-2926.
5. K. Sun, K. O'Neill, S.A. Haider, and K.D. Paulsen (2002). Simulation of electromagnetic induction scattering from targets with negligible to moderate penetration by primary fields, *IEEE Trans. Geosci. Remote Sens.*, vol 40, No 4, 910-927.
6. K. Sun, K. O'Neill, F. Shubitidze, I. Shamatava and K.D. Paulsen (2004). Theoretical analysis of TSA formulation and its domain of validity, *IEEE Trans. Geosci. Remote Sens.*, Vol 42, No. 9, 1871 - 1881.
7. F. Shubitidze, K O'Neill, K. Sun, I. Shamatava, and K.D. Paulsen (2005). Fast and accurate calculation of physically complete EMI response by a heterogeneous metallic object, *IEEE Trans. Geosci. & Remote Sensing*, Vol 43, No 8, 1736-1750.
8. K. Sun , K O'Neill, F. Shubitidze, I. Shamatava, K. D. Paulsen (2005). Fast data-derived fundamental spheroidal excitation models with application to UXO identification, *IEEE Trans. Geosci. & Remote Sensing*, Vol 43, No. 11, 2573 – 2583.
9. K. Sun, K. O'Neill, C.-C. Chen, H. S. Youn, B. L. Young, F. Shubitidze, I. Shamatava, K. D. Paulsen (2004). Highly contaminated UXO sites: dual sensor discrimination of clustered targets, *UXO/ Countermine Forum*, March 9-12, 2004. St. Louis.
10. H.A. Haus and J.R. Melcher ( 1989). *Electromagnetic Fields and Energy*, Prentice Hall, 742 pp; full text at [http://web.mit.edu/6.013\\_book/www/](http://web.mit.edu/6.013_book/www/).
11. J.D. Jackson (1999). *Classical Electrodynamics*, 3<sup>rd</sup> Edition, John Wiley & Sons, Inc, 808 pp.
12. K. O'Neill (2003). Ultra-Wideband Electromagnetic Induction for UXO Discrimination, Final Technical Report for SERDP Project CU 1122, UXO Discrimination by Mid-frequency Electromagnetic Induction, 178 pp.

13. F. Shubitidze, K O'Neill, K. Sun, I. Shamatava and K.D. Paulsen (2004). A hybrid full MAS and combined MAS/TSA algorithm for electromagnetic induction sensing, *Appl. Comp. Electromagn. Soc. J.*, vol 19, no 1b, 112-126.
14. F. Shubitidze, K O'Neill, K. Sun, I. Shamatava and K.D. Paulsen, "A combined MAS-TSA algorithm for low frequency electromagnetic induction problems," *Proc. Applied Computational Electromagnetic Symposium 2003*, Monterey, CA, March 24-28, 2003, pp. 566-572.
15. M. Abramowitz and I.A. Stegun (1972). *Handbook of Mathematical Functions*, Nat. Bur. Standards, <http://mintaka.sdsu.edu/faculty/wfw/ABRAMOWITZ-STEGUN/intro.htm>
16. C.D. Moss (2004). Numerical Methods for Electromagnetic Wave Propagation and Scattering in Complex Media, Ph.D. Thesis, MIT, Cambridge, MA.
17. J. Won, D. A. Keiswetter, D. R. Hanson, E. Novikova and T. M. Hall (1997). GEM-3: a monostatic broadband electromagnetic induction sensor, *J.. Envir. Eng. Geophysics*, Vol. 2, No. 1, pp53-64.
18. T.H. Bell, B.J. Barrow, and J.T. Miller (2001). Subsurface Discrimination Using Electromagnetic Induction Sensors, Vol: 39 , No: 6,: 1286 – 1293.
19. Massa, A.; Boni, A.; Donelli, M. (2005). A Classification Approach Based on SVM for Electromagnetic Subsurface Sensing, *IEEE Trans. Geosci. Remote Sens.*, Vol 43, No 9, 2084-2093
20. J.P. Fernandez, B.E. Barrowes, K. O'Neill, K.D. Paulsen, I. Shamatava, F. Shubitidze, and K. Sun (2006). Evaluation of SVM classification of metallic objects based on a magnetic-dipole representation, *proc. SPIE Defense and Security Symp.*, 17-21 April 2006, Orlando.
21. Y. Zhang, L. Collins, H. Yu, C. E. Baum, and L. Carin (2003). Sensing of unexploded ordnance with magnetometer and induction data: theory and signal processing. *IEEE Transactions Geoscience & Remote Sensing*, 41:1005-1015.
22. B.E. Barrowes, K O'Neill, T.M. Grzegorzcyk, Xudong Chen and J.A. Kong (2004). Broadband analytical magneto-quasistatic electromagnetic induction solution for a conducting and permeable spheroid, *IEEE Trans. Geosci. Remote Sens.*, Vol 42 , No. 11, 2479 – 2489.
23. B. E. Barrowes, K. O'Neill, T. M. Grzegorzcyk and J. A. Kong (2003). On the asymptotic expansion of the spheroidal wave function and its eigenvalues for complex size parameter, *Studies Appl. Math. J.*, vol. 113, no. 3, 271-301.
24. B.E. Barrowes (2004). Electromagnetic Scattering and Induction for Spheroidal Geometries. Ph.D. Thesis, MIT.
25. B. Zhang, K. O'Neill, J.A. Kong, and T.M. Grzegorzcyk (2007). Support vector machine and neural network classification of metallic objects using coefficients of the spheroidal MQS response modes, submitted for publ.

26. X. Chen, K. O'Neill, B. E. Barrowes, T. M. Grzegorzcyk, and Jin Au Kong (2004). Application of a spheroidal mode approach with Differential Evolution in inversion of magneto-quasistatic data for UXO discrimination, *Inverse Problems*, Vol 20, No. 6, 27-40.
27. X. Chen, K. O'Neill, T. M. Grzegorzcyk, and Jin Au Kong (2006). Spheroidal mode approach for the characterization of metallic objects using electromagnetic induction, *IEEE Trans. Geosci. Remote Sens.*, Vol 45, No. 3, 697-706.
28. F. Shubitidze, K. O'Neill, B. Barrows, J. P. Fernández, I. Shamatava, K. Sun, and K.D. Paulsen (2007). Application of the normalized surface magnetic charge model to UXO discrimination in cases with overlapping signals, *J. Appl. Geophys.*, Vol 61, Nos 3-4, 292-303.
29. D.K. Butler (2003). Implications of magnetic backgrounds for unexploded ordnance detection, *J. Appl Geophys.*, Vol 54, 111 –125.
30. J. E. Simms, R. J. Larson, and E. W. Smith (2003), UXO Standardized Test Sites: YPG Soils Description, at <http://aec.army.mil/usaec/technology/uxo03c02.html>.
31. J.R. Wait (1982). *Geo-Electromagnetism*, Academic press, 268 pp.
32. S.D. Billings, L.R. Pasion, D. W. Oldenburg, and J. Foley, J. (2003). The influence of magnetic viscosity on electromagnetic sensors: EUDEM-SCOT2 2003, *Int'l Conf. on Requirements & Technol. for Detection, Removal & Neutralization of Landmines and UXO*, Brussels, Sept. 15-18, 2003.
33. M. Dabas, A. Jolivet and A. Tabbagh (1992). Magnetic susceptibility and viscosity of soils in a weak time varying field, *Geophys. J. Int.*, Vol. 108, pp. 101-109.
34. Irma Shamatava, K. O'Neill, F. Shubitidze, K. Sun, and K.D. Paulsen (2005). Treatment of a permeable non-conducting medium with the EMI-BOR program, *SPIE Defense & Security Symp.*, 28 Mar – 1 Apr 2005, Orlando.
35. Irma Shamatava, K. O'Neill, F. Shubitidze, B. Barrows, J. P. Fernández, K. Sun, and P.D. Paulsen (2006). Investigation of electromagnetic induction scattering from magnetically susceptible rough surfaces, *proc. SPIE Defense and Security Symp.*, 17-21 April 2006, Orlando.
36. Storn R and Price K (1997). Differential evolution—a simple and efficient heuristic for global optimization over continuous spaces, *J. Global Optim.*, Vol 11, 341–59
37. H. Huang and I.J. Won (2003). Automated identification of buried landmines using normalized electromagnetic induction spectroscopy, *IEEE Trans. Geosci. Remote Sens.*, Vol 41, No 3, 640-651.
38. K.V. Price, R.M. Storn and J.A. Lampinen (2005). *Differential Evolution, A Practical Approach to Global Optimization*, Natural Computing Series, XX, 538 pp
39. L. M. Collins, P. Gao, P., and L Carin (1999). An improved Bayesian decision theoretic approach for land mine detection”, *IEEE Trans. Geoscience and Remote Sensing*, Vol 37, No 2, 811-819.
40. K. Sun, K. O'Neill, L. Liu, F. Shubitidze, I. Shamatava (2003). Application of Bayesian inversion of electromagnetic induction data for UXO discrimination, *Proc. Symp. Applic.*

Geophys. Engg & Environ. Problems (SAGEEP), San Antonio TX, 6-10 Apr 2003, p1469-1478.

41. K. Sun, K. O'Neill, L. Liu, F. Shubitidze, and I. Shamatava (2003). Application of Bayesian inversion of scatterer shape from EMI data, 2003 IEEE AP-S Int'l Symp. & USNC/CNC/URSI Nat'l Radio Sci. Mtg, Columbus, OH, June 22-27, 2003.
42. Wei Hu, S.L. Tatum, and L.M. Collins (2004). EMI-based classification of multiple closely spaced subsurface objects via independent component analysis, IEEE Trans. Geosci. Remote Sens., Vol 42, No 11, 2544- 2554.
43. C-C. Chen, M.B. Higgins, K. O'Neill and R. Detsch (2001). UWB Fully-polarimetric GPR Classification of Subsurface Unexploded Ordnance, TGARS, Vol 39, No 6, 1221-1230.
44. K. O'Neill (2005). Ultra-wideband, Fully Polarimetric Ground Penetrating Radar for UXO Discrimination, ESTCP Final Technical Report for project #199902.
45. M.B. Higgins, C-C Chen, and K. O'Neill (2001). Improvement of UXO classification based on fully polarimetric GPR data, Proc. UXO Forum, New Orleans, April 10-12, 2001 (CDROM).
46. Chi-Chih Chen, M. B. Higgins and K. O'Neill (2002). Advanced classification of buried UXO using a broadband, fully polarimetric ground penetrating radar, Proc. IGARSS'02, Toronto, June 24-28, 2002, Vol III, p.1569-71.
47. C. Jutten and J. Herault (1991). Blind Separation of Source, Signal Processing, Vol 24, 1-10.
48. T.M. Cover and J.A. Thomas (1991). *Elements of Information Theory*. Wiley
49. M. Jones and R. Sibson (1987). What is projection pursuit? *J. of the Royal Statistical Society, Ser. A*, 150:1-36
50. A.Hyvärinen and E. Oja (2000). Independent Component Analysis: Algorithms and Applications. *Neural Networks*, 13(4-5):411-430.
51. A. Hyvärinen (1998). New Approximations of Differential Entropy for Independent Component Analysis and Projection Pursuit. In *Advances in Neural Information Processing Systems 10*, pp. 273-279, MIT Press.
52. H-S. Youn and C-C Chen (2006). Study of Impact from Clustered Objects on GPR-based UXO Classification Technology, OSU-ESL Technical Report 743626.
53. H. Braunisch, C.O. Ao, K. O'Neill, and J.A. Kong (2000). Magneto-quasi-static response of a distribution of small conducting and permeable objects, proc. IGARSS'2000, Honolulu, 24-28 July 2000, Vol 4, 1424-1426.
54. F. Shubitidze, K O'Neill, K. Sun, and I. Shamatava (2003). Interaction between highly conducting and permeable metallic objects in the low frequency EMI range, Proc. ACES (Applied Computational Electromagnetics Symp), Monterey CA, 24-28 Mar 2003, 625-631.

55. F. Shubitidze, K. O'Neill, K. Sun, I. Shamatava and K.D. Paulsen (2003). Analysis of EMI Scattering to Support UXO Discrimination: Heterogeneous and Multiple Objects, SPIE'03, Orlando, 21-25 April 03.
56. J.R. Wait (1951). A conducting sphere in a time varying magnetic field, *Geophysics*, vol. 16, 666-672.
57. S. Ward and G. Hohmann (1987). Electromagnetic Theory for Geophysical Applications, in *Electromagnetic Theory in Applied Geophysics*, Soc. Exploration Geophys., Tulsa OK.

## 10. ABBREVIATIONS

BOR: Body of revolution

BSS: Blind source separation

CHEW: clutter horizontal east-west

CNR: complex natural resonance

CRREL: Cold Regions Research and Engineering Laboratory

DDC: Digital down converter

DDS: Direct digital frequency synthesis

DE: Differential evolution

DOT: Direction of travel

ELF: Estimated linearity factor

EMI: Electromagnetic induction

ERDC: U.S. Army Corps of Engineers Research and Development Center

ETO: Estimated target orientation

FA: False alarm

FD: Frequency domain

GUI: Graphical user interface

HFB: Horn-fed bowtie

HFE-BIEM: Hybrid Finite Element – Boundary Integral Equation Method

HNE(W): horizontal, nose east (west)

HNN: horizontal, nose north

IC: Independent component

ICA: Independent component analysis

MAS: Method of Auxiliary Sources

MQS: Magneto-quasistatic

NDN 45: angled nose down at 45 deg from the horizontal, facing to the north

NSMC: Normalized Surface Magnetic Charge

NUS(N) 45: angled nose up at 45 deg from the horizontal, facing south (north)

OSU-ESL: Ohio State University ElectroScience Laboratory

PDF: Probability density function

PI: Principal investigator

Rx: Receiver

SCR: Signal to clutter ratio

SEA: Standardized excitations approach

SLS: Simple least squares

SMA: SubMiniature version A connector

SNR: Signal to noise ratio

SWLS: Statistically weighted least squares

TD: Time domain

TSA: Thin skin approximation

Tx: Transmitter

UXO: Unexploded ordnance

UWB: Ultra-wideband

VND(U): vertical, nose down (up)

VNW: vertical (edge up) running east-west



## 11. PUBLICATIONS

The following publications were supported partly or wholly by this project.

### Journals

K. Sun, K O'Neill, I. Shamatava, F. Shubitidze, K. D. Paulsen (2003). A fast forward model for simulating EMI scattering with realistic sensors and elongated objects, *Applied Computational Electromagnetics Society (ACES) J.*, vol 18, no 4, p 97-106.

B. E. Barrowes, K. O'Neill, T. M. Grzegorzczuk and J. A. Kong (2003). On the asymptotic expansion of the spheroidal wave function and its eigenvalues for complex size parameter, *Studies Appl. Math. J.*, vol. 113, no. 3, 271-301.

B.E. Barrowes, K O'Neill, T.M. Grzegorzczuk, Xudong Chen and J.A. Kong (2004). Broadband analytical magneto-quasistatic electromagnetic induction solution for a conducting and permeable spheroid, *TGARS*, Vol 42 , No. 11, 2479 – 2489.

F. Shubitidze, K. O'Neill, K. Sun, and K.D. Paulsen (2004). Investigation of broadband electromagnetic induction scattering by highly conductive, permeable, arbitrarily shaped 3-D objects, *TGARS*, Vol 42, No. 3, pp 540-556.

F. Shubitidze, K O'Neill, K. Sun, I. Shamatava and K.D. Paulsen (2004). A hybrid full MAS and combined MAS/TSA algorithm for electromagnetic induction sensing, *Appl. Comp. Electromagn. Soc. J.*, vol 19, no 1b, 112-126.

F. Shubitidze, K O'Neill, K. Sun, I. Shamatava and K.D. Paulsen (2004). Coupling between highly conducting and permeable metallic objects in the EMI frequency range, *Appl. Comp. Electromagn. Soc. J.*, vol 19, No 1b, 139-148.

X. Chen, K. O'Neill, B. E. Barrowes, T. M. Grzegorzczuk, and Jin Au Kong (2004). Application of a spheroidal mode approach with Differential Evolution in inversion of magneto-quasistatic data for UXO discrimination, *Inverse Problems*, Vol 20, No. 6, 27-40.

K. Sun, K. O'Neill, F. Shubitidze, I. Shamatava and K.D. Paulsen (2004). Theoretical analysis of TSA formulation and its domain of validity, *TGARS*, Vol 42, No. 9, 1871 - 1881.

F. Shubitidze, K O'Neill, K. Sun, I. Shamatava, and K.D. Paulsen (2005). Fast and accurate calculation of physically complete EMI response by a heterogeneous metallic object, *IEEE Trans. Geosci. & Remote Sensing*, Vol 43, No 8, 1736-1750.

K. Sun , K O'Neill, F. Shubitidze, I. Shamatava, K. D. Paulsen (2005). Fast data-derived fundamental spheroidal excitation models with application to UXO identification, *IEEE Trans. Geosci. & Remote Sensing*, Vol 43, No. 11, 2573 – 2583.

K. O'Neill, K. Sun, F. Shubitidze, I. Shamatava, and K.D. Paulsen (2006). Accounting for the effects of widespread discrete clutter in subsurface EMI remote sensing and discrimination, IEEE Trans. Geosci. Remote Sens., Vol 44, No. 1, 32-46.

C.D. Moss, T.M Grzegorzczuk, K. O'Neill, and J.A. Kong (2006). A hybrid time domain model of electromagnetic induction from conducting, permeable targets, IEEE Trans. Geosci. Remote Sens., Vol 44, No. 10, 2916-2926.

F. Shubitidze, K. O'Neill, B. Barrows, J. P. Fernández, I. Shamatava, K. Sun, and K.D. Paulsen (2007). Application of the normalized surface magnetic charge model to UXO discrimination in cases with overlapping signals, J. Appl. Geophys., Vol 61, Nos3-4, 292-303.

X. Chen, K. O'Neill, T. M. Grzegorzczuk, and Jin Au Kong (2007). Spheroidal mode approach for the characterization of metallic objects using electromagnetic induction, IEEE Trans. Geosci. Remote Sens., Vol 45, No. 3, 697-706.

Conferences (full paper published):

F. Shubitidze, K O'Neill, K. Sun, and I. Shamatava (2003). Interaction between highly conducting and permeable metallic objects in the low frequency EMI range, Proc. ACES (Applied Computational Electromagnetics Symp), 2003, Monterey CA, 24-28 Mar 2003, p.625-631.

F. Shubitidze, K O'Neill, K. Sun, and I. Shamatava (2003). A combined MAS-TSA algorithm for low frequency broadband electromagnetic induction problems, Proc. ACES, 2003, Monterey CA, 24-28 Mar 2003, p.566-572.

K. Sun, K O'Neill, I. Shamatava, F. Shubitidze (2003). Application of prolate spheroid solutions in simulation of EMI scattering with realistic sensors and objects, Proc. ACES, 2003, Monterey CA, 24-28 Mar 2003, p.531-537.

C. D. Moss, K. O'Neill, T.M. Grzegorzczuk, and J.A. Kong (2003). A hybrid time domain method to calculate electromagnetic induction scattering from targets with arbitrary skin depths, Proc. ACES, 2003, Monterey CA, 24-28 Mar 2003, p.390-396.

F. Shubitidze, K. O'Neill, K. Sun, I. Shamatava and K.D. Paulsen (2003). Analysis of EMI scattering to support UXO discrimination: heterogeneous and multiple objects, SPIE Aerosense, Orlando, 21-25 April 03, Vol 5089, 928-939.

K. O'Neill, K. Sun, F. Shubitidze, I. Shamatava, L. Liu, K. D. Paulsen, Chi-Chih Chen, and R. Lee (2003). Dealing with clutter in inversion and classification schemes for buried UXO discrimination, SPIE'03, Orlando, 21-25 April 03, 916-927.

- K. Sun, K. O'Neill, Lanbo Liu, F. Shubitidze, I. Shamatava and K.D. Paulsen (2003). Analytical solutions for EMI scattering from general spheroids with application in signal inversion for UXO discrimination, SPIE'03, Orlando, 21-25 April 03, Vol 5089, 1035-1045.
- K. Sun, K. O'Neill, L. Liu, F. Shubitidze, I. Shamatava (2003). Application of Bayesian inversion of electromagnetic induction data for UXO discrimination, Proc. Symp. Applic. Geophys. Engg & Environ. Problems (SAGEEP), San Antonio TX, 6-10 Apr 2003, p1469-1478.
- K. Sun, K. O'Neill, L. Liu, F. Shubitidze, and I. Shamatava (2003). Application of Bayesian inversion of scatterer shape from EMI data, 2003 IEEE AP-S Int'l Symp. & USNC/CNC/URSI Nat'l Radio Sci. Mtg, Columbus, OH, June 22-27, 2003.
- F. Shubitidze, K. O'Neill, and K.D. Paulsen (2003). Investigation of side looking EM field scattering from a buried metallic object to support UXO discrimination, 2003 IEEE AP-S Int'l Symp. & USNC/CNC/URSI Nat'l Radio Sci. Mtg, Columbus, OH, June 22-27, 2003.
- F. Shubitidze, K. O'Neill, K. Sun, I. Shamatava and K.D. Paulsen (2003). Semi-analytical calculation of Jacobian in the electromagnetic inverse scattering problem, 2003 IEEE AP-S Int'l Symp. & USNC/CNC/URSI Nat'l Radio Sci. Mtg, Columbus, OH, June 22-27, 2003.
- F. Shubitidze, K. O'Neill, I. Shamatava, K. Sun and K.D. Paulsen (2003). Analysis of GPR scattering by multiple subsurface metallic objects to improve UXO discrimination, Int'l Geosci. & Remote Sens. Symp, 21-25 July 2003, Toulouse, Vol 7, 4163-65.
- F. Shubitidze, K O'Neill, K. Sun, I. Shamatava and K. D. Paulsen (2003). Fast direct and inverse EMI algorithms for enhanced identification of buried UXO with real EMI data, Int'l Geosci. & Remote Sens. Symp, 21-25 July 2003, Toulouse, Vol 7, 4160-62.
- K. Sun, K. O'Neill, F. Shubitidze, I. Shamatava and K. D. Paulsen (2003). Application of TSA formulation for inversion of a metallic object's electromagnetic properties from EMI data, Int'l Geosci. & Remote Sens. Symp, 21-25 July 2003, Toulouse, Vol 6, 3860-62.
- K. O'Neill, K. Sun, C.C. Chen, F. Shubitidze, and K.D. Paulsen (2003). Combining GPR and EMI data for discrimination of multiple subsurface metallic objects, Int'l Geosci. & Remote Sens. Symp, 21-25 July 2003, Toulouse, Vol 7, 4157-59.
- K. O'Neill, K. Sun, F. Shubitidze, I. Shamatava, and K. D. Paulsen and Chi-Chih Chen (2003). Dual mode UWB remote sensing and processing for enhanced subsurface discrimination and inversion, Proc. Tyrrhenian Int'l Workshop Remote Sens., 15-18 Sept 2003, 283-295.
- K. Sun, K. O'Neill, F. Shubitidze, and Chi-Chih Chen (2004). Highly contaminated UXO sites: dual sensor discrimination of clustered targets, UXO/Countermining Forum, St. Louis, 8-12 Mar 2004.
- I. Shamatava, F. Shubitidze, K. O'Neill, K. Sun, and K.D. Paulsen (2004). An efficient, user-friendly program for computing electromagnetic induction (EMI) responses from heterogeneous objects subject to state-of-the-art sensors, UXO/Countermining Forum, St. Louis, 8-12 Mar 2004.

K. Sun, K O'Neill, F. Shubitidze, I. Shamatava, K. D. Paulsen (2004). Fundamental Mode Approach to forward problem solutions in EMI scattering - Inferring fundamental solutions from training data, Appl. Comput. Electromagn. Symp, 19-23 Apr 2004, Syracuse NY, 531-537.

F. Shubitidze, K O'Neill, I. Shamatava, K. Sun and K.D. Paulsen (2004). A new numerical procedure for efficient and accurate representation of low frequency EM responses for a heterogeneous object, Appl. Comput. Electromagn. Symp, Syracuse NY, 19-23 Apr 2004.

K. O'Neill, IJ Won, A. Oren, Chi-Chih Chen, Hyoun-Sun Youn, X. Chen, and K. Sun (2004). Data diversity for UXO discrimination in realistic settings with a handheld EMI sensor, SPIE Defense & Security Symp., Orlando, FL, 12-16 April 2004, 253-262.

F. Shubitidze, K O'Neill, I. Shamatava, K. Sun and K.D. Paulsen (2004). Use of standardized source sets for enhanced EMI classification of buried heterogeneous objects, SPIE Defense & Security Symp., Orlando, FL, 12-16 April 2004, 263-274.

I. Shamatava, F. Shubitidze, C.C. Chen, H. S. Youn, K O'Neill, and K. Sun (2004). Potential benefits of combining EMI and GPR for enhanced UXO discrimination at highly contaminated sites, SPIE Defense & Security Symp., Orlando, FL, 12-16 April 2004, 1201-1210.

K. Sun, K O'Neill, F. Shubitidze, I. Shamatava, K. D. Paulsen (2004). Fast data-derived fundamental spheroidal excitation models with application to UXO identification, SPIE Defense & Security Symp., Orlando, FL, 12-16 April 2004, 855-865.

F. Shubitidze, K. O'Neill, I. Shamatava, K. Sun and K.D. Paulsen (2004). A standardized excitation approach for classification of buried UXO, Int'l Geosci. & Remote Sens. Symp, September 20-24, 2004, Anchorage, AK.

I. Shamatava, K. O'Neill, F. Shubitidze, K. Sun and K.D. Paulsen (2004). Investigation of EMI sensor orientation and position effects on buried metallic target discrimination, Int'l Conf. Math. Meth. Electromagn. Theory, Sept 14 - 17, 2004, Dnepropetrovsk, Ukraine.

F. Shubitidze, K. O'Neill, I. Shamatava, K. Sun and K.D. Paulsen (2004). Analyzing the effects of conductive and permeable soil on the EMI response for UXO discrimination, Int'l Conf. Math. Meth. Electromagn. Theory, Sept 14 - 17, 2004, Dnepropetrovsk, Ukraine.

I. Shamatava, F. Shubitidze, K. O'Neill, K. Sun and K.D. Paulsen (2004). A simple magnetic charge model for representation of EMI responses from a buried UXO, Proc. DIPED-2004, 155-159.

K. Sun, K. O'Neill, C.-C. Chen, H. S. Youn, F. Shubitidze, I. Shamatava and K. D. Paulsen (2005). Highly contaminated UXO sites: combination of GPR and EMI for discrimination of clustered scatterers, SAGEEP 2005, 1156-1165.

F. Shubitidze, K. O'Neill, I. Shamatava, K. Sun and K.D. Paulsen (2005). A simple magnetic charge model for classification of multiple buried metallic objects in cases with overlapping signals, SAGEEP 2005, 1270-1279..

K. O'Neill, F. Shubitidze, K. Sun, I. Shamatava, and K. D. Paulsen (2005). EMI obscuration of buried UXO by geophysical magnetic permeability, anthropogenic clutter, and by magnitude disparities, SPIE Defense & Security Symp., 28 Mar – 1 Apr 2005, Orlando.

F. Shubitidze, I. Shamatava, K O'Neill, K. Sun, and K.D. Paulsen (2005). Analysis of geological soil effects on EMI responses relevant to UXO discrimination, SPIE Defense & Security Symp., 28 Mar – 1 Apr 2005, Orlando.

K. Sun, K. O'Neill, I. Shamatava, F. Shubitidze, K. D. Paulsen (2005). UXO signature extraction from measurement data - Automatic weighting and regularization, SPIE Defense & Security Symp., 28 Mar – 1 Apr 2005, Orlando.

F. Shubitidze, I. Shamatava, K O'Neill, K. Sun, and K.D. Paulsen (2005). Analyzing multi-axis data versus scalar data for UXO discrimination, SPIE Defense & Security Symp., 28 Mar – 1 Apr 2005, Orlando.

K. Sun, K. O'Neill, I. Shamatava, F. Shubitidze, K. D. Paulsen (2005). Discrimination of UXO buried under magnetic soil, SPIE Defense & Security Symp., 28 Mar – 1 Apr 2005, Orlando.

Irma Shamatava, K. O'Neill, F. Shubitidze, K. Sun, and K.D. Paulsen (2005). Treatment of a permeable non-conducting medium with the EMI-BOR program, SPIE Defense & Security Symp., 28 Mar – 1 Apr 2005, Orlando.

F. Shubitidze, K O'Neill, I. Shamatava, K. Sun, and K.D. Paulsen (2005). Combined differential evolution and surface magnetic charge model algorithm for discrimination of UXO from non-UXO items: Simple and general inversions, SPIE Defense & Security Symp., 28 Mar – 1 Apr 2005, Orlando.

F. Shubitidze, B. E. Barrowes, K. O'Neill, I. Shamatava, J. P. Fernández, K. Sun, and K.D. Paulsen (2006). The generalized SEA for UXO discrimination in geophysical environments producing EMI response, proc. SPIE Defense and Security Symp., 17-21 April 2006, Orlando.

## **12. APPENDIX A: NEW IMPROVED GPR**

### **12.1. Introduction**

During the first project year, exercises in discriminating clustered subsurface objects with our pre-existing GPR indicated that the large antenna footprint presented a substantial limitation. The configuration produced significant antenna scattering from large antenna arms that were designed to couple more low frequency energy into the ground. Such scattering subsequently interacts with intended subsurface objects and complicates scattering pattern signatures. Developing a new antenna with reduced footprint and reduced antenna scattering was needed to enhance clarity and spatial resolution of surveys so that different objects could be more readily distinguished. More and more closely spaced GPR passes or even a 2-D grid data would only make sense with a more spatially concentrated system. Also, a new system was needed that could provide the greater data diversity and density without the long survey times that would be required if one attempted this with the older system. Therefore, the two GPR system development objectives pursued were

1. Design, fabrication and testing of a new faster GPR system that incorporates an advanced digital down converter (DDC) and direct digital frequency synthesis (DDS) technology suitable for UXO detection/classification tasks;
2. Design, fabrication and testing a new small footprint GPR antenna suitable for UXO detection/classification tasks.

### **12.2. Improved Radar Design**

Figure 149 shows the block diagram of the new GPR system suitable for UXO discrimination as well as many other GPR applications. It contains four major parts: (1) RF front-end components such as filters, amplifiers, couplers, switches and attenuators, (2) fast direct digital frequency synthesizers (DDS), (3) dual-channel digital down converter (DDC) and (4) new small dielectric-loaded quad-ridge horn antenna. Each will be described briefly below.

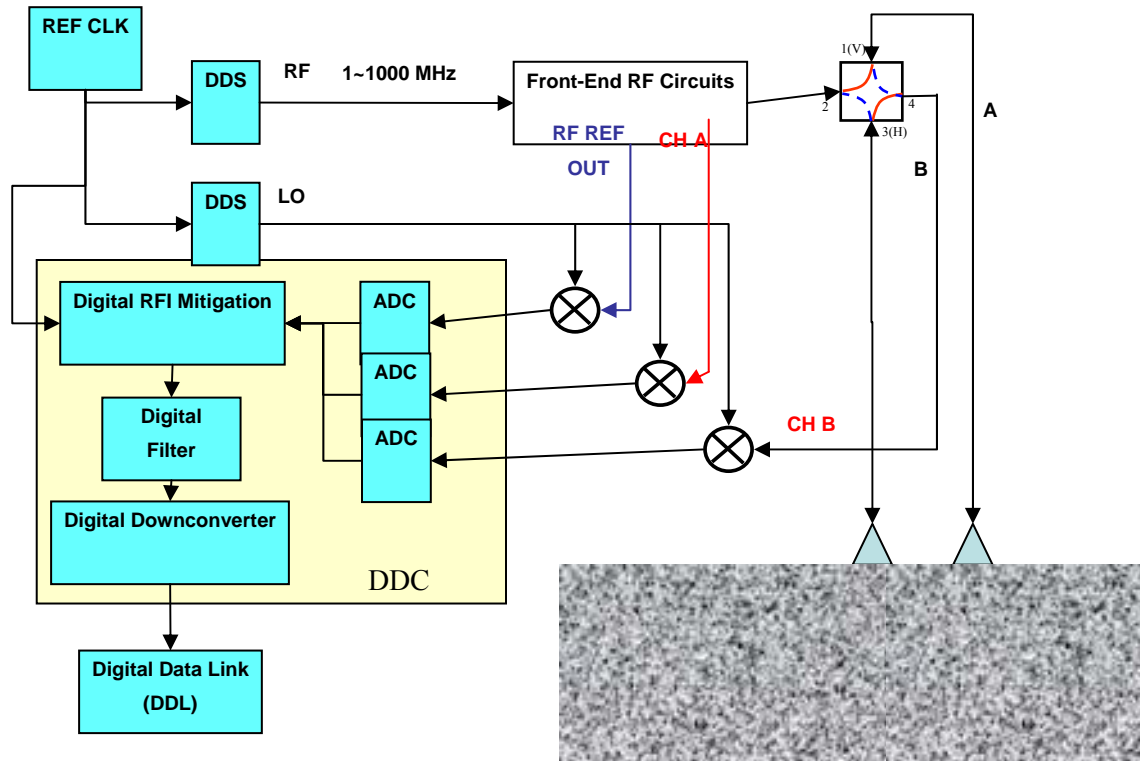


Figure 149 New OSU/ESL GPR System Block Diagram.

### 12.2.1. Front-End RF Design

The transmitting side of a conventional RF front-end circuitry is responsible for up-converting an IF (Intermediate Frequency, < 5MHz) signal to the actual RF (radio frequency, 10~1000 MHz) to be radiated. It does this by mixing the IF signal with a local reference signal (LO). For GPR applications below 1 GHz, the RF signal can be directly synthesized using DDS. RF amplifiers are also used to generate a desired radiation power level. For fully polarimetric measurements, RF switches are also required.

The receiving side of RF front-end circuitry is responsible for down-converting the RF signal to IF frequency such that its frequency is low enough for sampling. Again this frequency down-conversion is achieved by mixing the received RF signal with a local reference (LO) signal. During the frequency sweeping, both IF and LO sweep simultaneously and maintain a fixed frequency difference, i.e. IF frequency. The phase of both RF and LO signals are locked together with respect to a stable reference clock at 10 MHz.

Figure 150 shows the radar hardware where the RF front-end components as well as DDS and DDC parts are all indicated. Figure 63 shows the integrated radar system mounted on a wagon. An encoder in contact with a rear wheel of the wagon measures moving distance and triggers the radar system measurements automatically at predetermined intervals (here, usually every 3 inches).

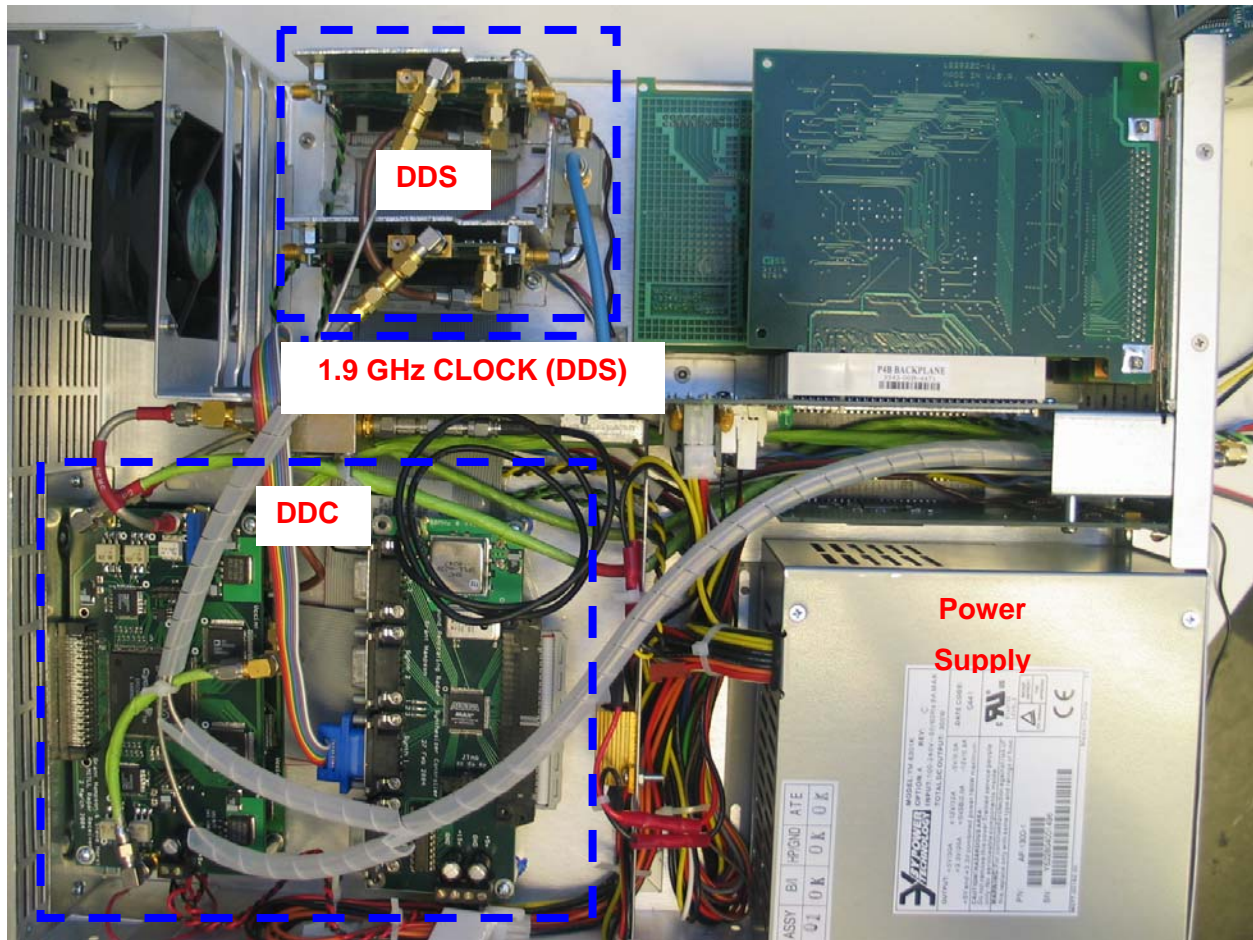


Figure 150 (a) Digital parts of the new radar system.





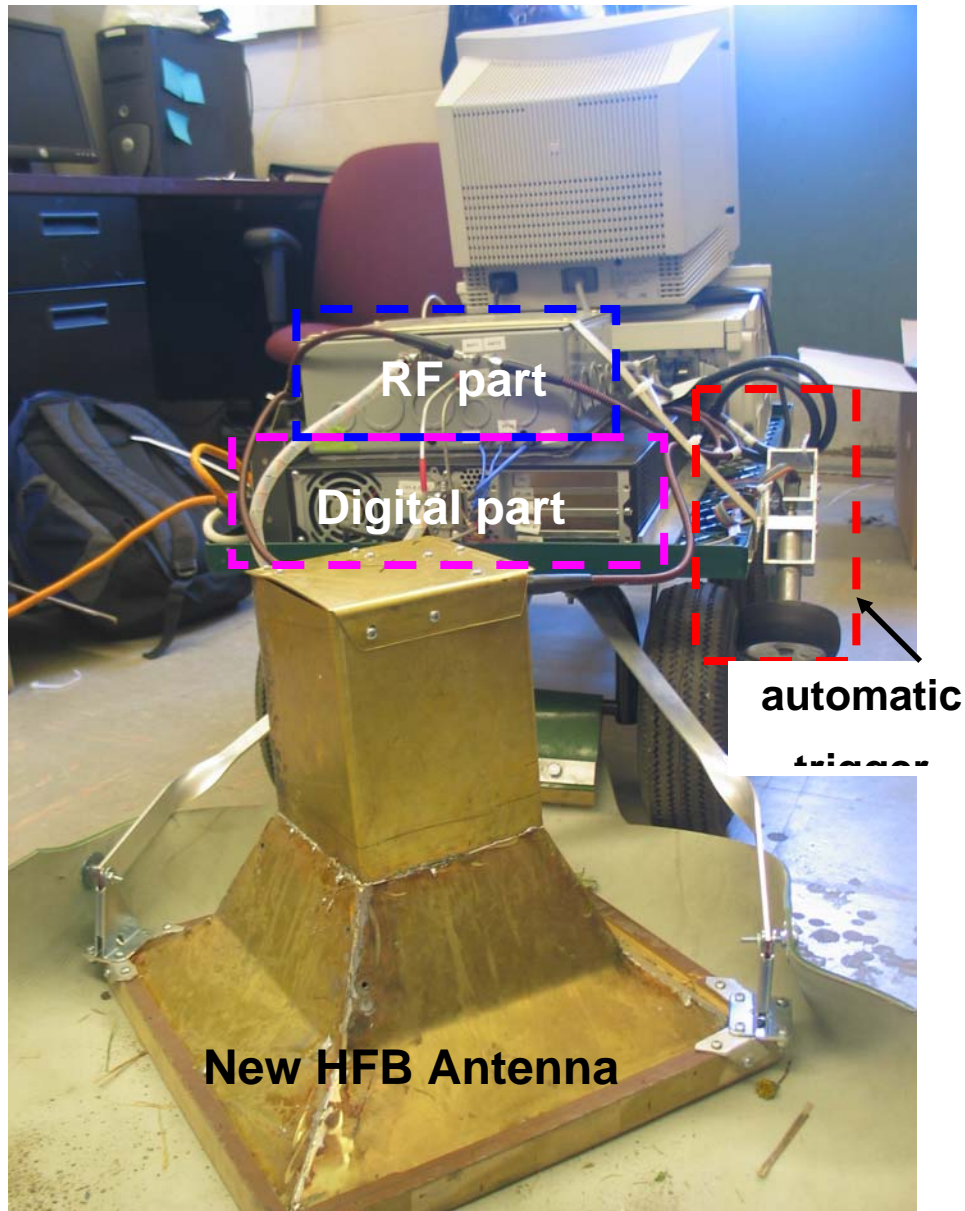


Figure 151 Integrated new dual-channel GPR radar with a miniaturated HFB antenna.

### **12.2.2. Digital Receiver**

Traditional coherent radar receivers employ an I/Q demodulator to extract the real and imaginary parts of the incoming signal or, equivalently, the magnitude and phase parts. This the structure of this function is shown in Figure 152. The down-converted IF signal is mixed with a pair of coherent local reference signals whose amplitudes should be the same and the phase difference should be 90 degrees. It is well known that the amplitude and phase errors (coming from LO generator or mixer characteristics) commonly seen in analog devices has caused undesired information distortion.

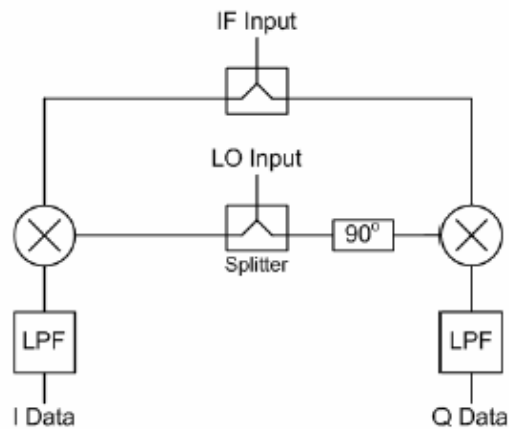


Figure 152 Conventional radar receiver architecture employing analog devices.

The recent advance in integrated RF technology driven by the wireless industry has led to a new generation of RF receiver design. The new technology not only eliminates the need for an analog mixing stage but also provides many desirable capabilities that are attractive for GPR application. Some of these features include compact dimension, lower power consumption, real-time interference mitigation, and simultaneous multiple channel reception. Figure 153 shows the simple architecture of a *Digital Down Converter* (DDC). The input RF signal (10~1000 MHz) is first down converted to an IF (5 MHz) by a conventional mixing method. At this point, all the magnitude and phase information are preserved in the IF signal. The IF signal is then digitized using a fast analog to digital converter (ADC). The digitized data is then fed into a DSP (or FPGA (field programmable gate array) chip inside which I/Q demodulation, integration, and filtering are performed in real time. The resultant data has no phase distortion and has much greater sensitivity compared to its conventional analog counterpart.

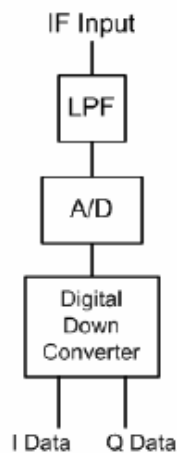


Figure 153 New radar receiver architecture utilizes digital receiver design.

Figure 154 shows a block diagram of the digital receiver, with the actual board shown in Figure 155. The data are sent back to a computer via a fast digital I/O (DIO) interface for storage, display or further processing. The dual-channel digital receiver developed as part of this project accepts two analog RF inputs on panel SMA connectors at 0 dBm full scale into 50 ohms. The A/D converter clock can be driven from an external sample clock supplied through a panel SMA connector, whose power level should be greater than 3 dBm. The receiver includes two independent DDCs, each of which has a numerically controlled oscillator (NCO). The NCO supplies the down-conversion frequency which is tunable from DC to  $f_s/2$ , where  $f_s$  is the sample clock frequency. In the OSU/ESL GPR system, two digital receivers are connected by hotwire and operated in parallel, since the GPR system requires 4 channels in order to realize fully polarimetric measurement. For hotwiring, wire was soldered directly on a pin connector, which controls data acquisition so that each receiver starts at the same time.

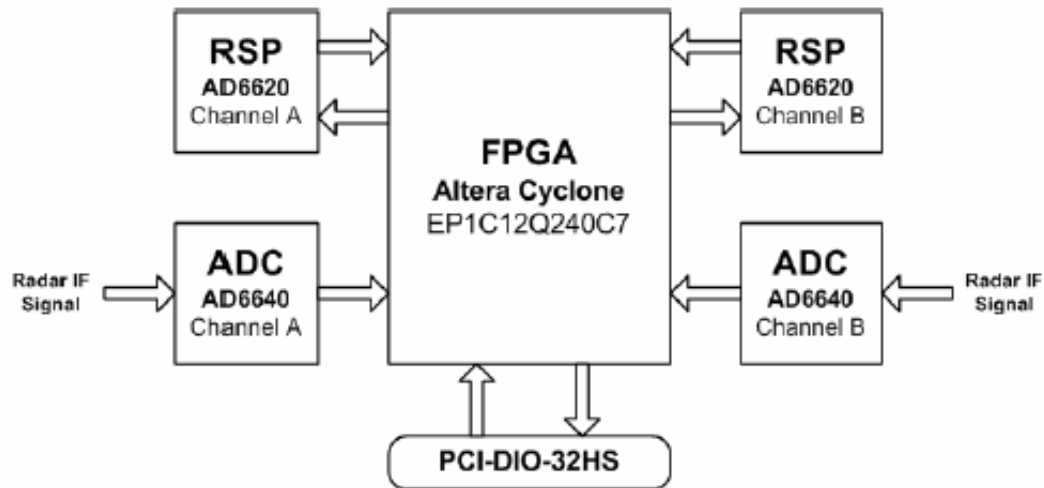


Figure 154 OSU/ESL digital receiver block diagram.



Figure 155. Dual channel digital receiver developed and built by OSU-ESL, originally with the support of the MIT Lincoln Laboratory.

### 12.2.3. Digital RF Source

For UXO application, the GPR needs to be able to cover a frequency range at least from 10 MHz to 800 MHz by sweeping the frequency at 4~20 MHz increments. Our pre-existing GPR utilizes a commercial network analyzer that is relative slow in sweeping. For instance it takes approximately 1 second to sweep 201 frequency points with 300 Hz bandwidth. In other words, it takes three seconds for one fully polarimetric measurement at each location. A new frequency source design was adopted using a high-speed direct digital frequency synthesizer (DDS) chip by Euvis DS852 and DS853 (Figure 157). The new design reduces the collection time by a factor of three, i.e. 0.3 seconds for 201 frequency points. Figure 156 shows the block diagram for the digital RF source that was adopted. Euvis DS853 DDS requires a clock source whose frequency is at least twice the maximum frequency of the output waveform. The clock source for the Euvis is generated in the components indicated by dotted box and supplied through the 50  $\Omega$  coaxial cable. The clock source component can be replaced by any stable phase-lock-loop (PLL) clock source which can generate waves up to 2 GHz.

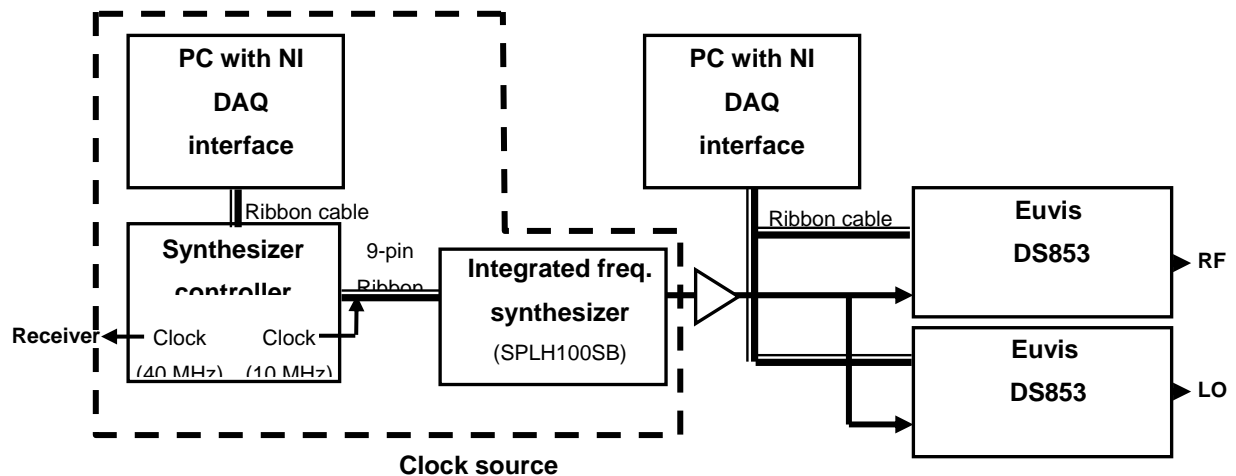


Figure 156. Digital RF source block diagram.

Following section presents some of the detail of each DDS.

### ***Euvis DS853***

The DS853 is a high-speed DDS with a frequency tuning resolution of 32 bits and an amplitude resolution of 10 bits. The inputs of this DDS chip include 32-bit single-ended digital signals Vi0 ~ Vi31 for frequency control providing fine frequency resolution, a reset signal RST for accumulator reset, a strobe signal STRP for strobe of frequency control input, and a pair of differential clock signals. All the input signals except the clock signals are connected to an on-board 50-pin IDC interface that can be controlled by a PC with a proper data interface. The clock input pair, allows the clock source to be presented in either single-ended or differential form, with SMA connectors. The outputs of the evaluation board consist of a pair of differential analog outputs OUTP/OUTN and an accumulator's carryout COUT.

### ***KEY FEATURES of EUVIS DS-852***

- 32-bit frequency tuning word
- On chip DAC with 10 bit linearity
- Clock rate up to 2 GHz
- Sine wave generation up to 1 GHz
- Complementary analog waveform outputs with 50 W back terminations
- Carry bit RF output from phase accumulator



- Worst SFDR > 50 dBc (DC to 1-GHz Bandwidth) at a 2 GHz clock rate
- TTL/CMOS digital pattern control input
- Reset (RST) pin to initiate phase 0 starting state
- High speed strobe LVPECL or LVDS compliant inputs (STRP/N) to change DDS output frequency
- 4.2 W power consumption with a single -5.2V power supply
- 64-pin QFN package

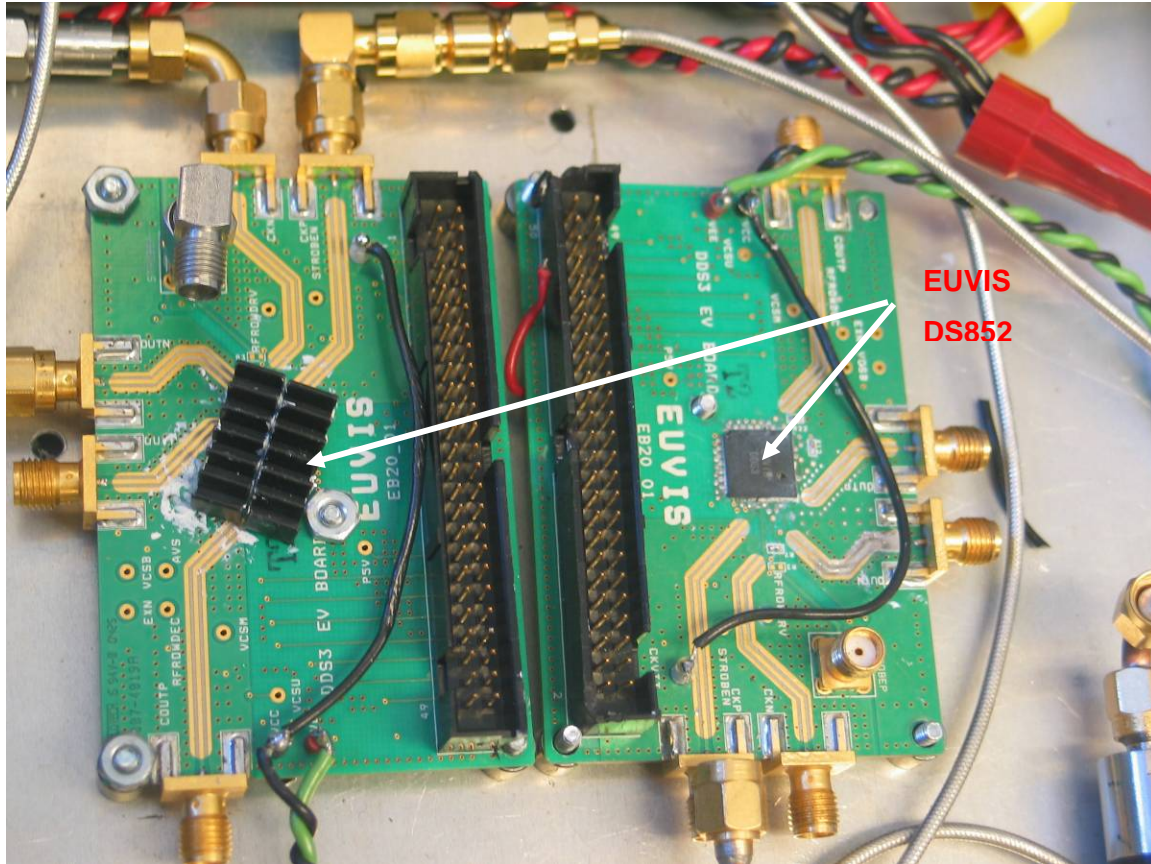


Figure 157 DDS boards for generating phase-locked RF and LO signals.

#### 12.2.4. System Clock Design

Clock input of the EUVIS DS-852 is supplied from another DDS (SPLH100SB) shown in Figure 158. The clock input frequency synthesizer adopts a surface mount integrated frequency synthesizer (SPLH100SB) and can generate 1000 – 2000 MHz of output frequency whose power level is 4 dBm. EUVIS DS-852 can handle the clock rate up to 2 GHz. However, it is found that EUVIS creates severe harmonics in the output waveform when the clock input is higher than 1.9 GHz. Therefore it is recommended for user of the radar system to supply the clock signal whose frequency is lower than 1.9 GHz. In the new radar system, the

default frequency of clock input is set to 1.875 GHz. When necessary, frequency of the clock input generated from SPLH100SB can be simply adjusted by modifying its control signal. The control signal is generated by the synthesizer controller which is connected to SPLH100SB thorough DB9 cable. Operating program supports controlling frequency of the clock input, which is done simply by setting new frequency value in the panel. The phase of the output signal is locked together with respect to a stable reference clock at 10 MHz supplied from the synthesizer controller. The synthesizer controller is responsible for controlling the clock input frequency synthesizer to generate a desired frequency output and also generates 40 MHz clock signal which is supplied to DDR and 10 MHz clock signal which is supplied to the synthesizer. The phase of both 40 MHz and 10 MHz clock signals are locked together so that DDC and DDR in the system can be synchronized.

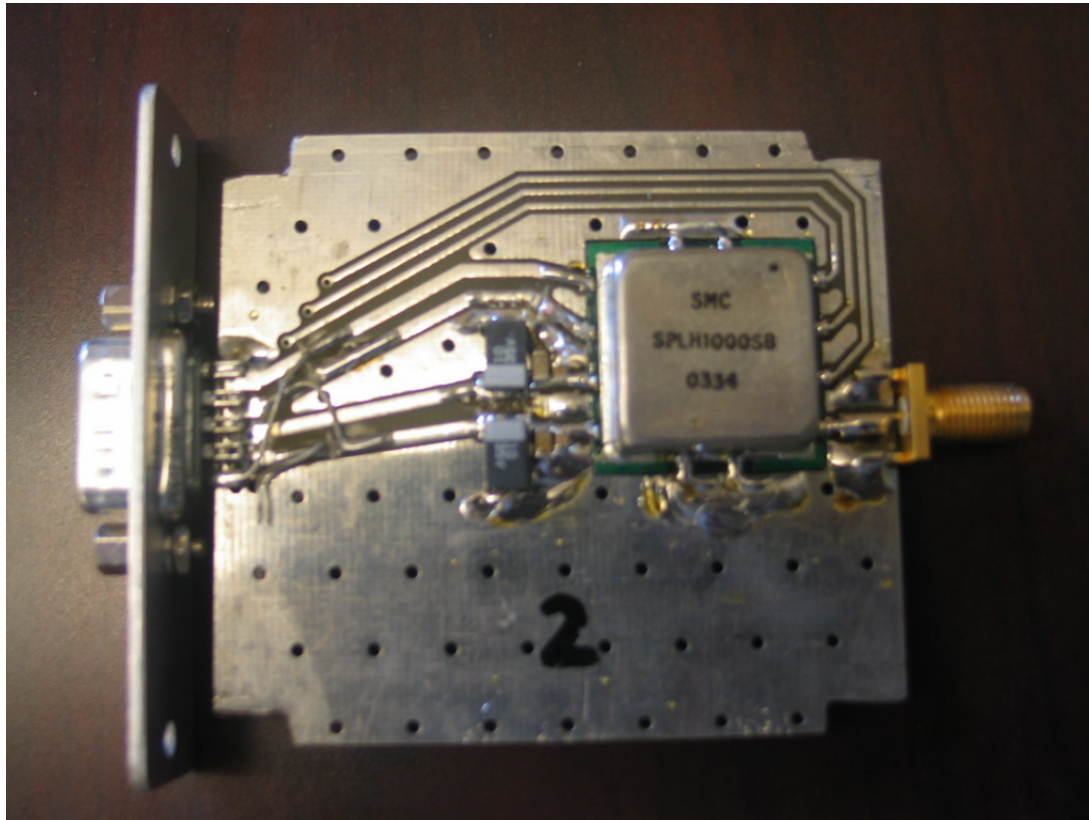


Figure 158. Digital synthesizer (SPLH100SB) for supplying clock source.

### 12.3. Operating Software

- The GPR operating software (GPROS) was programmed by the Labwindows (National Instrument) based on the graphical user interface (GUI). The GPROS provides full control of the GPR system including frequency sweep setup, data acquisition setup, display setup, and calibration for the system,



antenna, and encoder. This chapter will describe the procedure of the new GPR operation using the GPROS and functions of each step. Figure 159 shows the main screen of GPROS. The GPROS main screen consists of five major sections: frequency state, encoder state, target information, plot options, and data plot.

- Frequency state is located in the upper left-hand corner of the screen. This section shows the frequency range, step frequency of the sweep, and DDC and DDS information. All windows of the frequency state section are set to default values, which can sweep frequency from 10 to 810 MHz with 4 MHz increment. User can adjust frequency range and step frequency by inserting new values into windows in the dashed box in Figure 159. It is recommended for the UXO detection to use default setup.
- DDC frequency of the digital receiver and IF frequency of RF front-end circuitry can be adjusted by changing value in different frequency section which is located below frequency state section. Theoretically, range of the DDC frequency can be adjusted from DC to 20 MHz which is half of the sample clock frequency. However, DDC frequency is recommended to be selected in the range lower than 10 MHz. Default setup of DDC frequency is 5 MHz.
- Encoder state is located at the right-hand side of the frequency state. Encoder is a device which enables automatic triggering. The encoder state section shows the remained distance to the end of the entire measurement and remained distance to the next position. In this section, automatic triggering function can be turned on and off by clicking the “encoder ON” indicator.
- Target information is located at the bottom of the main screen. In this section, user can describe a target with information such as target ID or target number, orientation, path number and comment. Target information will be stored in a “filename.txt” file. The filename is assigned automatically depending on the time and date.
- Plot options select co- or cross-polarization data that are displayed on the data plot section by checking the polarization indicators. User can review a waterfall plot of the last measurement by clicking “Water fall plot” button.

- Data plot section consists of two graphs. The topmost of the two graphs displays the magnitude of the selected data trace in frequency domain. The other graph displays the time domain data of the selected data trace.
- Figure 160 shows flowchart of the new OSU/ESL GPR operating procedure. Data acquisition procedure is described below.

### ***12.3.1.Data acquisition procedure:***

- Set frequency range and step frequency of the sweep. (Recommend to use default setup)
- Click “Program DDC” button.
- Click “Calibration” button for the system calibration.
- Follow messages on the popup windows.
- Click “Encoder Calibration” button for the encoder calibration.
- Click “Start” button on the popup windows.
- Move the vehicle 3 inches forward.
- Press any key on the keyboard.
- Confirm if the indicator of “encoder ON” is checked.
- Set number of position. (10 ft requires 41 positions.)
- Move vehicle to the hot spot and dispose the antenna at the start position.
- Click “Acquire” button and drag the vehicle slowly.
- After the measurement, wait for popup window for data save and click “save” for saving data.
- Click “Water fall plot” button to observe a 2D GPR data. ( Figure 164 )
- Move the vehicle to the other hot spot and repeat from 12 to 14 for other measurements.

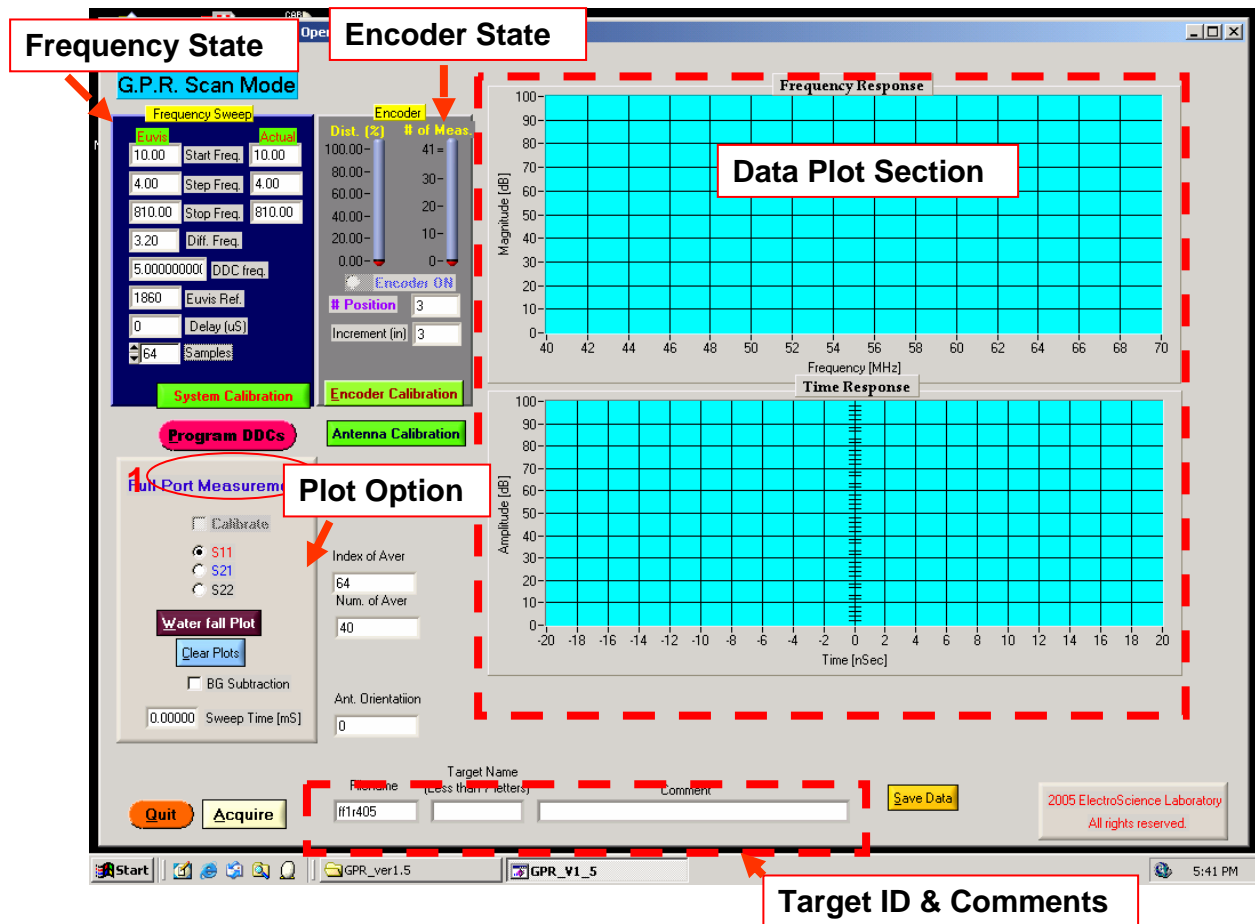


Figure 159 GPR Operating Software GUI Interface

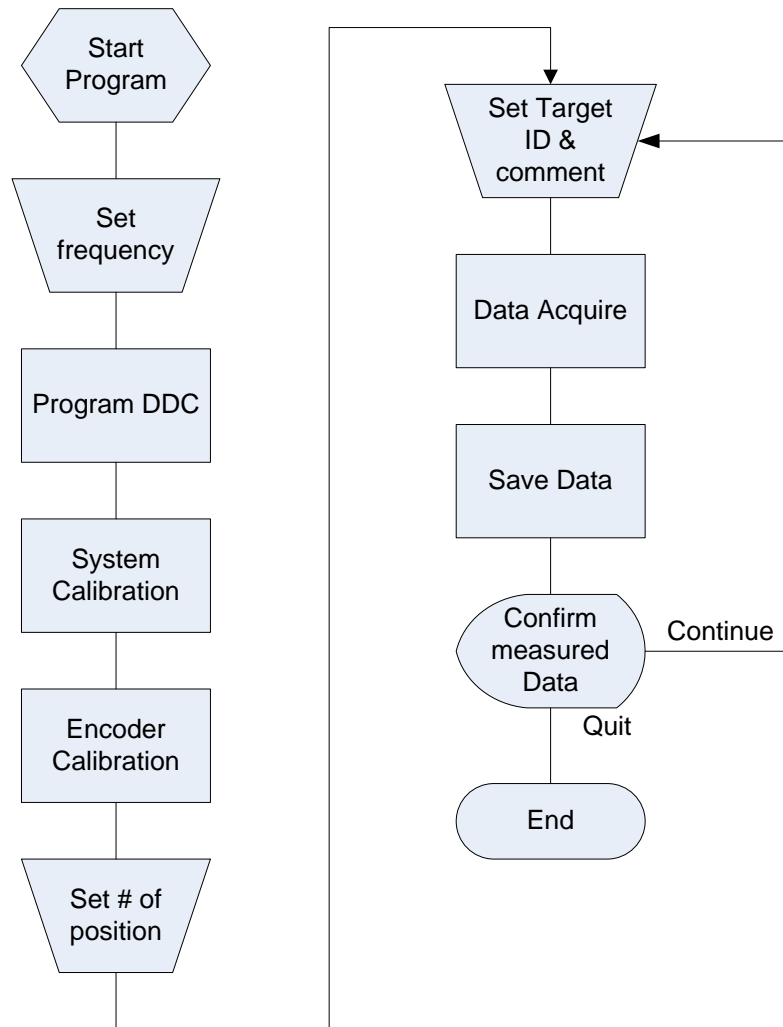


Figure 160 Flowchart of the New OSU/ESL GPR Operating procedure

### 12.3.2. Encoder Calibration

Encoder enables to measure the movement of a vehicle. By encoder calibration, actual distance and direction of the vehicle can be measured. “Encoder Calibration” button is in the encoder state section. Once user click this button, a popup window appears as shown in Figure 161. Then click “Start” button and move the vehicle 1ft forward slowly. If too fast, warning message will appear. During moving the vehicle, number in the encoder state window will increase or decrease depending on the direction of the vehicle. After moving the vehicle 1ft forward, press any key in the keyboard. It may not work sometimes. In this case, activate “DOS I/O” program by clicking “DOS I/O” icon on taskbar in bottom of the main screen. Then press any key again. If another popup window containing success message appears and “Encoder ON” indicator is marked, the encoder calibration is completed. From this point, the radar trigger is

controlled by the vehicle movement automatically. The automatic triggering can be activated and inactivated by toggling the “Encoder ON” indicator.

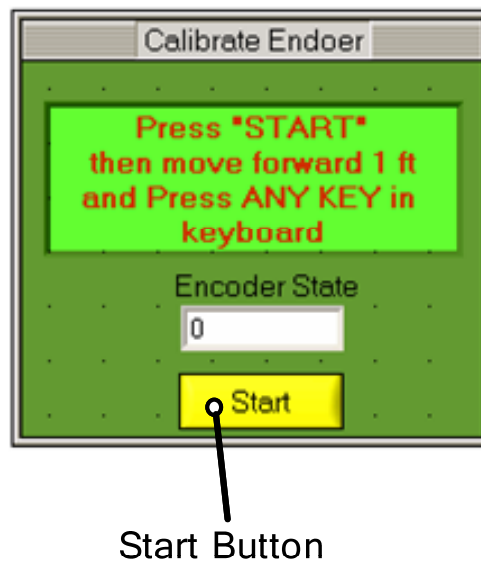


Figure 161 Popup window for the encoder calibration

### **12.3.3. System Calibration**

The GPROS also provides the system calibration procedure to remove signal form the system itself. The system calibration is performed in same manner that a network analyzer does on both channel (A and B). The system calibration starts from clicking the “calibration” button in the frequency state section located left top of the Figure 159. By following the massage, connect the short, load and through to the each port in turn. Figure 162 shows a popup window for the system calibration which shows the order of the system calibration. When each step is finished, the popup window will mark a check box on left side of that step to show the progress of the calibration. When the system calibration is completed, calibration result is plot in the data plot section.

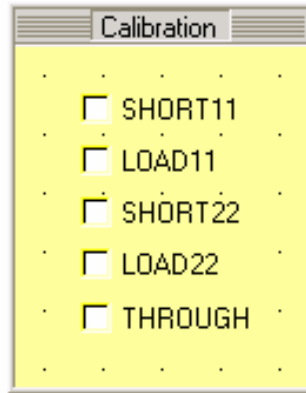
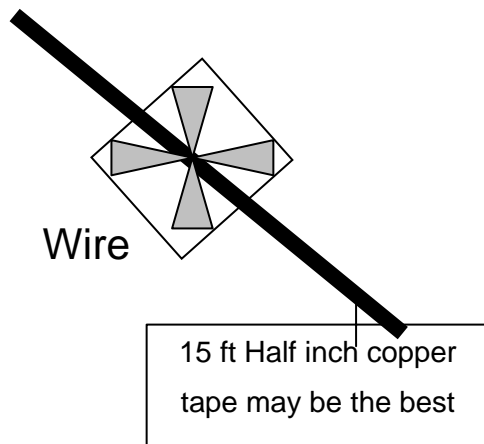


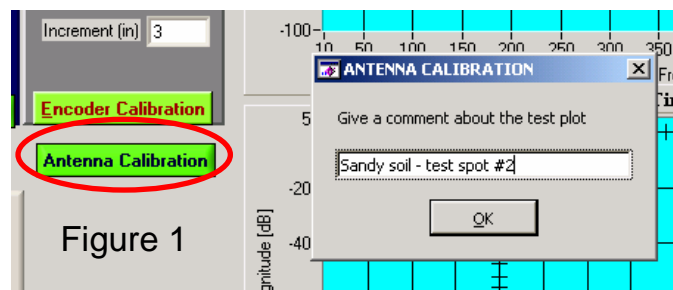
Figure 162 Popup window for the system calibration

#### **12.3.4. Antenna Calibration**

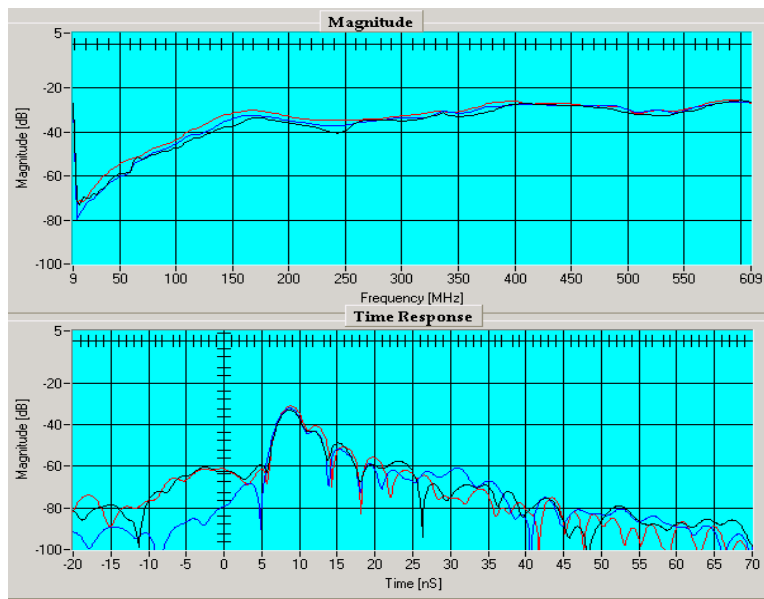
The purpose of the antenna calibration is to obtain response from a thin and long wire oriented 45 degree from both antenna 1 and 2. This 45 degree oriented wire data will be used to remove antenna transfer function on the soil from the measured data. For the antenna calibration procedure, a long wire should be located under the antenna on the ground surface with 45 degree orientation as shown in Figure 163 (a). The surface wire should be long enough (longer than 15 ft) to avoid resonance from the wire. After locating long wire under the antenna, click the “antenna calibration” button indicated by red circle in Figure 163 (b), then the radar system will collect the frequency data for both antenna 1 and 2. When it completes measurement of the wire response, the system will ask you to remove the wire at a popup window in order to measure the background response of the spot. Then, the wire should be very carefully removed to minimize antenna movement. Copper tape (1 inch width or less) is recommended as a surface wire because of its convenience of removing and enough length. After removing the surface wire, background measurement is conducted by clicking “OK” button in the popup window. At the beginning of antenna calibration procedure, an operator can record some comments about the ground. The comments can help to link the ground condition and measured data during post processing. The antenna calibration procedure should be repeated when the ground property changes significantly. Figure 163 shows an example of result of antenna calibration result. In the frequency domain plot, all three channels (S11, S21, S22) show similar responses as expected. If the responses show different behavior, antenna calibration should be repeated again.



(a) Long wire setup for the antenna calibration.



(b) Writable popup window for the antenna calibration.



(c) Antenna (small bow-tie horn) response for 45 degree wire.

Figure 163 Antenna calibration procedure.

### 12.3.5. Gray scale plot ( Waterfall data plot )

GPROS provides 2-D gray scale plot, after scanning a pass by clicking “waterfall plot’ button. The gray scale plot has several basic plotting functions, such as a time gating, slope gain, and color saturation. Each function has its own default value and the values can be adjusted by operator. To update the gray scale plot, operator should click “Modify” button.

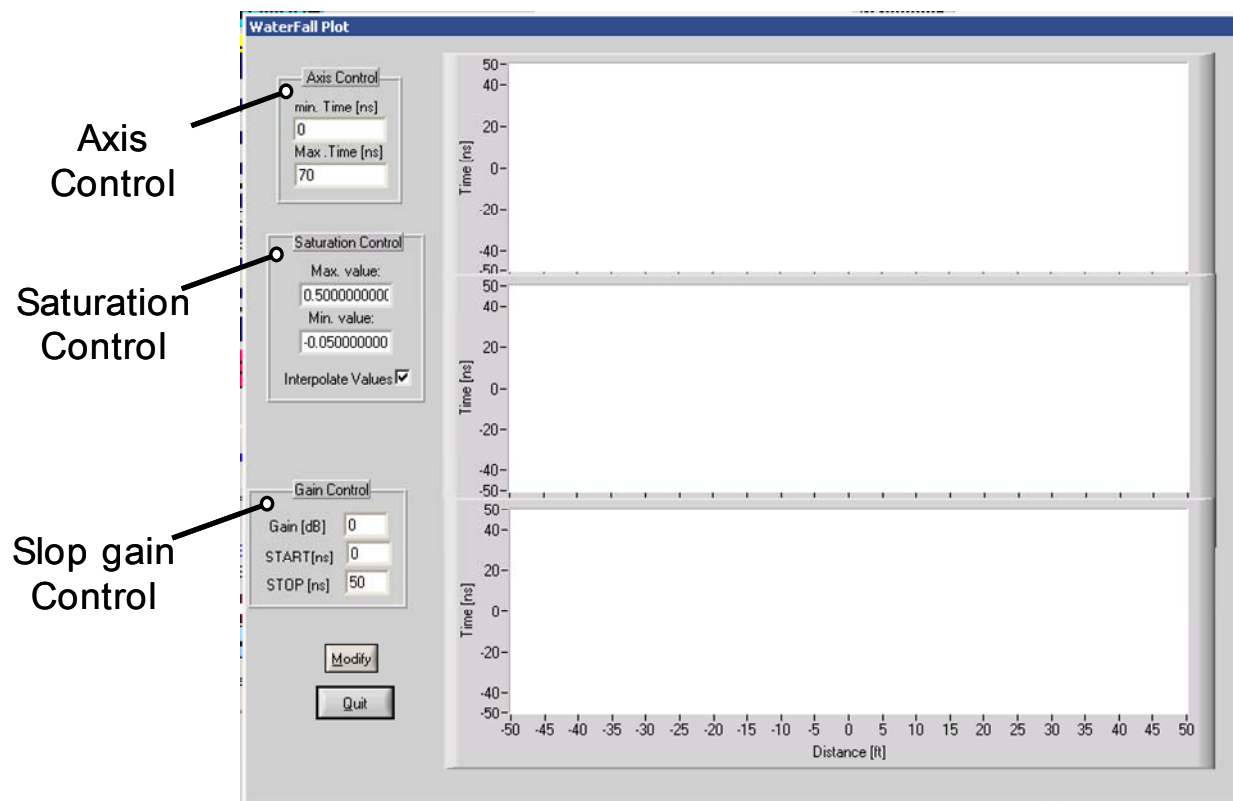


Figure 164 Window for the waterfall data plot

## 12.4. Improved small GPR ANTENNA

The miniaturized UWB dual-polarization HFB antenna was developed to improve the mobility and the spatial resolution for the shallow target by reducing size and weight of the antenna, while the antenna is properly operated in the frequency range for the UXO detection (30 – 810 MHz). This antenna has also the dual polarization feature and the dielectric loaded TEM horn feed. Dielectric constant of the loaded material was 16. The plate angle and horn angle were determined as 7° and 10°, respectively, to achieve a good impedance matching. Figure 165 shows the profile and actual design of the miniaturized UWB dual-



polarization HFB antenna. For the termination, a lump resistances ( $120\ \Omega$ ) were connected from the end of the each arms into the ground cavity as seen in Figure 166. Total width of the antenna aperture was 17 inches which is 2.5 times smaller size compared to that of the UWB HFB in the same operating frequency range. Figure 167 shows the miniaturized UWB HFB antenna covered with the ground cavity. This antenna has similar characteristics with the UWB HFB antenna and provides better mobility and fine spatial resolution for the shallow targets by reducing size of the antenna. Figure 168 and 3-5 shows the co-polarization response of both old and new HFB antenna taken at a parking lot above perpendicular drainage pipes. As one can see, the new HFB antenna gives comparable characteristics with better spatial resolution.

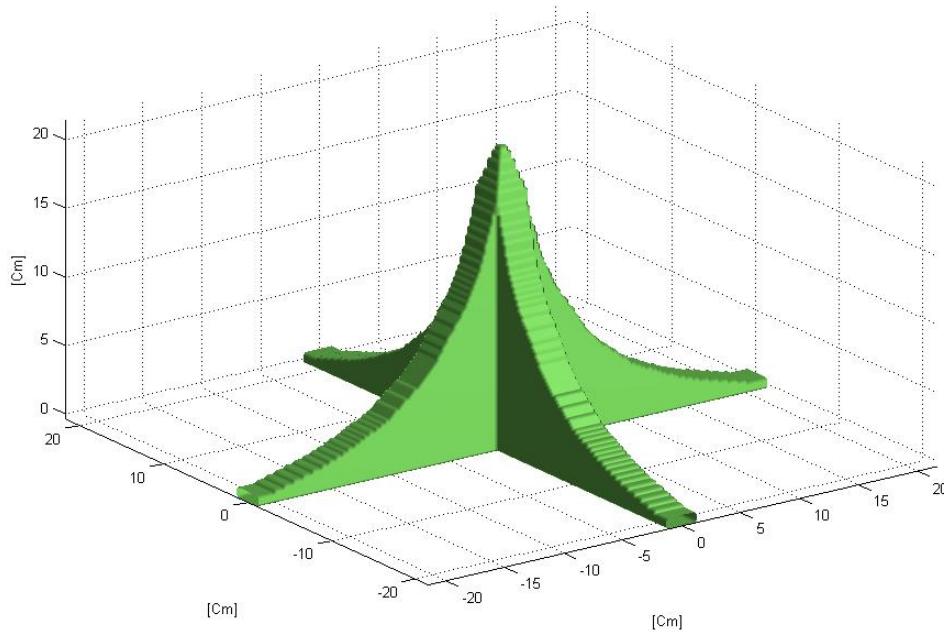


Figure 165 (a): Profile of the miniaturized UWB dual-polarization HFB antenna.



The actual design

Figure 165 Profile and actual design of the miniaturized UWB dual-polarization HFB antenna.



Figure 166 Termination of the antenna with a  $120\ \Omega$  lump resistances.

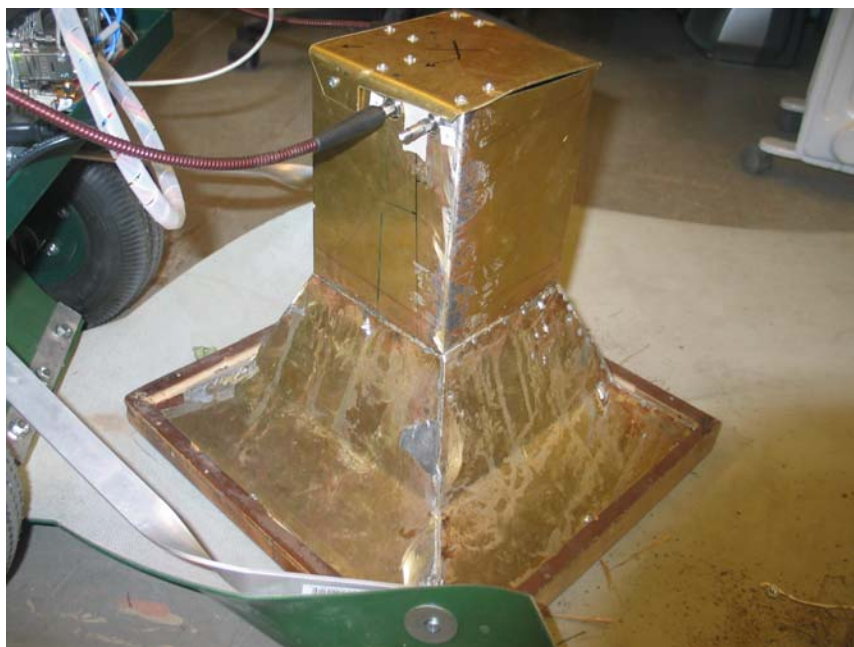


Figure 167 The miniaturized UWB HFB antenna shielded by the ground cavity.

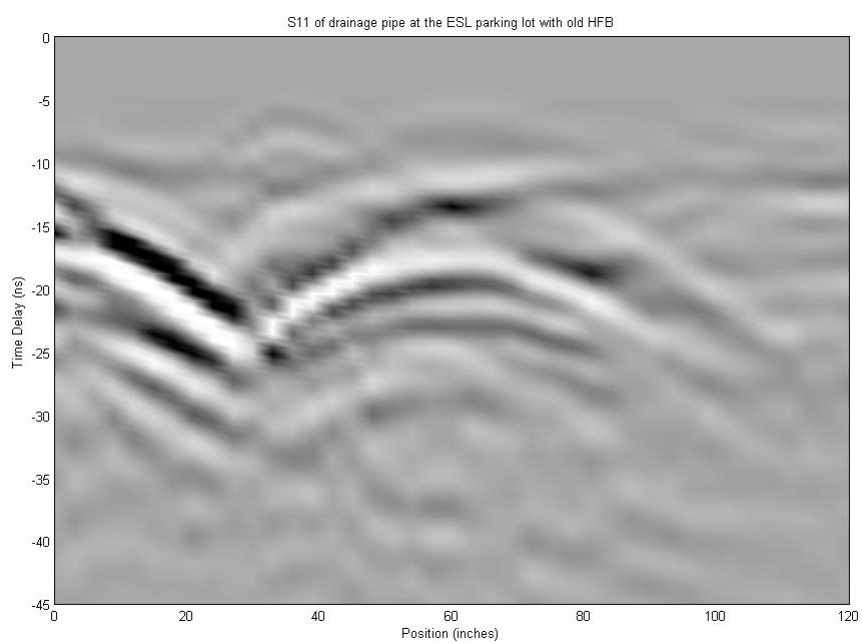
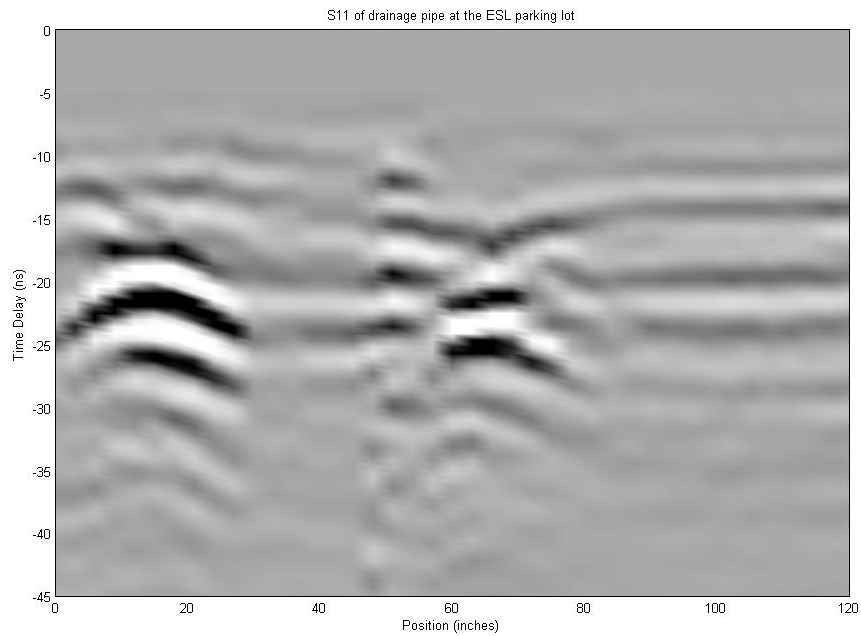
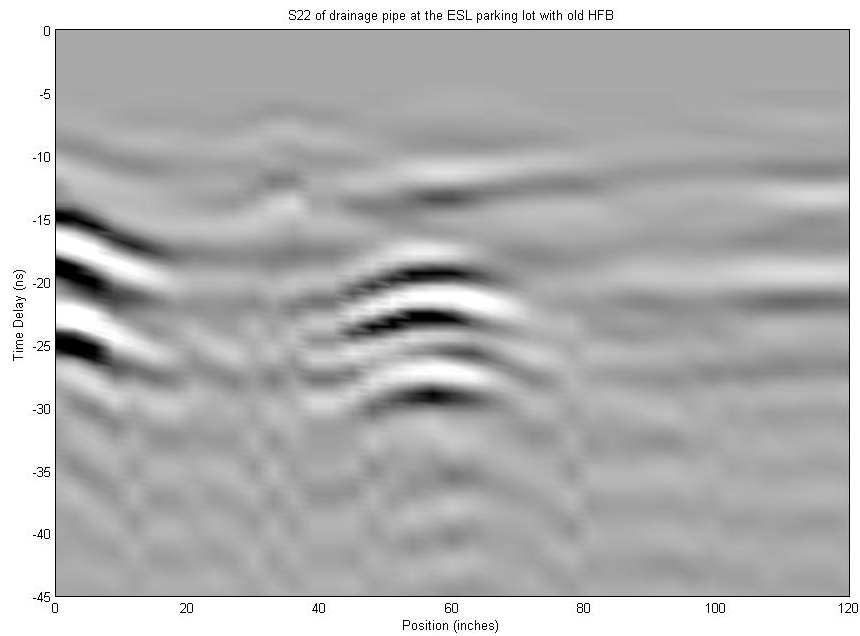


Figure 168(a) S11 response of the old OSU/ESL HFB antenna

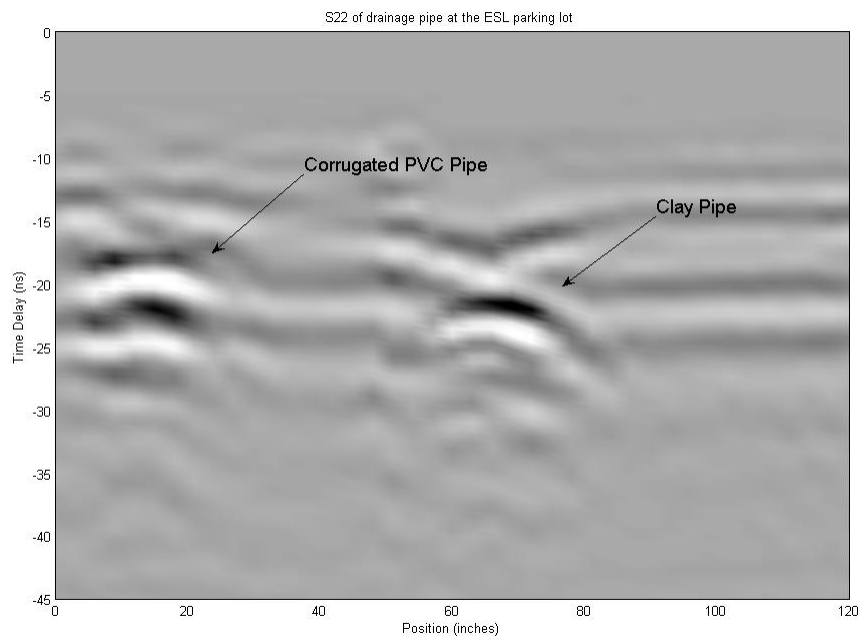


(b) S11 response of the new miniaturized UWB dual-polarization HFB antenna.

Figure 168 S11 response comparison between the old HFB and new miniaturized HFB antenna.  
(Targets were drainage pipes under a parking lot)



(a) S11 response of the old OSU/ESL HFB antenna



(b) S22 response of the new miniaturized UWB dual-polarization HFB antenna.

Figure 169 S22 response comparison between the old HFB and new miniaturized HFB antenna.  
(Targets were drainage pipes under a parking lot)

## 12.5. Conclusions

A new faster GPR system that incorporating the advanced digital down converter (DDC) and direct digital frequency synthesis (DDS) technology suitable for UXO detection/classification has been developed. This radar system is able to cover a frequency range at least from 10 MHz to 810 MHz by sweeping the frequency at 4 MHz increments, which is suitable for UXO detection/classification. The new frequency source design is adopted using a high-speed direct digital frequency synthesizer (DDS) chip by Euvis DS852 and DS853. The new design reduces the collection time by a factor of three compared with the network analyzer. It takes 0.3 seconds for 201 frequency sweep with the new system. The GPR operating software (GPROS) has also been developed based on the graphical user interface (GUI). This operating system enables a user control all over the new radar system include DDC, DDS, and the automatic triggering system and provides a simple data processing tool such as the IFFT, waterfall plot, slope gain adjuster, and band-pass filters.

The new miniaturized UWB dual-polarization HFB antenna was designed to improve the mobility and the spatial resolution by reducing size and weight of the antenna. The antenna is properly operated in the frequency range for the UXO detection (30 – 810 MHz) and provides the dual polarization feature. To reduce reflection from the end of the antenna, a lump resistances ( $120\ \Omega$ ) were loaded between the end of the each arms and the ground cavity. Size of the new antenna is 2.5 times smaller than that of the conventional UWB HFB in the same operating frequency range. Performance of the new miniaturized UWB HFB antenna is similar to the conventional UWB HFB antenna in terms of the target response, while the new antenna has better mobility and spatial resolution.

### **13. APPENDIX B: HFE-BIEM**

C.D. Moss, T.M Grzegorzczuk, K. O'Neill, and J.A. Kong (2006). A hybrid time domain model of electromagnetic induction from conducting, permeable targets, IEEE Trans. Geosci. Remote Sens., Vol 44, No. 10, 2916-2926.

# A Hybrid Time Domain Model of Electromagnetic Induction from Conducting, Permeable Targets

C. D. Moss, *Member, IEEE*, T. M. Grzegorzczuk, *Member, IEEE*,  
K. O'Neill, *Member, IEEE*, and J. A. Kong, *Fellow, IEEE*

Electromagnetic induction (EMI) is a popular technique to detect and discriminate buried unexploded ordnance (UXO). However, modeling of the EMI response from many types of UXO is difficult due to the small skin depth of the interior fields. In grid based numerical methods, meshing the target volume or surface to resolve the skin depth is often highly impractical, yet a failure to do so yields inaccurate results. This work addresses the problem with a time domain hybrid technique based on a Thin Skin Approximation (TSA) that is very accurate for small skin depths. The TSA method is applied to axisymmetric problems and is shown to be both fast and accurate when the skin depth is small. The method is compared with analytical results and excellent agreement is obtained. For magnetic materials (such as steel), the TSA method is accurate for the complete time domain EMI response. In such cases, the TSA method provides improved accuracy along with an order of magnitude reduction in CPU time compared to a dense mesh FEM. For nonmagnetic materials, the TSA loses accuracy as time progresses and must be combined with a coarse mesh FEM. In such cases the combined method still provides greater accuracy with comparable CPU time.

Electromagnetic induction, unexploded ordnance, conducting, permeable, finite elements, method of moments, impedance boundary condition

## I. INTRODUCTION

The detection and removal of buried unexploded ordnance (UXO) is a challenging task. In the United States, an estimated 11 million acres of land may contain buried UXO [1]. The problem is more widespread in European countries, where millions of buried UXO remain from two world wars. The overwhelming task of finding and removing these UXO is exacerbated by the fact that almost three-quarters of the costs and efforts are expended responding to sensor false-alarms caused by metallic clutter [2]. Hence, accurate detection and discrimination techniques are a popular area of active research. Ground penetrating radar is one area of focus, although it is hampered by significant clutter from the surface and surrounding soil [3]. Another promising technique is electromagnetic induction (EMI) [4], which uses frequencies at which the natural environment is transparent. Common practice is to use a static magnetic primary field that is cycled on and off periodically, causing currents to flow in the target. These currents induce a secondary magnetic field, also known as the EMI scattered field, that is measured with a receiver coil. The time or frequency domain profile of the scattered field reveals characteristics of the target such as dimension, permeability, and conductivity.

As a new detection and discrimination technology, research in EMI is concentrating on three areas: developing forward models, hardware, and inversion algorithms. This work concerns the first area, namely the development of an efficient and accurate forward model of EMI scattering. Most EMI systems operate in the time domain, which is our focus. Current models treat the problem at various levels of complexity, often trading off accuracy for efficiency. For example, UXO are typically approximated by canonical geometries, for which analytical solutions exist. Spheroidal geometries, both oblate and prolate, fall into this category and can model elongated as well as flat objects. The EMI response from spheroids has recently been developed [5], [6] and successfully applied to model spheroidal-like UXO geometries,



yielding a significant improvement over simple sphere models [7]. Note that this solution for the spheroidal geometries will be referred to as the 'analytical solution' in this paper, even though it requires the numerical solution of an infinite series. Other simplified models include approximations of the UXO as multiple dipoles [8], which has shown promise for basic shapes. However, UXO are usually heterogeneous and irregular objects, and in such cases general numerical solutions are required to obtain accurate results.

Common numerical methods for EMI scattering, such as finite differences or the finite element method (FEM), rely on a meshed discretization of the target's interior volume. However, the primary field penetrates only a very shallow depth (the skin depth) into the target over much of the EMI frequency range. To accurately model the interior fields, the spatial discretization must be small enough to resolve the skin depth yet also extend over the complete geometry of the target. For example, a typical non-magnetic UXO has a conductivity of  $10^7$  S/m, which results in a skin depth of approximately 3 mm at 1 kHz. For magnetic materials, such as steel ( $\mu_r = 100$ ), the skin depth is on the order of  $10^{-4}$  m. Given that most targets of interest are 0.1 m to 1 m in size, the stringent mesh requirements can become difficult to satisfy, even for a 2D body of revolution (BOR) mesh. Integral equation approaches also suffer from this problem [9], as the surface must be discretized finely enough to resolve the interior Green's function. Often numerical treatments have simply avoided the problematic high frequency regions [10], neglecting important EMI response characteristics. Other methods have treated the target as a perfect conductor and neglected the interior fields, which may work for the very high frequency response but leads to incorrect results at all other frequencies [11] where the interior fields cannot be neglected. Various other methods have been investigated, such as impedance boundary conditions [12], [13] and special finite element basis functions [14], [15], all with limited success. Even the analytical EMI scattering solutions for spheroids cannot be solved at high frequencies, and a Small Penetration Approximation [16] or asymptotic methods [17] must be used instead. Recently, a new numerical method called the Thin Skin Approximation (TSA) was developed to model the middle to high frequency EMI response, and accurate results were obtained [18]. However, it is still difficult to obtain an accurate time domain response from a frequency domain model that is only accurate at either low or high frequencies. For a time domain response from a step function primary field, the small skin depth exists for very early time, corresponding to the high frequency response. Contemporary time domain numerical methods can only accurately model the late time (low frequency) response, which might not yield usable information since the scattered fields decay rapidly and are often too weak to be measured in late time.

This paper will focus on an efficient numerical solution of the entire time domain EMI response from a BOR (axisymmetric) target. A method of moments (MoM) is used for the exterior region [19], and two separate formulations are used for the interior region: when the skin depth can be resolved on a reasonable mesh, a FEM is used to solve the interior magnetic vector potential [20]–[22]; while when the skin depth is small, the divergence equation for the magnetic field is implemented, similar to [18]. A new method is developed in which the normal derivative of the magnetic field is calculated using a type of TSA, so that no interior mesh is required. The two approaches, FEM and TSA, can both be solved separately in their regimes of validity to obtain the entire time domain response, regardless of skin depth. The accuracy of the method is compared with analytical solutions for spheres and spheroids. The results of this model can be used to identify characteristics of the time domain response that may be useful for inversion algorithms [23].

## II. FORMULATION

### A. General Formulation

The geometry under consideration is that of a conducting, permeable axisymmetric target, an example of which is shown in Figure 1. The object is assumed to have linear, piecewise constant constitutive parameters. The object has a conductivity on the order of  $\sigma_1 = 10^7$  S/m, may have a relative permeability,  $\mu_{1r}$  from 1 to 100, and has a relative permittivity  $\epsilon_{1r} = 1$ . The region outside the object,  $V_2$ , is considered weakly conducting,  $\sigma_2 < 1$  S/m, and nonpermeable. Consider the wave equation for the interior magnetic

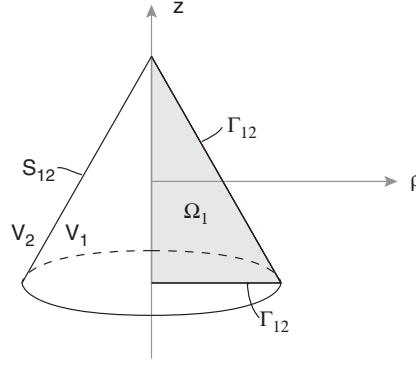


Fig. 1. Example body of revolution. The axisymmetric three dimensional object is volume  $V_1$  enclosed by surface  $S_{12}$ . The two dimensional generating surface and contour are  $\Omega_1$  and  $\Gamma_{12}$ .

field of a homogeneous object,

$$\nabla^2 \bar{H} - \mu_1 \epsilon_1 \frac{\partial^2 \bar{H}}{\partial t^2} - \sigma_1 \mu_1 \frac{\partial \bar{H}}{\partial t} = 0 \quad (1)$$

For the metallic objects of interest under EMI frequencies (25 Hz to 100 kHz), it is apparent that the  $\sigma_1 \mu_1 \partial \bar{H} / \partial t$  term is many orders of magnitude larger than the  $\epsilon_1 \mu_1 \partial^2 \bar{H} / \partial t^2$  term. Neglecting the  $\mu_1 \epsilon_1 \partial^2 \bar{H} / \partial t^2$  term reduces (1) to a diffusion equation. This is equivalent to neglecting the displacement current, and is known as the magnetoquasistatic (MQS) approximation. Hence, inside the object we have

$$\nabla \times \bar{H} = \bar{J} \quad (2)$$

which makes  $J$  a solenoidal conduction current density ( $\nabla \cdot J = 0$ ). It is more convenient to work with the magnetic vector potential,  $\bar{A}$ , resulting in [22]

$$\nabla \times \frac{1}{\mu_1} \nabla \times \bar{A} - \nabla \frac{1}{\mu_1} \nabla \cdot \bar{A} + \sigma_1 \frac{\partial \bar{A}}{\partial t} + \sigma_1 \nabla \Phi = 0 \quad (3)$$

where  $\Phi$  is the scalar electric potential and where the Coulomb gauge ( $\nabla \cdot \bar{A} = 0$ ) has been applied to obtain a vector Laplace equation. With (3),  $\nabla \cdot J = 0$  is no longer true and must be separately enforced with

$$\nabla \cdot J = \nabla \cdot \sigma_1 \left( \frac{\partial \bar{A}}{\partial t} + \nabla \Phi \right) = 0 \quad (4)$$

Furthermore, a boundary condition must be enforced such that the current does not flow into the nonconducting exterior region:

$$\hat{n}_1 \cdot \left( \frac{\partial \bar{A}}{\partial t} + \nabla \Phi \right) = 0 \quad (5)$$

In a finite volume, specifying the gauge of  $\bar{A}$  is not sufficient to guarantee uniqueness, and an appropriate boundary condition must also be chosen. A suitable boundary condition that results in a unique solution is  $\hat{n}_1 \cdot \bar{A} = 0$  (where  $\hat{n}_1$  is the normal vector pointing out of the object). Enforcing the normal component of  $\bar{A}$  to be zero on the boundary reduces (4) to the Laplace Equation for  $\Phi$  (for a piecewise continuous  $\sigma_1$ ) and (5) to  $\partial \Phi / \partial n_1 = 0$ . Hence  $\Phi$  becomes a constant or zero, and  $\bar{A}$  is the only field quantity in the interior volume. We refer the reader to [22] for more details.

The exterior wave equation can also be reduced to MQS, in this case due to the low frequencies of the EMI problem where the wavelengths of the exterior fields are large with respect to the object. Given the insignificant current, the magnetic field is irrotational and can be represented in terms of a scalar potential,

$$\bar{H} = -\nabla \psi \quad (6)$$

Combined with  $\nabla \cdot \bar{B} = 0$ , the equation for the nonmagnetic exterior becomes simply

$$\nabla^2 \psi = 0 \quad (7)$$

Green's theorem may then be used as the governing equation in the exterior:

$$\frac{\psi(\bar{r})}{2} + \int_{S_{12}} \left( \psi(\bar{r}') \frac{\partial g(\bar{r}, \bar{r}')}{\partial n'} - g(\bar{r}, \bar{r}') \frac{\partial \psi(\bar{r}')}{\partial n'} \right) dS' = \psi^{PR}(\bar{r}) \quad (8)$$

where  $\psi^{PR}(\bar{r})$  is the primary field. The free space Green's function is  $g = 1/(4\pi |\bar{r} - \bar{r}'|)$ . Across the boundary it is necessary to enforce continuity of  $\hat{n} \times \bar{H}$  and  $\hat{n} \cdot \bar{B}$ , which is ensured by

$$\hat{n}_1 \cdot (\nabla \times \bar{A}) - \mu_0 \hat{n}_2 \cdot \nabla \psi = 0 \quad (9)$$

$$\frac{1}{\mu_1} (\nabla \times \bar{A}) \times \hat{n}_1 - \nabla \psi \times \hat{n}_2 = 0 \quad (10)$$

where  $n_2$  is the normal vector pointing into the object.

The incident and scattered fields are expressed as Fourier series, allowing the azimuthal variation to be accounted for analytically and reducing the numerical problem to two dimensions. The exterior field may be represented by

$$\psi(\rho, \phi, z) = \sum_{p=0}^{\infty} \psi_p(\rho, z) \cos p\phi \quad (11)$$

in which case the magnetic vector potential is

$$\begin{aligned} \bar{A}(\rho, \phi, z) = \sum_{p=0}^{\infty} & \left[ \hat{\rho} A_p^{(\rho)}(\rho, z) \sin p\phi + \hat{\phi} A_p^{(\phi)}(\rho, z) \cos p\phi \right. \\ & \left. + \hat{z} A_p^{(z)}(\rho, z) \sin p\phi \right] \end{aligned} \quad (12)$$

For uniform axial excitation,  $\bar{H} = \hat{z} H_o$  and  $p = 0$ , whereas for uniform transverse excitation,  $\bar{H} = \hat{x} H_o$  and  $p = 1$ .

### B. The Finite Element Method and Method of Moments

The FEM is used to solve (3) for the interior region, and an MoM formulation is used to solve (8) for the open exterior region. Nodal scalar linear basis functions are used for the FEM and 'rooftop' linear basis functions are used for the FEM. The two methods are combined using the appropriate boundary conditions given by (9) and (10). Although this work concerns axisymmetric target geometries, the incident fields may be arbitrary. In particular, uniform axial ( $\hat{z}$ ) and transverse ( $\hat{x}$ ) excitation will be addressed.

The Galerkin method is applied to (3) with weighting function  $\bar{W}$ , and integration of parts is performed to obtain

$$\begin{aligned} & \int_{V_1} \frac{1}{\mu_1} (\nabla \times \bar{W}) \cdot (\nabla \times \bar{A}) dV - \int_{S_{12}} \frac{1}{\mu} \bar{W} \times (\nabla \times \bar{A}) \cdot \hat{n}_1 dS \\ & + \int_{V_1} \frac{1}{\mu_1} (\nabla \cdot \bar{W}) (\nabla \cdot \bar{A}) dV - \int_{V_1} \bar{W} \cdot \sigma_1 \frac{\partial \bar{A}}{\partial t} dV = 0 \end{aligned} \quad (13)$$

Integrating over the azimuthal variation of (13) results in a 2D integral equation. The volume  $V_1$  is reduced to the surface  $\Omega_1$ , and the surface  $S_{12}$  is reduced to a contour  $\Gamma_{12}$ . The surface  $\Omega_1$  is discretized into a triangular (Delaunay) mesh. The basis functions used in this work are linear, each defined with unity height at the corresponding node and decreasing to zero at adjacent nodes. The mesh contains the set of  $i = \{1, 2, \dots, N\}$  nodes, located at coordinates  $\{(\rho_1, z_1), (\rho_2, z_2), \dots, (\rho_N, z_N)\}$ . The contour  $\Gamma_{12}$  is

discretized into  $N_\Gamma - 1$  flat segments connected by  $N_\Gamma$  nodes. The location of node  $i$  on  $\Gamma_{12}$  is defined by  $(\rho_i, z_i)$  and is denoted by  $\Gamma_i$ .

In the exterior region, (8) can also be solved on the  $(\rho, z)$  plane. However, both the unknown functions and the Green's function are dependent on  $\phi$ , which must be integrated in order to reduce the problem into a two dimensional problem [24]. The functions of (8) are each decomposed into a Fourier series of azimuthal modes. After some manipulation in which the azimuthal modes decouple, we obtain

$$\int_\Gamma \left( \left[ \psi_p(\bar{r}') \frac{\partial \tilde{g}_p(\bar{r}, \bar{r}')}{\partial n'} - \tilde{g}_p(\bar{r}, \bar{r}') \frac{\partial \psi_p(r')}{\partial n'} \right] \right) \rho' d\Gamma' + C(\bar{r}) \psi_p(\bar{r}) = \psi_p^{PR}(\bar{r}) \quad (14)$$

The Green's functions may be derived for each  $p$ , and are included in the Appendix for  $p = 0$  and  $p = 1$ . Equation (14) is solved with the MoM, representing the unknowns of  $\psi$  and  $\frac{\partial \psi}{\partial n}$  with linear (rooftop) basis functions  $\alpha$ . The result is a matrix equation in terms of the nodal unknowns  $\psi_{p,i}$  and  $\frac{\partial \psi_{p,i}}{\partial n}$ .

The separate equations for the interior and exterior domains may be related through the boundary conditions. First, the surface integral of (13) is used to enforce the continuity of the tangential magnetic fields, becoming

$$\int_{S_{12}} \frac{1}{\mu_1} \bar{W} \times (\nabla \times \bar{A}) \cdot \hat{n}_1 dS = \int_{S_{12}} \bar{W} \cdot \nabla \psi \times \hat{n}_2 dS \quad (15)$$

The second boundary condition is the continuity of  $\hat{n} \cdot \bar{B}$ , and can be implemented in the MoM equation. The two unknowns in (14) are  $\psi$ , the scalar potential, and its normal derivative  $\frac{\partial \psi}{\partial n}$ . Given that  $\bar{H} = -\nabla \psi$  in the exterior region, we can write

$$\frac{\partial \psi}{\partial n} = \frac{(\nabla \times \bar{A}) \cdot \hat{n}_1}{\mu_o} \quad (16)$$

The two equations, (13) and (14), may then be solved for the two unknowns  $\bar{A}$  and  $\psi$ . The time domain solution may be obtained using an implicit Euler method [25] for the partial derivative with respect to time. For each azimuthal mode, the system may be written in matrix form as

$$\begin{bmatrix} \Delta t_m \bar{S}_{AA} + \bar{F}_{AA} & -\Delta t_m \bar{S}_{\psi A} \\ \bar{S}_{A\psi} & \bar{S}_{\psi\psi} \end{bmatrix} \begin{bmatrix} \bar{A}_{m+1} \\ \bar{\psi}_{m+1} \end{bmatrix} = \begin{bmatrix} \bar{F}_{AA} & \bar{A}_m \\ \bar{\Psi}^{PR} \end{bmatrix} \quad (17)$$

where  $\bar{F}_{AA}$ ,  $\bar{S}_{AA}$ , and  $\bar{S}_{\psi A}$  arise from the integrations over the FEM mesh in (13) ( $\bar{F}_{AA}$  from the integral with the  $\frac{\partial}{\partial t}$  term). The matrices  $\bar{S}_{A\psi}$ ,  $\bar{S}_{\psi\psi}$  and  $\bar{\Psi}^{PR}$  arise from the integrations over the MoM patches of (14).  $\bar{A}_m$  and  $\bar{\psi}_m$  are the unknowns at time step  $m$ .  $\bar{A}_m$  contains the three vector components of  $\bar{A}$  for the transverse case. The time step size is  $\Delta t_\gamma$ , that may be increased in time as  $\Delta t_m = m^2 \Delta t_0$  [26]. Note that it is not necessary for the primary field to shut off as an ideal step function. Other functions, such as a ramp or exponential decay, can be included in the system as a time dependent  $\bar{\Psi}^{PR}$  on the right hand side of (17). Furthermore, a frequency domain solution may be obtained by simply replacing the  $\partial/\partial t$  by  $-i\omega$ .

The FEM/MoM method outlined thus far can solve the EMI scattered fields from an axisymmetric target under a uniform axial or transverse primary field. Other uniform excitations can be found from a direct superposition of these two cases. Non-uniform cases may be studied using higher order modes for which the Green's functions must be derived. In UXO sensing devices, the primary field is often a very short duration (e.g. 50  $\mu s$ ) ramp that cycles on and off in time. Generally, the induced field is measured after the primary field is shut off, partly so that the primary field does not interfere with the induced field measurement. The periodicity of the primary field cycling is usually chosen such that the induced field has decayed to zero (below the sensor's sensitivity) before the primary field is turned on again. In this

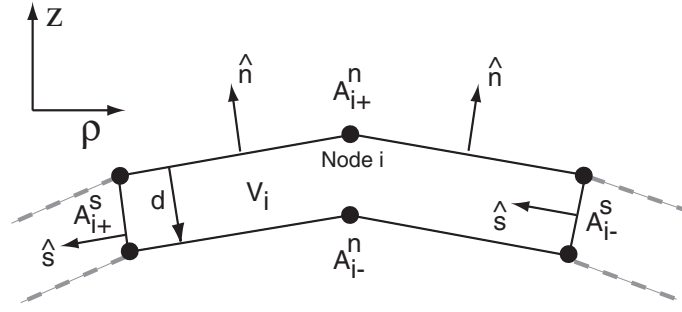


Fig. 2. Interior control volume used in the divergence equation for the TSA approximation, shown in the  $(\hat{\rho}, \hat{z})$  plane. The volume is a ring in three dimensions.

work we approximate the primary field as a step function that is either turned on or off at  $t = 0$ . The turn on case will be studied first to compare with semi-analytical solutions.

As mentioned earlier, and as will be shown in the Section III, the FEM/MoM method cannot resolve the small skin depths that exist in early time after the primary field is turned on or off. However, for an increasing time step, it is apparent from (17) that the solution will always converge to the static ( $\frac{\partial}{\partial t} \rightarrow 0$ , late time) solution. Hence, it is necessary to develop a new method that will demonstrate early time accuracy.

### C. Thin Skin Approximation - Method of Moments

The TSA method has been developed in an earlier work [18] for high frequency EMI scattering from a three dimensional target. The method has two steps; the first step is the derivation of a new interior integral equation in terms of the scalar potential  $\psi(\vec{r})$ , the normal component of the interior magnetic field  $H^{(n)}$ , and its derivative. The second step of the method involves deriving a semi-analytical approximate form of  $H^{(n)}$  such that the field and its derivative can be represented with one unknown. The new interior equation is used with (17) to solve for the two unknowns  $\psi(\vec{r})$  and  $H^{(n)}$  ( $= \frac{\partial \psi}{\partial n}$ ). In this work, the TSA governing equation will first be derived for the axisymmetric case, and then a new time domain approximation for  $H^{(n)}$  is introduced. The TSA method begins by enforcing  $\nabla \cdot \vec{B} = 0$  inside the target, or equivalently a divergence free magnetic field for a piecewise continuous permeability. A volume  $V_i$  is first defined as an interior control volume directly beneath node  $i$  on the target surface, as shown in Figure 2. Note that the problem is still in three dimensions at this point, such that  $V_i$  is a three dimensional ring-like volume, and node  $i$  is on a circular contour  $L_i$  around the axis of symmetry.  $A_{i+}^n$  and  $A_{i-}^n$  are the inner and outer areas, joined by surfaces  $A_{i+}^s$  and  $A_{i-}^s$ . A weighted integral expression of the divergence equation for the magnetic field in the control volume is then

$$\int_{V_i} dV_i \alpha'_i \nabla \cdot \vec{H} = \int_{V_i} dV_i \{ \nabla \cdot (\alpha'_i \vec{H}) - \vec{H} \cdot \nabla \alpha'_i \} = 0 \quad (18)$$

where  $\alpha'_i$  is a weighting function.  $\alpha'_i$  is chosen to be tent shaped in  $\hat{s}$  such that  $\hat{n}_1 \cdot \nabla \alpha'_i = 0$  everywhere except the line connecting node  $i$  and its complement. The magnetic field in the local coordinate system is  $\vec{H} = \hat{n}H^{(n)} + \hat{\phi}H^{(\phi)} + \hat{s}H^{(s)}$ . Applying the divergence theorem to (18) and dividing through by the volume depth  $d$  yields [18]

$$\begin{aligned} & \frac{1}{d} \int_{A_{i+}^n} dA \alpha'_i H^{(n)} - \frac{1}{d} \int_{A_{i-}^n} dA \alpha'_i H^{(n)} + \frac{1}{d} \int_{A_{i+}^s} dA \alpha'_i H^{(s)} - \frac{1}{d} \int_{A_{i-}^s} dA \alpha'_i H^{(s)} \\ & - \frac{1}{d} \int_{V_i} dV \vec{H} \cdot \nabla \alpha'_i = 0 \end{aligned} \quad (19)$$

As  $d$  is reduced, the first two integrals merge to a normal derivative of the integral over  $A_{i+}^n$ . The integrals over  $A_{i+}^s$  and  $A_{i-}^s$  reduce to line integrals over  $L_{i+1}$  and  $L_{i-1}$ , which are the paths created by nodes  $(i+1)$  and  $(i-1)$  around the axis of symmetry. Both line integrals reduce to zero, because  $\alpha'_i$  (the linear rooftop/tent function in  $\rho$  and  $z$ ) is zero at  $L_{i+1}$  or  $L_{i-1}$ . The magnetic field in the final integral of (19) may be expressed in terms of  $\psi$  using (6) to obtain

$$\frac{\partial}{\partial n_1} \int_{A_i^n} dA \alpha'_i H^{(n)} + \int_{A_i^n} dA \nabla \psi \cdot \nabla \alpha'_i = 0 \quad (20)$$

The two remaining unknowns in (20) are  $H^{(n)}$  and  $\psi$ , which need to be expanded in terms of  $\alpha'_i$ . We assume the same form of  $\psi$  for the object interior (see (11)), and by taking its gradient the magnetic field may be expressed as

$$\overline{H} = \sum_{p=0}^{\infty} \left[ \hat{\rho} H_p^{(\rho)}(\rho, z) \cos(p\phi) + \hat{\phi} H_p^{(\phi)}(\rho, z) \sin(p\phi) + \hat{z} H_p^{(z)}(\rho, z) \cos(p\phi) \right] \quad (21)$$

For an axisymmetric target,  $\hat{n}$  has only  $\hat{\rho}$  and  $\hat{z}$  dependence, and therefore  $H^{(n)}$  has only  $\cos(p\phi)$  azimuthal variation. As a result, the weighting function for (20) can now be written as

$$\alpha'_i(\rho, \phi, z) = \sum_{q=0}^{\infty} \alpha_i(\rho, z) \cos(q\phi) \quad (22)$$

The normal component of the magnetic field can be written as a summation of basis functions over the contour:

$$H^{(n)} = \sum_{j=1}^{N_\Gamma} H_j^{(n)} \alpha'_j = \sum_{j=1}^{N_\Gamma} \sum_{p=0}^{\infty} H_{pj}^{(n)} \alpha_j \cos(p\phi) \quad (23)$$

The weighting and basis functions are defined such that  $\hat{n}_1 \cdot \nabla \alpha'_i = 0$  (everywhere except at  $A_{i+}^n$ ), so the first term of (20) can be approximated as

$$\begin{aligned} & \sum_{j=1}^{N_\Gamma} \sum_{p=0}^{\infty} \frac{\partial}{\partial n_1} \int_{A_i^n} dA \alpha'_i H_{pj}^{(n)} \alpha_j \cos(p\phi) \\ &= \sum_{j=1}^{N_\Gamma} \sum_{p=0}^{\infty} \left( \frac{1}{A_i^n} \frac{\partial A_i^n}{\partial n_1} H_{pj}^{(n)} + \frac{\partial H_{pj}^{(n)}}{\partial n_1} \right) \int_{A_i^n} dA \alpha'_i \alpha_j \cos(p\phi) \end{aligned} \quad (24)$$

Equation (24) can be substituted into (20). The azimuthal part is integrated out, for which the terms where  $p \neq q$  yield zero. The result is a one dimensional integral over the entire surface contour:

$$\begin{aligned} & \sum_{j=1}^{N_\Gamma} \sum_{p=0}^{\infty} \left( \frac{1}{A_i^n} \frac{\partial A_i^n}{\partial n_1} H_{pj}^{(n)} + \frac{\partial H_{pj}^{(n)}}{\partial n_1} \right) \int_{\Gamma_{i-1}}^{\Gamma_{i+1}} ds \rho \alpha_i \alpha_j \\ &= \sum_{j=1}^{N_\Gamma} \sum_{p=0}^{\infty} \psi_{pj} \int_{\Gamma_{i-1}}^{\Gamma_{i+1}} ds \left( \rho \nabla \alpha_i \cdot \nabla \alpha_j + \frac{p^2}{\rho} \alpha_i \alpha_j \right) \end{aligned} \quad (25)$$

for  $i = 1, \dots, N_\Gamma$ . Equation (25) is an equation in terms of  $\psi$ ,  $H^{(n)}$ , and  $\frac{\partial H^{(n)}}{\partial n_1}$  along the surface. In order to yield an equation with two unknowns that can be solved with (17),  $\frac{\partial H^{(n)}}{\partial n_1}$  must be expressed in terms of  $H^{(n)}$

The TSA was shown in [18] to be successful in the frequency domain using  $\frac{\partial H^{(n)}}{\partial n_1} = -ik\xi_n H^{(n)}$ , where  $\xi_n$  is a correction factor. For a time domain (TD) TSA, we begin by considering that the interior magnetic field is governed by the diffusion equation, similar to (3). One dimensional solutions of the diffusion

equation for a step change at a boundary is the complementary error function [26], denoted as ‘erfc’. A time domain (TD) TSA can be implemented by assuming that the normal component of the magnetic field at each node can be approximated by the one dimensional solution in the normal direction. Hence, the magnetic field is defined as a function of time and the normal direction,  $H^{(n)}(n, t)$ . The initial condition for the magnetic field on the contour at  $n = 0$  is denoted as  $H^{(n)}(0, 0) = H_{(0)}^{(n)}$ , where the subscript refers to  $t = t_0$  (usually  $t_0 = 0$ ). If the normal component of the magnetic field on the contour is to change to  $H^{(n)}(0, t_1) = H_{(1)}^{(n)}$ , we can approximate the normal dependence of the solutions as

$$H^{(n)}(n, t_1) = H_{(0)}^{(n)} + (H_{(1)}^{(n)} - H_{(0)}^{(n)})f(n, t_1 - t_0) \quad (26)$$

where

$$f(n, t) = \text{erfc}\left(\frac{n}{2\sqrt{t\Lambda}}\right) \quad (27)$$

where  $\Lambda = 1/\sqrt{\sigma\mu}$ . Equation (26) can be found directly from the one dimensional diffusion equation for the given parameters and appropriate boundary conditions. At time  $t = t_2$ , the magnetic field would again change, this time to  $H_{(2)}^{(n)}$ , and the solution of the interior magnetic field would be

$$H^{(n)}(n, t_2) = H_{(0)}^{(n)} + (H_{(1)}^{(n)} - H_{(0)}^{(n)})f(n, t_2 - t_0) + (H_{(2)}^{(n)} - H_{(1)}^{(n)})f(n, t_2 - t_1) \quad (28)$$

and so on, such that the solution for any  $t = t_M$  would be

$$H^{(n)}(n, t_M) = H_{(0)}^{(n)} + \sum_{m=1}^M (H_{(m)}^{(n)} - H_{(m-1)}^{(n)})f(n, t_M - t_{m-1}) \quad (29)$$

which can be cast in integral form as

$$H^{(n)}(n, t_M) = H_{(0)}^{(n)} + \int_0^{t_M} d\tau \frac{\partial H^{(n)}(\tau)}{\partial \tau} f(n, t_M - \tau) \quad (30)$$

The normal derivative of  $H^{(n)}$  for mode  $p$  at node  $i$  in (25) can then be written as

$$\frac{\partial H_{pj,(M)}^{(n)}}{\partial n_1} = \frac{2}{\sqrt{\Lambda\pi}} \sum_{m=1}^M \left( \frac{H_{pj,(m)}^{(n)} - H_{pj,(m-1)}^{(n)}}{\Delta t_m} \right) R(t_M, t_m) \quad (31)$$

where  $R(t_M, t_m) = \left[ \sqrt{(t_M - t_m)} - \sqrt{(t_M - t_{m-1})} \right]$  and  $\Delta t_m = t_m - t_{m-1}$ . Equation (31) is obtained by assuming  $\partial H^{(n)}(\tau)/\partial \tau$  is constant over each timestep. The normal derivative may then be substituted into (25), resulting in an equation with two unknowns on the surface:  $H_{(M)}^{(n)}$  and  $\psi_{(M)}$ . The final form of the interior equation is then

$$\begin{aligned} & \sum_{j=1}^{N_\Gamma} \sum_{p=0}^{\infty} H_{pj,(M)}^{(n)} \left[ \frac{-2}{\sqrt{\Delta t_M \Lambda \pi}} + \frac{1}{A_i^n} \frac{\partial A_i^n}{\partial n_1} \right] \int_{\Gamma_{i-1}}^{\Gamma_{i+1}} ds \rho \alpha_i \alpha_j \\ & - \sum_{j=1}^{N_\Gamma} \sum_{p=0}^{\infty} \psi_{pj,(M)} \int_{\Gamma_{i-1}}^{\Gamma_{i+1}} ds \left( \rho \nabla \alpha_i \cdot \nabla \alpha_j + \frac{p^2}{\rho} \alpha_i \alpha_j \right) = \sum_{j=1}^{N_\Gamma} \sum_{p=0}^{\infty} \frac{2}{\sqrt{\Lambda \pi}} \\ & \times \left[ -\frac{H_{pj,(M-1)}^{(n)}}{\sqrt{\Delta t_M}} - \sum_{m=1}^{M-1} \left( \frac{H_{pj,(m)}^{(n)} - H_{pj,(m-1)}^{(n)}}{\Delta t_m} \right) R(t_M, t_m) \right] \int_{\Gamma_{i-1}}^{\Gamma_{i+1}} ds \rho \alpha_i \alpha_j \end{aligned} \quad (32)$$

Equations (32) and (14) can then be used to solve for the unknowns on the surface,  $H_{(M)}^{(n)}$  and  $\psi_{(M)}$ . An interior mesh is not required, and hence the TSA method is much more efficient than the FEM method

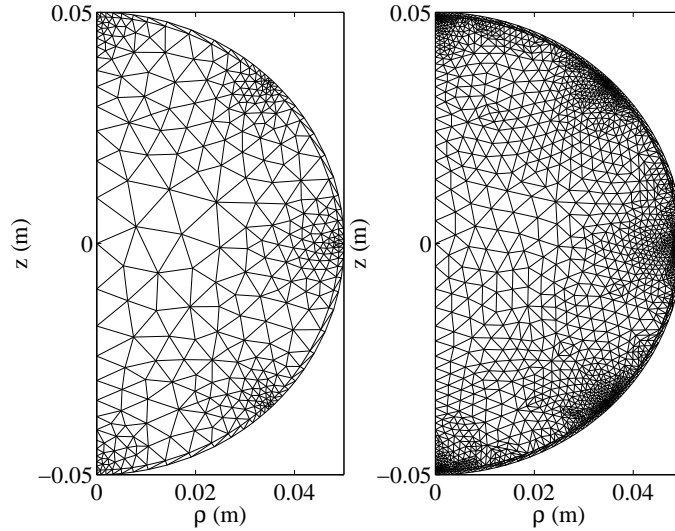


Fig. 3. Coarse and fine meshes for the sphere

(note that as both use the MoM so the acronym is dropped) whenever applicable. Furthermore, there is no restriction on the skin depth in early time. However at some later time, when the fields have significant penetration into the object, the semi-analytical form of  $H^{(n)}$  is no longer valid and the method fails. The regime of validity of TSA method is therefore investigated in the following section.

### III. RESULTS

In this section, the numerical results are first compared with analytical solutions. The limitations of the FEM are first demonstrated by comparison with the frequency and time domain solutions for a conducting and permeable sphere. Comparison is then made between the FEM and semi-analytical solutions for prolate and oblate spheroids. Denoting the numerical result as  $f_{num}(t)$  and the analytical solution as  $f_{ana}(t)$ , we define the normalized error  $f_{err}(t)$  to be:

$$f_{err}(t) = \frac{|f_{num}(t) - f_{ana}(t)|}{\max(|f_{ana}(t)|)} \quad (33)$$

The normalized error is used to demonstrate the accuracy of the FEM for spheroidal geometry solutions. The TSA method is then investigated in the same manner. The results from both methods is combined, and the error is also compared with the analytical solutions.

#### A. FEM Comparison with EMI Scattering from a Sphere

The FEM is first compared to the analytical solution for a 5 cm radius sphere. Both a magnetic sphere with  $\mu_r = 100$  and a nonmagnetic sphere with  $\mu_r = 1$  are investigated. Both spheres have a conductivity of  $\sigma = 10^7$ . The uniform primary magnetic field is turned on as a step function, and the induced field is calculated at 20 cm above the origin. Given the expected small skin depths, it is natural to use an FEM mesh that has a finer discretization near the surface. Two meshes are used, as shown in Figure 3. The first is referred to as a coarse mesh, containing 365 nodes and 57 boundary nodes. The second is referred to as a fine mesh, containing 1875 nodes with 113 boundary nodes. The fine mesh contains more unknowns and yields greater accuracy at the expense of computational efficiency.

Figure 4 shows the axial and transverse responses from the nonmagnetic sphere. In early time, or equivalently at high frequencies, currents are set up along the circumference of the sphere to oppose the changing magnetic field. The induced magnetic field from these currents is therefore in the opposite direction to the primary field. As time progresses, these currents diffuse and decay into the sphere, until



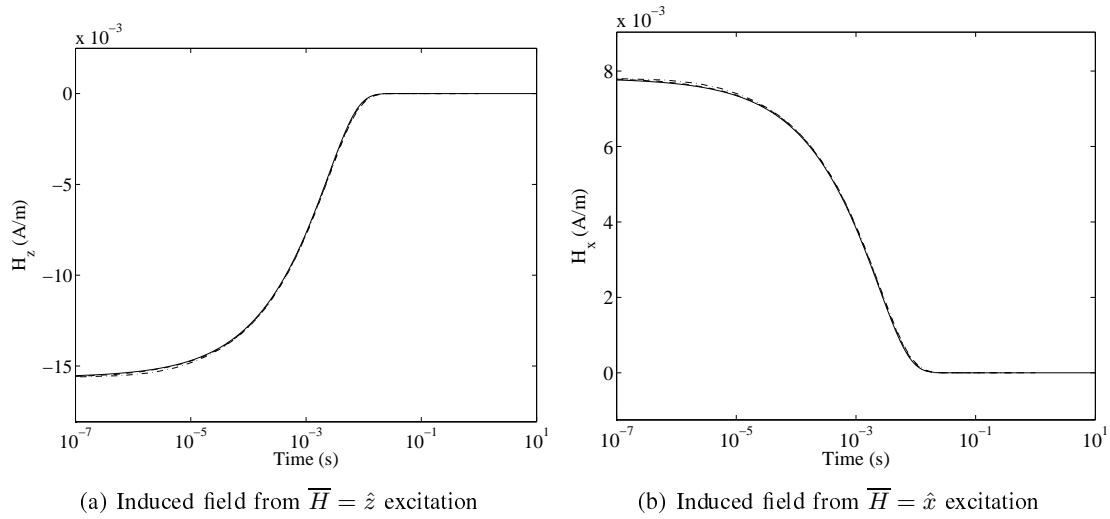


Fig. 4. Induced magnetic field at  $z = 0.2$  m, from a sphere with  $r = 0.05$  m,  $\mu_r = 1$ ,  $\sigma = 10^7$  S/m. Uniform primary field turned on at  $t = 0$  s. Solid line is the analytical solution, dashed line is the fine mesh, dash-dot line is the coarse mesh.

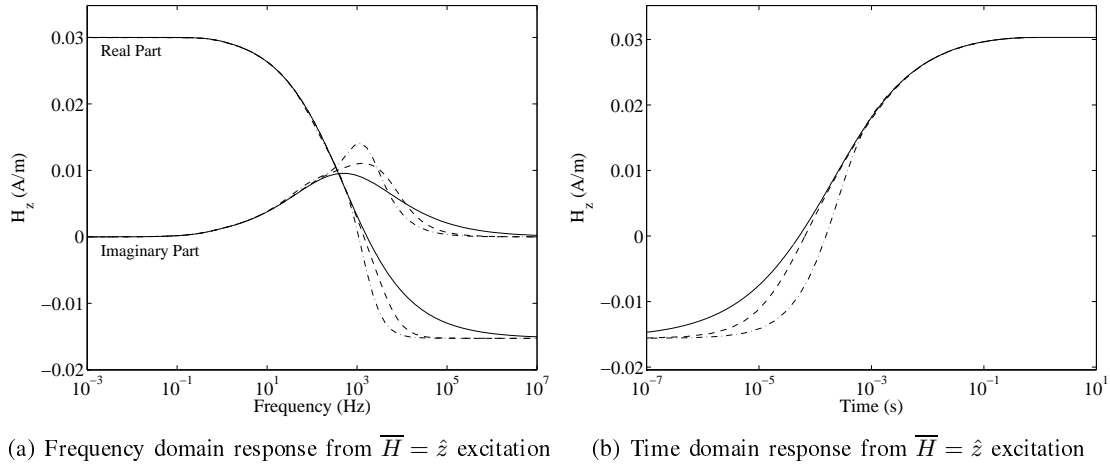


Fig. 5. Induced magnetic field at  $z = 0.2$  m, from a sphere with  $r = 0.05$  m,  $\mu_r = 100$ ,  $\sigma = 10^7$  S/m. Uniform primary field turned on at  $t = 0$  s. Solid line is the analytical solution, dashed line is the fine mesh, dash-dot line is the coarse mesh.

finally the late time static response becomes zero. In both the axial and transverse cases, the agreement between the analytical solution and the coarse mesh FEM solution is excellent.

Figure 5 and Figure 6 show the axial and transverse responses, respectively, from the magnetic sphere with  $\mu_r = 100$ . The frequency domain solution is shown for comparison. In these cases, the early time (high frequency) response is similar to the nonmagnetic sphere. In late time the induced field is nonzero in the same direction as the primary field (the static solution). The FEM mesh cannot resolve the smaller skin depths that appear in these cases, and significant error is observed over 1 kHz in the frequency domain and before 1 ms in the time domain. However, as predicted in the previous section, the FEM does converge to late time static solution. The FEM also converges in very early time or high frequency, at which time the fields are zero within the object and the integral equation alone provides an accurate solution. Note that the FEM is very slow to converge to the analytical solution; increasing the mesh resolution from 365 nodes to 1875 nodes has only achieved a small gain in accuracy.

Finally,  $\vec{A}$  inside the 5 cm magnetic sphere is plotted for the axial and transverse turn off cases in Figure 7 and Figure 8, respectively. In the axial case, the vector potential  $\hat{\phi}A_\phi$  is maximum around the the equator of the sphere at  $t = 247\mu\text{s}$ , decaying rapidly in latitude and away from the surface. Later in

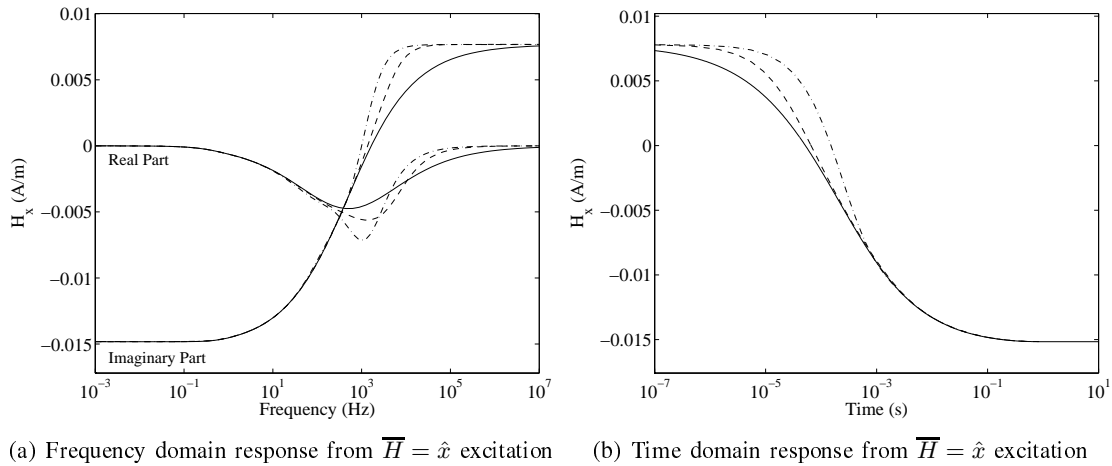


Fig. 6. Induced magnetic field at  $z = 0.2$  m, from a sphere with  $r = 0.05$  m,  $\mu_r = 100$ ,  $\sigma = 10^7$  S/m. Uniform primary field turned on at  $t = 0$  s. Solid line is the analytical solution, dashed line is the fine mesh, dash-dot line is the coarse mesh.

time at 193ms, the maximum potential is in the interior of the sphere. For the transverse case, the vector potential  $\hat{\rho}A_\rho$  is maximum at the poles of the sphere, circulating around the  $\hat{x}$  axis. Similar behavior is observed to the axial excitation case, with fields varying with latitude and depth. In later time, the field has decayed into the sphere and continues to circulate around the  $\hat{x}$  axis.

### B. Finite Element Error

Using (33), the accuracy of the FEM solution can be compared to the analytical solution [6]. In addition to the sphere, the EMI scattered field will be calculated from spheroidal geometries shown in Figure 9. Five different spheroids will be used for this comparison, with elongations ( $e = b/a$ ) between 0.25 and 4, relative permeability  $\mu_r = 100$ , and conductivity  $\sigma = 10^7$  S/m. Figure 10 shows the error of the FEM solution using the coarse and fine mesh similar to the sphere case. The maximum error in the FEM solution occurs in early time from  $10^{-5}$  s to  $10^{-4}$  s. The maximum error for the fine mesh is varies from 0.04 for the  $e = 4$  (prolate) spheroid to 0.14 for the  $e = 0.25$  (oblate) spheroid. For axial excitation, the induced currents (related to  $\partial\bar{A}/\partial t$ ) circle the spheroid and diffuse inwards, with largest magnitude near the equator. The current profile varies in latitude and the radius of curvature of the spheroid. For the prolate spheroid, the radius of curvature is larger at the equator and the currents vary smoothly with latitude. For the oblate spheroid, the opposite is true. Hence the FEM mesh is better able to resolve  $A$  for the prolate cases, and the error is lower. With the exception of the sphere, the fine mesh offers little improvement in early time error for all spheroid geometries. However, the coarse mesh solutions exhibit further error of up to 0.05 in intermediate time ( $10^{-3}$  s to  $10^{-2}$  s). Results are similar for the transverse case and are omitted here for brevity. The CPU times for the FEM solutions are shown in Table I.

### C. TSA Error

The TSA solution can also be compared to the analytical solution for a sphere. Figure 11 shows the sphere's induced magnetic field at  $z = 0.2$  m for the magnetic and nonmagnetic cases. In both cases, the TSA method is very accurate in early time but begins to diverge from the analytical solution at approximately  $t = 10^{-4}$  s. At that time the skin depth begins to depend on the geometry and the 1D semi-analytical approximation of (27) is no longer accurate. For the magnetic case accuracy is greater, as the skin depth remains smaller for a longer period of time. The normalized error analysis can be performed for the TSA method, shown in Figure 12 for the axial case. For the nonmagnetic case the TSA method is very accurate in early time, and begins to diverge from the analytical solution at approximately  $10^{-4}$  s for each spheroid. At 0.1 s, the error ranges from 0.1 to greater than 0.6, and continues to diverge

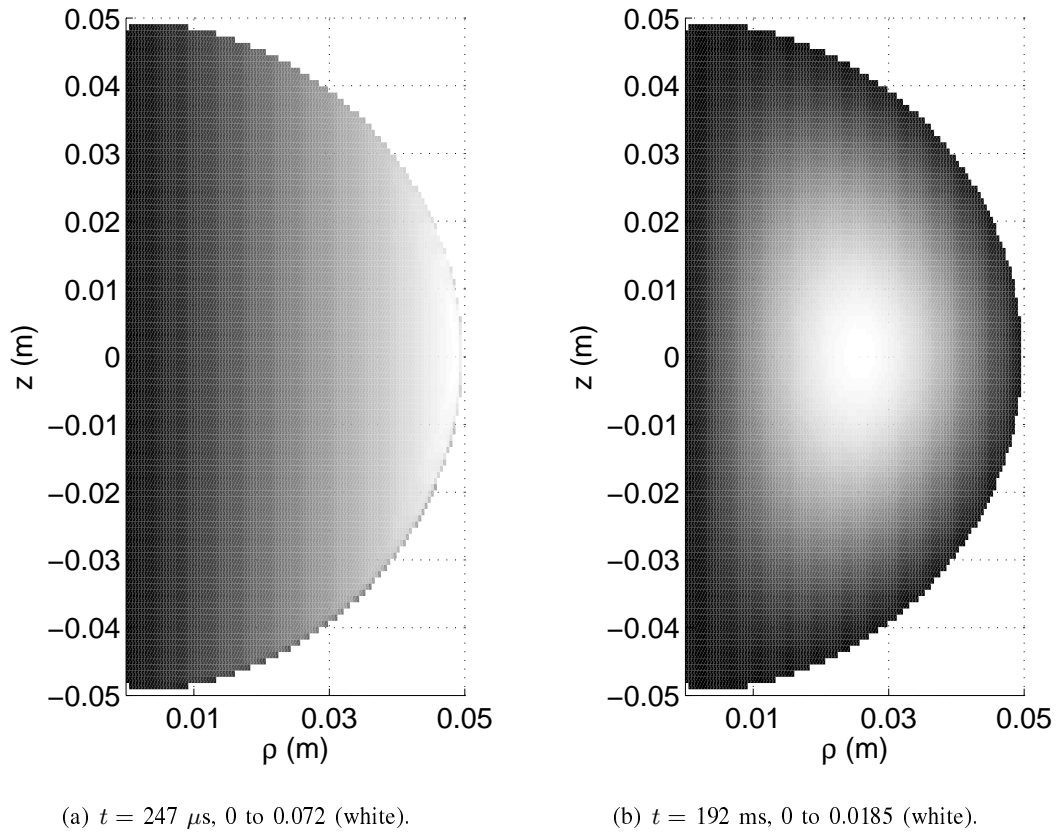


Fig. 7. Interior magnetic vector potential  $A_\phi$  for a sphere with  $r = 0.05 \text{ m}$ ,  $\sigma = 10^7 \text{ S/m}$ . Uniform axial primary field turned off at  $t = 0 \text{ s}$ .

$e$	Total Nodes	Surface Nodes	Axial Solve (s)	Transverse Solve (s)
4	596/3287	89/177	27/104	80/704
2	491/2611	73/149	22/79	61/491
1	400/2085	65/129	20/62	52/347
0.5	524/2745	73/145	23/82	69/558
0.25	634/3645	93/185	29/122	89/893

TABLE I

CPU TIMES (SECONDS) AND MESH SIZES FOR THE COARSE/FINE MESHES. MATLAB MESH GENERATOR USED, ENFORCING A 1 MM DISCRETIZATION AT THE SURFACE (2 GHz PENTIUM 4 WITH 512 MB OF RAM).

in time. For the  $\mu_r = 100$  case, the error is very low over the entire time history, with a maximum of between 0.01 and 0.05 at 0.1 s. Figure 13 shows the TSA normalized error for the induced field from the 5 cm radius sphere with various permeabilities. As the permeability increases, the skin depth decreases, and the TSA method accuracy improves. The maximum error is approximately 0.275 for the  $\mu_r = 1$  case. Without the interior mesh, the TSA method is very fast, solving the induced field in 6.2 seconds for the sphere and 9.0 seconds for the prolate ( $e=4$ ) spheroid (see Table I for FEM times). For magnetic objects (steel and iron for example), the TSA solution alone is sufficient to characterize the induced field for almost the entire time history. In such cases, TSA provides greater accuracy than the FEM as well as an order of magnitude reduction in CPU time.

For nonmagnetic materials, given that the TSA method is accurate in early to intermediate time, and

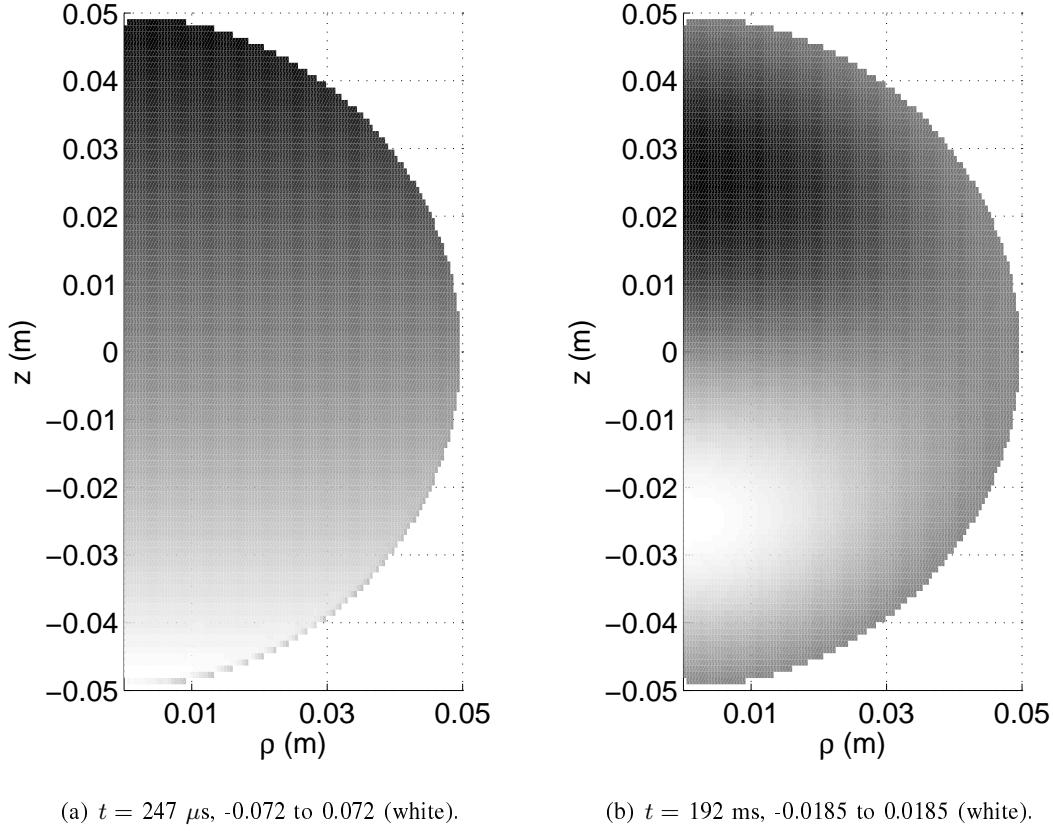


Fig. 8. Interior magnetic vector potential  $A_\rho$  for a sphere with  $r = 0.05 \text{ m}$ ,  $\sigma = 10^7 \text{ S/m}$ . Uniform transverse primary field turned off at  $t = 0 \text{ s}$ .

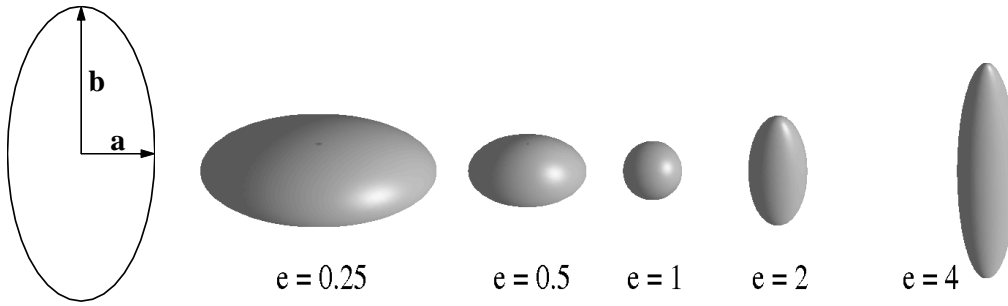


Fig. 9. Spheroid shapes whose EMI response is used to compare the FEM results with exact solutions. Elongation  $e$  is the ratio of  $b$  (on the  $z$  axis) to  $a$  (on the  $\rho$  axis).

the FEM method is accurate in intermediate to late time, it is natural to combine the two methods. The FEM method can be run efficiently on a relatively coarse mesh, while the TSA method is run separately. The two results are combined at the point in time where they converge the closest. Figure 14 shows the results for the axial and transverse excitation cases when  $\mu_r = 100$ . For the combined method, the maximum error occurs in intermediate time when the two methods converge. For the axial excitation case, the maximum error is 0.035 which occurs in the solution for the  $e = 0.5$  oblate spheroid (see Figure 12). Figure 15 shows the normalized error using the combined method for a sphere with various permeabilities. The maximum error is 0.025, which occurs for the  $\mu_r = 50$  case. The error of the combined method is very low regardless of the permeability.

Finally, it is useful to study the error of the combined method for larger time steps. In general, the

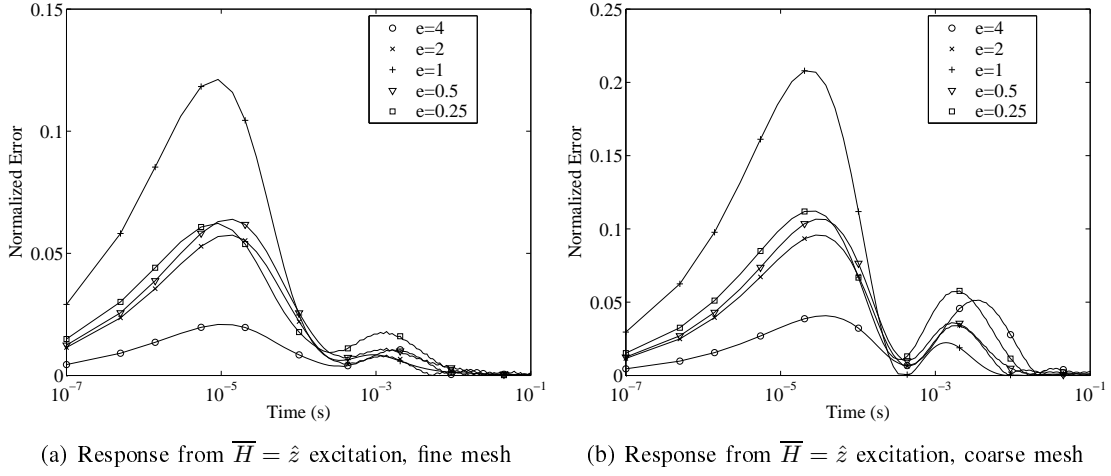


Fig. 10. FE Result. Normalized error of the induced magnetic field at  $z = 4b$  m, from spheroids with minor axis 0.05 m,  $\sigma = 10^7$  S/m,  $\mu_r = 100$ . Uniform primary field turned on at  $t = 0$  s.

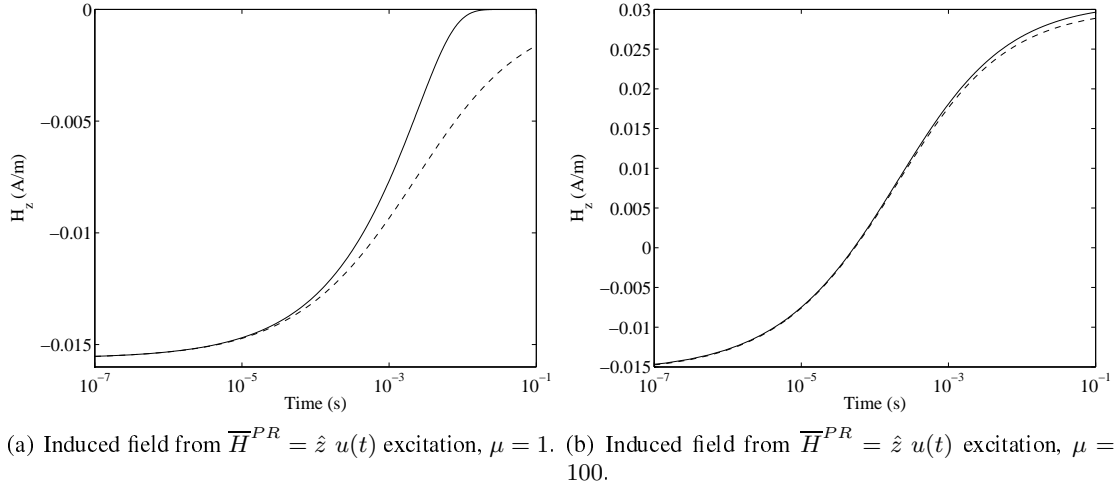


Fig. 11. Induced magnetic field at  $z = 0.2$  m, from a sphere with  $r = 0.05$  m,  $\sigma = 10^7$  S/m. Uniform primary field turned on at  $t = 0$ . Solid line is the analytical solution, dash line is the TSA-BI method.

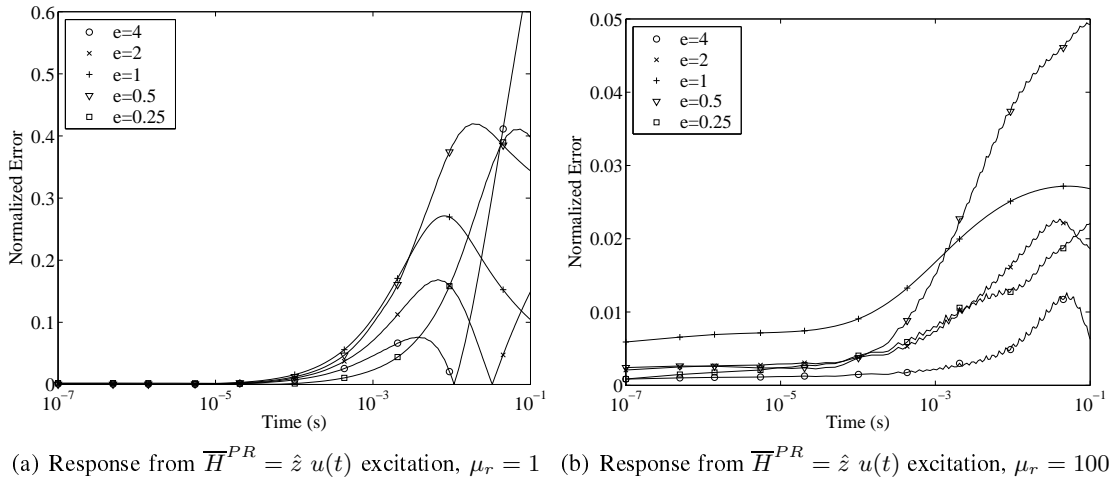


Fig. 12. TSA Result. Normalized error of the induced magnetic field at  $z = 4b$  m from various spheroids. Minor axis  $a$  or  $b = 0.05$  m  $\sigma = 10^7$  S/m. Uniform primary field turned on at  $t = 0$  s.

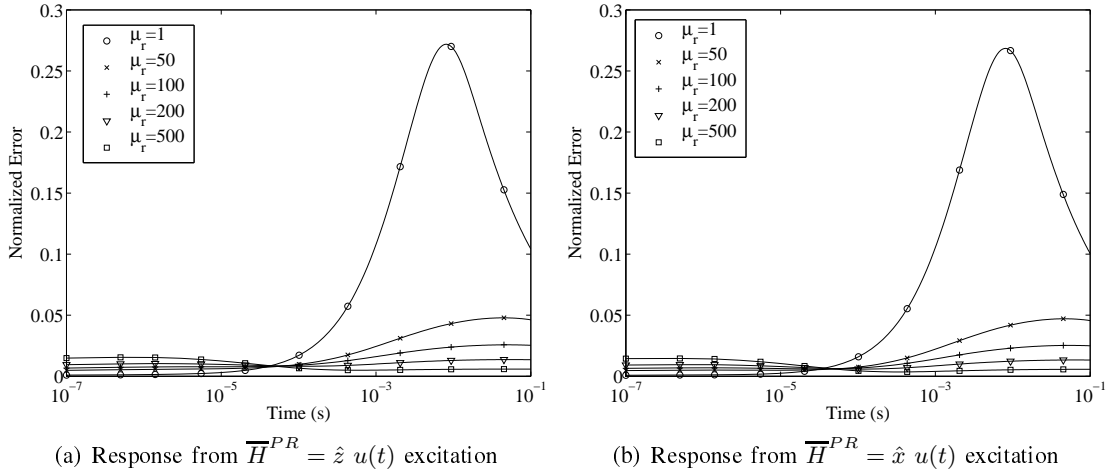


Fig. 13. TSA Result. Normalized error of the induced magnetic field at  $z = 0.2$  m, from a sphere with  $r = 0.05$  m,  $\sigma = 10^7$  S/m. Uniform primary field turned on at  $t = 0$  s.

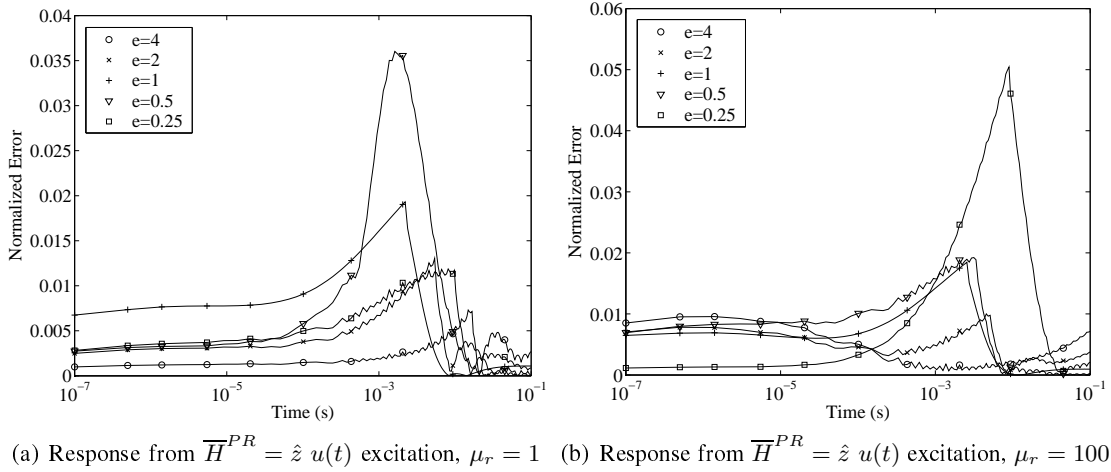


Fig. 14. FEM and TSA Combined result. Normalized error of the induced magnetic field at  $z = 4b$  m from various spheroids. Minor axis  $a$  or  $b = 0.05$  m  $\sigma = 10^7$  S/m. Uniform primary field turned on at  $t = 0$  s.

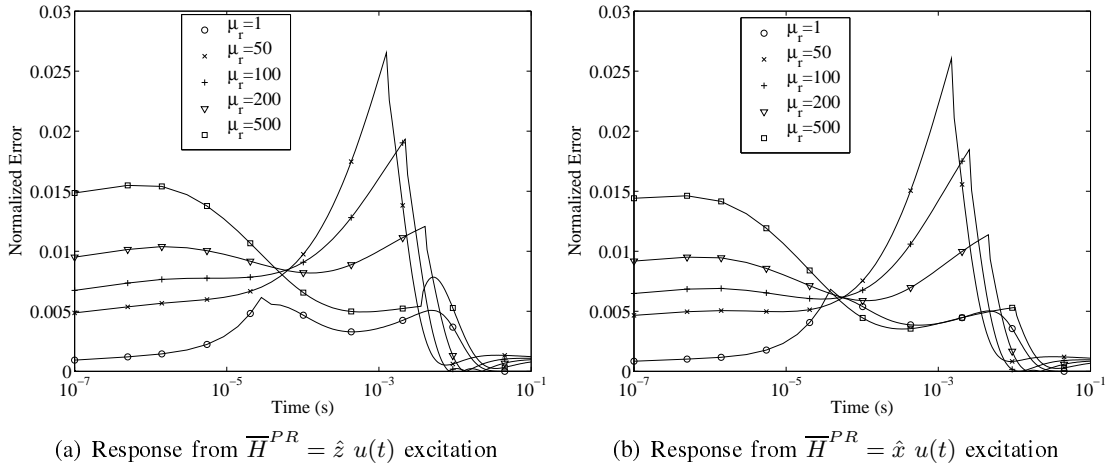


Fig. 15. FEM and TSA Combined result. Normalized error of the induced magnetic field at  $z = 0.2$  m, from a sphere with  $r = 0.05$  m,  $\sigma = 10^7$  S/m. Uniform primary field turned on at  $t = 0$  s.

Case	Solution Time (s)			
	$\gamma = 2$	$\gamma = 2.5$	$\gamma = 3$	$\gamma = 4$
$e = 4$ , Ax	38.6804	18.8927	12.2039	7.5153
$e = 4$ , Tr	92.5527	47.1724	30.9015	19.5674
$e = 2$ , Ax	33.1828	16.1154	9.7389	5.8130
$e = 2$ , Tr	73.3687	37.5907	23.7468	14.7628
$e = 1$ , Ax	31.7138	14.7736	9.0409	5.2574
$e = 1$ , Tr	63.0937	30.9593	19.9475	12.2008
$e = 0.5$ , Ax	45.6018	21.4460	13.1201	7.3437
$e = 0.5$ , Tr	91.0218	45.2780	29.0230	17.3571
$e = 0.25$ , Ax	49.2875	24.2587	15.2836	9.0718
$e = 0.25$ , Tr	111.3347	55.9075	36.2661	22.5182

TABLE II

CPU TIMES OF THE COMBINED METHOD FOR DIFFERENT TIME STEPS -  $t = m^\gamma \Delta_t$  WHERE  $\Delta_t = 10^{-7} s$  (2 GHz PENTIUM 4 WITH 512 MB OF RAM).

FEM and TSA methods may be adjusted to march in time as  $t = m^\gamma \Delta t_0$  (where  $\Delta t_0 = 10^{-7} s$ ). The implicit Euler method used for both methods accumulates error on order of  $\Delta t$ . For the previous results in Table I,  $\gamma = 2$  was chosen due to the  $\sqrt{t}$  evolution of diffusion equations. For this particular time step, the TSA and FEM methods are very accurate in their respective regions of validity, so any error due to time stepping is small. Hence,  $\gamma$  can be increased to achieve faster solution times while still maintaining reasonable accuracy. Tables II and III provide the CPU times and normalized error as  $\gamma$  is increased. All the cases dealt with earlier are presented in the tables. The maximum error increases slightly as  $\gamma$  increases, and the user can ultimately decide what compromise to make between accuracy and efficiency.

#### D. Turn Off Case

Some brief results for the turn off case are presented in this Section. The induced field from the 5 cm magnetic sphere is shown in Figure 16 for the TSA and FEM methods. In the axial excitation case, the induced field is initially positive as the circulating currents attempt to oppose the changing magnetic field. In the transverse case, the induced field is negative for the same reasons. In both cases the induced magnetic fields reach larger magnitudes than the turn on case (compare with Figure 4 for example) but have the same relative change before decaying to zero.

## IV. CONCLUSIONS

This paper presents a hybrid time domain numerical method that can calculate the EMI response from a UXO target with greater accuracy and speed than previously available. In response to a transient primary field, a conducting and permeable UXO target produces a transient secondary field. In early time, the fields within the target have a small skin depth that is difficult to model with conventional numerical methods like the FEM. To demonstrate this, an FEM/MoM method was implemented and shown to be inaccurate in early time. The ability to resolve very small skin depths in early time (or high frequency) was enabled by the TSA method that replaces the interior FEM and does not require an interior mesh. The TSA method produced a faster and more accurate solution to the EMI problem for early to intermediate time scales, compared to the FEM method. For certain materials, such as steel, the TSA method was shown to be accurate throughout the entire time of interest. In addition, for nonmagnetic materials, the methods were combined, so that the TSA solution was used for early time and the FEM method was used

Case	$\gamma = 2$	$\gamma = 2.5$	$\gamma = 3$	$\gamma = 4$
$e = 4, \text{Ax}, \mu = 1$	0.0149	0.0157	0.0169	0.0298
$e = 4, \text{Ax}, \mu = 100$	0.0073	0.0148	0.0101	0.0152
$e = 4, \text{Tr}, \mu = 1$	0.0150	0.0158	0.0170	0.0296
$e = 4, \text{Tr}, \mu = 100$	0.0096	0.0135	0.0192	0.0369
$e = 2, \text{Ax}, \mu = 1$	0.0080	0.0090	0.0145	0.0304
$e = 2, \text{Ax}, \mu = 100$	0.0130	0.0139	0.0153	0.0236
$e = 2, \text{Tr}, \mu = 1$	0.0078	0.0087	0.0141	0.0298
$e = 2, \text{Tr}, \mu = 100$	0.0100	0.0432	0.0163	0.0323
$e = 1, \text{Ax}, \mu = 1$	0.0280	0.0282	0.0282	0.0350
$e = 1, \text{Ax}, \mu = 100$	0.0174	0.0188	0.0216	0.0333
$e = 1, \text{Tr}, \mu = 1$	0.0219	0.0221	0.0228	0.0329
$e = 1, \text{Tr}, \mu = 100$	0.0276	0.0276	0.0278	0.0293
$e = 0.5, \text{Ax}, \mu = 1$	0.0036	0.0073	0.0132	0.0279
$e = 0.5, \text{Ax}, \mu = 100$	0.0192	0.0200	0.0216	0.0392
$e = 0.5, \text{Tr}, \mu = 1$	0.0065	0.0092	0.0140	0.0299
$e = 0.5, \text{Tr}, \mu = 100$	0.0360	0.0313	0.0338	0.0394
$e = 0.25, \text{Ax}, \mu = 1$	0.0037	0.0067	0.0118	0.0270
$e = 0.25, \text{Ax}, \mu = 100$	0.0118	0.0122	0.0133	0.0235
$e = 0.25, \text{Tr}, \mu = 1$	0.0165	0.0171	0.0180	0.0317
$e = 0.25, \text{Tr}, \mu = 100$	0.0504	0.0541	0.0553	0.0622

TABLE III

MAXIMUM NORMALIZED ERROR OF THE COMBINED METHOD FOR DIFFERENT TIME STEPS  $t = m^\gamma \Delta_t$  WHERE  $\Delta_t = 10^{-7} \text{ s}$ .

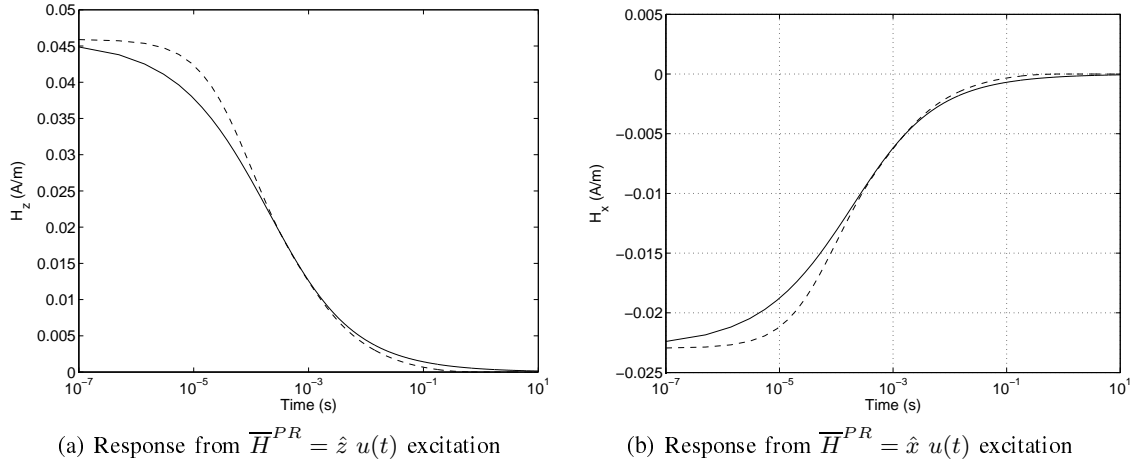


Fig. 16. Induced magnetic field at  $z = 0.2 \text{ m}$ , from a sphere with  $r = 0.05 \text{ m}$ ,  $\sigma = 10^7 \text{ S/m}$ . Uniform primary field turned off at  $t = 0 \text{ s}$ . The FEM is the solid line and the TSA is the dashed line.



(on an efficient mesh) for late time. Compared to the standard FEM method, the new combined method is much more accurate with comparable CPU requirements.

## V. APPENDIX

For the axial case where  $p = 0$ , the Green's function can be integrated over  $\phi$  to obtain

$$\tilde{g}_0(\bar{r}, \bar{r}') = \frac{K(m)}{\pi\sqrt{a+b}} \quad (34)$$

where  $K(m)$  is the complete elliptical integral of the first kind, and

$$\begin{aligned} a &= \rho^2 + \rho'^2 + (z - z')^2 \\ b &= 2\rho\rho' \\ m &= \sqrt{\frac{2b}{a+b}} \end{aligned}$$

The normal derivative of the Green's function integrated over  $\phi$  is

$$\begin{aligned} \frac{\partial \tilde{g}_0(\bar{r}, \bar{r}')}{\partial n'} &= \hat{n}' \cdot \hat{z}' \frac{E(m)(z - z')}{\pi(a-b)\sqrt{a+b}} \\ &+ \hat{n}' \cdot \hat{\rho}' \frac{\rho}{b\pi\sqrt{a+b}} \left( \frac{(a - 2\rho'^2)E(m)}{a-b} - K(m) \right) \end{aligned} \quad (35)$$

where  $E(m)$  is the complete elliptical integral of the second kind. For the transverse case where  $p = 1$ , we have

$$\tilde{g}_1(\bar{r}, \bar{r}') = \frac{-1}{\pi\sqrt{a+b}} \left[ \left( 1 - \frac{2}{m^2} \right) K(m) + \frac{2}{m^2} E(m) \right] \quad (36)$$

and

$$\begin{aligned} \frac{\partial \tilde{g}_1(\bar{r}, \bar{r}')}{\partial n'} &= -\hat{n}' \cdot \hat{z}' \frac{z - z'}{\pi b\sqrt{a+b}} \left[ K(m) - \frac{a}{a-b} E(m) \right] \\ &- \hat{n}' \cdot \hat{\rho}' \frac{1}{\pi b\rho'\sqrt{a+b}} \\ &\times \left[ (a - \rho'^2)K(m) - \frac{a(a - \rho'^2) - 2\rho^2\rho'^2}{a-b} E(m) \right] \end{aligned} \quad (37)$$

## REFERENCES

- [1] B. Johnson, T. G. Moore, B. J. Blejer, C. F. Lee, T. P. Opar, S. Ayasli, and C. A. Primmerman, "A research and development strategy for unexploded ordnance sensing," *Lincoln Laboratory Project Report, EMP-1*, Apr. 1996.
- [2] H. Nelson, *ESTCP Ongoing Project Review*, 1998.
- [3] C. D. Moss, "Finite-difference time-domain simulation of electromagnetic scattering from objects under random media," M.S. thesis, Massachusetts Institute of Technology, 2000.
- [4] D. K. Keiswetter, I. J. Won, B. Barrow, and T. Bell, "Object identification using multi-frequency EMI data," in *Proc. UXO Forum*, 1999.
- [5] H. Braunsch, C. O. Ao, K. O'Neill, and J.A Kong, "Magnetoquasistatic response of conducting and permeable prolate spheroid under axial excitation," *IEEE Trans. Geoscience and Remote Sensing*, vol. 39, no. 12, pp. 2689–2701, Dec. 2001.
- [6] B. E. Barrowes, K. O'Neill, T. Grzegorzczuk, X. Chen, and J.A Kong, "Broadband analytical magnetoquasistatic electromagnetic induction solution for a conducting and permeable spheroid," *IEEE Trans. Geoscience and Remote Sensing*, vol. 42, no. 11, pp. 2479–2489, Nov. 2004.
- [7] J. R. Wait and K. P. Spies, "Quasi-static transient response of a conducting permeable sphere," *Geophysics*, vol. 34, no. 5, pp. 789–792, Oct. 1969.
- [8] Y. Zhang, L. Collins, H. Yu, C.E. Baum, and L. Carin, "Sensing of unexploded ordnance with magnetometer and induction data: theory and signal processing," *IEEE Trans. Geoscience and Remote Sensing*, vol. 41, no. 5, pp. 1005–1015, May 2003.
- [9] N. Geng, C. E. Baum, and L. Carin, "On the low frequency natural response of conducting and permeable targets," *IEEE Trans. Geoscience and Remote Sensing*, vol. 37, no. 1, pp. 347–359, 1999.

- [10] L. Carin, H. Yu, Y. Dalichaouch, A. R. Perry, P. V. Czipott, and C. E. Baum, "On the wideband EMI response of a rotationally symmetric permeable and conducting target," *IEEE Trans. Geoscience and Remote Sensing*, vol. 39, no. 6, pp. 1206–1213, 2001.
- [11] F. Shubitidze, K. O'Neill, S. A. Haider, K. Sun, and K. D. Paulsen, "Application of the method of auxiliary sources to the wide band electromagnetic induction problem," *IEEE Trans. Geoscience and Remote Sensing*, vol. 40, no. 4, pp. 928–942, Apr. 2002.
- [12] D. Rodger, P. J. Leonard, H. C. Lai, and P. C. Coles, "Finite element modelling of thin skin depth problems using magnetic vector potential," *IEEE Trans. Magnetics*, vol. 33, no. 2, pp. 1299–1301, Mar. 1997.
- [13] A. Sebak, L. Shafai, and Y. Das, "Near-zone fields scattered by three-dimensional highly conducting permeable objects in the field of an arbitrary loop," *IEEE Trans. Geoscience and Remote Sensing*, vol. 29, pp. 9–15, 1991.
- [14] K. R. Shao and J. D. Lavers, "On the application of hinged finite elements to eddy current problems," *IEEE Trans. Magnetics*, vol. 23, no. 5, pp. 3059–3061, Sep. 1987.
- [15] K. R. Shao and J. D. Lavers, "A new hybrid method using hinged finite element formulations for the skin effect eddy current problems," *IEEE Trans. Magnetics*, vol. 26, no. 5, pp. 2765–2767, Sep. 1990.
- [16] C.O. Ao, H. Braunsch, K. O'Neill, and J.A Kong, "Quasi-magnetostatic solution for a conducting and permeable spheroid with arbitrary excitation," *IEEE Trans. Geoscience and Remote Sensing*, vol. 40, no. 4, pp. 887–897, Apr. 2002.
- [17] B. E. Barrowes, K. O'Neill, T. Grzegorzczuk, and J.A Kong, "On the asymptotic expansion of the spheroidal wave function and its eigenvalues for complex size parameter," *Studies in applied mathematics*, vol. 113, no. 3, pp. 271–301, Oct. 2004.
- [18] K. Sun, K. O'Neill, F. Shubitidze, S. A. Haider, and K. D. Paulsen, "Simulation of electromagnetic induction scattering from targets with negligible to moderate penetration by primary fields," *IEEE Trans. Geoscience and Remote Sensing*, vol. 40, no. 4, pp. 910–927, Apr. 2002.
- [19] C. A. Brebbia, J. C. F. Telles, and L. C. Wrobel, *Boundary Element Techniques*, Springer-Verlag, first edition, 1984.
- [20] Q. Chen, A. Konrad, and P. P. Biringer, "A finite element - Green's function method for the solution of unbounded three-dimensional eddy current problems," *IEEE Trans. Magnetics*, vol. 30, no. 5, pp. 3048–3051, Sep. 1994.
- [21] M. Ayoub, F. Roy, F. Bouillault, and A. Razek, "Numerical modelling of 3D magnetostatic saturated structures with a hybrid FEM-BEM technique," *IEEE Trans. Magnetics*, vol. 28, no. 2, pp. 1052–1055, Mar. 1992.
- [22] P. P. Silvester and R. L. Ferrari, *Finite Elements for Electrical Engineers*, Cambridge University Press, third edition, 1996.
- [23] X. Chen, K. O'Neill, B. E. Barrowes, T. M. Grzegorzczuk, and J. A. Kong, "Application of a spheroidal-mode approach and a differential evolution algorithm for inversion of magneto-quasistatic data in UXO discrimination," *Inverse Problems*, vol. 20, pp. 27–40, 2004.
- [24] F. J. Rizzo and D. J. Shippy, "A boundary integral approach to potential and elasticity problems for axisymmetric bodies with arbitrary boundary conditions," *Mechanics Research Communications*, vol. 6, no. 2, pp. 99–103, 1979.
- [25] C. Pozrikidis, *Numerical Computation in Science and Engineering*, Oxford University Press, first edition, 1998.
- [26] J. Crank, *The Mathematics of Diffusion*, Clarendon Press, second edition, 1975.